X-ray Study of the Outer Regions of Clusters of Galaxies

Akio Hoshino

Department of Physics, Tokyo Metropolitan University
1-1 Minami-Ohsawa, Hachioji, Tokyo 192-0397, Japan

February 2010

ABSTRACT

X-Ray Study of the Outer Regions of Clusters of Galaxies

Northern outskirts of the relaxed cluster of galaxies A1413 was observed with Suzaku in the radial range of $2.'7 - 26'$ covering the virial radius of $r_{200} = 14'.8$. We excised 15 point sources above a flux of $\sim 1 \times 10^{-14}$ erg cm^{-2} s^{-1} (2–10 keV), and the CXB level after the point source excision was evaluated. We quantify all known systematic errors, and show statistical errors are dominant. Suzaku detected X-ray emission of the ICM up to the $15' - 20'$ annulus beyond the virial radius.Significant temperature decrease to ~ 3 keV (factor of ~ 2) at r_{200} is confirmed. Such profile is also reported in a few other clusters, PKS0745−191, A1795.

We also analyzed the outer regions of A2204 with *Suzaku* and *XMM-Newton*. A2204 is $z = 0.1523$ and $r_{200} = 11'.5$. We extracted four cluster region ($0' - 3'.5$, $3'.5 - 7'.5$, $7'.5 - 11'.5$, and $11'.5 - 15'.5$) and background region in $15'.5 - 19'.5$. We fixed CXB normalization as 100% CXB. Because in the observation period of *Suzaku*, proton density origined by solar activities is relatively high, the energy spectra is contaminated by SWCX below 1 keV. For example, oxygen line emissions are 10 times higher than in the case of A1413. In the spectral analysis, we ignored below 0.7 keV. We could measured temperature profile of A2204 within r_{200}. We could measured temperature over r_{200}.

We analyzed two pointing observation of the outer region of AWM7 to find out difference of direction to filament. AWM7 has anti-symmetric elliptical shape with about 0.8 of ellipticity. We fit 2 dimensional 2β egg model to *XMM-Newton* image. We generated ARF with this simulated image. We detected 4 and 6 point sources in east and south region. We measured electron temperature in east and south FOVs with $1.62^{+0.62}_{-0.37}$ keV and $0.45^{+0.13}_{-0.06}$ keV. When we correct stray light with *xissim* simulation, the south ICM component is negligible and the east temperature is turn to $2.53^{+3.88}_{-1.50}$ keV.

We tried to explain our measured temperature and surface brightness of A1413 and A2204 with SSM model which is cluster model with 6 parameters assuming spherical symmetry and hydrostatistic equilibrium. We found that, although we could fit either the temperature or surface brightness profile, it was not possible to simultaneously fit both despite an exhaustive search of parameter space. The likely reason for this result is that the ICM is out of equilibrium in the outer regions of the cluster.

Our entropy profile in the outer region ($> 0.5\, r_{200}$) joins smoothly onto that of XMM-Newton at 0.15–0.5 r_{200}, and shows a flatter slope of $\gamma = 0.90 \pm 0.12$ for A1413 and $\gamma = 0.45 \pm 0.27$ for A2204 in $3'.5 - 15'.5$ than $\gamma = 1.1$ obtained with numerical simulations of adiabatic gas accretion. The flattening of entropy profile also can be measured by PKS0745-191 and A1795. These common point is that entropy profiles wind and start flattening from about 1 Mpc except for A1413. Because A1413 shows different trend, it is possible not to be the universal profile. These indication suggests that electron and ion temperatures are different in clusters of galaxies depending on their evolution. Especially, over the 1 Mpc which is about $0.6 r_{200}$, their thermal conditions have the border of their phase observationally because of the out of their equilibration timescale.

Deviation of the entropy profile would show electron temperature is not equal to gas temperature in outer region, where equilibration timescale for electron-ion collision, $t_{\rm ei}$,

is comparable with 1 Gyr order. These results means that if merging gas within 1 Gyr order, the gas conditions are not in equilibrium still now.

The integrated mass of the cluster at the virial radius is approximately $7.5 \times 10^{14}\ M_{\odot}$ for A1413 and varies by $\sim 30\%$ depending on temperatures ($T_{\rm e}$, $T_{\rm gas}$) and < 8.2 % depending on definition of temperatuers ($T_{\rm ew}$, and $T_{\rm sl}$) which we use.

CONTENTS

List of Figures

List of Tables

Chapter 1

Introduction

A wide variety of cosmological observations now support a model which explains the overall architecture of the universe and the development of galaxies and other structures within it. In this picture, regions in which matter density exceeds the mean density are collapsed, gravitationally bound and evolve to large scale structures hierarchically. Such evolution model is called "bottom-up scenario", which is one of the reliable model of dynamical evolution of the universe (Voit 2005).

Clusters of galaxies form from such collapse of density perturbations having a typical size of the order of 10 Mpc. They are the largest self-gravitating system in the universe which contains dozens to thousands of galaxies bound gravitationally within a few Mpc scale. Clusters of galaxies consist of X-ray emitting hot plasma with typical temperatures of a few times 10^7 K with about 5 times the mass of galaxies. The evolution of structures involving clusters and larger scales is mainly driven by gravitational instability of the dark matter (DM) density perturbations.

Cluster of galaxies can be used as both invaluable cosmological tools and astrophysical laboratories. These two aspects are clearly interconnected with each other. The evolution of the population of clusters and their overall baryonic content provide powerful constraints on cosmological parameters. Also we learn a lot of unique physics from the observed properties of the intra-cluster medium (ICM) and its interaction with the galaxy population.

Observations of clusters of galaxies offer a number of well established cosmological tests relying on the cold dark matter (CDM) paradigm, in which clusters are composed mostly of collision-less CDM and virialized objects form from initial density perturbations. CDM paradigm predicts dynamical evolution and structure of our universe through numerical simulations, and are used to calibrate essential theoretical ingredients for cosmological tests, such as detailed shape of mass functions or average baryon bias within clusters. In this framework, clusters of galaxies have self-similarity as their basic properties (Zhang et al. 2007; Borgani et al. 2004; Roncarelli et al. 2006). They predict that physical parameters such as temperature, surface brightness, gravitational mass profiles distribute in almost the same way when normalized with redshift or virial radius.

In understanding the structure and evolution of dark-matter dominated clusters, the

most important parameters are temperature and gravitational mass profile because these parameters indicates dark matter distribution and its fraction compared with baryons. Especially, Navarro et al. (1996) has reported common density profile of dark matter in clusters of galaxies called as NFW profile. Suto et al. (1998) analytically derived gas density and temperature profile (non-isothermal SSM model) based on dark matter distribution in clusters of galaxies in the case of NFW and Moore models.

The main aim of this thesis is to look into the mass structure and ICM properties to the outermost regions of clusters of galaxies. Past X-ray observations, even with *Chandra* and *XMM-Newton*, have explored only a small fraction of the total volume of clusters. Outer regions of cluster carry a large fraction of baryons. These are the places where matter accretes from the surrounding field and where the ICM is heated. These low surface brightness regions are also connected to the large scale filamens which should be filled with warm-hot intergalactic medium (WHIM), namely the dark baryons in the present universe. With these original sciences, regions near the virial radii of clusters are regarded as a new frontier in the X-ray astronomy. Our aim is to obtain the first real observational knowledge about the ICM in these regions.

Outer regions of clusters have so far escaped from detailed observational study, mainly due to its extremely low surface brightness. The flux from a unit solid angle goes down by a factor of more than 10^4, and X-ray measurement has been severely hampered by both X-ray and non-X-ray background. These technical difficulties are the reason why cluster temperatures have not been measured much beyond about half of the virial radius and, until recently, the shape of the temperature radial profile was a matter of heated debate even to that radius. Now independent measurements using several different observatories are consistent with a factor of ~ 2 decline of the projected temperature from the center to half the virial radius, at least for relaxed clusters (Markevitch et al. 1998; De Grandi & Molendi 2002; Vikhlinin et al. 2005; Piffaretti et al. 2005; Pratt et al. 2007).

ASCA with the first application of CCD instruments along with gas scintillation proportional counters opened the possibilities of imagin X-ray spectroscopy. *ASCA* observations, despite their modest spatial resolution, have established that most of the clusters show significant departures from isothermality, with negative temperature gradients characterized by a remarkable degree of similarity, out to the largest radii sampled (Markevitch et al. 1998). *Beppo-SAX* observations confirmed these features for a larger number of clusters (e.g. De Grandi & Molendi 2002). *Chandra* and *XMM-Newton* provided great knowledge on clusters of galaxies with their improved sensitivity. *Chandra* showed detailed picture of the ICM distribution and central temperature profiles (Vikhlinin et al. 2005; Baldi et al. 2007) with their ASIS X-ray CCD camera. At the same time, *XMM-Newton* observations gave a concrete evidence for the absence of large-scale cooling flows (Peterson et al. 2001) and showed the presence of a negative temperature gradient at radii $> 0.1\, r_{200}$ (Piffaretti et al. 2005; Pratt et al. 2007; Pointecouteau et al. 2005). They revealed clusters of galaxies are generally characterized by a declining temperature profile toward the center and outer region within 60% of virial radius.

Suzaku is the fifth in the series of Japanese X-ray astronomy satellites devoted to observations of celestial X-ray sources by Japan Aerospace Exploration Agency (JAXA) launched on July 10, 2005. One of the main instruments is the X-ray Imaging Spectrometer (XIS), consisting of four X-ray charge-coupled devices (CCDs). Three sensors out of four have front-illuminated (FI) CCDs, while the other one has a back-illuminated (BI) CCD (Koyama et al. 2007). The background levels for unit field of view are much lower than those of the *XMM-Newton* EPIC and the *Chandra* ACIS. *Suzaku* XIS is, therefore, best suitable for the measurement of faint and extended sources such as the outermost regions of clusters.

In the study of extended X-ray objects, background subtraction is critical in obtaining accurate information about the emission region. The background can be broadly divided into non X-ray background (NXB), cosmic X-ray background (CXB) and the Galactic emission. The Galactic emission is considered to originate from the local hot bubble (LHB) and the Milky Way halo (MWH). CXB is the sum of emission from all the extra-galactic sources in the X-ray energy band. Reliable modeling of these components is particularly important in studying the density and temperature of ICM in the outer regions of clusters.

In this thesis, we present results from Suzaku observations of A1413, A2204 and AWM7. The targets are suitable for the study of outer regions because of their relaxed nature, high intensity, and adequate ICM temperatures. By taking advantage of the low-background nature of *Suzaku* XIS, we are able to measure the temperture and surface brightness profiles near the virial radius. With these new data, we look into the ICM properties such as entropy profile and equilibration time scales, and compared with model predictions. These results are combined for the estimation of the gravitational mass profile out to the virial radius. We use $H_0 = 70$ km s^{-1} Mpc^{-1}, $\Omega_\Lambda = 1 - \Omega_M = 0.73$. Unless otherwise noted, we employ the solar abundance table by Anders & Grevesse (1989).

Chapter 2

Review of Cluster of Galaxies

2.1 Structure and evolution of the universe

2.1.1 Expansion dynamics

We will briefly look into the general view about the dynamical evolution of the unverse, following the review by Voit (2005). On very large scales, the universe appears homogenous and isotropic. Time-dependent behavior of the scale factor a obeys the Friedmann-Lemaitre model of the universe,

$$\frac{\ddot{a}}{a} = -\frac{4}{3}\pi G\left(\rho + \frac{3p}{c^2}\right), \tag{2.1}$$

where $\rho(t)c^2$ is the mean density of mass-energy and $p(t)$ is the pressure due to the energy density. If the equation of state takes the form $p = w\rho c^2$, density changes with the expansion as $\rho \propto a^{-3(1+w)}$. The scale factor is set to be unity at the current time. Then the cosmological redshift z of distant objects is simply related to the scale factor as $a = (1+z)^{-1}$. This definition gives the following relation,

$$\left(\frac{\dot{a}}{a}\right)^2 = H_0^2\left[\Omega_0(1+z)^{3(1+w)} + (1-\Omega_0)(1+z)^2\right], \tag{2.2}$$

where Ω_0 is the current energy density ρ_0 in units of the current critical density $\rho_{\rm cr0} = 3H_0^2/8\pi G$. Including all the components, we obtain the dynamical equation

$$H^2(z) = \left(\frac{\dot{a}}{a}\right)^2 = H_0^2\left[\Omega_M(1+z)^3 + \Omega_R(1+z)^4 + \Omega_\Lambda + (1-\Omega_0)(1+z)^2\right], \tag{2.3}$$

with Ω_R the radiation energy density and all Ω parameters indicating the current mass-energy density in units of $\rho_{\rm cr0}$. Also, the density parameter is given as $\Omega_0 = \Omega_M + \Omega_R + \Omega_\Lambda$. If non relativistic particles with a mass density ρ_M contibutes negligible pressure, then $w = 0$. The energy density $\rho_R c^2$ in photons and other relativistic particles exerts a pressure with $w = 1/3$. Einstein's cosmological constant acts like an energy density $\rho_\Lambda c^2$ that remains constant while the universe expands and therefore exerts a pressure corresponding to $w = -1$.

In figure.2.1, we show the evolution of energy densities for ΛCDM universe. Structure in the universe grows most rapidly while $\Omega_M(z) \simeq 1$, because positive density perturbations then exceed the critical density. The redshift at which $\Omega_M(z)$ begins to decline depends on the characteristics of dark energy. Observations of clusters and their evolution provide opportunities to constrain the values of Ω_M, Ω_Λ and w because these parameters influence the properties of the cluster population.

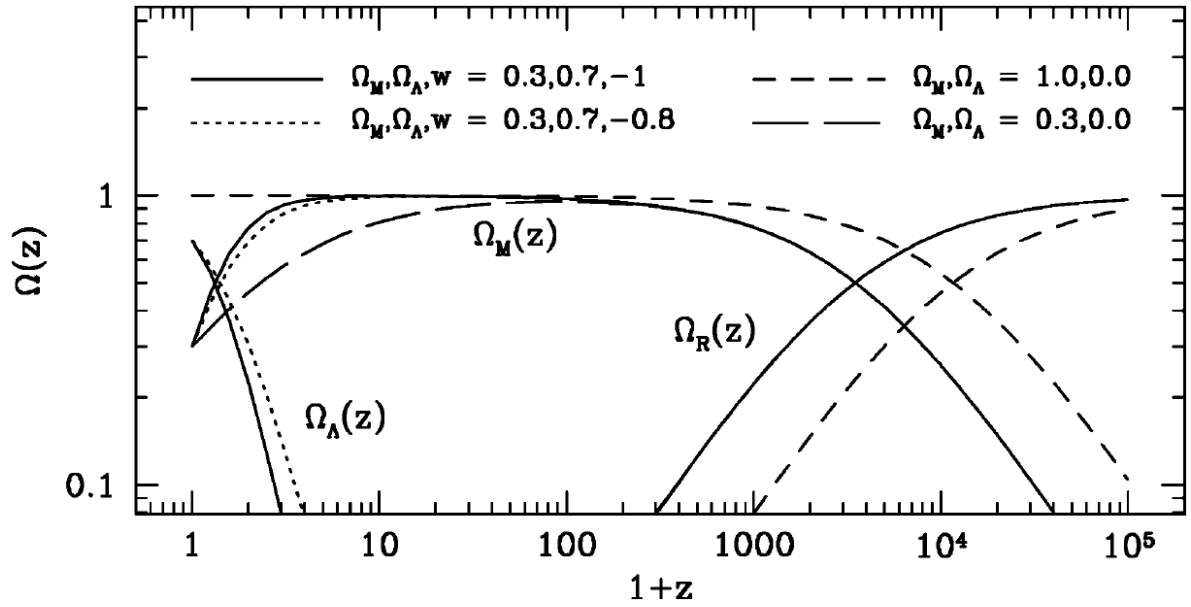

Fig. 2.1: Evolution of energy densities with redshift for different cosmological models(Voit 2005). Solid lines: the concordance model with $\Omega_M = 0.3, \Omega_\Lambda = 0.7$, and $w = -1$; dotted lines: a dark-energy model with $\Omega_M = 0.3, \Omega_\Lambda = 0.7$, and $w = -0.8$; long-dashed lines: an open-universe model with $\Omega_M = 0.3, \Omega_\Lambda = 0.0$; short-dashed lines: a critical-universe model with $\Omega_M = 1.0, \Omega_\Lambda = 0$ (Einstein-de-Sitter model).

2.1.2 Hierarchical structure formation

At present, the hierarchical clustering scenario is widely supported, because it is naturally expected from the cold dark matter model. Also, the fact that the galaxies at redshifts ~ 5 have been observed, whereas the most distant observed clusters is at $z \sim 1$, indicates that small systems have been formed first.

According to the bottom-up scenario, large-scale structures of the universe have formed from infinitesimally small density perturbations at the early universe through the gravitational interaction, and we can recognize three fundamental building blocks: stars, galaxies, and clusters of galaxies. A number of numerical simulations for the structure formation have shown producing the large-scale structures and clusters of galaxies. This result is recognized as a strong support to the hierarchical clustering scenario. Following an early work by White's 700-body simulations (1976), calculations such as the one by

Eke et al. (1998) include N-body/gas-dynamical simulations which are designed to investigate the evolution of clusters. Borgani & Guzzo (2001) compared the evolution of universe in different universe models of $\Omega_m = 0.3$ of low Ω_m cosmology and $\Omega_m = 1$ of Einstein-deSitter (EdS) cosmology in figure 2.2. Despite the similar pattern produced at the present time (z = 0), the past pattern of the universe is very different. This evolutionary difference represents one of the motivations for the deep X-ray searches of clusters down to a very faint flux levels. Clusters at z $\simeq$ 0.5 are no longer considered as exceptions, and even a few examples at $z > 1$ are now known. The main result reached these surveys is the evidence for a weak evolution of the bulk of the cluster population out to $z \simeq 1$, again consistent with the picture of a low-Ω_m universe.

Hierarchical clustering for the hot gas and dark matter from matter aggregates that have reached an approximate dynamical equilibrium giving them their characteristic shapes, and indicates that the clusters are formed through sub-cluster mergers and/or absorption of groups of galaxies. Thus, the evolution of the galaxy cluster population is tightly connected to the evolution of the large-scale structures and the universe as a whole. It is for this reason that observations of galaxy clusters can be used to trace the evolution of the universe and to test cosmological models.

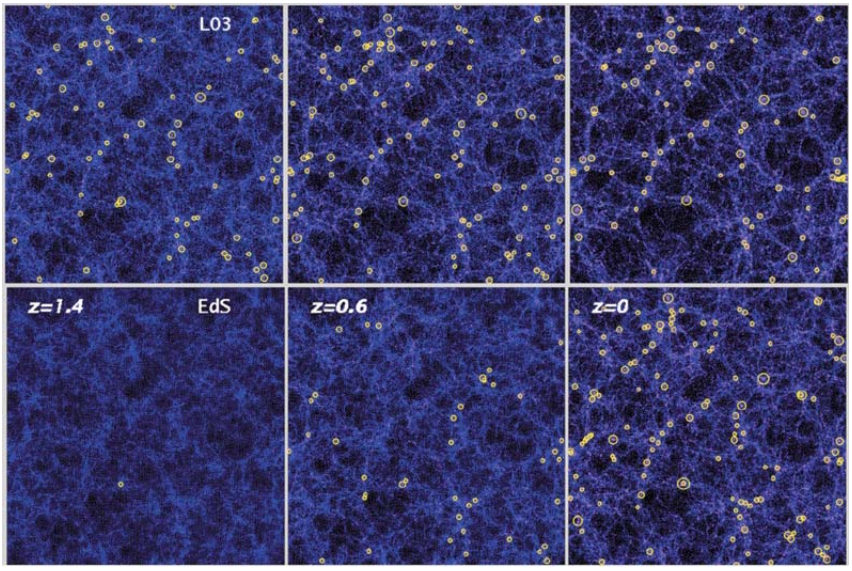

Fig. 2.2: Evolution of gravitational clustering simulated using an N-body code for two different models (Borgani & Guzzo 2001). Each of the three red shift snapshots shows a region with sides of $250h^{-1}$Mpc and thickness of $75h^{-1}$ Mpc comoving with the cosmic expansion. The upper panels describe a flat low-density model with $\Omega_m = 0.3$ and $\Omega_\Lambda = 0.7$, and the lower panels show an Einstein-de-Sitter model (EdS) with $\Omega_m = 1$. In both cases the amplitude of the power spectrum is consistent with the number density of nearby galaxy clusters and with the large-scale CMB anisotropies. Yellow circles mark the positions of galaxy clusters with $kT > 3$ keV. The size of the circles is proportional to temperature.

2.1.3 Collapse condition

We will briefly review the collapse scenario according to the spherical collapse model. First of all, consider a mass shell designated by i with a radius r_i at epoch $t = t_i$, which is moving with the general expansion until $t = t_i$ (Peebles 1980). The kinetic energy per unit mass of the shell relative to the center is,

$$K_i = \frac{1}{2}(H_i r_i)^2, \tag{2.4}$$

where H_i is the Hubble constant at $t = t_i$. Suppose that the average density inside the shell, $\bar{\rho}_i$, is higher than the homogeneous background, $\rho_{b,i}$, by a factor $1 + \delta$, i.e.

$$\begin{aligned} \bar{\rho}_i &= \rho_{b,i}(1+\delta) && (2.5)\\ &= \frac{3}{8\pi G}\Omega_i H_i^2(1+\delta), && (2.6) \end{aligned}$$

where Ω_i is the density parameter at $t = t_i$. Then the potential energy per unit mass of the shell whose mass is M_i is,

$$\begin{aligned} W_i &= -\frac{GM_i}{r_i} = -\frac{4\pi G\bar{\rho}_i r_i^3}{3r_i} && (2.7)\\ &= -\Omega_i K_i(1+\delta). && (2.8) \end{aligned}$$

Thus, the total energy is

$$\begin{aligned} E &= K_i + W_i && (2.9)\\ &= \frac{W_i}{1+\delta}\left[\delta - \left(\frac{1}{\Omega_i} - 1\right)\right]. && (2.10) \end{aligned}$$

Since $W_i < 0$ and $\Omega_i < 1$, the following condition

$$\delta > \frac{1}{\Omega_i} - 1, \tag{2.11}$$

in other words,

$$\bar{\rho}_i = (1+\delta)\Omega_i\rho_{crit,i} > \rho_{crit,i}, \tag{2.12}$$

gives the total energy negative and the shell will eventually collapse. Here, we use the critical density $\rho_{crit,z}$ at the redshift z as,

$$\rho_{crit,z} = \frac{3H_z^2}{8\pi G}, \tag{2.13}$$

where

$$H_z = H_0\ E(z), \tag{2.14}$$

$$E^2(z) = \Omega_0(1+z)^3 + \Omega_\Lambda, \tag{2.15}$$

$$\Omega_0 = \frac{8\pi G\rho_0}{3H_0^2}; \qquad \Omega_\Lambda = \frac{\Lambda}{3H_0^2}. \tag{2.16}$$

Here ρ_0 is the non-relativistic matter density, H_0 is the current Hubble constant, and Λ is the cosmological constant.

If the density parameter, Ω_i, is close to unity, density perturbations with a small amplitude can collapse. Thus clusters of galaxies are effectively formed in such epochs. Figure.2.3 shows the dynamics of over-dense spheres. The larger initial over-density, the earlier the sphere's expansion halts. A system would expand spherically without self-gravitation in an acceralating universe, while gravity stops the expansion and collapses it into a virialized system with sufficiently high density. A system with larger initial over-density collapses earlier into smaller virialized system. The clusters of galaxies, which are the largest virialized systems, have $\rho/\rho_{\rm crit} > 200$ or $\delta > 500$.

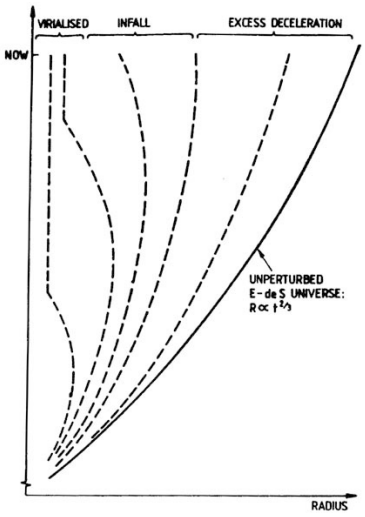

Fig. 2.3: The dynamics of over-dense spheres in the expanding universe. (Rees 1992)

2.1.4 Warm-Hot Inter-cluster Medium

The study of warm-hot intergalactic medium (WHIM) is the remaining frontier of X-ray astronomy. The importance of the observational study of WHIM are as follows. First, WHIM carries about 50% of the baryonic matter in the present universe. Locating WHIM gives us an answer to the question of missing baryon problem paused by Fukugita et al.(1998) . WHIM is the best tracer of the large-scale structure of the universe. Galaxies by optical surveys or clusters of galaxies by X-rays only shows us the densest part of the filamentary structure. WHIM reveals the fainter part of the filament and enables us to see the structure of dark matter very clearly. WHIM holds the thermal history of the universe. WHIM has been ionized, heated and metal-enriched through the past star, galaxy structure-formation processes, therefore thermal and chemical properties of the WHIM would be very useful source to look into the thermal history of the universe.

2.2 Clusters of Galaxies

Clusters of galaxies are the largest well-defined structures in the universe, with a typical linear dimension of 1-3 Mpc. A cluster consists of 100-1000 member galaxies, with the size ranging from the cD galaxy, which belongs to the most luminous galaxy class in the universe, to dwarf galaxies.

In the early 1930s, Zwicky measured velocities of member galaxies in the Coma cluster, and found that they are traveling too fast (~ 1000 km s^{-1} in average) to be gravitationally bound unless the total mass in the cluster greatly exceeds that corresponding to optical luminosities of member galaxies. This is the first evidence for large-scale dark matter. Subsequent measurements velocity dispersions of rich clusters were found typically to be 700 km s^{-1}, implying mass-to-light ratios of $M_{\rm total}/L_{\rm total} \sim 150 - 400\ M_\odot/L_\odot$ (e.g. Peebles 1993). Here $M_{\rm total}$ and $L_{\rm total}$ are the total dynamical mass and the total optical luminosity, respectively. In contrast, individual galaxies typically have mass-to-light ratios of 10 $M_\odot/L_\odot$ in their luminous central regions.

With cosmic X-ray observation, witch started in the 1960s, clusters were found to be the most luminous class of X-ray sources in the universe after some types of active galactic nuclei (AGNs). The X-ray emission originates from the intracluster medium (ICM), namely a hot ($10^7 - 10^8$ K) and low density ($10^{-4} - 10^{-2}$ cm^{-3}) plasma in the intracluster space. Extensive observation with previous X-ray satellites provided measurements of densities and temperatures of the ICM. These results implied that the mass if the ICM is greater than that of the stellar component in member galaxies. Characteristic emission lines from ionized heavy elements were detected in the X-ray spectra of clusters. The implied sub-solar metallicity of the ICM indicates that the ICM is a mixture of the primordial gas and that reprocessed in the stellar interior. Moreover, X-ray observations of the ICM have provided independent and more accurate measurements of the total mass, and hence of the dark matter, in clusters of galaxies. According to a contemporary consensus, about $5 - 10$ % of a cluster mass is in the stellar component, another $10 - 20$ % is in the ICM, and the rest is in dark matter.

2.2.1 Virial radius and the virial density

Let us consider a time variation of a radius $r(t)$ fixed on a spherical shell. The force on the shell comes from the gravity due to a mass M inside the shell. Since our shell is fixed to matter, the change of r does not affect M. The, the equation of motion is,

$$\frac{d^2r}{dt^2} = -\frac{GM}{r^2} \tag{2.17}$$

Using a simple relation,

$$\frac{d}{dt}\left[\left(\frac{dr}{dt}\right)^2\right] dt = 2\frac{d^2r}{dt^2}dr, \tag{2.18}$$

we obtain the first integral of this equation as,

$$\left(\frac{dr}{dt}\right)^2 = \frac{2GM}{r} + 2\epsilon. \tag{2.19}$$

ϵ is a constant, corresponding to the energy per unit mass. In case of $\epsilon < 0$, the collapse will occur. The solution of equation 2.19 is given in a parametric form,

$$t = \frac{GM}{|2\epsilon|^{3/2}}(\theta - \sin\theta) \tag{2.20}$$

$$r = \frac{GM}{|2\epsilon|}(1 - \cos\theta). \tag{2.21}$$

The radius, r, is 0 at $t = 0$, i.e. $\theta = 0$. Then it increases with increasing θ. It takes the maximum,

$$r_m = \frac{GM}{|\epsilon|} \tag{2.22}$$

at $\theta = \pi$, i.e.

$$t = t_m = \frac{\pi GM}{|2\epsilon|^{3/2}} \tag{2.23}$$

(turn around). Then, it shrinks to 0 again at $\theta = 2\pi$, i.e.

$$t = t_c = \frac{2\pi GM}{|2\epsilon|^{3/2}} \tag{2.24}$$

(collapse). After collapse, the system will be virialized. In the virialized system, the potential energy W is related to the total energy $E(= \epsilon M)$ as $W = 2E$ (Virial theorem). Assuming the radius of the system after virialization is r_{vir}, we have

$$W = -\frac{GM^2}{r_{vir}} = 2E = -2\frac{GM^2}{r_m}. \tag{2.25}$$

Therefore, $r_{vir} = r_m/2$. The average density inside the virial radius r_{vir} is

$$\bar{\rho}_{vir} = \frac{6}{\pi}\frac{|\epsilon|^3}{G^3M^2}. \tag{2.26}$$

On the other hand, the solution of equation 2.19 with $\epsilon = 0$ describes the background expansion, because $\Omega \sim 1$. The solution is

$$\rho_{vir} = \left(\frac{9}{2}GM\right)^{1/3} t^{2/3}. \tag{2.27}$$

Thus we obtain the important relation,

$$\Delta_{crit} = \frac{\bar{\rho}_{vir}}{\rho_{crit}} = 18\pi^2. \tag{2.28}$$

We can assume that a cluster is virialized within the radius in which the average density is equal to Δ_{crit} times the critical density of the collapsed epoch.

For a ΛCDM cosmology, Δ_{crit} is described as

$$\Delta_{crit} = 18\pi^2 + 82x - 39x^2, \tag{2.29}$$

where

$$x = \Omega(z) - 1, \tag{2.30}$$

$$\Omega(z) = \frac{\Omega_0(1+z)^3}{\Omega_0(1+z)^3 + \Omega_\Lambda}, \tag{2.31}$$

(Bryan & Norman 1998).

As discussed in Navarro et al. (1996), clusters of different scales are expected to show similar structures when scaled to such a virial radius. For the calculation of r_{180}, we used the $r_\delta - T$ relation obtained from the numerical simulation by Evrard et al. (1996),

$$r_{180} = 1.95h^{-1}(T_X/10\ \mathrm{keV})^{1/2}(1+z)^{-3/2}\ \ \mathrm{Mpc}, \tag{2.32}$$

where T_X is emission-weighted temperature of the ICM.

2.2.2 X-ray emission process

The X-ray spectrum emitted from an ionized plasma of the low density ($\sim 10^{-3}$ cm^{-3}) ICM is described with a combination of thermal bremsstrahlung (free-free) emission and line emission from heavy elements. In the temperature range of typical cluster (1 keV$<$ $kT < 10$ keV) the total emission is dominated by the free-free emission if the abundance of heavy elements does not greatly exceed the solar abundance. The emissivity of the free-free emission at a frequency ν from a hot plasma with an electron temperature of T_g is given by,

$$\epsilon_\nu = \frac{2^5\pi e^6}{3m_e c^3}\left(\frac{2\pi}{2m_e k}\right)^{1/2} n_e \sum_i Z_i^2 n_i g_{ff}(Z, T_g, \nu) \times T_g^{-1/2}\exp(-h\nu/kT_g) \tag{2.33}$$

$$= \Lambda(T, Z, \nu) n_e^2 \tag{2.34}$$

where Z_i and n_i are the charge and number density of the ion i, respectively, and n_e is the electrons number density (e.g. Rybicki & Lightman 1979). The Gaunt factor is a correction factor for quantum mechanical effects and is approximately $g_{ff} \sim 0.9(h\nu/kT)^{-0.3}$. The emissivity in a given bandpass, $\nu_1 < \nu < \nu_2$, is then

$$\epsilon^{ff} = \int_{\nu_1}^{\nu_2} \epsilon_\nu^{ff} d\nu \tag{2.35}$$

$$= \Lambda(T, Z) n_e^2. \tag{2.36}$$

The $\Lambda(T, Z)$ is the cooling function, with T and Z representing the plasma temperature and the heavy element abundance, respectively. Figure 2.4 shows the cooling function as a function of the plasma temperature assuming the cosmic abundances. The contribution of the bremsstrahlung continuum to Λ increases as $\propto T^{1/2}$.

We can obtain the total X-ray luminosity by integrating equation (2.36). It is useful to define the emission integral as

$$EI = \int n_e^2 dV, \tag{2.37}$$

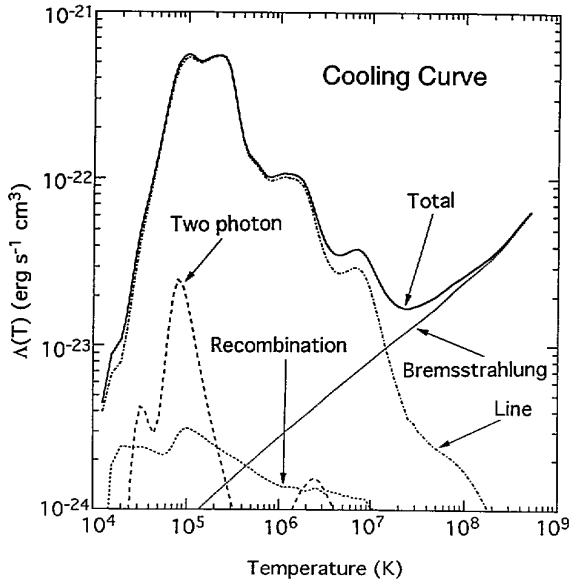

Fig. 2.4: Temperature dependence of the cooling function with its components for optically thin plasma containing cosmic abundances of elements (Gehrels & Williams (1993)).

where V is the volume of the cluster. If we assume that th ICM has a spatially-uniform temperature and abundance in the volume V, and that the ICM density is constant over the projected sky area S, then the luminosity L_X is given as

$$L_X = \int \epsilon^{ff} dV \tag{2.38}$$
$$= EI \times \Lambda(T, Z) \tag{2.39}$$
$$= EM \times S \times \Lambda(T, Z). \tag{2.40}$$

The EM is the emission measure defined as

$$EM = \int n_e^2 dl, \tag{2.41}$$

where l is the depth of the plasma along the line of sight. The emission integral determines the normalization of the spectrum, and the shape of the spectrum depends only on the temperature T and the heavy element abundance Z, and EI (or EM if S is known) from the observed X-ray spectra.

Emission of atomic lines becomes significant when the ICM temperature falls below a few keV. Since the temperature of the ICM is of the same order as the K-shell ionization potentials of heavy elements such as O, Ne, Mg, Si, S and Fe, these elements become mainly He/H-like ions and are completely ionized. These ions are collisionally excited, and then emit their resonance K-lines. In lower temperature clusters, in which Fe ions are not only He-like but also of a low ionization status, the spectrum exhibits resonance L-lines at $\sim$ 1 keV. We show predicted X-ray spectra for various temperature in figure 2.5.

The emission lines and continuum spectra from the ionization equilibrium plasma have been calculated by various authors, e.g. Raymond & Smith (1977), Kaastra & Mewe

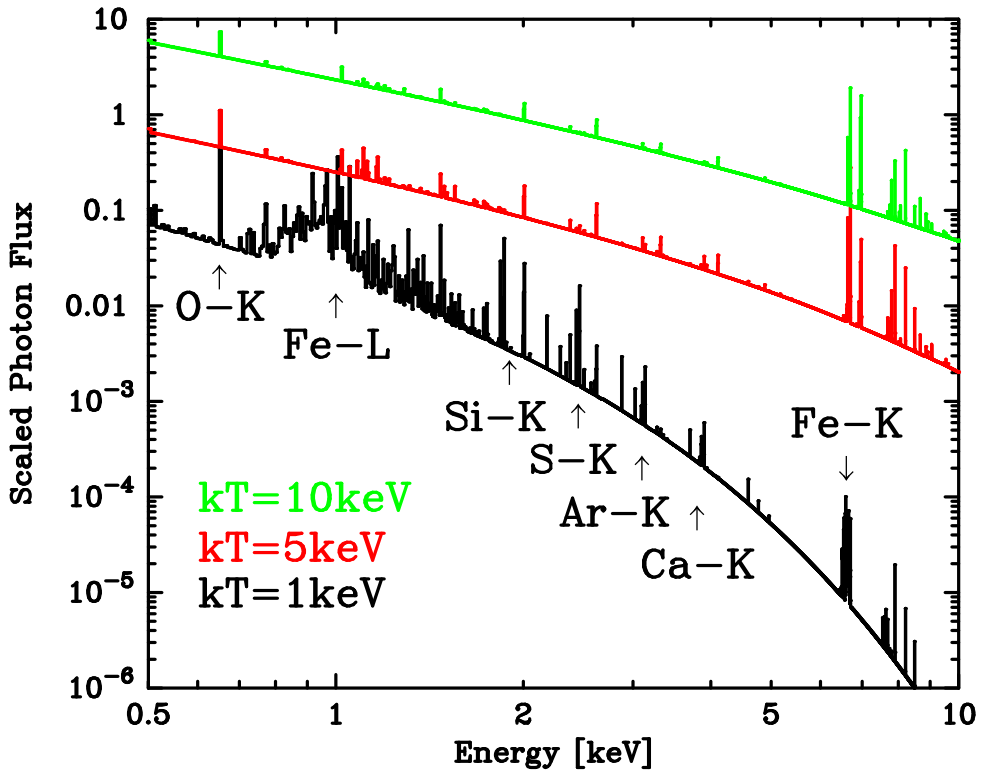

Fig. 2.5: Calculated X-ray spectra from optically thin hot plasma with various temperatures. The MEKAL plasma emission code is used, assuming a metal abundance of 0.3 solar. Vertical scale is arbitrary.

(1993), and so on. In this thesis, we use the APEC code, which reproduce an emission spectrum from collisionally-ionized diffuse gas calculated using the APEC code v1.10 [1] in the XSPEC data analysis package.

2.2.3 Mass Distribution

The precise knowledge of the mass distribution of the most massive, gravitationally confined objects is not only interesting itself, but it is also a prerequisite to many of the astrophysical and cosmological studies with clusters. A possible test for the mass measurement with an independent method is the comparison with the implications from gravitational lensing effect of clusters, velocity desperesion of gas and Sunyaev-Zeldovich effect.

Hydrostatic equilibrium and gravitational mass distribution

The force balance between the gas pressure, P_g, and gravitational force, both acting on the ICM, is expressed as

$$\nabla P_g = -\rho_g \nabla \phi, \tag{2.42}$$

[1] http://hea-www.harvard.edu/APEC

where ϕ is the gravitational potential and ρ_g is the gas density which can be written as $\rho_g = \mu n_g m_p$. Here, n_g is the number density including electron and ions, μ ($\simeq 0.62$) is the mean molecular weight, and m_p is the proton mass. The electron density of ICM, n_e, is computed assuming $n_e = 1.2 n_p$ for a fully ionized gas with hydrogen. If we assume spherically symmetry, the above equation is reduced to

$$\frac{dP_g}{dr} = -\mu n_g m_p \frac{d\phi}{dr}, \tag{2.43}$$

where r is the three dimensional radius. Because of the low density ($n_g < 10^{-2}$ cm^{-3}), the ICM can be treated as an ideal gas that follows the equation of state as

$$P_g = n_g kT. \tag{2.44}$$

Hydrogen and helium mass fractions are $X = 0.7$ and $Y = 0.28$. The ion density including helium is $n_i = 0.92 n_e$, therefore the gas pressure is calculated as

$$P_{gas} = 1.92 n_e kT. \tag{2.45}$$

The gas mass density ρ_{gas} is expressed as

$$\rho_{gas} = 1.92 \mu m_p n_e. \tag{2.46}$$

When time scale of scattering between ion and electron is shorter than that of heating or cooling, we can treat gas as hydrostatic matter. Assuming the hydrostatic equilibrium, the total integrated gravitational mass, $M_{<R}$, within the 3-dimensional radius of R is given by

$$M_{<R} = -\frac{R^2}{\rho_{gas} G} \frac{dP_{gas}}{dR} \tag{2.47}$$

$$= -\frac{kTR}{\mu m_p G} \left(\frac{d \ln \rho_{gas}}{d \ln R} + \frac{d \ln T}{d \ln R} \right). \tag{2.48}$$

in which G is the gravitational constant. The differential mass density , $M(R)$, is given by

$$M(R) = \frac{1}{4\pi R^2} \frac{dM_{<R}}{dR} \tag{2.49}$$

So, we can derive gravitational mass from mass density $\rho_{gas}(r)$ of ICM, and temperature profile $T(r)$. When we calculated equation(7.8), we derived r_{200} from matter density profile, $\rho(r) = (dM(r)/dr)/dV$ to define concentration parameter of NFW profile.

Polytropes

We consider a case where adiabatic conditions in ideal gas

$$\begin{aligned} TV^{\gamma-1} &= \text{Const.} \\ PV^{\gamma} &= \text{Const.} \\ P^{\gamma-1}T^{\gamma} &= \text{Const.} \end{aligned} \tag{2.50}$$

play a central role. To the extent that the chemical composition of a cloud can critically alter the ratio of heat capacities, γ, cloud chemistry can be decisive in determining the stability conditions. Turbulent velocities in such clouds play a role similar to those of thermal velocities and may be assigned a corresponding temperature.

Replacing the volume V in expressions equation.(2.50) by its reciprocal, the density ρ, leads to

$$P = K\rho^{\gamma} \equiv K\rho^{1+1/N} \tag{2.51}$$

where N is a pure number, a characterizing constant called the *polytropic index*. The ratio $1+1/N$ is just the ratio of specific heats γ. The polytropic index $N = 3/2$ is particularly important since it corresponds to $\gamma = 5/3$, which applies to regions consisting of atomic hydrogen, molecular hydrogen at low temperatures, or fully ionized hydrogen. It also applies to non-relativistic degenerate fermions and, to the physics of white dwarfs and neutrons stars.

We now assume that the density takes the form

$$\rho = \rho_c[\theta]^N, \tag{2.52}$$

where ρ_c is a constant and $\theta(\xi)$, called the polytropic temperature, is a function of radius. Under an assumption of the hydrostatic equilibrium,

$$\frac{dM_r}{dr} = 4\pi r^2\rho, \quad \frac{dP}{dr} = -\frac{GM_r\rho}{r^2} \tag{2.53}$$

$$\frac{d}{dr}\left(\frac{r^2}{\rho}\frac{dP}{dr}\right) = -G\frac{dM_r}{dr} = -4\pi G\rho r^2 \tag{2.54}$$

If we normalize equation.2.53 with the normalized radius

$$r = \alpha\xi \tag{2.55}$$

$$\alpha = (N+1)^{1/2}\left[\frac{1}{4\pi G}\frac{P_c}{\rho_c^2}\right]^{1/2} \tag{2.56}$$

We can derive Lane-Emden equation

$$\frac{1}{\xi^2}\frac{d}{d\xi}\left(\xi^2\frac{d\theta}{d\xi}\right) = -\theta^N. \tag{2.57}$$

If this equation includes boundary conditions are $\theta(0) = 1$ and $\theta'(0) = 0$, we can solve this equation. In figure 2.6, we show some example profiles of Lane-Emden equation. It turn to flat depending on the index N

Polytropic gas on DM potential

Suto, Sasaki, & Makino (1998) considered a family of density profiles describing the dark matter halo including NFW model (Navarro et al. 1996),

$$\rho_{DM}(x) = \frac{\rho_s}{x^{\mu}(1+x^{\nu})^{\lambda}}, \tag{2.58}$$

Fig. 2.6: Normalized radial density profile in politropes

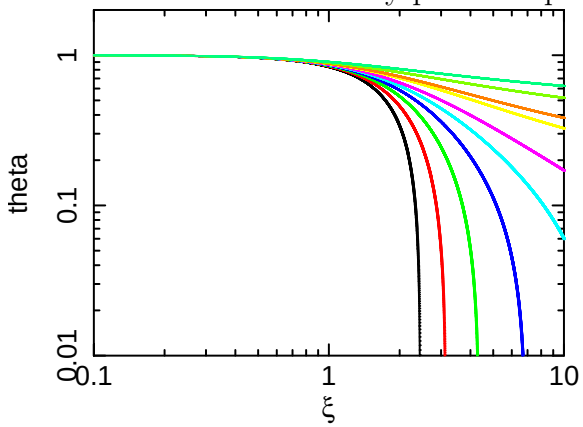

n = 0(black), 1(red), 2(green), 3(blue), 4(right blue), 5(majenda), 7(yellow), 8(orange), 11.5(right green), and 16 (emerald green).

where $x \equiv r/r_s$ is the dimensionless radius in units of the characteristic scale r_s.

In this section, we deal with non-isothermal features which actual clusters do show. Actually, Markevitch et al. (1998), Vikhlinin et al. (2005), Vikhlinin et al. (2006), Snowden et al. (2007) have reported nonisothermal temperature structure in clusters. Now we assume negligible contribution of total mass to gas mass. In this assumption, we consider that gas density profile is polytropic profile of gas pressure on dark matter potential. We adopt the following form for the gas pressure: P,

$$P = P_0 \left(\frac{\rho_g}{\rho_{g0}} \right)^{1+1/N}, \tag{2.59}$$

in which polytropic index $\Gamma = 1 + 1/N$. If one neglects the gas and galaxy contributions to the gravitational mass, the gas density profile ρ_{gas} in hydrostatic equilibrium with the above dark matter potential satisfies the equation (7.8) and described as

$$\frac{1}{\rho_g}\frac{dP}{dr} = -\frac{GM(r)}{r^2} \tag{2.60}$$

$$\frac{d\epsilon}{dx} = -Bp\frac{m(x)}{x^2} \tag{2.61}$$

$$B_p \equiv \frac{4\pi G}{N+1}\frac{\mu m_p \rho_{c0}\delta_c r_s^2}{kT_{g0}}. \tag{2.62}$$

We ignore self gravitation, and we define $\epsilon(x)$ as follows,

$$\epsilon(x) = \left[\frac{\rho_g(x)}{\rho_{g0}} \right]^{1/N} = \frac{T_g(x)}{T_{g0}} \tag{2.63}$$

$$\epsilon = 1 - B_p f(x) \tag{2.64}$$

In some specific cases, this equations are analytically integrated and $f(x)$ is described as follows.

1. $\mu = 1, \nu = 1, \lambda = 2$ (NFW) [See Appendix.B.]

$$f(x) = 1 - \frac{1}{x}\ln(1+x) \tag{2.65}$$
$$m(x) = \ln(1+x) - \frac{x}{1+x} \tag{2.66}$$
$$\delta_c = \frac{200}{3}\frac{c^3}{\ln(1+c) - c/(1+c)} \tag{2.67}$$

2. $\mu = 3/2, \nu = 3/2, \lambda = 1$ (Moore's profile)

$$f(x) = \frac{x-2}{3x}\ln(1+\sqrt{x^3}) + \ln(1+\sqrt{x}) + \frac{2}{\sqrt{3}}\tan^{-1}\frac{2\sqrt{x}-1}{\sqrt{3}} + \frac{\sqrt{3}}{9}\pi \tag{2.68}$$
$$m(x) = \frac{2}{3}\ln(1+x^{3/2}) \tag{2.69}$$
$$\delta_c = \frac{100c^3}{\ln(1+c^{3/2})} \tag{2.70}$$

3. $\mu = 3/2, \nu = 1, \lambda = 3/2$

$$f(x) = 2\sqrt{\frac{1+x}{x}} - \frac{2}{x}\ln(\sqrt{x} + \sqrt{1+x}) \tag{2.71}$$
$$m(x) = 2\ln(\sqrt{x} + \sqrt{1+x}) - 2\sqrt{\frac{x}{1+x}} \tag{2.72}$$
$$\delta_c = \frac{100}{3}\frac{c^3}{\ln(\sqrt{c} + \sqrt{1+c}) - \sqrt{c/(1+c)}} \tag{2.73}$$

2.2.4 Previous studies up to r_{200}

The cluster outer regions are elementally important as the cosmological probe because these region record evolution of structure formation without contamination of AGN feedbacks. Also we constrain cluster properties from the boundary conditions of cluster outskirts.

Recent studies of cluster outskirt have been progressed by *Suzaku* XIS observation because of low background below 1 keV. Now that A1795 (Bautz et al. 2009), PKS0745-191 (George et al. 2008), A2204 (Reiprich et al. 2009), and A223 & A224 (Fujita et al.(2008)) have been studied up to r_{200} with X-ray. Recently Basu et al. (2009) measured temperature and density profiles with SZ and X-ray observations of A2204 outer region. These observations commonly measured temperature decreasing to half of averaged temperature in the range from $0.5r_{200}$ to r_{200}.

In the outer regions of clusters of galaxies, it is possible that gas conditions are not in hydrostatic equilibrium and spherical symmetry because these regions connects large scale structure filaments and considering as the accretion shock region. Such physical

state suggests low density and low temperatures order to polytropic relations between gas pressure and density with polytropic index. However, because thermal conductance between electron - ion is not equilibrated, Fox & Loeb (1997), Takizawa (1998) and Rudd & Nagai (2009) predicts inconsistency between electron and ion temperatures in the outer one third of the shock radius of a cluster with one dimensional and three dimensional simulations for some individual clusters. And entropy profiles defined as $S = kTn_e^{-2/3}$ turn to be flattening. Wong et al. (2009) found out the signatures of nonequipartition on X-ray and SZ observations in their studies and the effect of electron shock heating efficiency in the outer regions because the effect of nonequipartition is important if shock heating efficient of electrons is low and the equilibration afterward is due to Coulomb collisions alone. Then we have possibilities that we have not observed the real averaged temperature which is not equal to electron temperature.

2.2.5 Self-Similarity of Cluster Structure

If cluster formation is modeled by the gravitational collapse of a homogeneous spherical overdensity of noninteracting dark matter, we expect that the collapse process is self-similar as well as the produced "dark matter halos". Therefore, we expect that less massive systems are scaled down versions of the more massive clusters. In general, the central density is then proportional to the background density of the universe at a characteristic formation time of the cluster. We will look into self-similar nature of X-ray clusters based on observational results.

Temperature structure

Recent instruments made it possible to obtain spatially resolved spectra of clusters, and are revealing the temperature structure. Markevitch et al. (1998) analyzed spatially resolved X-ray spectra of 30 nearby clusters with *ASCA* and *ROSAT*. They reported that most of them show a similar temperature decline at large radii, and about a half of the sample shows signs of merging. X-ray study of an unbiased sample of clusters shows a variety of shapes, probably linked to various dynamical states (Zhang et al. 2004; Snowden et al. 2008). The self-similarity of shape seem to be confirmed by *Chandra* and *XMM-Newton* data for relaxed clusters as shown figure 2.9.

Vikhlinin et al. (2005) showed with *Chandra* that the temperature reaches at a peak at $r \sim 0.15\, r_{180}$ and then declines to ~ 0.5 of its peak value at $r \simeq 0.5\, r_{180}$, in good agreement with Markevitch et al. (1998). At the same time, *XMM-Newton* observations show the presence of a negative gradient at radii $> 0.1\, r_{180}$ (Piffaretti et al. 2005; Pratt et al. 2007; Pointecouteau et al. 2005). They revealed that clusters of galaxies generally show a declining profile toward to center and to outer region within 60% of virial radius. They also found that clusters whose temperature profiles peak at $r < 70$ kpc $\ll 0.15\, r_{180}$ show a larger peak-to-average temperature ratio of $T_{\rm p}/\langle T \rangle \sim 1.35$.

However, no consensus has been reached yet on the exact shape of the profiles over

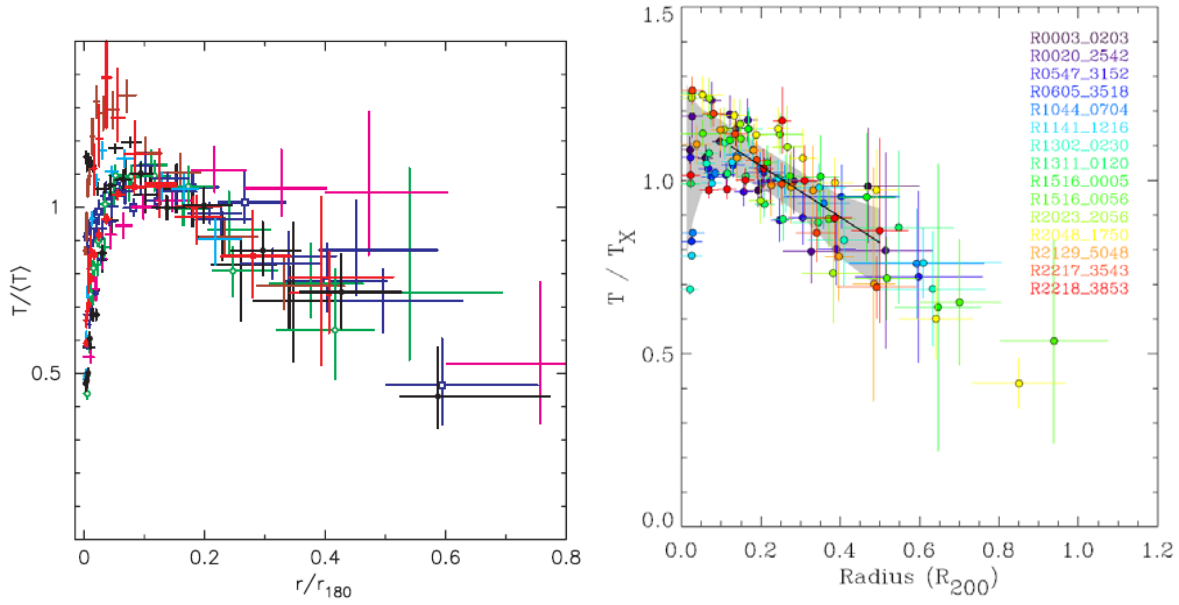

Fig. 2.7: Temperature profiles for clusters and groups observed by *Chandra* (left) and *XMM-Newton* (right). Left: Vikhlinin et al. (2005), and Right: Pratt et al. (2007).

$0.5\,r_{180}$ before the launch of *Suzaku* because *XMM-Newton* and *Chandra* have high background above $\sim$ 3 keV. It was difficult to observe temperature structure in the cooler region like outer regions of clusters of galaxies.

Density structure

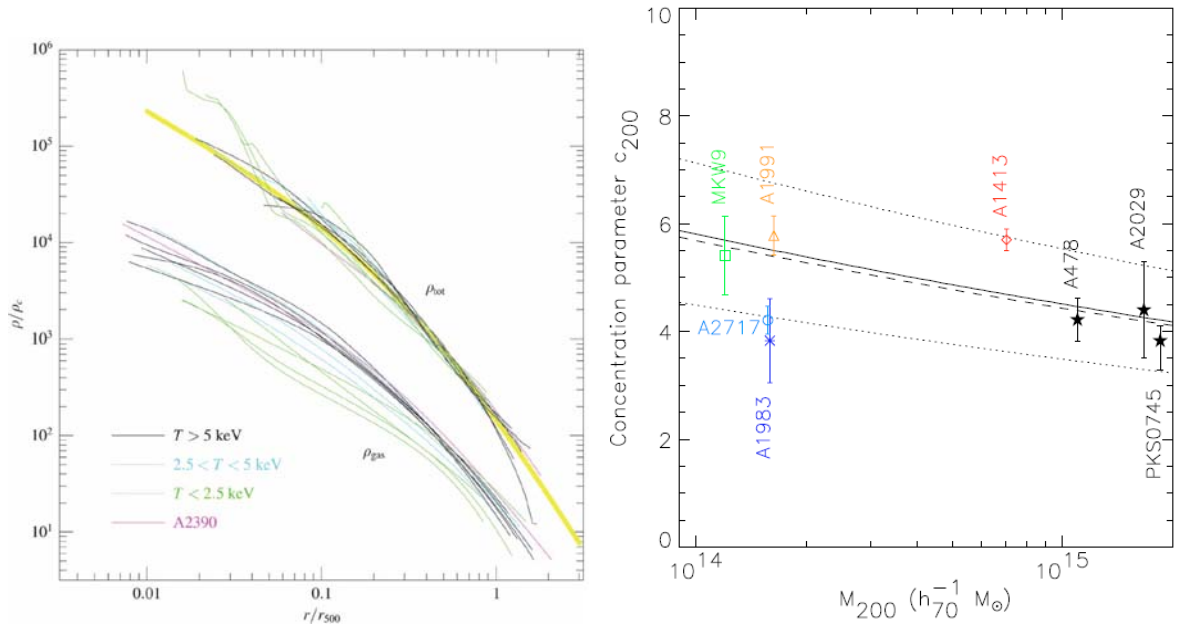

Fig. 2.8: Density profiles and concentration parameter observed by *Chandra* (Vikhlinin et al. 2005).

One of the key theoretical predictions of the hierarchical CDM models is the universal density distribution within dark matter halos (Navarro et al. 1996). Specifically, the shape of the radial density profiles of CDM halos is characterized by a gradually changing slope $\alpha = d\ln\rho/d\ln r$ from $\alpha \simeq -1$ in the inner regions to $\alpha \simeq -3$ at large radii (Dubinski et al. 1991; NFW). The profiles are characterized by a concentration parameter, c_{180}, defined as the ratio of the halo virial radius and the scale radius, r_s: $c_{180} \equiv r_{180}/r_s$. The scale radius is defined as the radius where the logarithmic slope of the density profile is $\alpha = -2$. Concentrations of CDM halos are tightly correlated with the characteristic epoch of object formation (Wechsler et al. 2002). The correlation found between halo concentration and mass accretion rate suggests a physical mechanism: for high mass infall rates, the central density is related to the background density; when the mass infall rate slows, the mean concentration is only a weakly decreasing function of the virial mass, $c_{180} \propto M_{180}^{0.1}$ (Navarro et al. 1997; Bullock et al. 2001; Eke et al. 2001). Because of the direct connection between halo concentration and velocity rotation curves and because of probable connections between halo mass assembly history and star formation history, the tight correlation between these properties provides an essential new ingredient for galaxy formation modeling.

Gas entropy

Fig. 2.9: S-kT relation and entropy profiles (left:Ponman et al. (2003), right:Pratt & Arnaud (2005)).

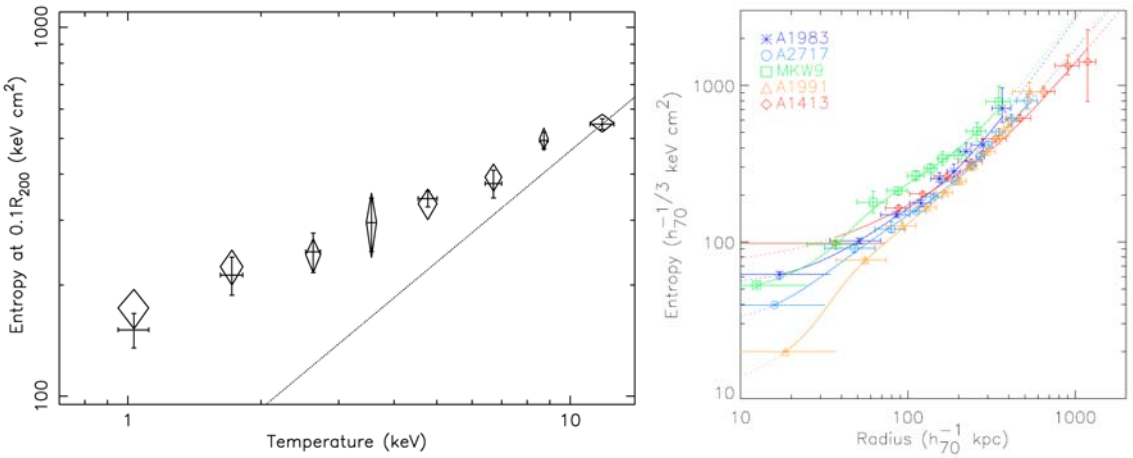

Entropy defines structure of ICM and records history for thermodynamics of clusters of galaxies (Voit 2005). We adopts the typical electron entropy formula,

$$S = \mathrm{k_B} T n_e^{-2/3} \tag{2.74}$$

, which is related to the true thermodynamic entropy via a logarithm and an additive constant. As we show the equation (2.74), entropy is made up with gas temperature $k_B T$ and electron density n_e. Cluster evolution through effects like AGN feedbacks and

accretion flow change temperature in the cluster core. In the outer regions, clusters connects large scale structure filaments with accretion gas through shock region. Such events affects temperature and entropy. Then we can measure cluster evolution as physical parameter with entropy.

Since the pioneering work, it is known that the entropy measured at $0.1\,r_{vir}$ exceeds the value attainable through gravitational heating alone, an effect that is especially noticeable in low mass systems.

Various non-gravitational processes have been proposed to explain this entropy excess, such as heating before or after collapse from SNs or AGNs or radiative cooling. A recent study of 66 nearby systems observed by *ASCA* and *ROSAT* shows that the $S - T$ relation follows a power law but with a smaller slope than expected: the entropy measured at $0.1\ r_{vir}$ scales as $S \propto T^{0.65}$. *XMM-Newton* observations show a remarkable self-similarity in the shape of the entropy profiles down to low mass ($kT \sim 2$ keV). Stacking analysis of *ROSAT* data gives the same results. Except in the very center, the *XMM-Newton* entropy profiles are self-similar in shape, with close to power law behavior in the $0.05\,r_{vir} < r < 0.5\,r_{vir}$ range. The slope is slightly shallower than predicted by shock heating models. $S \propto r^{0.94\pm0.14}$. the normalization of the profiles is consistent with the $S \propto T^{0.65}$ scaling. Similar results were obtained more recently on a larger sample observed with *XMM-Newton*. (Pratt et al. 2009). The distribution of outer entropy slopes is unimodal, with 0.98. Cool core clusters have a narrow range of outer entropy slopes 0.8–1.2 while morphologically disturbed systems have a much wider range of outer slopes (0.5-1.9), suggesting a relationship between the properties of the cores and the outer regions of clusters.

The self-similarity of shape of the entropy profile is a strong constraint for models. Simple pre-heating models, which predict large isentropic cores, must be ruled out. In addition to the gravitational effect, the gas history probably depends on the interplay between cooling and various galaxy feedback mechanisms.

2.2.6 Evolution of Clusters of Galaxies

In the standard hierarchical model of large-scale structure, where small mass aggregates collapse and form first and first star was birth in $z \sim 5$, clusters of galaxies grow by the inhomogeneous accretion of matter.

With $XMM - Newton$ and *Chandra*, we now extend the study of substructures to the distant Universe. As expected from the hierarchical formation models, we observe a variety of morphology (and thus dynamical state) up to very high z. The observation of cluster galaxies in deep field means the verification of cosmological model by itself because different cosmological models shows different evolution histories in the past by numerical simulations. And these observation we show in this section are traced the low-Ω_m universe mentioned as before.

A clear case of a double cluster is RX J1053.7+5735, observed with XMM-Newton at

$z = 1.14 \pm 0.01$ (Hashimoto et al. 2004) in figure 2.10. This cluster is very probably a merger between two nearly equal mass systems and now one of the first clusters whose X-ray redshift is directly measured. After the report of Hashimoto et al. 2004, JKCS 041 is a cluster of galaxies at z = 1.9 with deep potential well. making it the highest redshift cluster currently known, with extended X-ray emission (Andreon et al. 2009).

In contrast, RXJ1226.9+3332 ($z = 0.9$) observed with XMM-Newton is a massive cluster (the temperature is $kT = 11 \pm 1$ keV), with a very regular morphology indicative of a relaxed state . Note that the existence of massive and relaxed clusters at so high z is expected in low Universe but is very unlikely in a critical $\Omega_M = 1$ Universe. We also see unambiguous evidence of merging activity up to $z = 0.8$. The crude Chandra temperature map shows a temperature increase between the two subclusters of RX J0152.7-1357, indicating that they have started to merge. Interestingly, when the two subunits will have completely merged the cluster will have the mass of Coma.

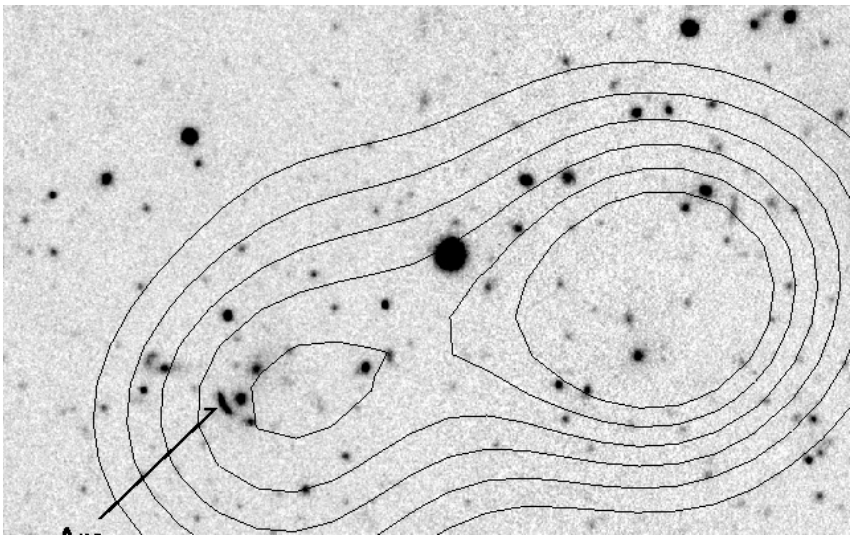

Fig. 2.10: The contours of XMM image of the cluster RXJ1053.7+5735 overlaid on a CFHT I band image (Hashimoto et al. 2004). The image was created by combining all events in the 0.2 - 8.0 keV band from three(pn, MOS1, and MOS2) cameras. North is up and East is left. The image is $2'.3 \times 1'.5$ on a side. The raw data were smoothed with a Gaussian with $\sigma = 7''$. The lowest contour is 1.9 counts arcsec^{-2} and the contour interval is 0.2 counts arcsec^{-2}.

2.2.7 Heavy Element Enrichment of the ICM

Study of heavy element enrichment of the ICM is important in the respect of the chemical evolution and the activity of supernovae (SNe). A large amount of metals in the ICM are mainly produced by supernovae (SNe) in galaxies (Arnaud et al. 1992; Renzini et al. 1993) and are classified roughly as Type Ia (SN Ia) and Type II (SN II). Elements suh as Si, S and Fe are synthesized in both SN Ia and SN II, while lighter α elements such as O,

Ne, and Mg are mainly produced in SN II, which are explosions of massive stars with initial mass above $\sim 10 M_{\odot}$. The metals produced in galaxies are transfered into the ICM by galactic wind and/or ram pressure stripping. These means that metal abandunce and these distribution in clusters and groups of galaxies record the history of activities of past stars and SNe.

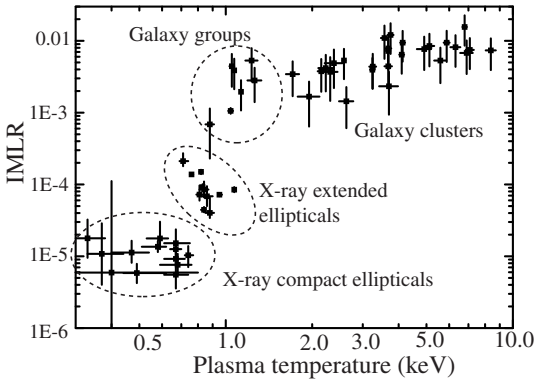

Fig. 2.11: Iron Mass-to-Light Ratio as a function of the system mass (Makishima et al. 2001), where the IMLR is calculated within a radius where the ICM density falls below 3×10^{-4} cm^{-1}. Those for elliptical galaxies refer to Matsushita (1997), where the IMLR is calculated within 4-times the optical effective radius.

ASCA first measured the distributions of Si and Fe in the ICM (Fukazawa et al. 1998; Fukazawa et al. 2000; Finoguenov et al. 2000; Finoguenov et al. 2001). Makishima et al. (2001) summarize the IMLR of various objects, as a function of their plasma temperature serving as a measure of the system richness with *ASCA* (figure 2.11:left). The derived iron-mass-to-light ratios (IMLR) are nearly constant in rich clusters and decrease toward poorer systems. Recent observations with *Chandra* and *XMM-Newton* allowed detailed studies of the metals in the ICM. These observations, however, showed abundance profiles of O, Mg, Si and Fe only for the central regions of very bright clusters or groups of galaxies dominated by cD galaxies in a reliable manner (Finoguenov et al. 2002; Fukazawa et al. 2004; Matsushita et al. 2003; Tamura et al. 2003). The abundance profiles of O and Mg, in particular for outer regions of clusters, are still poorly determined, because data from *Chandra* and *XMM-Newton* both show relatively high intrinsic background levels. Tamura et al. (2004) derived IMLR for five clusters within 250 h_{100}^{-1} kpc to be $\sim 0.01\ M_{\odot}/L_{\odot}$, and the oxygen mass within 50 h_{100}^{-1} kpc for several clusters. However, oxygen-mass-to-light ratios (OMLR) for rich clusters are not reliable due to the low emissivity of O_{VII} and O_{VIII} lines in high temperatures. De Grandi & Molendi (2002) and Hayakawa et al. (2006) found that clusters associated with cD galaxies and central cool components showed abundance concentration in the cluster center, while clusters without cD galaxies indicated flatter profiles. The central metallicity enhancement in the cool core clusters were further studied and the excess metals were shown to be supplied from the cD galaxies (De Grandi et al. 2004).

Suzaku enabled efficient determination of various emission lines, especially those of O and Mg, and Sato (2007) estimated the fractional contribution to the metal production by SN Ia and SN II for the first time. They revialed that the metal mass-to-light ratios (OMLR, IMLR etc.) decrease toward the central region of the clusters and groups, even though the metal to hydrogen number ratios (abundances) generally increase to the center.This trend is similar to the IMLR obtained with *XMM-Newton* for M 87 and the Centaurus cluster by Matsushita et al. (2007) within $r \lesssim 100$ kpc. The steep increase in the $r \lesssim 100$ kpc region suggests that the Fe and O ions which were synthesized in the central galaxies have been distributed to a wide region in the ICM. On the other hand, as pointed out in Ezawa et al. (1997), abundance gradient over a few hundred kpc scale in clusters of galaxies follows the mass ratio between the ICM and the galaxies. This is because heavy ions released from galaxies without much kinetic energy would not diffuse out more than 10 kpc over the Hubble time. Böhringer et al. 2004 showed that it takes about 10^{10} yr to synthesize Fe mass within $r \lesssim 100$ kpc range. These considerations suggest that the gas enriched by Fe and O was released to the cluster space with significant kinetic energy and/or the gas stripping was efficiently occurred in the ~ 100 kpc range due to the galactic motion. From their result, the number ratio of SN II to SN Ia is about ~ 3, based on the fit of the observed abundance patterns as shown in figure.2.12. Furthermore, the abundance of oxygen is lower than those of other elements and about half the solar value in the central region. This is partly because oxygen may be contained in the stars or dusts, and because of the simple assumption of the Salpeter IMF. The predicted IMLR, assuming the present SN Ia rate over the Hubble time, is much lower than the observed values for the whole cluster regions. Renzini et al. (1993) suggest that the SN Ia rate was higher in the past.

Their results indicate the following scenario for the metal enrichment. In the early stage of the cluster formation, a large number of SN II, as indicated by the 3 to 1 ratio of SN II to SN Ia in total, were occurred. And, a wide region in or around the cluster space was enriched by galactic winds and/or mass loss from stars. Then, as the gravitational collapse of clusters of galaxies proceeds, the enhanced SN II activity ceases and the metals produced in galaxies are brought in to the cluster space by mild outflows and/or ram pressure strippings. In this epoch, the metals are mainly produced by SN Ia and the high metal production in the central elliptical galaxies causes abundance gradient in clusters.

The future sensitive observations of emission lines from various clusters and groups at different redshifts will enable us to look directly into the enrichment process of the cluster space. For those studies, X-ray microcalorimeters are expected to play a major role.

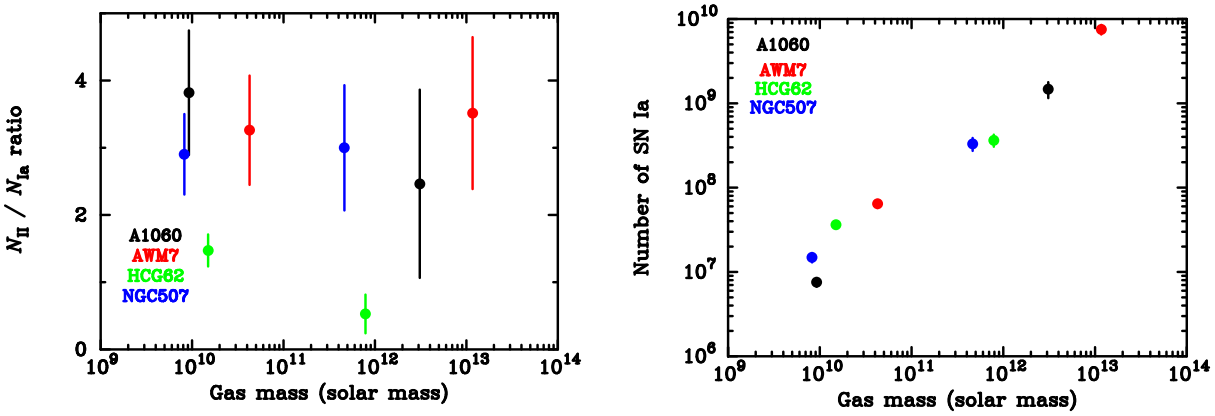

Fig. 2.12: Left: The number ratio of SN II to SN Ia. It is almost ~ 3. Right: The number of SN Ia to gas mass (Sato 2007).

Chapter 3

Instrumentation

3.1 The *Suzaku* satellite

3.1.1 Mission Description

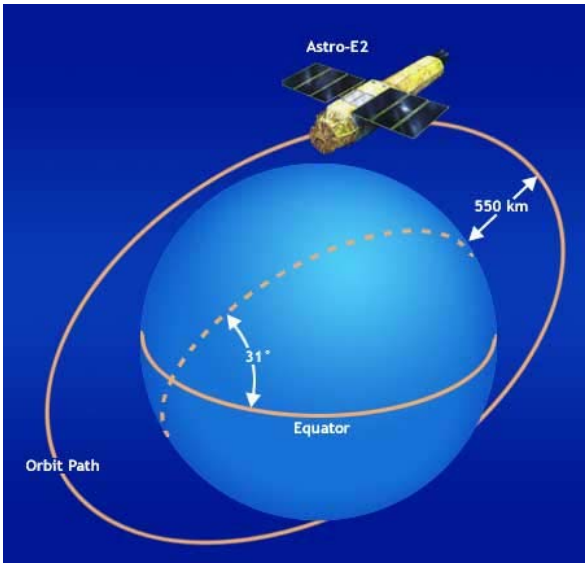

Fig. 3.1: The 96 minute *Suzaku* orbit (The *Suzaku* technical Discription).

Suzaku, the Japanese 5th X-ray astronomical satellite, was launched on July, 2005 (Mitsuda et al. 2007; Serlemitsos et al. 2007; Koyama et al. 2007; Takahashi 2007; Kokubun et al. 2006). *Suzaku* is placed in a near-circular orbit with an apogee of 568 km, an inclination of 31.9 degrees, and an orbital period of about 96 minutes. The maximum slew rate of the spacecraft is 6 degrees/min, and settling to the final attitude takes $\sim$ 10 minutes, using the star trackers.

A Brief Introduction of *Suzaku*

The scientific payload of *Suzaku* (Fig. 3.2) initially consisted of three distinct co-aligned scientific instruments. There are four X-ray sensitive imaging CCD cameras (X-ray Imag-

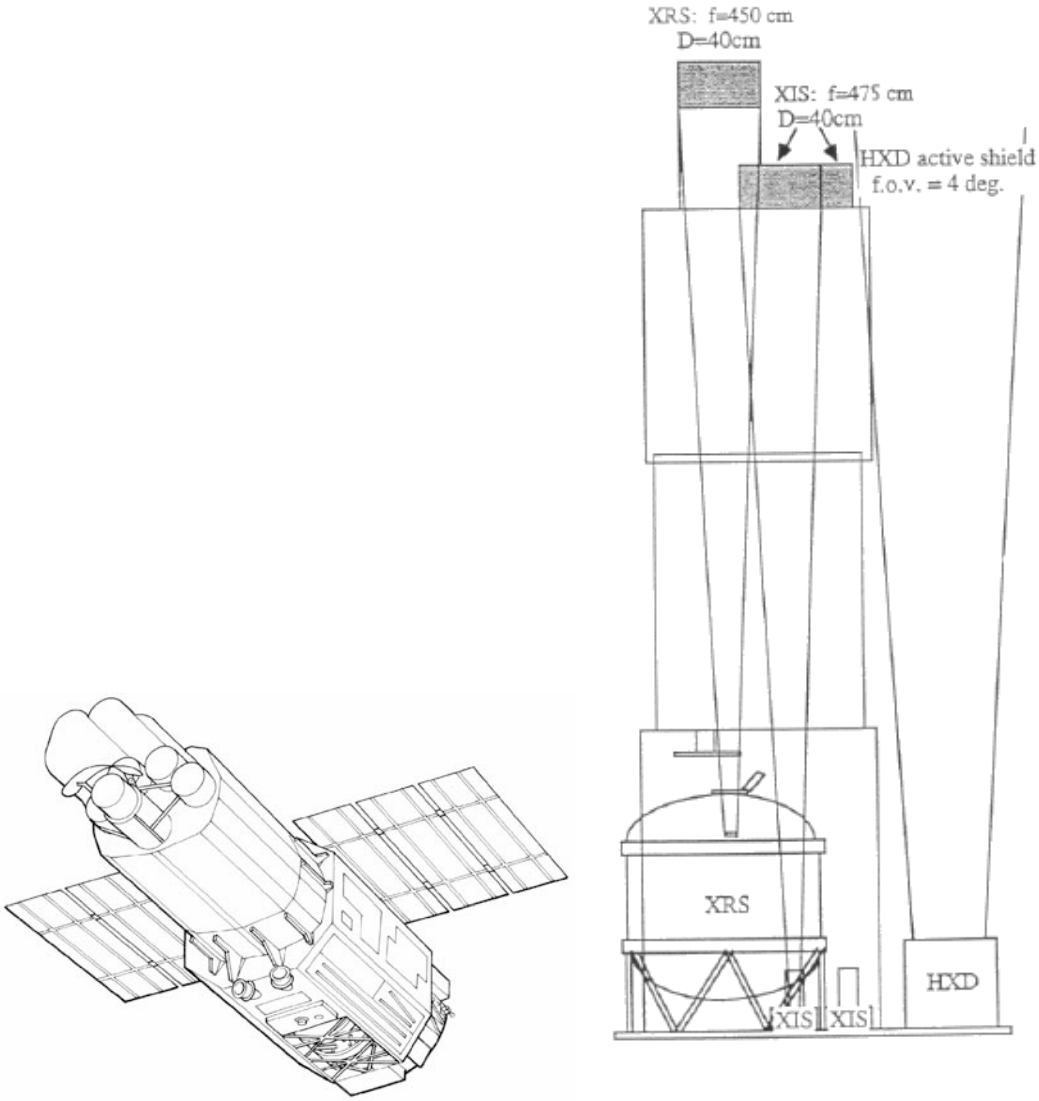

Fig. 3.2: Left: Schematic picture of the *Suzaku* satellite. Right: A side view of the instruments and telescopes on *Suzaku* (Serlemitsos et al. 2007).

ing Spectrometers, or XISs), three front-side illuminated (FI; energy range 0.4-12 keV corresponding to XIS0, XIS2 and XIS3) and one back-side illuminated (BI; energy range 0.2-12 keV for XIS1), capable of moderate energy resolution. Each XIS is located in the focal plane of a dedicated X-ray telescope. The second instrument is the non-imaging, collimated Hard X-ray Detector (HXD), which extends the bandpass of the observatory to much higher energies with its 10–600 keV pointed bandpass. The X–Ray Spectrometer (XRS) is no longer operational.

All of the instruments on *Suzaku* operate simultaneously. Each of the co-aligned XRTs features an X-ray mirror with an angular resolution (expressed as Half-Power Diameter, or HPD) of $\sim 2'$ (Fig. 3.3). Figure 3.3 shows the total effective area of the XIS+XRT. K-shell absorption edges from the oxygen (0.54 keV) and aluminum (1.56 keV) in the blocking filters are present, as well as a number of weak M-shell features between 2–3 keV arising from the gold coated on the front surface of the XRT reflector.

Table 3.1: Overview of *Suzaku* capabilities

S/C	Orbit Apogee	568 km
	Orbital Period	96 minutes
	Observing Efficiency	$\sim 45\%$
XRT	Focal length	4.75 m
	Field of View	$17'$ at 1.5 keV
		$13'$ at 8 keV
	Plate scale	0.724 arcmin/mm
	Effective Area	440 cm^2 at 1.5 keV
		250 cm^2 at 8 keV
	Angular Resolution	$2'$ (HPD)
XIS	Field of View	$17.8' \times 17.8'$
	Bandpass	0.2–12 keV
	Pixel grid	1024×1024
	Pixel size	24 μm× 24 μm
	Energy Resolution	~ 130 eV at 6 keV
	Effective Area	340 cm^2 (FI), 390 cm^2 (BI) at 1.5 keV
	(incl XRT-I)	150 cm^2 (FI), 100 cm^2 (BI) at 8 keV
	Time Resolution	8 s (Normal mode), 7.8 ms (P-Sum mode)
HXD	Field of View	$4.5^\circ \times 4.5^\circ$ (≥ 100 keV)
	Field of View	$34' \times 34'$ (≤ 100 keV)
	Bandpass	10 – 600 keV
	– PIN	10 – 60 keV
	– GSO	30 – 600 keV
	Energy Resolution (PIN)	~ 3.0 keV (FWHM)
	Energy Resolution (GSO)	$7.6/\sqrt{E_{MeV}}$ % (FWHM)
	Effective area	$\sim 160\,cm^2$ at 20 keV, $\sim 260\,cm^2$ at 100 keV
	Time Resolution	61 μs
HXD-WAM	Field of View	2π (non-pointing)
	Bandpass	50 keV – 5 MeV
	Effective Area	800 cm^2 at 100 keV / 400 cm^2 at 1 MeV
	Time Resolution	31.25 ms for GRB, 1 s for All-Sky-Monitor

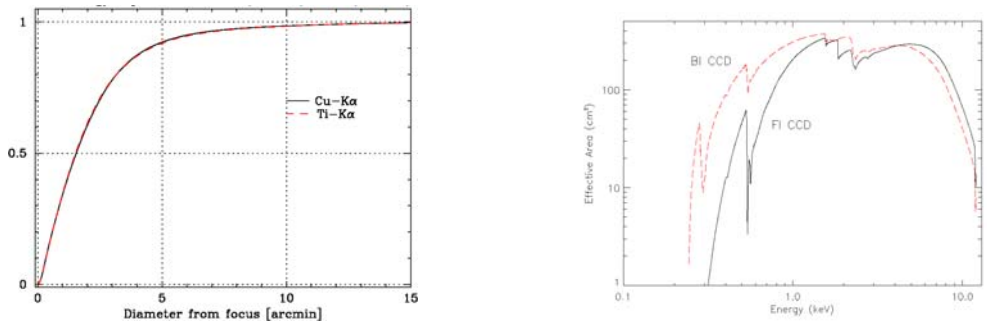

Fig. 3.3: Left: XIS Effective area of one XRT + XIS system, for the FI and BI CCDs. no contamination. Right: The Encircled Energy Function (EEF) showing the fractional energy within a given radius for one quadrant of the XRT-I telescopes on *Suzaku* at 4.5 and 8.0 keV(Serlemitsos et al. 2007).

The four XISs are true imagers, with a large field of view ($\sim 18' \times 18'$), and moderate spectral resolution.

The HXD is a non-imaging instrument with an effective area of $\sim 260\,\mathrm{cm}^2$, featuring a compound-eye configuration and an extremely low background. It extends the bandpass of the mission with its nominal sensitivity over the 10 – 600 keV band (cf. Fig. 3.4). The HXD consists of two types of sensors: 2 mm thick silicon PIN diodes sensitive over 10 – 60 keV, and GSO crystal scintillators placed behind the PIN diodes covering 30 – 600 keV. The HXD field of view is actively collimated to $4.5° \times 4.5°$ by the well-shaped BGO scintillators, which, in combination with the GSO scintillators, are arranged in the so-called phoswich configuration. At energies below $\sim$ 100 keV, an additional passive collimation further reduces the field of view to $34' \times 34'$. The energy resolution is $\sim$ 3.0 keV (FWHM) for the PIN diodes, and $7.6/\sqrt{E}$ % (FWHM) for the scintillators (where E is energy in MeV). The HXD time resolution for both sensors is 61 μs. While the HXD is intended mainly to explore the faintest hard X-ray sources, it can also tolerate very bright sources up to $\sim$ 10 Crab. The HXD also has an all-sky monitor (the Wide-band All-sky Monitor (WAM), which can detect GRB and other sources (3.1). In this paper, we do not use HXD.

3.1.2 X–Ray Telescopes (XRTs)

Suzaku has five light-weight thin-foil X–Ray Telescopes (XRTs). The XRTs have been developed jointly by NASA/GSFC, Nagoya University, Tokyo Metropolitan University, and ISAS/JAXA. These are grazing-incidence reflective optics consisting of compactly nested, thin conical elements. Because of the reflectors' small thickness, they permit high density nesting and thus provide large collecting efficiency with a moderate imaging capability in the energy range of 0.2-12 keV, all accomplished in telescope units under 20 kg each.

Four XRTs onboard *Suzaku* (XRT-I) are used for the XIS, and the other XRT (XRT-S)

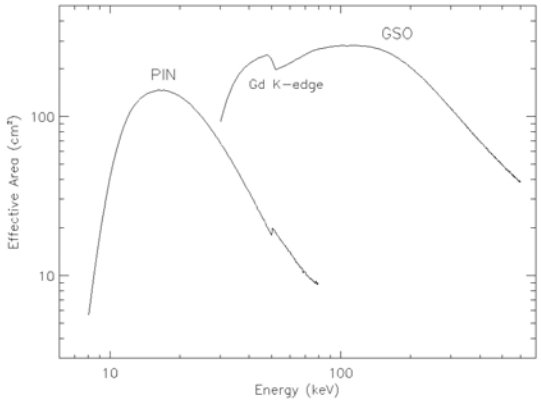

Fig. 3.4: Total effective area of the HXD detectors, PIN and GSO, as a function of energy (Kokubun et al. 2006).

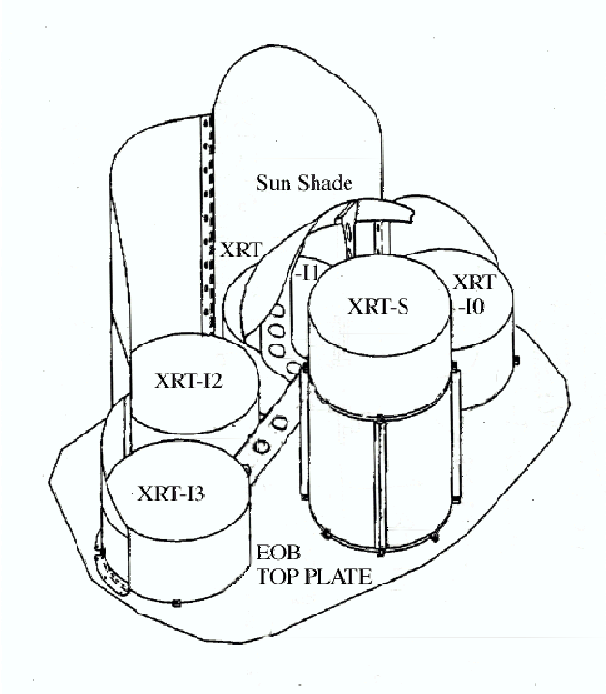

Fig. 3.5: Layout of the XRTs on the *Suzaku* spacecraft (Serlemitsos et al. 2007).

is for the XRS. The XRTs are arranged on the top plate of the Extensible Optical Bench (EOB) in the manner shown in Figure 3.5. The external dimensions of the 4 XRT-Is are the same (See Table 3.2, which also includes a comparison with the ASCA telescopes).

The HPD of the XRTs range from 1.8′ to 2.3′, which is the diameter within which half of the focused X-ray is enclosed. The angular resolution does not significantly depend on the energy of the incident X-ray in the energy range of *Suzaku*, 0.2-12 keV. The effective areas are typically 440 cm^2 at 1.5 keV and 250 cm^2 at 8 keV. The focal lengths are 4.75 m for the XRT-I. Individual XRT quadrants have their component focal lengths deviated from the design values by a few cm. The optical axis of the quadrants of each XRT are aligned within 2′ from the mechanical axis. The field of view (the diameter for a half of

Table 3.2: Telescope dimensions and design parameters of XRT-I, compared with ASCA XRT.

	Suzaku XRT-I	ASCA
Number of telescopes	4	4
Focal length	4.75 m	3.5 m
Inner Diameter	118 mm	120 mm
Outer Diameter	399 mm	345 mm
Height	279 mm	220 mm
Mass/Telescope	19.5 kg	9.8 kg
Number of nested shells	175	120
Reflectors/Telescope	1400	960
Geometric area/Telescope	873 cm^2	558 cm^2
Reflecting surface	Gold	Gold
Substrate material	Aluminum	Aluminum
Substrate thickness	155 μm	127 μm
Reflector slant height	101.6 mm	101.6 mm

the effective area) for XRT-Is is about $17'$ at 1.5 keV and $13'$ at 8 keV.

Basic Components of XRT

The *Suzaku* XRTs consist of closely nested thin-foil reflectors, reflecting X-ray at small grazing angles. An XRT is a cylindrical structure, having the following layered components: 1. a thermal shield at the entrance aperture to help maintain a uniform temperature; 2. a pre-collimator mounted on metal rings for stray light elimination; 3. a primary stage for the first X-ray reflection; 4. a secondary stage for the second X-ray reflection; 5. a base ring for structural integrity and interface with the EOB. All these components, except the base rings, are constructed in 90° segments. Four of these quadrants are coupled together by interconnect-couplers and also by the top and base rings (Figure 3.6). The telescope housings are made of aluminum for an optimal strength to mass ratio.

Including the alignment bars, collimating pieces, screws and washers, couplers, retaining plates, housing panels and rings, each XRT-I consists of over 4112 mechanically separated parts. In total, nearly 7000 qualified reflectors were used and over 1 million cm^2 of gold surface was coated.

Reflectors Each reflector consists of a substrate also made of aluminum and an epoxy layer that couples the reflecting gold surface to the substrate. The reflectors are nominally 178 μm in thickness. In shape, each reflector is a 90° segment of a section of a cone. The cone angle is designed to be the angle of on-axis incidence for the primary stage and 3 times that for the secondary stage. They are 101.6 mm in slant length and with radii extending approximately from 60 mm at the inner part to 200 mm at the outer part.

Fig. 3.6: A *Suzaku* X–Ray Telescope (Serlemitsos et al. 2007).

All reflectors are positioned with grooved alignment bars, which hold the foils at their circular edges. There are 13 alignment bars at each face of each quadrant, separated at approximately 6.4° apart.

In the *Suzaku* XRTs, the conical approximation of the Wolter-I type geometry is used. This approximation fundamentally limits the angle resolution achievable. More significantly, the combination of the figure error in the replication mandrels and the imperfection in the thermo-forming process (to about 4 micrometers in the low frequency components of the figure error in the axial direction) limits the angular resolution to about 1 minute of arc (Misaki et al. 2004).

Pre-collimator The pre-collimator, which blocks off stray light that otherwise would enter the detector at a larger angle than intended, consists of concentrically nested aluminum foils similar to that of the reflector substrates (Mori et al. 2005). They are shorter, 22 mm in length, and thinner, 120 μm in thickness. They are positioned in a fashion similar to that of the reflectors, by 13 grooved aluminum plates at each circular edge of the pieces. They are installed on top of their respective primary reflectors along the axial direction. Due to their smaller thickness, they do not significantly reduce the entrance aperture in that direction more than the reflectors already do. Pre-collimator foils do not have reflective surfaces (neither front nor back). The relevant dimensions are listed in Table 3.3.

Thermal Shields The *Suzaku* XRTs are designed to function in a thermal environment of 20±7.5 °C (figure 3.7). The thermal shield is mechanically sustained by a frame made of aluminum, with a thickness of 4 mm. The frame has thirteen spokes which are along the alignment bars of the XRT. A stainless steel mesh with a wire pitch, width and

Table 3.3: Design parameters for pre-collimator

	XRT-I
Number of Collimators	4
Height	32 mm
Blade Substrate	Aluminum
Blade Thickness	120 μm
Blade Height	22 mm
Height from Blade Top to Reflector Top	30 mm
Number of nested shells	175
Blade/Telescope	700
Mass/Collimator	2.7 kg

Fig. 3.7: A thermal shield (Serlemitsos et al. 2007).

thickness of 3 mm, 0.1 mm and 0.15 mm, respectively. Finally, polyethylene teleftalate (PET) film as thin as 0.24 μm, coated with aluminum layer with thickness of 30 nm on the surface oriented to the space, is adhered to the mesh with epoxy. The reflectors, due to its composite nature and thus its mismatch in coefficients of thermal expansion, suffer from thermal distortion that degrades the angular resolution of the telescopes in temperature outside this range. Thermal gradient also distorts the telescope in a larger scale. Even though sun shields and other heating elements on the spacecraft help in maintaining a reasonable thermal environment, thermal shields are integrated on top of the pre-collimator stage to provide the needed thermal control.

XRT Performance in Orbit

Focal Positions and Angular Resolutions Verification of the imaging capability of the XRTs has been made with the data of SS Cyg in quiescence taken during 2005 November 2 01:02UT–23:39UT. The total exposure time was 41.3 ks. SS cyg is selected for this purpose because it is a point source and moderately bright (3.6, 5.9, 3.7 and 3.5 c s^{-1} for XIS0 through XIS3), and hence, it is needless to care about pile-up even at the image core. A constant value, evaluated from source-free corner regions was subtracted as

a background, from all the pixels. The data taken only during the star-tracker calibration is on was used. Fig. 3.8 shows the images and the point spread functions (PSFs) of all the XRT-I+XIS modules. The HPD is obtained to be 1.′8, 2.′3, 2.′0, and 2.′0 for XRT-I0, 1, 2 and 3, respectively. These values are in general consistent with those expected from ground-based calibration measurements.

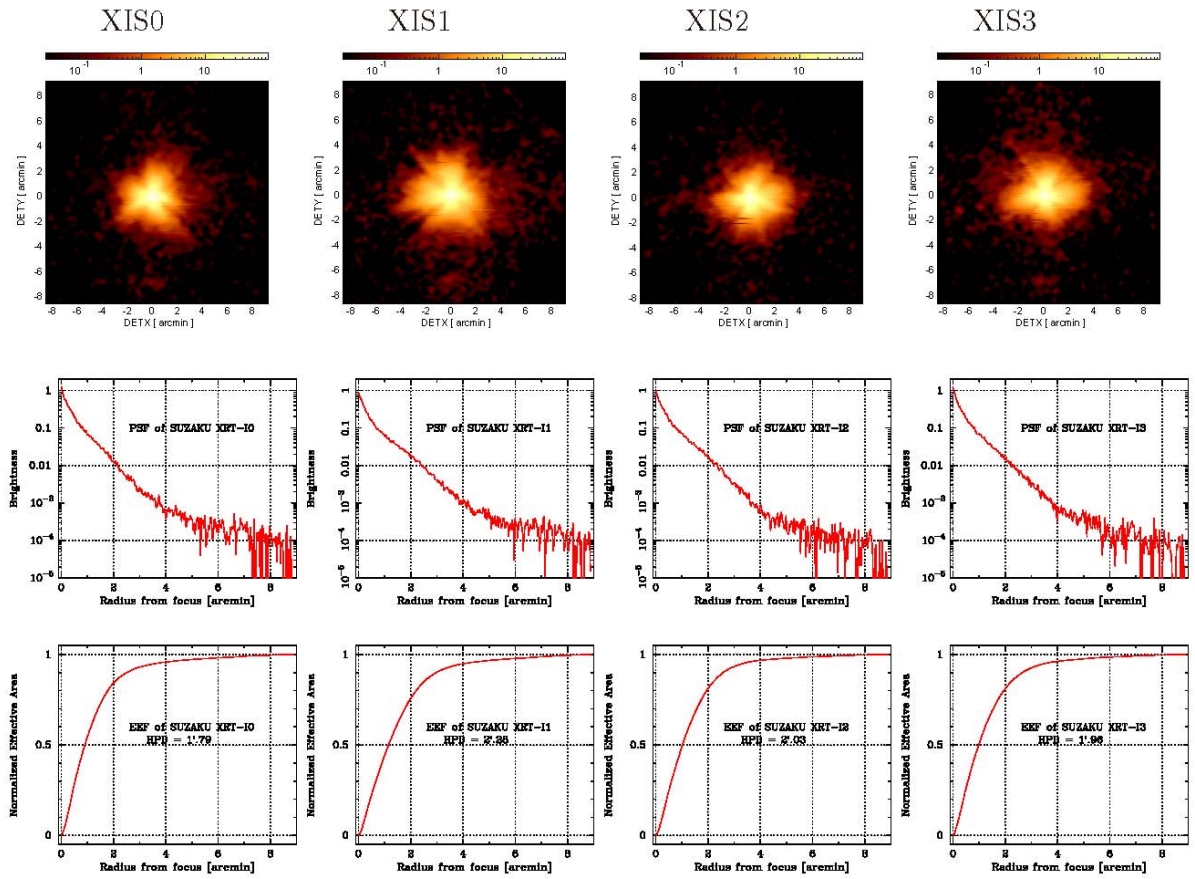

Fig. 3.8: Image, Point-Spread Function (PSF), and EEF of the four XRT-I modules in the focal plane (Serlemitsos et al. 2007). All the images are binned with 2×2 pixels followed by being smoothed with a Gaussian with a sigma of 3 pixels, where the pixel size is 24 μm. The EEF is normalized to unity at the edge of the CCD chip (a square of 17.′8 on a side). With this normalization, the HPD of the XRT-I0 through I3 is 1.′8, 2.′3, 2.′0 and 2.′0, respectively.

Figure 3.9 shows the focal position of the XRT-Is, that the source is focused when the satellite points at the XIS aimpoint. The focal positions locate roughly within 0.′5 from the detector center with an deviation of $\sim$ 0.′3. This implies that the fields of view of the XIS coinsides each other within $\sim$ 0.′3.

Optical Axes, Effective Area and Vignetting Functions A series of offset observations of the Crab observations were carried out in August and September at various off-axis angles of 0′, 3.′5, 7′. The intensity of the Crab nebula is evaluated for each point-

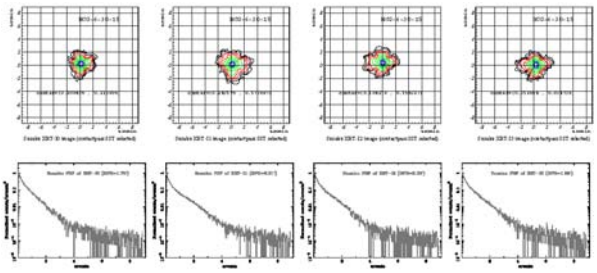

Fig. 3.9: Images and PSFs are shown in the upper, middle, and lower panels for the XIR-I0 through XRT-I3 from left to right. In each image drawn are ten contours in logarithmic spacing with the outermost contour being 1% surface brightness of the peak. the position of the maximum surface brightness is written as a caption in each panel in a unit of arcmin. Its typical error is $\pm 0.1'$. Each PSF is normalized by the number of total photons collected over the entire XIS aperture.

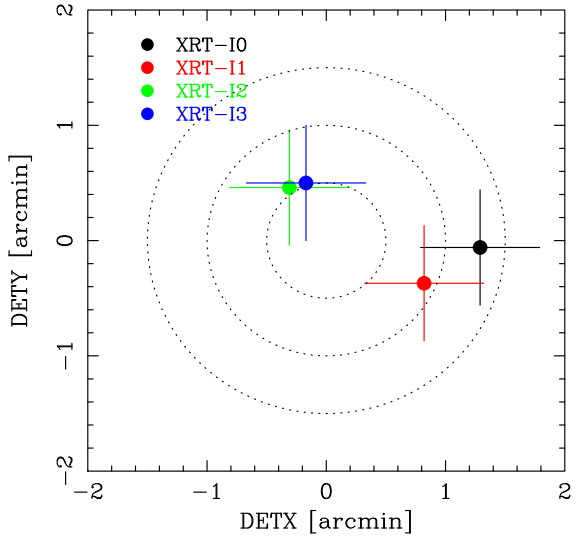

Fig. 3.10: Locations of the optical axis of each XRT-I module in the focal plane determined from the observations of the Crab Nebula in 2005 August-September. This figure implies that the image on each XIS detector becomes brightest when a target star is placed at the position of the corresponding cross. The dotted circles are drawn every 30″ in radius from the XIS-default position.

ing and for each XIS module separately. By finding the maximum throughput angle, we also have obtained a direction of the optical axis of each telescope. The result is shown in Fig. 3.10 The optical axes locate roughly within $1'$ from the XIS aim point. This implies that the efficiency of all the XRT-Is is more than 97 % even at 10 keV when we observe a point source on the XIS aimpoint.

The vignetting curves calculated by the ray-tracing simulator are compared with the observed intensities of the Crab Nebula at various off-axis angles in 3.11. These figures roughly show that effective area is calibrated to within $\sim 10\%$ over the XIS field of view. We expect most of these deviations can be attributed to scattering of the optical axis orientations of the four quadrants within a telescope.

Stray Light In-flight stray-light observations were carried out with Crab at off-axis angles of $20'$ (4 pointings), $50'$ (4 pointing) and $120'$ (4 pointing) in August and September. Fig. 3.12 shows an example of $20'$-off image of XRT-I3 together with simulation results of

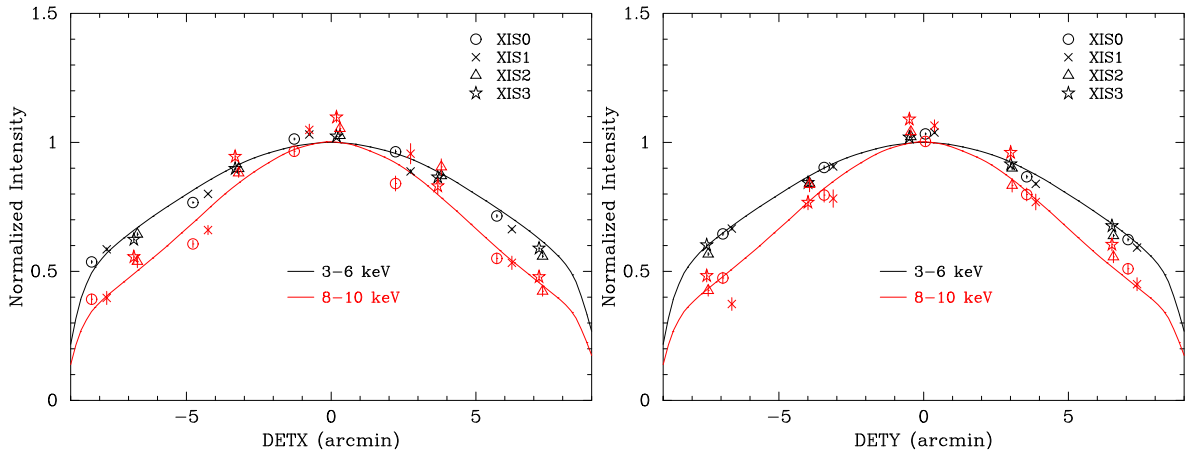

Fig. 3.11: Vignetting of the four XRT-I modules using the data of the Crab Nebula taken during 2005 August 22−27 in the two energy bands 3−6 keV and 8−10 keV. The model curves are calculated with the ray-tracing simulator with the spectral parameters of $N_{\rm H} = 0.33 \times 10^{22}$ cm^{-2}, photon index = 2.09, and the normalization = 9.845 photons cm^{-2} s^{-1} keV^{-1} at 1 keV. Note that the abrupt drop of the model curves at $\sim 8'$ is due to the source approaching the detector edge. The excess of the data points of XIS1 is probably due to insufficient calibration of the BI CCD.

the same off-axis angle for the cases with and without the pre-collimator.

It is seen that the pre-collimator works for reducing the stray light in orbit.

Figure 3.13 shows angular responses of the XRT-I at 1.5 and 4.5 keV up to 2 degrees. The effective area is normalized at on-axis. The integration area is corresponding to the detector size of XIS ($17'.8 \times 17'.8$). The plots are necessary to plan observations of diffuse sources or faint emissions near bright sources, such as outskirts of cluster of galaxies.

The three solid lines in the plots correspond to different parameters of ray-tracing program while the crosses are the normalized effective area using the Crab pointings. For example, the effective area of the stray lights at 1.5 keV is $\sim 10^{-3}$ at angles smaller than 70 arcmin off axis and $< 10^{-3}$ at angles larger than 70 arcmin off. The measured flux of stray lights are in good agreement with that of raytracing within an order.

3.1.3 X-ray Imaging Spectrometer (XIS)

Overview of the XIS

Suzaku has four X-ray Imaging Spectrometers (XISs), which are shown in Figure 3.14. These employ X-ray sensitive silicon charge-coupled devices (CCDs), which are operated in a photon-counting mode, similar to that used in the ASCA SIS, *Chandra* ACIS, and *XMM-Newton* EPIC. In general, X-ray CCDs operate by converting an incident X-ray photon into a charge cloud, with the magnitude of charge proportional to the energy of the absorbed X-ray. This charge is then shifted out onto the gate of an output transistor

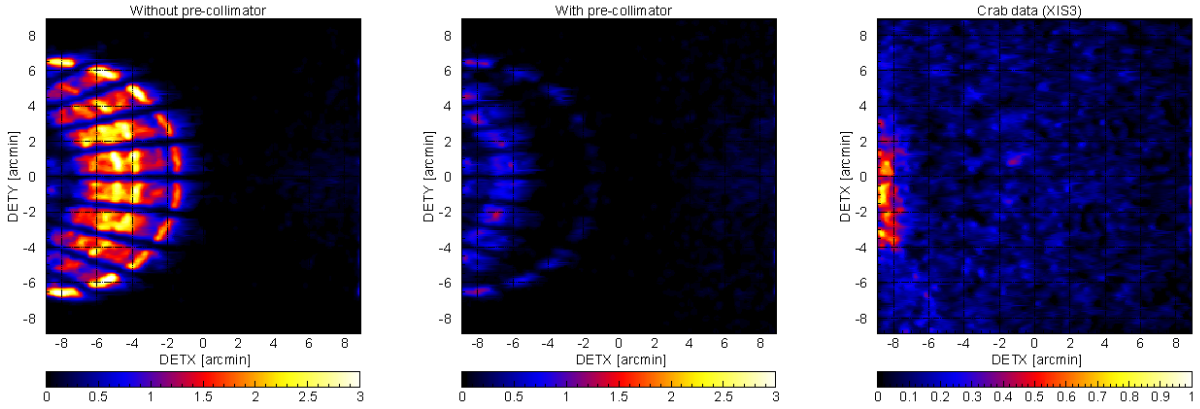

Fig. 3.12: Focal plane images formed by stray light (Serlemitsos et al. 2007). The left and middle panels show simulated images of a monochromatic point-like source of 4.51 keV locating at (DETX, DETY)=($-20'$,$0'$) in the cases of without and with the pre-collimator, respectively. The radial dark lanes are the shades of the alignment bars. The right panels is the in-flight stray image of the Crab Nebula in the 2.5−5.5 keV band located at the same off-axis angle. The unit of the color scale of this panel is counts per 16 pixels over the entire exposure time of 8428.8 s. The counting rate from the whole image is 0.78±0.01 c s^{-1} including background. Note that the intensity of the Crab Nebula measured with XIS3 at the XIS-default position is 458±3 c s^{-1} in the same 2.5-5.5 keV band. All the images are binned with 4×4 pixels followed by being smoothed with a Gaussian with a sigma of 2 pixels, where the pixel size is 24 μm.

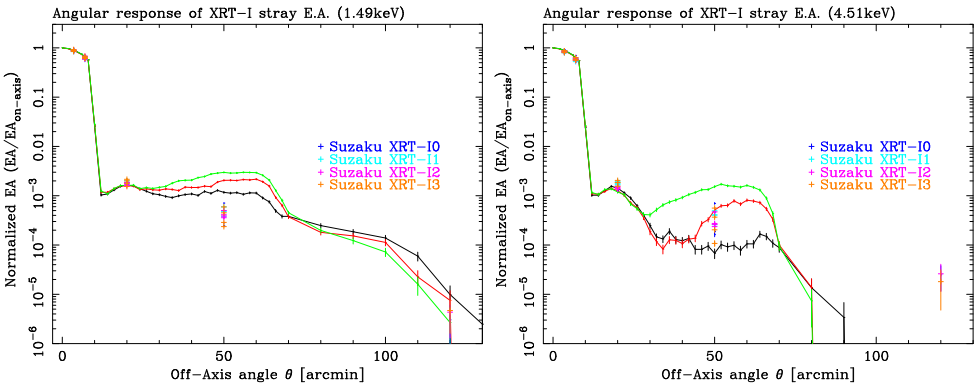

Fig. 3.13: Angular responses of the XRT-I at 1.5 (left) and 4.5 keV (right) up to 2 degrees (Serlemitsos et al. 2007). The effective area is normalized at on-axis. The integration area is corresponding to the detector size of XIS ($17'.8 \times 17'.8$). The three solid lines in the plots correspond to different parameters of ray-tracing program while the crosses are the normalized effective area using the Crab pointings.

via an application of time-varying electrical potential. This results in a voltage level (often referred to as "pulse height") proportional to the energy of the X-ray photon.

The four *Suzaku* XISs are named XIS0, XIS1, XIS2 and XIS3, each located in the focal plane of an X-ray Telescope; those telescopes are known respectively as XRT-I0, XRT-I1,

Fig. 3.14: The four XIS detectors before installation onto *Suzaku* (Koyama et al. 2007).

XRT-I2, and XRT-I3. Each CCD camera has a single CCD chip with an array of 1024 × 1024 picture elements ("pixels"), and covers an $17.8' \times 17.8'$ region on the sky. Each pixel is 24 μm square, and the size of the CCD is 25 mm × 25 mm. One of the XISs, XIS1, uses a back-side illuminated (BI) CCDs, while the other three use front-side illuminated (FI) CCDs. The XIS has been partially developed at MIT (CCD sensors, analog electronics, thermo-electric coolers, and temperature control electronics), while the digital electronics and a part of the sensor housing were developed in Japan, jointly by Kyoto University, Osaka University, Rikkyo University, Ehime University, and ISAS.

A CCD has a gate structure on one surface to transfer the charge packets to the readout gate. The surface of the chip with the gate structure is called the "front side". A front-side illuminated CCD (FI CCD) detects X-ray photons that pass through its gate structures, i.e. from the front side. Because of the additional photo-electric absorption at the gate structure, the low-energy quantum detection efficiency (QDE) of the FI CCD is rather limited. Conversely, a back-side illuminated CCD (BI CCD) receives photons from "back," or the side without the gate structures. For this purpose, the undepleted layer of the CCD is completely removed in the BI CCD, and a thin layer to enhance the electron collection efficiency is added in the back surface. A BI CCD retains a high QDE even in sub-keV energy band because of the absence of gate structure on the photon-detection side. However, a BI CCD tends to have a slightly thinner depletion layer, and the QDE is therefore slightly lower in the high energy band. The decision to use only one BI CCD and three FI CCDs was made because of both the slight additional risk involved in the

new technology BI CCDs and the need to balance the overall efficiency for both low and high energy photons.

To minimize the thermal noise, the sensors need to be kept at ~ -90°C during observations. This is accomplished by thermo-electric coolers (TECs), controlled by TEC Control Electronics, or TCE. The Analog Electronics (AE) drives the CCD clocks, reads and amplifies the data from the CCDs, performs the analog-to-digital conversion, and routes the signals to the Digital Electronics (DE). The AE and TCE are located in the same housing, and together, they are called the AE/TCE. *Suzaku* has two AE/TCEs; AE/TCE01 is used for XIS-S0 and S1, and AE/TCE23 is used for XIS-S2 and S3. The digital electronics system for the XISs consists of two Pixel Processing Units (PPU) and one Main Processing Unit (MPU); PPU01 is associated with AE/TCE01, and PPU23 is associated with AE/TCE23. The PPUs receive the raw data from AE, carry out event detection, and send event data to the MPU. The MPU edits and packets the event data, and sends them to the satellite's main digital processor.

To reduce contamination of the X-ray signal by optical and UV light, each XIS has an Optical Blocking Filter (OBF) located in front of it. The OBF is made of polyimide with a thickness of 1000 Å, coated with a total of 1200 Å of aluminum (400 Å on one side and 800 Å on the other side). To facilitate the in-flight calibration of the XISs, each CCD sensor has two ^{55}Fe calibration sources. One is installed on the door to illuminate the whole chip, while the other is located on the side wall of the housing and is collimated in order to illuminate two corners of the CCD. The door-mounted source will be used for initial calibration only; once the door is opened, it will not illuminate the CCD. The collimated source can easily be seen in two corners of each CCD. A small number of these X-rays scatter onto the entire CCD. In addition to the emission lines created by these sources, we can utilize a new feature of the XIS CCDs, "charge injection capability," to assist with calibration. This allows an arbitrary amount of charge to be input to the pixels at the top row of the imaging region (exposure area), i.e. the far side from the frame-store region. The charge injection capability may be used to measure the CTI (charge transfer inefficiency) of each column, or even to reduce the CTI. How the charge injection capability will be used is still in progress as of this writing.

Pulse Height Determination, Residual Dark-current Distribution, and Hot Pixels

When a CCD pixel absorbs an X-ray photon, the X-ray is converted to an electric charge, which in turn produces a voltage at the analog output of the CCD. This voltage ("pulse-height") is proportional to the energy of the incident X-ray. In order to determine the true pulse-height corresponding to the input X-ray energy, it is necessary to subtract the *Dark Levels* and correct possible *optical Light Leaks*.

Dark Levels are non-zero pixel pulse-heights caused by leakage currents in the CCD. In addition, optical and UV light may enter the sensor due to imperfect shielding ("light leak"), producing pulse heights that are not related to X-rays. In the case of the ASCA

SIS, these were handled via a single mechanism: Dark Levels of 16×16 pixels were sampled and their (truncated) average was calculated for every exposure. Then the same average Dark Level was used to determine the pulse-height of each pixel in the sample. After the launch of ASCA, it was found that the Dark Levels of different pixels were actually different, and their distribution around the average did not necessarily follow a Gaussian. The non-Gaussian distribution evolved with time (referred to as Residual Dark-current Distribution or RDD), and resulted in a degradation of the energy resolution due to incorrect Dark Levels.

For the *Suzaku* XIS, Dark Levels and Light Leaks are calculated separately in normal mode. Dark Levels are defined for each pixel; those are expected to be constant for a given observation. The PPU calculates the Dark Levels in the Dark Initial mode (one of the special diagnostic modes of the XIS); those are stored in the Dark Level RAM. The average Dark Level is determined for each pixel, and if the dark level is higher than the hot-pixel threshold, this pixel is labeled as a *hot pixel*. Dark Levels can be updated by the Dark Update mode, and sent to the telemetry by the Dark Frame mode. Unlike the case of ASCA, Dark Levels are not determined for every exposure, but the same Dark Levels are used for many exposures unless they are initialized or updated. Analysis of the ASCA data showed that Dark Levels tend to change mostly during the SAA passage of the satellite. Dark Update mode may be employed several times a day after the SAA passage.

Hot pixels are pixels which always output over threshold pulse-heights even without input signals. Hot pixels are not usable for observation, and their output has to be disregarded during scientific analysis. The ASCA SIS did not identify hot pixels on-board, and all the hot pixel data were telemetered and removed during the data analysis procedure. The number of hot pixels increased with time, and eventually occupied significant parts of the telemetry. In the case of XIS, hot pixels are detected on-board by the Dark Initial/Update mode, and their positions and pulse-heights are stored in the Hot-pixel RAM and sent to the telemetry. Thus, hot pixels can be recognized on-board, and they are excluded from the event detection processes. It is also possible to specify the hot pixels manually. There are, however, some pixels which output over threshold pulse-heights intermittently. Such pixels are called flickering pixels. It is difficult to identify and remove the flickering pixels on board; they are inevitably output to the telemetry and need to be removed during the ground processing. Flickering pixels sometimes cluster around specific columns, which makes it relatively easy to identify.

The Light Leaks are calculated on board with the pulse height data after the subtraction of the Dark Levels. A truncated average is calculated for 64×64 pixels (this size may be changed in the future) in every exposure and its running average produces the Light Leak. Thus, the Light Leak is basically the same as the Dark Level in ASCA SIS.

The Dark Levels and the Light Leaks are merged in the parallel-sum (P-Sum) mode, so Dark Update mode is not available in P-Sum mode. The Dark Levels, which are defined for each pixel as the case of the normal mode, are updated every exposure. It may be

considered that the Light Leak is defined for each pixel in P-Sum mode.

On-board Event Analysis

The main purpose of the on-board processing of the CCD data is to reduce the total amount transmitted to ground. For this purpose, the PPU searches for a characteristic pattern of charge distribution (called an event) in the pre-processed (post- Dark Levels and Light Leaks subtraction) frame data. When an X-ray photon is absorbed in a pixel, the photoionized electrons can spread into at most four adjacent pixels. An event is recognized when a valid pulse-height (one between the Event Lower and Upper Thresholds) is found that exceeds the pulse-heights in the eight adjacent pixels (e.g. it is the peak value in the 3×3 pixel grid). The coordinates of the central pixel are considered the location of the event. Pulse-height data for the adjacent 5×5 square pixels are sent to the Event RAM as well as the pixel location.

The MPU reads the Event RAM and edits the data to the telemetry format. The amount of information sent to telemetry depends on the editing mode of the XIS. All the editing modes (in normal mode) are designed to send the pulse heights of at least 4 central pixels of an event to the telemetry, because the charge cloud produced by an X-ray photon can spread into at most 4 pixels. Information of the surrounding pixels may or may not output to the telemetry depending on the editing mode. The 5×5 mode outputs the most detailed information to the telemetry, i.e. all 25 pulse-heights from the 5×5 pixels containing the event. The size of the telemetry data per event is reduced by a factor of 2 in 3×3 mode.

Photon pile-up

The XIS is essentially a position-sensitive integrating instrument, with the nominal interval between readouts of 8 s. If during the integration time one or more photons strike the same CCD pixel, or one of its immediate neighbors, these cannot be correctly detected as independent photons: this is the phenomenon of photon pile-up. Here, the modest angular resolution of the *Suzaku* XRT is an advantage: the central 3×3 pixel area receives 2% of the total counts of a point source, and $\sim$10% of the counts fall within $\sim$0.15 arcmin of the image center. We calculated the count rate at which 50% of the events within the central 3×3 pixels are piled-up (the pile-up fraction goes down as we move out of the image center; this fraction is $<$5% for the 0.15 arcmin radius) — although we offer no formal justification for this particular limit, this is compatible with our ASCA SIS experience (i.e., at this level, the pile-up effects do not dominate the systematic uncertainties).

XIS background rate

All four XISs have low backgrounds, due to a combination of the *Suzaku* orbit and the instrumental design. Below 1 keV, the high sensitivity and energy resolution of the XIS-S1 combined with this low background means that *Suzaku* is the superior instrument for

Table 3.4: Major XIS Background Emission Lines

Line	Energy	XIS-S0	XIS-S1	XIS-S2	XIS-S3
	keV	10^{-9} ct/s/pix	10^{-9} ct/s/pix	10^{-9} ct/s/pix	10^{-9} ct/s/pix
O K	0.5249	18.5 ± 0.5	$69.3^{+2.7}_{-2.6}$	$14.3^{+1.5}_{-1.3}$	$14.1^{+1.1}_{-1.2}$
Al K	1.846	1.98 ± 0.23	3.01 ± 0.51	$1.50^{+0.31}_{-0.28}$	$1.57^{+0.25}_{-0.23}$
Si K	2.307	$0.299^{+0.2080}_{-0.2074}$	2.21 ± 0.45	$0.0644(< 0.282)$	$0.543^{+0.212}_{-0.213}$
Au M	2.1229	0.581 ± 0.234	$1.13^{+0.280}_{-0.291}$	$0.359^{+0.211}_{-0.212}$	$6.69^{+2.91}_{-2.90}$
Mn Kα	5.898	$8.35^{+0.36}_{-0.34}$	0.648 ± 0.289	$0.299^{+0.209}_{-0.2086}$	$0.394^{+0.181}_{-0.18}$
Mn Kβ	6.490	$1.03^{+0.22}_{-0.216}$	$0.294(< 0.649)$	$0.00(< 0.111)$	$0.428^{+0.225}_{-0.226}$
Ni Kα	7.470	7.20 ± 0.31	6.24 ± 0.53	$3.78^{+0.26}_{-0.25}$	$7.13^{+0.36}_{-0.37}$
Ni Kβ	8.265	0.583 ± 0.183	$1.15^{+0.5}_{-0.489}$	0.622 ± 0.206	$0.983^{+0.247}_{-0.249}$
Au Lα	9.671	$3.52^{+0.27}_{-0.28}$	$3.28^{+1.16}_{-0.99}$	$1.88^{+0.31}_{-0.28}$	$3.54^{+0.36}_{-0.35}$
Au Lβ	11.514	$2.25^{+0.73}_{-0.59}$	2.91 ± 1.29	$0.752^{+0.428}_{-0.304}$	$2.67^{+0.61}_{-0.53}$

Note: Typical accumulation time are 110-160 ks

observing soft sources with low surface brightness. At the same time, the large effective area at Fe K (comparable to the XMM pn) combined with this low background make *Suzaku* a powerful tool for investigating hot and/or high energy sources as well.

In the XIS, the background originates from the cosmic X-ray background (CXB) combined with charged particles (the non-X-ray background, or NXB). Currently, flickering pixels are a negligible component of the background. When observing the dark earth (*i.e.* the NXB), the background rate between 1-12 keV in is 0.11 cts/s in the FI CCDs and 0.40 cts/s in the BI CCD; see Figure 3.15:left. Note that these are the fluxes after the grade selection is applied with only grade 0, 2, 3, 4 and 6 selected. There are also fluorescence features arising from the calibration source as well as material in the XIS and XRTs. The Mn lines are due to the scattered X-rays from the calibration sources. As shown in Table 3.4 the Mn lines are almost negligible except for XIS-S0. The O lines are mostly contamination from the day earth (3.1.3). The other lines are fluorescent lines from the material used for the sensor. Table 3.4 shows the current best estimates for the strength of these emission features, along with their 90% upper and lower limits.

The background rate on the FI chips (including all the grades) is normally less than 400 counts/frame (50 cts/s) when no class discriminator is applied. On the BI chip, the rate is normally less than 150 counts/frame (18.75 cts/s). The background rate on the FI chips is expected to reduce significantly when the class discriminator is applied. But little change is anticipated for the BI chip. Since 5×5, 3×3, and 2×2 modes require on average 40, 20, and 10 bytes per event, the minimum telemetry required for any source is ~ 58 kbits/s for 5×5 mode, ~ 31 kbits/s for 3×3, and ~ 17 kbits/s for 2×2 mode, if no class discriminator is used.

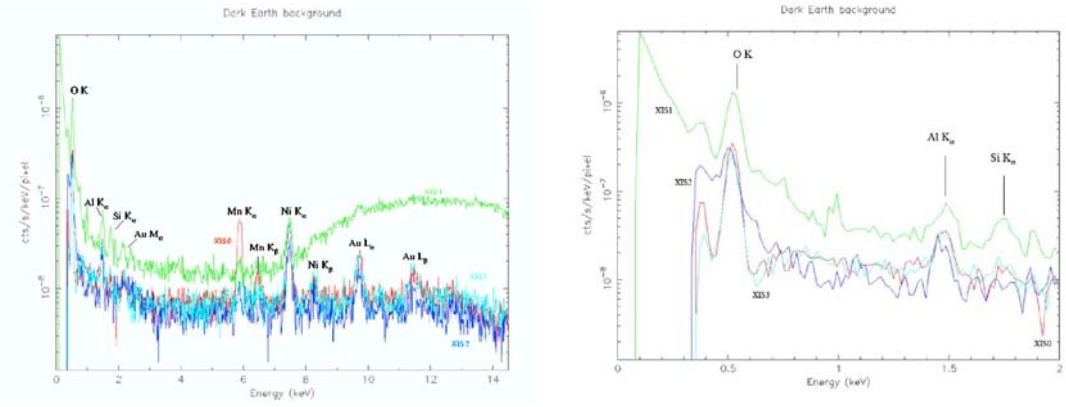

Fig. 3.15: Left: The XIS background rate for each of the four XIS detectors, with prominent fluorescent lines marked. These spectra are based on $\sim 110 - 160$ ksec of observations towards the dark Earth. These spectra does not included Cosmic X-ray background (CXB). Right: The XIS background rate for each of the four XIS detectors, showing only energies between 0.1-2.0 keV. Below 0.3 keV the background rate for the FI chips cannot be determined due to their low effective area.

Out-of-time events X-ray photons detected during the frame-store transfer do not correspond to the true image, but instead appear as a streak or blur in the readout direction. These events are called out-of-time events., and they are an intrinsic feature of CCD detectors. Similar streaks are seen from bright sources observed with *Chandra* and *XMM-Newton*. Out-of-time events produce a tail in the image, which can be an obstacle to detecting a low surface brightness feature in an image around a bright source. Thus the out-of-time events reduce the dynamic range of the detector. Since XIS spends 25 ms in the frame-store transfer, about 0.3% ($= 0.025/8 \times 100$) of all events will be out-of-time events. However, because the orientation of the CCD chip is different among the sensors, one can in principle distinguish a true feature of low surface brightness and the artifact due to the out-of-time events by comparing the images from two or more XISs.

Day Earth Contamination When the XIS field of view is close to the day earth (i.e. Sun lit Earth), fluorescent lines from the atmosphere contaminate low-energy part of the XIS data, especially in the BI chip. Most prominent is the oxygen line, but the nitrogen line may be also noticed (Fig. 3.15:right). These lines are mostly removed when we apply the standard data screening criteria (XIS FOV is at least 20 degree away from the day earth) during the ground processing. However, small amount of contamination can remain. This contamination may be further reduced if we subtract appropriate background. This subtraction, however, may be imperfect. Thus, when neutral oxygen or nitrogen lines are detected in the XIS data, contamination from day earth should be suspected.

Radiation Damage and On-board Calibration of the XIS

The performance of X-ray CCDs gradually degrades in the space environment due to the radiation damage. This generally causes an increase in the dark current and a decrease of the charge transfer efficiency (CTE). In the case of XIS, the increase of the dark current is expected to be small due to the low (–90°C) operating temperature of the CCD. However, a decrease in CTE is unavoidable. Thus, continuous calibration of CCD on orbit is essential to the good performance of the XIS. For this purpose, we use a radio isotope source and charge injection as explained below:

(i) Each XIS carries ^{55}Fe calibration sources near the two corners of the chip, which will be used to monitor the instrument gain.

(ii) Each XIS CCD is equipped with charge injection capability, which may be useful to measure and even suppress CTI.

Nonetheless, it is difficult to predict based on existing data how well we can calibrate the long-term performance change of XIS on orbit.

On-ground event selection

Internal (non X-ray) background events can be effectively removed using the pattern on CCD pixels (GRADE), the position (STATUS) and time of an event. The definition of GRADE is shown in Figure 3.16. Most of X-ray events take GRADE = 0, 2, 3, 4, or 6. On the other hand, most of the events of other GRADEs are dominated by non X-ray events, and should be excluded. STATUS parameter stores the information of pixel quality of an event. Known hot pixels, bad CTE columns, flickering pixels, and pixels on the segment boundaries can be removed by selecting the events with STATUS$<$ 131072. The parameters used in good time interval (GTI) selection are shown in Table 3.5. The signal to noise ratio can be improved with an appropreate GTI criteria, indicated in Table 3.5.

Table 3.5: Parameters used in GTI selection of *Suzaku*

Parameter	Definition	Recommended value to use
SAA	Whether the satellite was in the SAA[a] or not	eq.0
T_SAA	Time after the last SAA duration (s)	> 255
ELV	Elevetion angle from the Earth limb (degree)	> 5
DYE_ELV	Elevation angle from the day Earth limb (degree)	> 20
COR	Cut off rigidity of the cosmic ray (GeV/c/particle)	> 8

[a]: South Atlantic anomaly

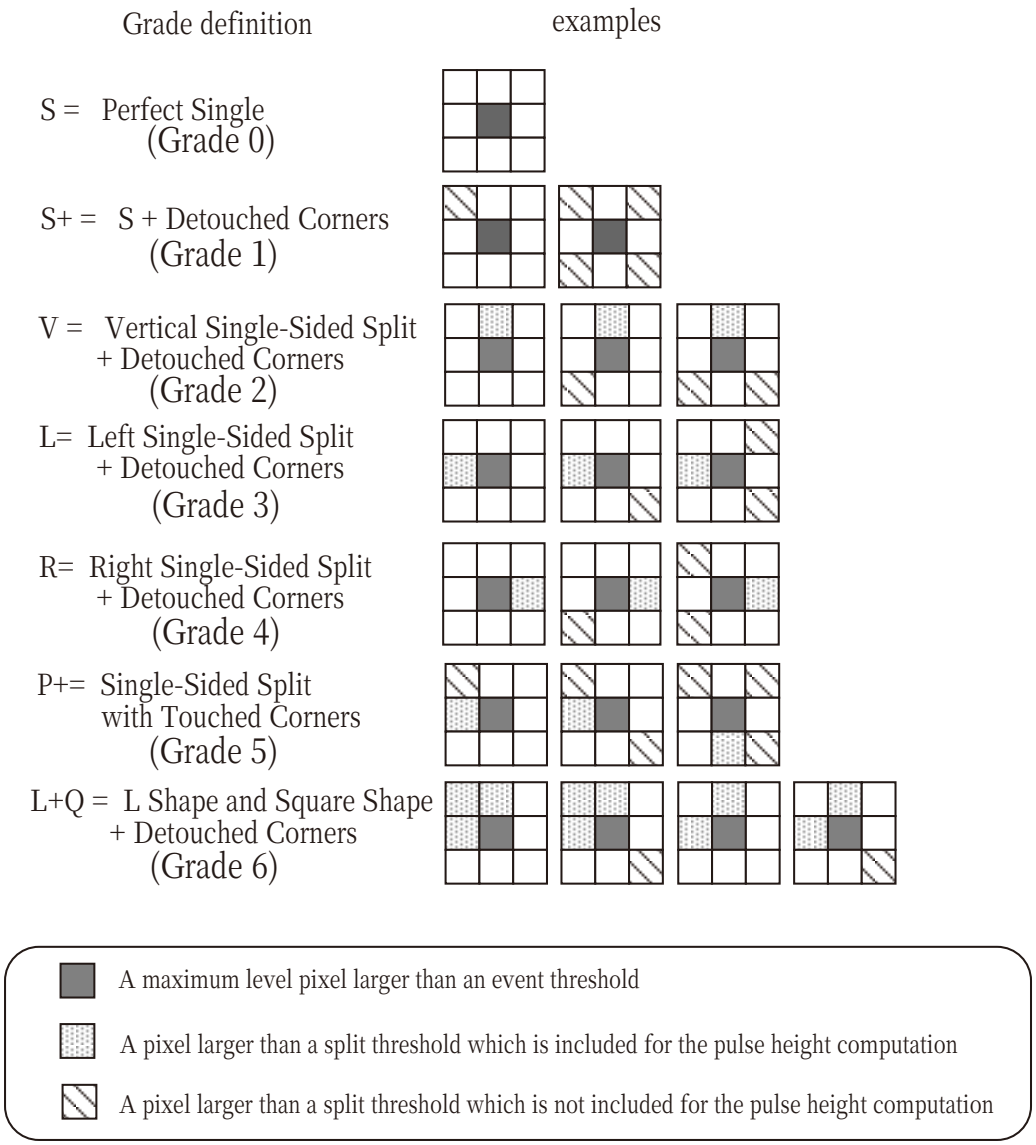

Fig. 3.16: Definition of GRADE of CCD events.

Contamination crrection

The OBF has been gradually contaminated in time by out-gassing from the satellite. The contamination rate af- ter the XIS door-open is unexpectedly high, and the rate is dierent from sensor to sensor. Moreover, the thickness of the contamination varies with position on the OBF.

The contamination has caused a signicant reduction in low-energy response since launch. We therefore need to include additional, time-varying low energy absorption in the response function. This is given as a function of both the observation date after the XIS door-open, and of de- tector coordinates (specifying the position on the OBF). For this purpose, we measured the on-axis extra absorp- tion by observing a SNR 1E0102–72 and an isolated neu- tron star RX J1856.5–3754. At the time of writing, we have not conclusively determined the chemical composi- tion for the contamination material(s). From the overall spectral shape in the low energy absorption for all the available X-ray

sources and the best guess for the out- gassing source in *Suzaku*, we assume that the contami- nant contains predominantly C and O with the number ratio C/O 6. Figure 3.17 shows the time histories of the contamination accumulated on the OBF. Empirically, the time dependence of the contamination thickness is assumed to follow the exponential form as; $N_c = a - b \times \exp -day/c$, where N_c is the carbon column density in units of 10^{18} cm^{-2} (C/O = 6). To measure the off-axis absorption, we used diuse X-rays from the bright Earth rim and the Cygnus Loop. The former emits characteristic K lines of N_I and O_I (neutral atoms) and the latter provides K lines from C_{VI}, N_{VII}, O_{VII} and O_{VIII} (He-like or H-like atoms). Since the for-mer can be observed frequently, we trace the time history of o-axis absorption over successive one-month periods after the XIS door-open (13 August, 2005). With the two reasonable assumptions that (1) the N:O line ratio is uniform over the eld of view and (2) the contamination is azimuthally constant, we can derive the radial prole of the dierence of contamination thickness from the center value. We show the radial proles of the column den- sity of carbon in gure 15 for one month and ve months after the door-open. This radial prole is approximated by a function of $1/[1 + \{r/a(t)\}^{b(t)}]$. The time dependent parameters, $a(t)$ and $b(t)$ are determined and up-dated regularly.

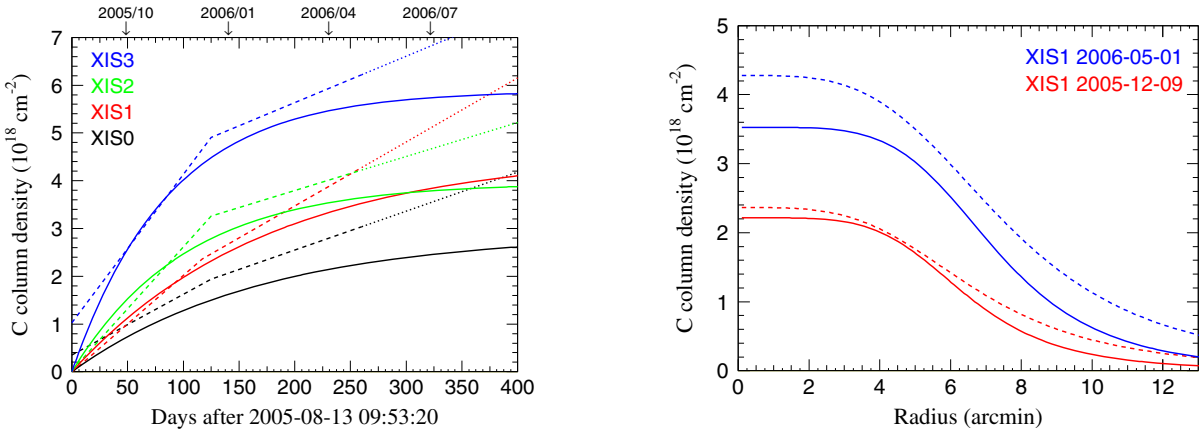

Fig. 3.17: Left: The time history of the contamination of all four XIS detectors, measured at the center of the OBF. The dotted and solid line denoted the models used by CALDB file of 2006-5-24 and 2006-10-24 version, respectively. Right: The radial prole of the contamination of the BI (XIS1).

3.1.4 Uncertainties of metal abundance

We must consider three uncertaities for metal abundance, especially oxygen and magnesium, analizing the spectra of XIS.

1. Systematic uncertainties (NXB and CXB level, gain and CTI correction and so on.)

2. Our Galactic components

3. Contamination on XIS

(1): We check the effects by changing the NXB and CXB levels by ±10%. (2): Because the O VII and O VIII lines emitted from ICM are coupled with these emitted from our Galaxy, the estimation of the emission from our Galaxy is very impotant to decide the oxygen abundance of ICM. (3): As descibed in 3.1.3, because the observed spectra are absorbed by the contaminant on XIS, the effect are taken into account with the arfs, and we also check the uncertainty of the arfs by changing the amount of contaminant by $10 \sim 20\%$.

It is the negligible effects for the central brightness region of the cluster, however it is the severe effects, especially (2) and (3), for the faint region such as the outskirts of the cluster. Especialy the soft X-ray band (below $\sim$1 keV), the effects of (2) and (3) are impotant. Thus, we are careful to analyze the spectra for the decision of the oxygen and magnesium abundance. In addtion, the abundance may vary whether we use a one or multi temperature model.

3.2 *XMM-Newton*

The ESA (European Space Agency) X-ray satellite *XMM-Newton* was launched on 10 December 1999 from Kourou (French Guiana), by the Ariane-V rocket (Jansen et al. 2001). It was placed into a highly eccentric orbit, with an apogee of about 115,000 km, a perigee of about 6,000 km, and an orbital inclination of 33°, which provides the best visibility in the southern celestial sky. Although the orbital period is 48 hours, the exposure available for scientific data analysis is limited to 39 hours (140 ksec) per orbit. This is because observations are not carried out when the satellite altitude is less than 46,000 km, where the radiation background related to the Earth's magnetosphere is severe. *XMM-Newton* provides the following three types of science instrument.

- European Photon Imaging Camera (EPIC)
- Reflection Grating Spectrometer (RGS)
- Optical Monitor (OM)

The three EPIC cameras; the two different types of CCD camera, MOS and pn, and the two detectors of the RGS spectrometers reside in the focal planes of the X-ray telescopes, while the OM has its own telescope. A sketch of the *XMM-Newton* payload is displayed in Fig.3.18.

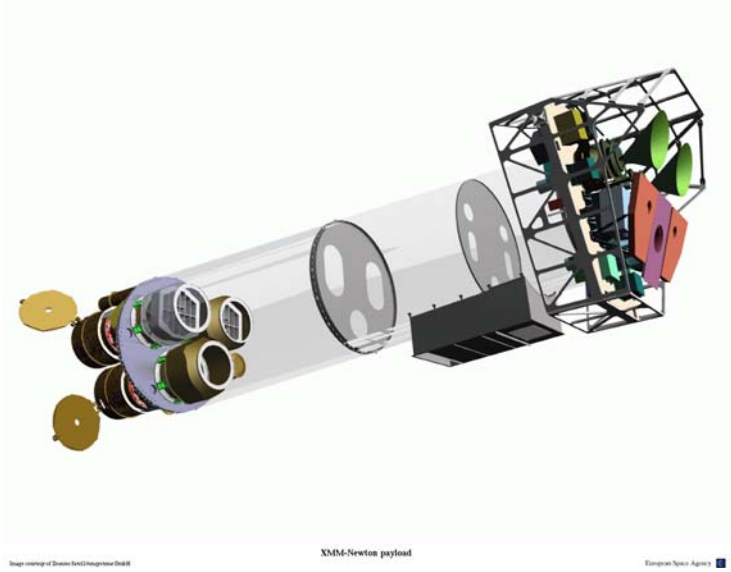

Fig. 3.18: Sketch of the *XMM-Newton* payload. The mirror modules, two of which are equipped with Reflection Grating Arrays, are visible at the lower left. At the right end of the assembly, the focal X-ray instruments are shown: The EPIC MOS cameras with their radiators (black/green horns), the radiator of the EPIC pn camera (violet) and those of the (light blue) RGS detectors (in pink). The OM telescope is obscured by the lower mirror module.

There are in total six science instruments on board *XMM-Newton*, which are operated simultaneously. The instruments can be operated independently and each in different modes of data acquisition.

In the following sections, we describe the X-ray telescopes and EPIC cameras, because we mainly use these instruments in our study. We summarize the basic performance of the EPIC cameras in table 3.6.

Table 3.6: Basic performance of the EPIC detectors

	EPIC-MOS	EPIC-pn
Illumination method	Front illuminated	Back illuminated
Pixel size	40 μm	150 μm
	$1.1''$	$4.1''$
Field of view (FOV)	$30'$	$30'$
PSF (FWHM/HEW)	$5''/14''$	$6''/15''$
Spectral resolution	$\sim$70 eV	$\sim$80 eV
Timing resolution	1.5 ms	0.03 ms
Bandpass	0.15-12keV	0.15-15keV

3.2.1 X-ray Telescopes

Design Structure

XMM-Newton's three XRTs are co-aligned with an accuracy of better than about 1 arcmin. Each of the three telescopes consists of 58 Wolter type-I mirrors, and the mirror grazing incidence angles range between 17 and 42 arcmin. The focal length is 7.5 m and the diameter of the largest mirrors is 70 cm. One telescope with the PN camera at the focal point has a light path as shown in Figure 3.19. The two others have grating assemblies in their light paths, diffracting part of the incoming radiation onto their secondary focus (see Figure 3.20). About 44 % of the incoming light focused by the XRT is directed onto the MOS camera at the prime focus, while 40 % of the radiation is dispersed by a grating array onto a linear strip of CCDs. The remaining light is absorbed by the support structures of the RGAs.

Point-spread function (PSF) of XRTs

A point-spread function (PSF) determines the imaging quality of an XRT. Figure 3.21 shows the in orbit on-axis images obtained by each detector. The radial substructures are caused by the spiders holding the mirror shells. Figure 3.22 displays the azimuthally averaged profile of the PSF of one XRT together with the best-fit King profile, which has the form $A(1/[\{1 + (r/r_c)^2\}^{\alpha}])$, where r is the radial distance from the center of the PSF, r_c is the core radius and α is the slope of the King model. Figure 3.22 shows

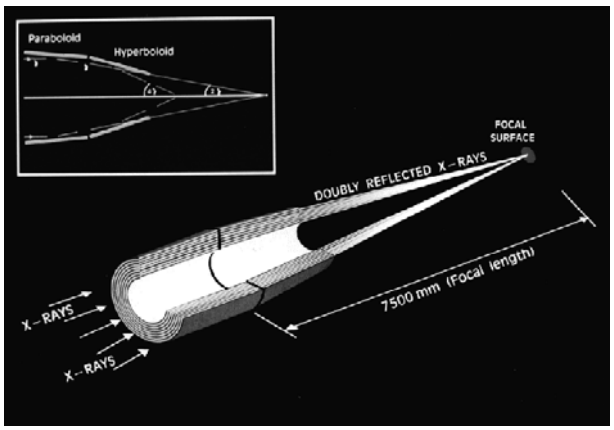

Fig. 3.19: The light path in *XMM-Newton*'s XRT with the PN camera in focus.

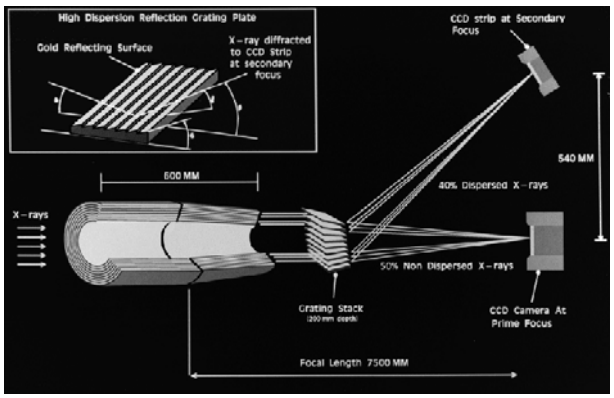

Fig. 3.20: The light path in *XMM-Newton*'s XRT with the MOS camera and RGA.

the encircled energy function (EEF) as a function of radius from the center of the PSF for several different energies. For on-axis source, high energy photons are reflected and focused predominantly by the inner shells of the XRTs. The inner shells apparently give better focus than the average of all shells, hence the EEF increase with increasing photon energy. A half energy width (HEW), which means the width including half of all the reflected photons, of the PSF can be derived from EEF. Table 3.7 lists the on-axis HEW of the different XRTs measured in orbit and on ground.

The PSFs of the XRTs depend on the source off-axis angle. As the off-axis angle increases, the HEW of PSF becomes larger.

Table 3.7: The on-axis in orbit and on ground 1.5 keV HEW of the different XRT.

Instr.	PN	MOS1	MOS2
	orbit/ground	orbit/ground	orbit/ground
HEW [arcsec]	15.2/15.1	13.8/13.6	13.0/12.8

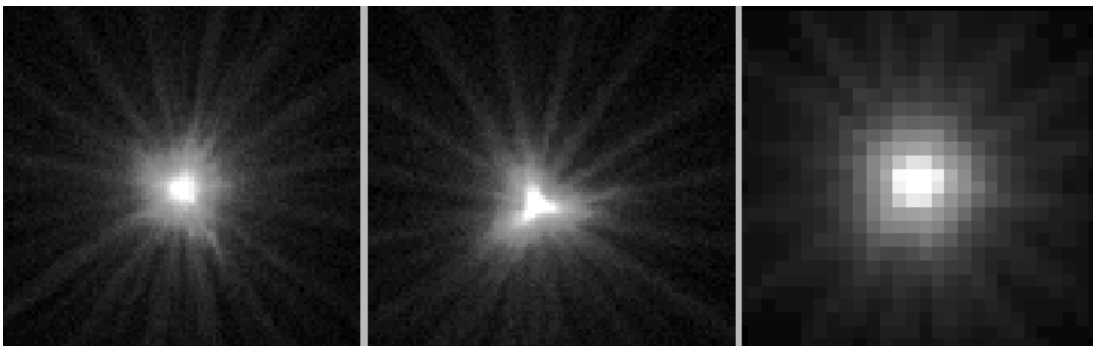

Fig. 3.21: On-axis images of the MOS1, MOS2 and PN XRTs (left to right). The images are 110 arcsec wide and a logarithmic scale has been used to visualize the wings of the point spread function.

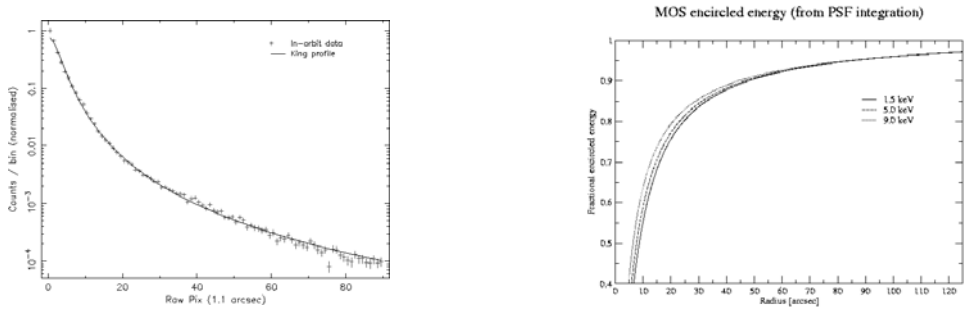

Fig. 3.22: Left: Radial counts distribution for the on-axis PSF of the MOS1 XRT in the 0.75–2.25 keV energy range. The solid line indicates the best-fit King profile. Right: The encircled energy function as a function of angular radius (on-axis) at different energies. The curves are calculated assuming a fractional encircled energy of 100 % at a radial distance of 5 arcmin.

Effective Area (EA) of XRTs

An effective area is an indicator of ability of collecting photons. *XMM-Newton* carries the XRT with the largest effective area of focusing telescope ever. The total mirror geometric effective area (EA) at 1.5 keV energy is about 1,550 cm^2 for each telescope, i.e., 4,650 cm^2 in total. Figure 3.23 shows the on-axis effective area of all *XMM-Newton* XRTs. The EAs of the two MOS cameras are lower than that of the pn, because only part of the incoming radiation falls onto these detectors, which are partially obscured by the RGAs (see Figure 3.20). Not only the shape of the X-ray PSF, but also the effective area of the XRT is a function of off-axis angle within the field of view. Decreasing of photons reflected effectively in the XRT arises from an increasing off-axis angle. This effect is called vignetting. Figure 3.23 displays the vignetting function as a function of off-axis angle for several different energies. The vertical axis is normalized by the on-axis effective area.

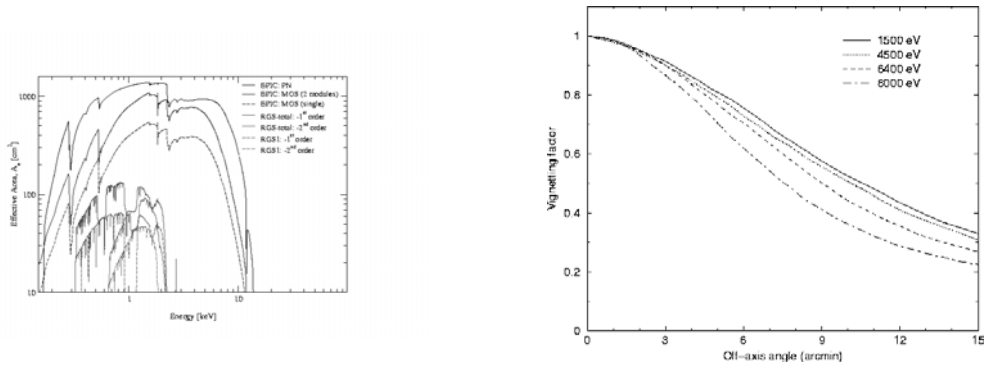

Fig. 3.23: Left: The net effective area of all *XMM-Newton* XRT, combined with the response characteristics of the focal detectors. Right: Vignetting function as a function of off-axis angle at several different energies (based on simulations).

Straylight Rejection

X-ray straylight is produced by rays which are singly reflected by the mirror hyperbolas and which reach the sensitive area of the focal plain detectors. Thus, an X-ray baffle was implemented to shadow those singly reflected rays. It consists of two sieve plates made of concentric annular aperture stops located in front of the mirrors at 85 mm and 145 mm, respectively. The design is such that the entrance annular aperture of each mirror remains unobstructed for on-axis rays. The collecting area of straylight in the EPIC detector as a function of off-axis angle for a point source is about 3 cm^2 for stray sources located between 20 arcmin and 1.4° from the optical axis. The ratio of the X-ray straylight collecting area to the on-axis effective area is smaller than 0.2 % at 1.5 keV for a point source located at off-axis angles of 0.4–1.4° and negligible at higher off-axis angles. Figure 3.24 displays the effect of straylight, which is obtained from the observation of GRS 1758-258 (a black hole candidate near the Galactic center). Some sharp arcs are caused by single mirror reflections of photons possibly from GX 5-1 which is located at off-axis angle of 40 arcmin to the north and outside the field of view.

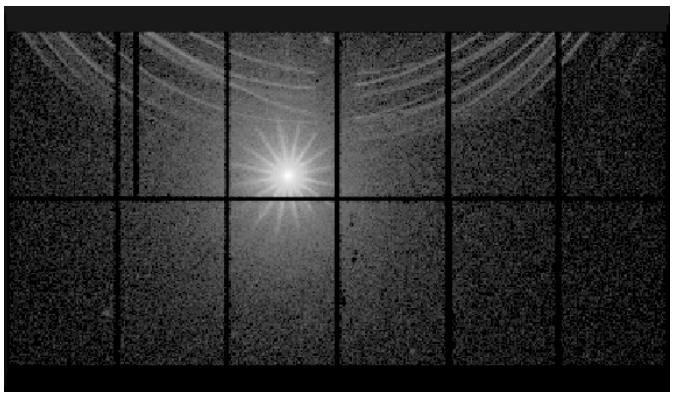

Fig. 3.24: The effect of straylight appeared in PN image of GRS 1758-258.

3.2.2 European Photon Imaging Camera (EPIC)

Two of *XMM-Newton*'s X-ray telescopes are equipped with EPIC MOS (Metal Oxide Semi-conductor, Turner et al. (2001)) CCD arrays, the third carries a different CCD camera called EPIC PN (Strüder et al. 2001). The EPIC cameras offer the possibility to perform extremely sensitive imaging observations over a field of view of 30 arcmin and the energy range from 0.15 to 15 keV, with moderate spectral ($E/\Delta E \sim 20$–50) and angular resolution (15 arcsec HEW). The detector layout and the baffled X-ray telescope FOV of both types of EPIC cameras are shown in Figure 3.25. The PN chip array is slightly offset with respect to the optical axis of its X-ray telescope so that the nominal, on-axis observing position does not fall on the central chip boundary. This ensures that more than 90 % of the energy of an on-axis point source are collected on one PN CCD chip. Two EPIC MOS cameras are rotated by 90° with respect to each other. The dead spaces between the MOS chips are not gaps, but unusable areas due to detector edges (the MOS chip physically overlap each other, the central one being located slightly behind the ones in the outer ring). All EPIC cameras are operated in photon counting mode with a fixed, mode dependent frame read-out frequency.

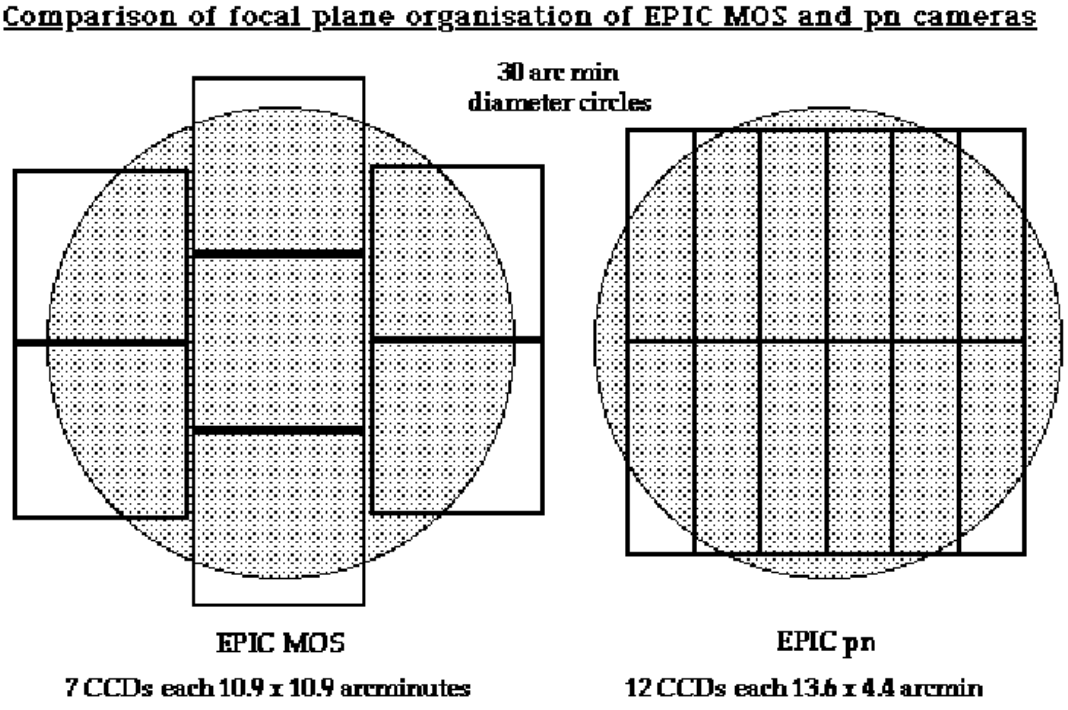

Fig. 3.25: A rough sketch of the field of view of the two types of EPIC cameras (MOS, left; PN, right). The shaded circle depicts a 30 arcmin diameter area which is equivalent with the XRT field of view.

Angular resolution

The EPIC MOS and PN cameras have pixels with sizes of 40 and 150 μm, respectively. For the focal length of the X-ray telescopes (7.5 m), these pexel size corresponds to 1.1 arcsec and 4.1 arcsec on the sky. Since they are smaller than the HEW of XRT (15 arcsec), EPIC's angular resolution is basically determined by the PSF of the mirror modules.

Energy resolution

The resolving power of EPIC cameras is determined by the intrinsic energy resolution of the individual pixels. Figure 3.26 and 3.26 show the energy resolution (FWHM) of MOS and PN, respectively. The measured in-flight FWHM of the Al Kα (1.5 keV) and Mn Kα (5.9 keV), which are the on-board calibration lines, are also plotted in Figure 3.26. It is well known that the energy resolution of MOS cameras has been gradually decrease due to the CTI (charge transfer inefficiency) effect, which means the imperfect transfer of charge as it is transported through the CCD to the output amplifiers. The latest calibration status is found at *XMM-Newton* Science Operation Centre.[1] The accuracy of the energy determination is about 10 eV over the full energy range and for all modes except for MOS timing mode.

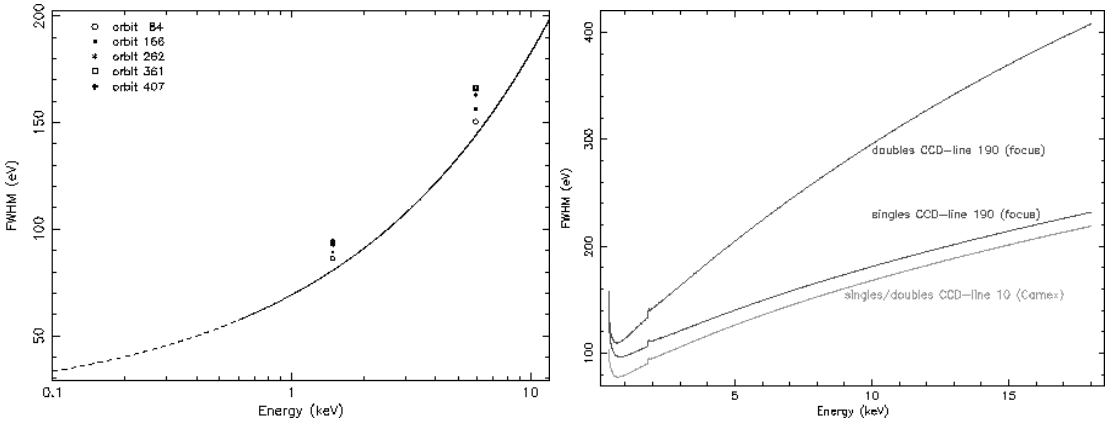

Fig. 3.26: Left: The EPIC MOS energy resolution (FWHM) as a function of energy. The solid curve is a best-fit $E^{0.5}$ function to ground calibration data between 0.1–12.0 keV. Below around 0.6 keV (shown by the dotted region), surface charge loss effects distort the main photopeak significantly from a Gaussian form and, hence the effective energy resolution. The measured in-flight FWHM of the Al Kα (1.487 keV) and Mn Kα (5.893 keV) lines are also plotted. Right: The EPIC PN energy resolution (FWHM) as a function of energy. Curves are given for single and double events (full frame mode) at the focus position node.

[1] *http://xmm.vilspa.esa.es/external/xmm_sw_cal/calib/documentation.shtml#EPIC*

Quantum efficiencies

The quantum efficiency of both types of EPIC CCD chips as a function of photon energy is displayed in Figure 3.27 and 3.27. These chips were calibrated using laboratory X-ray beams, synchrotron generated monochromatic X-ray beams, before launch, and celestial X-ray source measurements. We can see the typical X-ray absorption fine structure (XAFS) behavior around the silicon K edge at 1.838 keV. Ground calibration measurements have shown that the quantum efficiency of MOS CCDs is uniform above 400 eV. Below this energy, spatial variations are seen as patches in the outer parts of the CCDs where the response is degraded. This inhomogeneity is currently not taken into account by the *XMM-Newton* science analysis system (SAS).

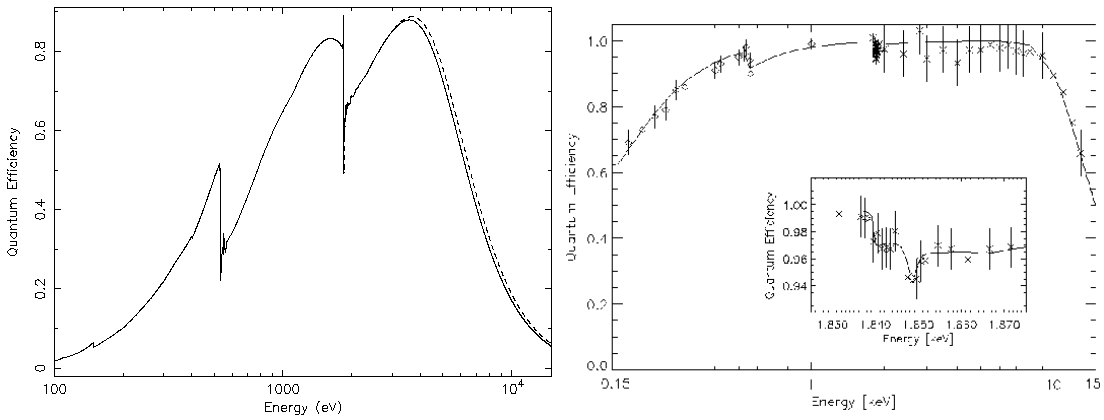

Fig. 3.27: Left: Quantum efficiency of the EPIC MOS camera as a function of photon energy. Right: Quantum efficiency of the EPIC PN camera as a function of photon energy.

EPIC Filters

The EPIC CCDs are not only sensitive to X-ray photons, but also to IR, visible and UV light. Therefore, if an astronomical target has a high optical to X-ray flux ratio, there is a possibility that the X-ray signal becomes contaminated by those photons. To prevent such a contribution, each EPIC camera is equipped with a set of 3 separate aluminised optical blocking filters, named *thick*, *medium* and *thin*. The thick filter should be used for all point source targets up to m_V of 1–4 (MOS) or 0–3 (PN). The medium filter is about 10^3 less efficient than the thick filter, therefore, it is useful for preventing optical contamination from point sources as bright as $m_V = 8$–10. The thin filter is about 10^5 less efficient than the thick filter, so the use of this filter will be limited to point sources with optical magnitudes about 14 magnitudes fainter than the corresponding thick filter limitations.

Event pattern

An absorbed sometimes deposits its energy over more than one pixels. This is called split event, and in this case the charges mus be summed up over the relevent pixels. This

process is automatically done by analysis software. The split pattern is classified in Figure 3.28. The patterns 0-12 for MOS and 0-4 for pn are considered to be X-ray events, while the others are false events induced by charged particles. Because of its much larger pixel size than MOS, the charge split occurs less frequently in pn (Turner et al. 2001).

Any events which located at around an edge or bad pixel are flagged by negative value. These events have possibility that the energy of these events are not correct. If we make a condition that the events have flag=0, we remove the events which are rocated around the edge ore bad pixel.

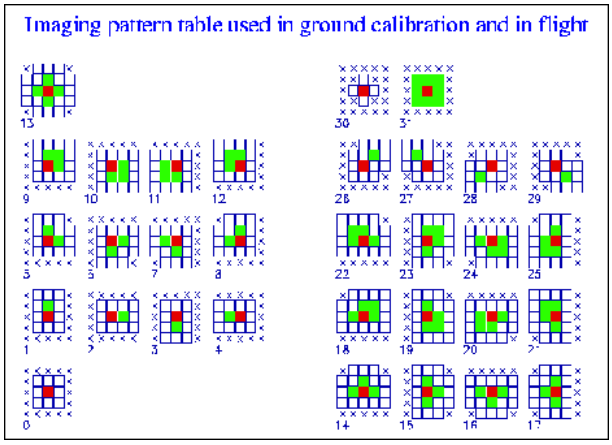

Fig. 3.28: Event patterns recognized by the MOS (pn) detectore. The red pixel is the centre pixel, its signal is above threshold and is the largest signal in the 3×3 inner matrix. The green pixels have signals above threshold. The white pixels have signal below threshold. The crosses indicate pixels no considered.

3.2.3 EPIC Background

The EPIC background can be divided into two parts: a cosmic X-ray background (CXB), and an instrumental background. The latter component may be further divided into a detector noise component, which becomes important at low energies (i.e. below 200eV) and a second component which is due to the particles interaction. This component is characterized by a flat spectrum and is particularly important at high energies (i.e. above a few keV).

The particle induced background can be divided into two components: an external 'flaring' component, characterized by strong and rapid variability, which is often totally absent and a second more stable internal component. The flaring component is currently attributed to soft protons, which are presumably funneled towards the detectors by the X-ray mirrors. The stable component is due to the interaction of high-energy particles with the structure surrounding the detectors and possibly the detectors themselves. We summarize the all background component below.

In the following we describe some of the main properties of both components.

Back Ground

- Cosmic X-ray Background
- Instrumental Background
  - Detector noise component (below 200eV)
  - Particle component (above a few keV)
    - flaring component (attributed soft photons)
    - stable component (attributed high-energy particles)

Temporal properties

As shown in Figure 3.29, the EPIC background count rate often exhibits sudden increases by as large as two orders of magnitudes, called 'flares'. Such phenomena are not observed in the *ASCA* SIS. This is mainly due to the difference in their orbits. *ASCA* had an almost circular orbit with an altitude of 520-620 km, while XMM-Newton take highly eccentric orbits, with apogees of $\sim 115,000$ km and perigees of $\sim 6,000$ km. Therefore, XMM-Newton fly mostly outside the Earth's magneto-sphere. Now it is known that the background flares are caused by soft protons with energies below 1 MeV, reflected and focused by the X-ray mirrors. The spectra of soft proton flares are variable and no clear correlation is found between intensity and spectral shape. The current understanding is that soft protons are most likely organized in clouds populating the Earth's magneto-sphere. The number of such clouds encountered by XMM-Newton in its orbit depends upon many factors, such as the altitude of the satellite, its position with respect to the magneto-sphere, and the amount of solar activity.

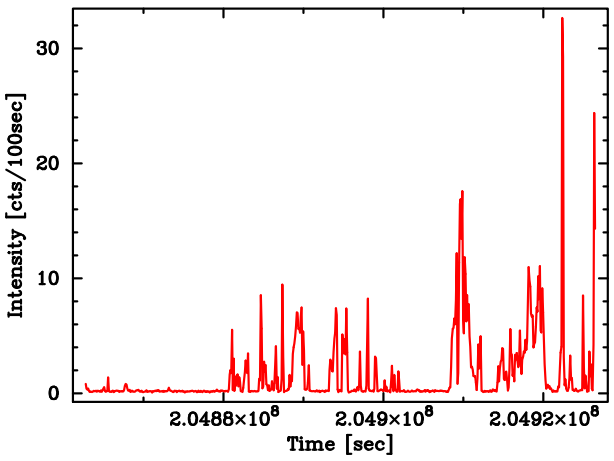

Fig. 3.29: An example of light Curve from a MOS1 observation badly affected by proton flares.

The EPIC background events in quiescent (non-flaring) periods are produced mainly by the interaction of high energy particles with the structure surrounding the detectors,

and the detectors themselves. This component varies only by a small fraction, and on relatively longer timescales. On a representative time scale of several tens ksec, the standard deviation of both PN and MOS count rates is about 8 % (Katayama et al. 2004; Pizzolato 2001; Read & Ponman 2003).

Spectral properties

In Figure 3.30, we show the MOS1 and PN spectra extracted from a blank sky region. These background spectra consist of non X-ray background (NXB) and cosmic X-ray background (CXB). The NXB is induced mainly by charged particles. The CXB is mainly dominates at lower energies by soft thermal emission around the solar system. The entire background spectra are dominated by the NXB at high energy regions, and the CXB becomes more important as the energy decreases. Their contributions are comparable at the energy of $\sim$ 1 keV.

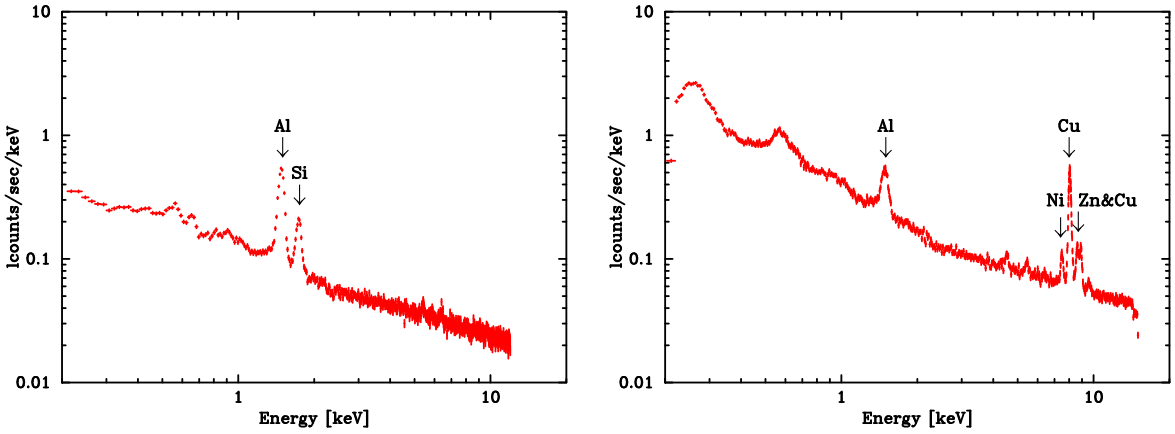

Fig. 3.30: MOS1(left) and PN(right) background spectrum from a blank sky region. In the left figure, the prominent features around 1.5 and 1.7 keV are Al K and Si K fluorescence lines, respectively. On the other hands, he prominent features, in right figure, are identified as Al-K (1.5 keV), Cr-K (5.5 keV), Ni-K, Cu-K, Zn-K (8.0 keV) and Mo-K (17.5 keV), respectively.

Fig. 3.30 shows several distinct fluorescence lines. In PN spectra, Al-K, Ni, Cu, and Zn-K complex lines are prominent, while Al and Si-K lines are outstanding in the MOS. These lines are emitted from surrounding materials such as electronic circuit boards for the signal readout, excited by high energy charged particles. Both the PN and MOS spectra rise below $\sim$ 0.5 keV, due to the detector noise which is more time variable than the continuum above 0.5keV.

Spatial properties

Because the CXB surface brightness is highly uniform, its brightness distribution on the focal plane obeys the effective area. Due to the vignetting effect, the CXB brightness is highest at the detector center, and gradually decreases toward the periphery.

The distribution of the Si-K line in the MOS is concentrated along the edges of some CCDs. This is attributed to Si-K X-rays escaping from the back side of a neighboring CCD. The asymmetric distribution arises because the 7 CCD chips slightly overlap with one another when viewed from the telescope, although their 3-dimensional positions are offset along the optical axis. This layout is intended to reduce the gaps between CCD chips.

Spatial distributions of emission lines are rather complicated. Figure 3.31 show some background images in limited energy bands. The emission in the Cu-K band is very weak at the center of PN (fig. 3.31 right). Actually, the Cu-K line is insignificant in the spectrum extracted there. The Cu-K line image with the central hole agrees with the layout of electronics boards beneath the PN CCDs, indicating that the Cu-K photons come from them. The same mechanism produces semicircular dark regions at the right and reft sides.

The continuum components of the NXB also have inhomogeneous distribution on the focal plane. The NXB image shows central excess brightness, by about 25 %. The shape is similar to the central hole seen in the Cu-K band image (fig. 3.31), although in this case the brightness shows excess, not a deficit.

As is implied by these non-uniform distributions of various components, the background spectrum strongly depends on the detector position. Therefore, when we use other observations as the background fields, we must extract the background spectrum from the same detector region as the analyzing target.

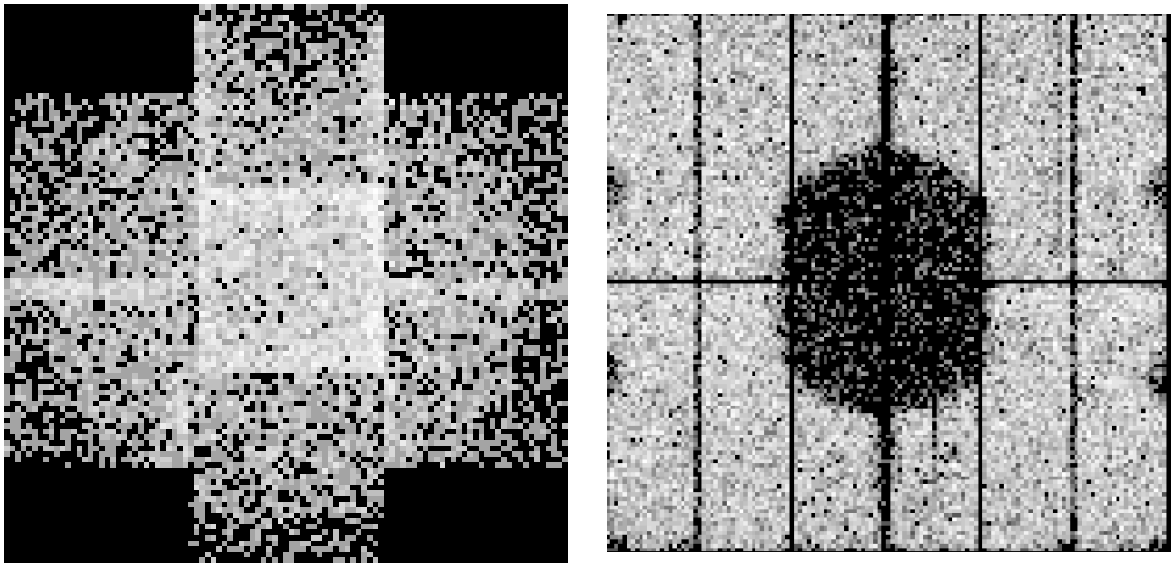

Fig. 3.31: The MOS(left) and PN(right) background image. The MOS image in the energy band centered on Si-K fluorescent line region. As the same, the PN image in the Cu-K fluorescent line energy region.

Chapter 4

Observation and Data reduction

4.1 Sample clusters

We selected 4 Suzaku observations of 3 sample clusters where outer regions (r$> 0.5r_{200}$) were observed using XIS and whose overall X-ray morphology is appeared with regular. Moreover, we also analyzed and these cluster samples with 11 *XMM-Newton* observations to look into their global morphology of surface brightness in the center regions. These clusters and their observations with Suzaku and *XMM-Newton* are listed in tables 4.1, 4.3, and 4.2 respectively.

We will normalize the radial temperatures of clusters and calculate their virial radius from a global gas temperature, $T_{\rm X}$, which should be representative of cluster's virial temperatures. However, because of the limited angular resolution of the Suzaku XRT and the small FOV of the XIS, the XIS is not suited for the measurement of the global temperature. Therefore, we mainly utilize the global temperatures measured using other satellites, as shown in table 4.1.

4.1.1 A1413

The systemic red-shift of A1413 is 0.1427 (Böhringer et al. 2000), which yields an angular diameter distance of 519.8 h_{72}^{-1} Mpc, luminosity distance of 679.1 h_{72}^{-1} Mpc and a scale of

Table 4.1: Cluster samples

Target	N_H^* (10^{20}cm^{-2})	z	D_A Mpc	D_L Mpc	T_X keV	r_{200} Mpc	1kpc/1′
A1413	2.19	0.143	519.8	679.1	6.8	2.2	151.2
A2204	6.07	0.152	548.0	727.6	7.5	1.8	159.4
AWM7	9.83	0.017	71.3	73.8	7.5	2.8	20.8

* Dickey & Lockman 1990

(a) A1413 (XMM)

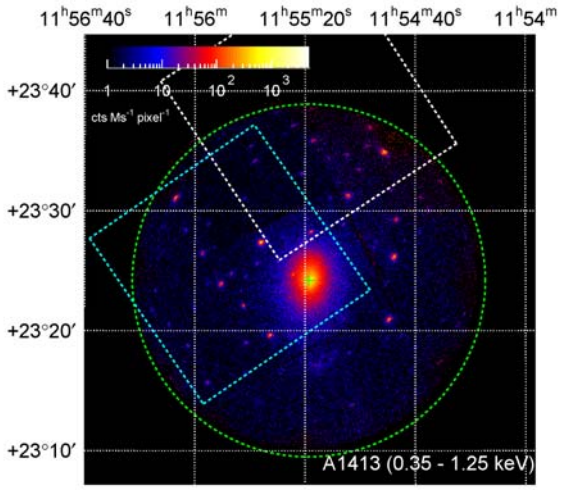

(b) A1413 (Suzaku)

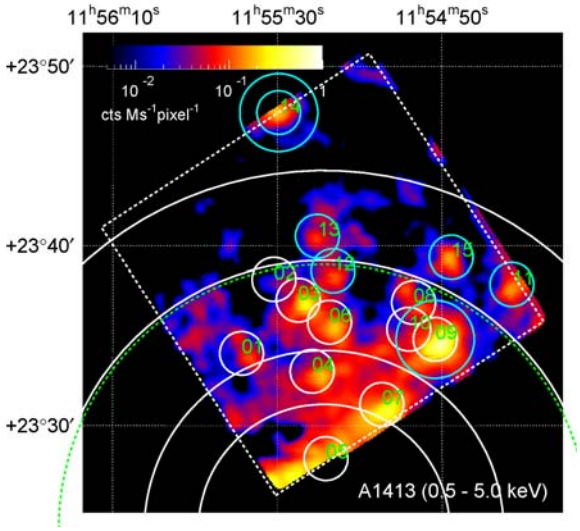

Fig. 4.1: (a) *XMM-Newton* MOS1 + MOS2 image of A1413 in the 0.35-1.25 keV band. The image is corrected for exposure, vignetting and background. The white and blue boxes show the fields of view of the Suzaku XIS and Chandra ACIS (Vikhlinin et al. 2006). The green circle shows r_{200} of $14'.8$. (b) Background subtracted Suzaku FI+BI image of the outskirts of A1413 in the 0.5–5 keV band smoothed by a 2-dimensional gaussian with $\sigma = 16''$. The image is corrected for exposure time but not for vignetting. COR2 > 8 GV and $100 <$ PINUD < 300 cts s^{-1} screening was applied. The ^{55}Fe calibration source regions are also included in the figure, because they have negligible counts in this energy band. Large white circles denote $7'$,

Table 4.2: List of *XMM-Newton* observations

Target	Obs. ID	Obs.date	Type	Filter	Pointing direction	Exp. (MOS1, MOS2)	
A1413	0112230501	2000-12-06	U	Thin	(178.°829, 23.°410)	23.6	23.7
	0502690101	2003-02-02	S	Thin	(178.°829, 23.°404)	0.2	0.2
	0502690101	2003-02-02	U	Thin	(178.°829, 23.°404)	36.4	36.3
	0502690201	2007-12-11	S	Thin	(178.°829, 23.°404)	61.9	61.5
	0502690201	2007-12-12	U	Thin	(178.°829, 23.°404)	0.3	0.2
A2204	0112230301	2001-09-12	S	Medium	(24.°819, 55.°800)	18.0	18.1
	0306490101	2006-02-06	S	Medium	(24.°920, 55.°750)	15.2	15.2
	0306490201	2006-02-08	S	Medium	(24.°820, 55.°750)	12.7	13.0
	0306490301	2006-02-12	S	Medium	(24.°820, 55.°750)	12.7	13.0
	0306490401	2006-02-14	S	Medium	(24.°820, 55.°750)	15.6	17.1
AWM7	0135950301	2003-02-02	S	Medium	(43.°614, 41.°579)	29.5	29.1

* Average pointing direction of the XIS, shown by the RA_NOM and DEC_NOM keywords of the FITS event files.

151.2 h_{72}^{-1} kpc per arcminute for our assumed cosmology. The neutral Hydrogen column density in this direction is 2.19 $\times 10^{20}$ cm^{-2} (Dickey & Lockman 1990). The average temperature of the cluster integrated over the radial range of 70 h_{72}^{-1} kpc to r_{500} is 7.38 $\pm$ 0.11 keV (Vikhlinin et al. 2006), where r_{500} is the radius within which the cluster average density is 500 times the critical density needed to halt the expansion of the universe.

Previous observations indicate the cluster is relaxed and there are high quality temperature and mass radial profiles available from both XMM-Newton and Chandra (Pointecouteau et al. 2005; Vikhlinin et al. 2006).

We show the FI+BI image in the 0.5–5 keV energy band in figure 8.4(b). The non X-ray background (NXB), cosmic X-ray background (CXB), and the Galactic background components (GAL) are subtracted as described below, and the result smoothed by a 2-dimensional gaussian with $\sigma = 16''$ are shown. The image is corrected for exposure time variations, but not for vignetting. Screening requirements are COR2 > 8 GV and $100 <$ PINUD < 300 cts s^{-1}, where COR2 is the cut-off-rigidity calculated with the most recent geomagnetic coordinates and PINUD is the count rate from the upper level discriminatory of the Hard X-ray Detector (HXD) PIN silicon diode detectors (see Tawa et al. 2008). The circles with $70''$ and $125''$ radii enclose excluded point sources. The small white circles indicate point sources detected in the XMM-Newton data. Blue circles show sources selected by eye in the Suzaku image.

There is some disagreement about the mass profile of A1413 in the literature. Pointecouteau et al. 2005 find $r_{500} = 1.13 \pm 0.03 h_{70}^{-1}$ Mpc and $M_{500} = 4.82 \pm 0.42 \times 10^{14} h_{70}^{-1} M_{\odot}$,

Table 4.3: List of *Suzaku* observations

	Target	Seq. Number	Obs.date	Pointing direction*	Exp.	Net exposure
A1413		800001010	2005/11/15 - 2005/11/18	(178.°829, 23.°641)	108	72
A2204		801091010	2006/09/17 - 2006/09/18	(21.°089, 33.°243)	49.0	46.9
AWM7	OFFSET South	802044010	2008/01/29 - 2008/01/31	(43.°219, 40.°631)	38.6	23.9
	OFFSET South	802045020	2008/02/23 - 2008/02/25	(43.°220, 40.°631)	91.2	69.7
	OFFSET East	802045010	2008/01/27 - 2008/01/29	(41.°975, 41.°579)	78.3	63.1

* Average pointing direction coordinate in J2000 of the XIS, shown by the RA_NOM and DEC_NOM keywords of the FITS event files .

while Vikhlinin et al. 2006 find $1.34 \pm 0.04 h_{70}^{-1}$ Mpc and $7.79 \pm 0.78 \times 10^{14} h_{70}^{-1} M_{\odot}$, respectively, where M_{500} is the mass within r_{500}. Note that both observations measure the temperature out to r_{500}. Errors are at 90% confidence for one interesting parameter. We applied Balucinska-Church et al. (1998) for the photoelectric absorption cross-sections.

Generalizing to a spherical collapse for our adopted cosmology at the red-shift of A1413 gives an over density of 112 for the virialized region. However for A1413 r_{112} is only 18% larger than r_{180} (Henry 2000). So for comparison with previous work we adopt the latter as our definition of the virial radius and will measure it in this paper.

4.1.2 A2204

(a) A2204 (XMM) (b) A2204 (Suzaku)

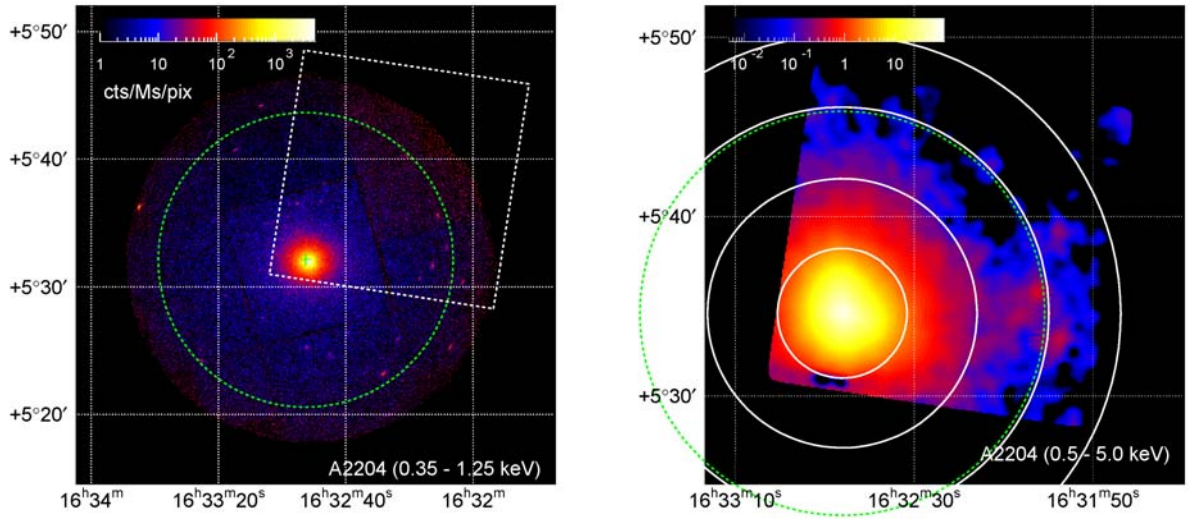

Fig. 4.2: (a) *XMM-Newton* MOS1 + MOS2 image of A2204 in the 0.35-1.25 keV band. The image is corrected for exposure, non-vignetting but background is subtracted with blank sky. 1pixel is 50″.The white box is FOV for Suzaku XIS. The green circle shows the virial radius of 1.8 Mpc. (b) Suzaku FI+BI image for outskirts of A2204 in the 0.5 – 5.0 keV band smoothed by a Gaussian with $\sigma = 16''$. The image is not corrected for exposure time and non-vignetting but background is not subtracted. COR>8 GV screening is applied. ^{55}Fe calibration source regions are also included in the figure, but the sources has no photons at this energy band. White circles denote 3′.5, 7′, 11′.5 and 15′.5 from the surface brightness peak.

A2204 is the second massive cooling flow cluster of the systematic red-shift $z = 0.1523$ (Struble & Rood 1987), which yields an angular diameter distance of 548.0 h_{70}^{-1} Mpc, luminosity distance of 727.6 h_{70}^{-1} Mpc and a scale of 159.4 h_{70}^{-1} kpc per arcminute for our assumed cosmology. The neutral hydrogen column density in this direction is 6.07×10^{20}cm^{-2} (Dickey & Lockman 1990).

Though A2204 is high z, but morphologically symmetric and relaxed cluster. Snowden et al. (2008) included their calalog of 78 clusters with A2204 which is observed with *XMM-*

Newton. Reiprich et al. (2009) reported the first result of A2204 with *Suzaku* observation which is observed within r_{200}. Basu et al. (2009) has also observed A2204 of submillimeter band with APEX-SZ by utilizing SZ-effect.

We observed the northern region of A2204 at radii from $0'$ to $19'.5$ from the XMM surface brightness peak with the Suzaku XIS detectors. In table 4.3, we give the details of our observation, and in figure 4.2(a), we show the XIS field of view (FOV) superimposed on the XMM-Newton image of A1413. The XIS instrument consists of 4 CCD chips; one back-illuminated (BI: XIS1) and three front-illuminated (FI: XIS0, XIS2, XIS3), with each is combined with an X-ray telescope (XRT). The IR/UV blocking filters had accumulated a significant contamination by the time of the observation since its launch (July 2005); we include its effects on the effective area in our analysis. The XIS was operated with normal clocking mode, in 5×5 or 3×3 editing modes. The spaced-row charge injection (SCI) was not applied, and all the four CCDs were working at the time of the observation.

We show the FI+BI image in the 0.5–5 keV energy band in figure 4.2(b). Data reduction method is same as the case of A1413. We show data log in table 4.3.

4.1.3 AWM7

AWM7 (z = 0.0172) is a poor cluster that is not listed in Abell catalog. However the X-ray luminosity is comparable to other Abell clusters, and it forms part of the Pisces-Perseus super-cluster filament at the 4.5 °west of Perseus cluster which runs roughly in the east-west direction. The morphology of AWM7 shows significant elongation along the filament, approximated by an ellipse with minor to major axis ratio of about 0.8. (Neumann & Boehringer 1995). These morphological properties suggest that the formation of this cluster has some relation with the super-cluster filament.

X-ray emission from this cluster has been studied with Einstein (Kriss et al. 1983), Ginga (Tsuru et al. 1992), ROSAT (Neumann & Boehringer 1995), ASCA (Xu et al. 1997; Ezawa et al. 1997; Finoguenov & Ponmann 1999), and Suzaku (Sato et al. 2008). The mapping data of Suzaku in the range from center of surface brightness to $27'$ were previously analyzed by Sato et al. (2008). The temperature dropped by about 10% at 0.35 r_{200}. This was slower than those observed in other clusters which showed the temperature drop by 30-40%. There was no significant positional shift in the Fe-K line energy, corresponding to $\Delta v < 2000$ km s^{-1}. This indicated that the ellipticity of AWM7 was not supported by a rotation of the gas.

We looked into morphology of center region to $14'$ by XMM-Newton because it advantages to the spatial resolution to conform ellipcity with X-ray observation. Suzaku is the only appropriate observatory to make clear in this dark and outer region of cluster. By Suzaku, we observed outer regions of AWM7 which were offset by 1 °(0.65-0.88r_{200}) in the east and south directions with Suzaku, aiming for measuring the ICM properties close to the virial radius, and to find possible connection with the structure of the super-cluster filament.

(a) AWM7 East (*Suzaku*)

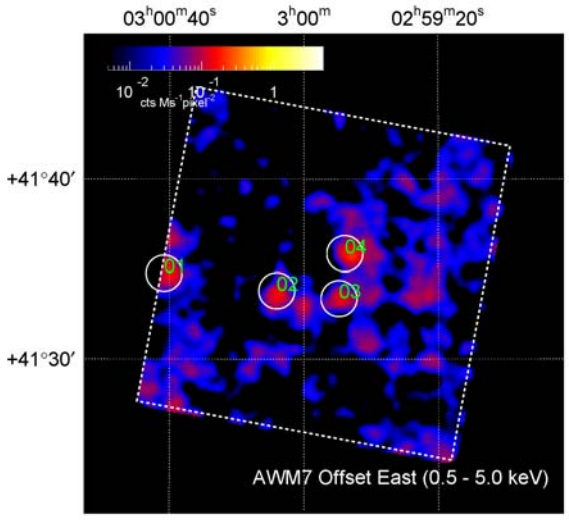

(b) AWM7 South(*Suzaku*)

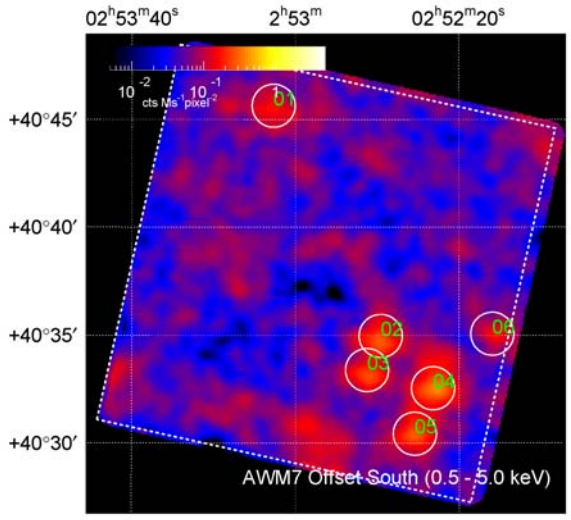

(c) AWM7 (*XMM-Newton*)

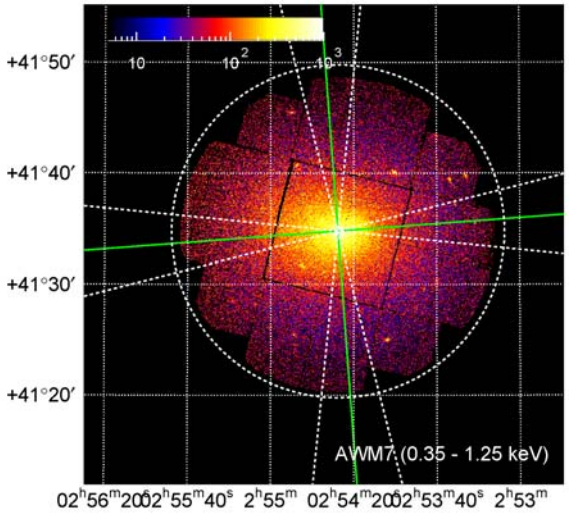

Fig. 4.3: AWM7 images observed by *Suzaku* and *XMM-Newton*. (a) Offset east of AWM7, (b) Offset South of AWM7, and (c) AWM7 observed by *XMM-Newton*. (a) and (b) are smoothed with 4 bin per 1 pixel and 4 σ.

4.2 Data reduction

4.2.1 *Suzaku*

Procedure of analysis

We used HEAsoft ver 6.4.1 and CALDB version 2008-06-21 for all the Suzaku analysis presented here. We started the event screening from the cleaned event file, We extracted pulse-height spectra in annular regions from the XIS event files.

Here, we explain the procedure used for the spectral analysis of each cluster. However, we explain background analysis in the latter chapter.

1. The observation data are screened.
2. From observed images, we excluded bright point sources avoiding contamination by them.
3. The spectra are extracted from the annular regions centered on clusters.
4. For each annular region, the NXB model spectrum is created using PINUD. These NXB spectra are subtracted from the observed cluster spectra extracted in step 2.
5. We generated the RMF for the epoch of the cluster observation using the *xisrmfgen* (version 2007-05-14).
6. We analyzed point source spectra and estimated flux contamination by all of them in FOV (A1413 and AWM7).
7. By assuming surface brightness profiles, we created simulated cluster images.
8. We generated uniform ARFs for NXB, CXB, and galactic components, and cluster ARFs for each region by *xissimarfgen* with 2M photons.
9. We carried out simoltanious fitting with all regions, all detectors (FI+BI), and all background model components (CXB and galactic components).
10. We estimated "stray light" fractions for each region by *xissim*.
11. We looked into all of uncertainties for CXB fluctuations, NXB fluctuations, Contaminations on IR/UV blocking filters.
12. We simulated NXB, CXB, galactic components, and also ICM with *xissim* to create surface brightness profiles with photon counts with the best-fit results.

Data screening

We carried out the standard screening criteria for each observation data with *cleansis*.

Region

Spatial and spectral responses

We need to prepare the spatial and spectral responses which are necessary for reducing and analyzing our observations of A1413. These responses have complicated properties for extended sources. Indeed they depend on the surface brightness distribution of the source and so are unique for each annular region. Monte Carlo simulators are used to generate some of the responses. The X-ray telescope + XIS simulator is called *xissim*, and the ARF generator using the simulator is called *xissimarfgen* (Ishisaki et al. 2007). We used version 2008-04-05 of the simulator.

A surface brightness distribution is necessary for *xissim* and *xissimarfgen*, because the point spread function (PSF) of the XRT produces an efficiency that is correlated among adjacent spatial cells. Since the XIS FOV did not include the brightness peak of A1413, we used the KBB model of Pratt & Arnaud (2002) to generate the ARF. We numerically projected the KBB 3-dimensional model of the gas density to generate the input surface brightness distribution. Since the ARF describes the detection efficiency as a function of energy, no particular spectral shape is required for input. The effect of the XIS IR/UV blocking filter contamination is included in the ARF based on the calibration of November 2006. The normalization of the ARF is such that the measured flux in a spectral fit for a given spatial region is the flux from the entire input surface brightness. The flux just from the spatial region is the fit flux times the *xissimarfgen* output parameter *SOURCE_RATIO_REG* (table 5.10). The surface brightness from a given spatial region is then the usual flux from the region divided by the solid angle that subtends from the observer.

4.2.2 *XMM-Newton*

For the morphological analysis, we utilized *XMM-Newton* observation data set. To create images and surface brightness profiles, we due to the standard analysis method in Hayakawa 2006 with the initial processing with *mos-filter* which is a part of XMM-Newtion Extended Spectral Analysis Software (XMM-ESAS) [1].We utilized blank sky data to estimate background intensities. Hayakawa 2006 carried out background subtraction with blank sky data. However, they did not utilize exposure-corrected images for blank sky. In the outer region, we must care for background subtraction in slite photon counts. We carried out correction of background with exposure map.

In §3.2.3, we described the EPIC background properties, and found that the background was divided into following components.

(1) CXB

(2) detector noise component

[1]http://xmm.esac.esa.int/external/xmm_sw_cal/background/index.shtml

(3) high energy particle background (stable component)

(4) soft photon background (flaring component)

The components of (1)-(3) were basically removed when we use the blank sky data subtraction (see §4.2.2). The remaining component (4) was excluded using the timing analysis. Here, we briefly explain the background elimination process, using the case of AWM7 as an example.

Initial Processing

We reprocessed the event files with the current SAS version and CCF with *mos-filter* which runs the SAS tasks *cifbuild*, *odfingest* and *emchain*.

Figure 4.4 show the filtering result for the MOS1 and MOS2 of AWM7. The upper panel plots the light curve histogram for the 2.5-12 keV band from the FOV, the middle panel displays the 2.5-12.0 keV band FOV light curve, and the lower panel displays 2.5-12 keV band light curve from the unexposed corners of the instrument. In the upper panel, the blue vertical lines show the range for the gaussian fit, the green curve shows the Gaussian fit, while the red vertical lines show the upper and lower bounds for filtering the data. In the bottom two panels green points indicate accepted data while black points indicates data excluded by the filtering algorithm.

AWM7 observation has not been contaminated by high count rated flare of soft protons. Some observations are contaminated with soft proton background.

(a) MOS1 (b) MOS2

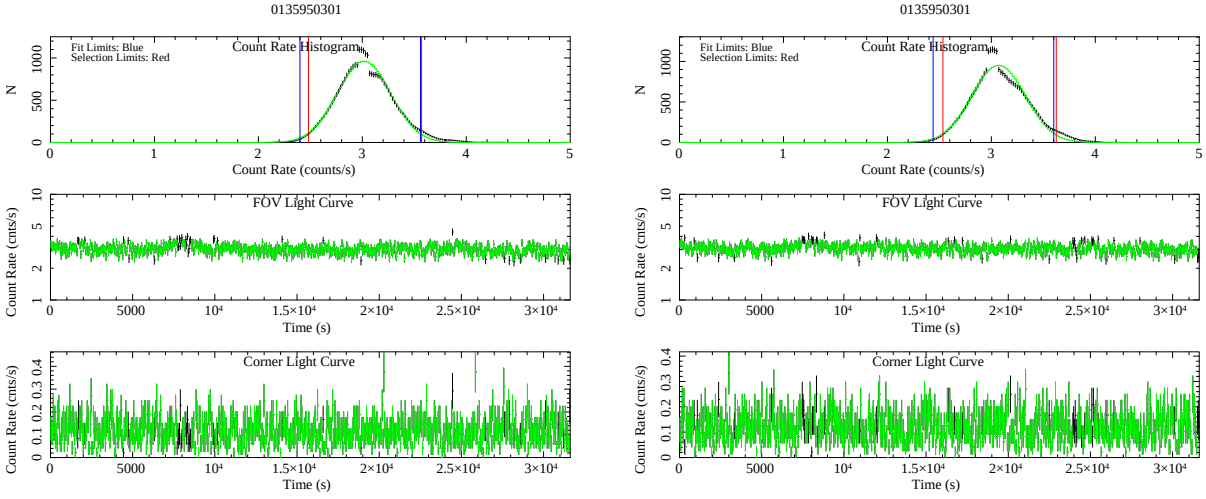

Fig. 4.4: Light curve and its count rate histogram of AWM7 reprocessed data (MOS1(a) and MOS2(b)).

Merging multiple observations

When we merge multiple observations like A1413 and A2204 in table 4.2, we merged multiple observation event files with *merge* command of SAS package after the initial

processing with *mos-filter*. *merge* command can carry out merging two different observations, instruments, and exposure files. These may be EPIC event lists or two other additional files like attitude files, orbit files etc. The files are checked via their extension names (EVENTS, ATTHK, ORBIT) for their type, and depending on the type, certain attributes are checked to see whether the files are compatible with each other. In the attitude and orbit cases, any files can be merged together (so long as they are both attitude or both orbit files), whereas in the events case, some care should be taken.

merge command can correct difference between two different cloth pointing direction. We processed *merge* command for all event files of A1413 and A2204. And net exposure time is 122.4 and 121.9 ks for MOS1 and MOS2 in the case of A1413, and 70.9 and 72.5 ks in the case of A2204. We also merged attitude files of all observations of A1413 and A2204.

Blank sky data as background

We are forced to extract the background spectrum from the blank sky data sets of Read & Ponman (2005) in the same detector region, in order to exclude the background events of (1)-(3). In this case, the remaining problem is that the non X-ray background (2), (3) is time variable, although the CXB (1) is nearly identical everywhere. Katayama et al. (2004) studied this problem and found that the count rate in the high energy band (above 10 keV) well represent the particle origin background. Therefore, the source-to-background count rate ratio was calculated from the count rates in the bands 10-12 keV and 12-14 keV for MOS and the background spectrum is scaled by this factor when it is subtracted.

Chapter 5

Background Analysis

Accurate estimation of the background is particularly important when constraining the ICM surface brightness and temperature in the outer region of clusters. We assumed that the background is comprised of three components: non-X-ray background (NXB), cosmic X-ray background (CXB) and Galactic emission (GAL), which itself is comprised of two components. In this section we describe how we estimate all these background components.

5.1 Point Source Analysis

We want to excise point sources because we are only interested in this paper in the ICM. However, since the CXB is comprised of faint point sources, we then need to correct the background level for the resolved sources. This and the next section describe the procedure we used for these tasks.

In the case of A1413, We used the XMM-Newton image to detect point sources in the XIS FOV because its spatial resolution (14″ half power diameter; HPD) is better than Suzaku's (2′ HPD). We detected 10 point sources using *wavdetect* of CIAO, and extracted source and background spectra by setting the extraction radius of 33″ and 33″ − 66″, respectively. First, we checked that the MOS1 and MOS2 spectra of each source were consistent. Then we summed the MOS1 and MOS2 spectra to increase the statistics, and fitted the spectrum of each source to evaluate individual spectral parameters. Finally we added the spectra of all the point sources to estimate how much of the CXB these sources resolve. We fitted the spectra by *wabs* × *pegpwrlw*. The best-fit parameters for the individual point sources and their sum are shown in table 5.1. We obtained χ^2/dof = 87.2/77 for the power-law fit to the combined spectrum (figure 5.1(a)), indicating a reasonable spectral fit. The photon index is $\Gamma = 1.92 \pm 0.09$ and the flux is $3.23^{+0.48}_{-0.44} \times 10^{-13}$ erg cm^{-2} s^{-1}.

We also searched for point sources located outside of the XMM-Newton field with Suzaku, finding an additional five sources by eye in A1413, 4 in AWM7 offset east, and 6 in AWM7 offset south. We found out probabilities of point source detection by eye in table5.2.

We can calculate probabilities of point source detection with following equation,

$$\frac{C_{\rm sr}}{\delta_{\rm sr}} = \frac{C_{\rm OBS} - \frac{A_{\rm sr}}{A_{\rm bg}} C_{\rm bg}}{\sqrt{C_{\rm OBS} + \left(\frac{A_{\rm sr}}{A_{\rm bg}}\right)^2 C_{\rm bg}}} \tag{5.1}$$

, in which $C_{\rm sr}$, $C_{\rm OBS}$, $C_{\rm bg}$ are row counts of ICM, observed spectra, and background spectra. $\delta_{\rm sr}$ is fluctuation of source counts. $A_{\rm sr}$ and $A_{\rm bg}$ are source and background area respectively. We could detect point sources larger than 3.9σ as shown in table 5.2. We performed spectral fits to all the point sources with Suzaku according to the following procedure. The source photons came from a circle of $40''$ radius with encircling annular background region of $40'' - 100''$ radii. We selected the source regions so they did not overlap each other. These source and background areas could be slightly different among the detectors and sources due to filtering by the *calmask* regions and the presence of hot pixels. We added the FI spectra from XIS0, XIS2, and XIS3 detectors, and summed the BACKSCAL keyword in the FITS header, which correspond to the area of extraction region, $A_{\rm sr}$ or $A_{\rm bg}$. Then, we carried out spectral fits for the FI and BI spectra simultaneously using the same spectral model as before, first for the individual sources and then the sum of all the point sources.

We show the best-fit parameters for the individual point sources and their sum in table 5.1 except for sources 04, 05, and 08, because they were faint so that we could not estimate their background reasonably in A1413. Obtained fluxes of the sources are slightly affected by leaked photons of the target to the surrounding background regions. To correct for this effect, we calculated the ratio, $f_{\rm leak}$, of the leaked photons in each background region to the detected photons in the source region using the "*xissim*" FTOOL (Ishisaki et al. 2007). We corrected the original source flux by multiplying a factor $1/(1 - f_{\rm leak}\ A_{\rm sr}/A_{\rm bg}) \simeq 1/(1 - 0.2\ f_{\rm leak})$ in the $F_{\rm X}$ columns of Suzaku in table 5.1 and table 5.3. Figures 5.1(b), (c) and figures 5.2 show the combined spectra of all sources for FI and BI for A1413 and A2204. In the case of A1413, we obtained $\chi^2/{\rm dof} = 113.1/117$ for the power-law fit to the combined spectrum, indicating a reasonable spectral fit, too. The photon index is $\Gamma = 1.82 \pm 0.12$ and the flux is $4.83^{+0.60}_{-0.56} \times 10^{-13}$ erg cm^{-2} s^{-1} (2–10 keV).

The total flux of all the point sources agrees well between Suzaku and XMM-Newton within the error in A1413. The number of sources we found and their total flux are consistent with that expected from the $\log N$–$\log S$ relation summarized in figure 20 of Kushino et al. (2002) in A1413. The detected sources ranges from $\sim 10^{-14}$ to $\sim 10^{-13}$ erg cm^{-2} s^{-1}. We excised all the point sources detected in either the Suzaku or XMM-Newton observations. Normally we excluded a region of $70''$ radius but used $125''$ radius for two sources (09 and 14 in table 5.1) in A1413 and $60''$ radius for AWM7.

5.2 Stray light

We examined how many photons accumulated in the each region of A1413, A2204, and AWM7 actually came from somewhere else on the sky because of the extended telescope

Table 5.1: Best-fit parameters of detected point sources of A1413.

Source		FI+BI (Suzaku) *				MOS1+MOS2 (XMM-Newton) †		
ID	(R.A., Dec.) in J2000	Γ	$F_{\rm x}$ ‡	χ^2/dof	$f_{\rm leak}$	Γ	$F_{\rm x}$ ‡	χ^2/dof
01	($11^{\rm h}55^{\rm m}38\overset{\rm s}{.}7$, 23°34′02″)	$2.5^{+1.3}_{-0.8}$	< 2.4	28.0/18	1.53	$1.9^{+0.5}_{-0.4}$	$2.4^{+1.8}_{-1.2}$	16.6/17
02	($11^{\rm h}55^{\rm m}30\overset{\rm s}{.}8$, 23°38′09″)	1.7 (fixed)	< 2.1	14.7/12	1.41	$1.9^{+0.6}_{-0.5}$	$2.3^{+2.3}_{-1.4}$	5.7/12
03	($11^{\rm h}55^{\rm m}24\overset{\rm s}{.}9$, 23°37′00″)	$2.2^{+0.5}_{-0.4}$	$1.6^{+0.8}_{-0.6}$	37.4/30	1.34	$1.7^{+0.6}_{-0.5}$	$1.6^{+1.6}_{-1.0}$	11.2/9
04	($11^{\rm h}55^{\rm m}21\overset{\rm s}{.}6$, 23°33′02″)					$1.8^{+0.3}_{-0.3}$	$3.6^{+1.6}_{-1.3}$	11.1/24
05	($11^{\rm h}55^{\rm m}18\overset{\rm s}{.}2$, 23°28′10″)					$1.1^{+0.4}_{-0.4}$	$5.9^{+2.9}_{-2.4}$	63.6/58
06	($11^{\rm h}55^{\rm m}17\overset{\rm s}{.}3$, 23°35′47″)	$1.4^{+0.4}_{-0.4}$	$4.2^{+1.6}_{-1.4}$	28.1/27	1.39	$2.0^{+0.2}_{-0.2}$	$5.0^{+1.7}_{-1.4}$	28.2/28
07	($11^{\rm h}55^{\rm m}04\overset{\rm s}{.}6$, 23°31′11″)	$1.9^{+0.3}_{-0.3}$	$4.7^{+2.1}_{-1.9}$	39.2/37	1.26	$2.1^{+0.2}_{-0.2}$	$4.1^{+1.2}_{-1.0}$	40.9/37
08	($11^{\rm h}54^{\rm m}56\overset{\rm s}{.}9$, 23°36′52″)					$1.3^{+0.5}_{-0.5}$	$6.8^{+4.4}_{-3.1}$	5.4/5
09	($11^{\rm h}54^{\rm m}51\overset{\rm s}{.}7$, 23°34′49″)	$1.7^{+0.2}_{-0.1}$	$16.0^{+2.6}_{-2.4}$	79.1/58	1.43	$2.2^{+0.2}_{-0.2}$	$8.1^{+2.4}_{-2.1}$	42.5/41
10	($11^{\rm h}54^{\rm m}58\overset{\rm s}{.}1$, 23°35′23″)	1.7 (fixed)	< 1.8	18.0/17	1.21	$1.7^{+1.3}_{-1.2}$	$1.1^{+2.9}_{-1.1}$	5.1/7
11	($11^{\rm h}54^{\rm m}33\overset{\rm s}{.}0$, 23°37′51″)	$1.7^{+0.6}_{-0.5}$	$3.1^{+2.3}_{-1.9}$	13.5/13	1.24			
12	($11^{\rm h}55^{\rm m}16\overset{\rm s}{.}5$, 23°38′37″)	$2.0^{+0.7}_{-0.5}$	$1.06^{+0.8}_{-0.6}$	15.7/19	1.44			
13	($11^{\rm h}55^{\rm m}20\overset{\rm s}{.}3$, 23°40′32″)	$0.1^{+1.0}_{-1.0}$	< 2.8	18.7/18	1.44			
14	($11^{\rm h}55^{\rm m}29\overset{\rm s}{.}7$, 23°47′26″)	$2.0^{+0.7}_{-0.5}$	$2.7^{+1.7}_{-1.3}$	22.4/14	1.28			
15	($11^{\rm h}54^{\rm m}47\overset{\rm s}{.}7$, 23°39′23″)	$1.5^{+0.3}_{-0.3}$	$6.6^{+2.0}_{-1.8}$	23.2/19	1.43			
Total		$1.82^{+0.12}_{-0.12}$	$48.3^{+6.0}_{-5.6}$	113.1/117	1.36	$1.92^{+0.09}_{-0.09}$	$32.3^{+4.8}_{-4.4}$	87.2/77

* Source–04, 05, and 08 are excluded because they exhibited negative counts after the background subtraction.

† Source–11, 12, 13, 14, and 15 are out of MOS1 and MOS2 FOVs.

‡ Unit of flux is 10^{-14} erg cm^{-2} s^{-1} (2–10 keV).

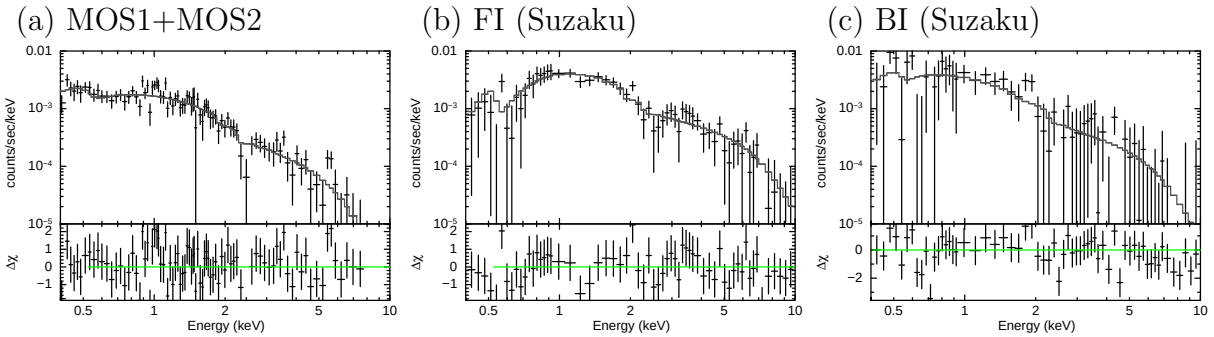

Fig. 5.1: Power-law model fit to the sum of all point source spectra. (a) MOS1+MOS2, (b) FI, and (c) BI (black: source spectra, grey: best-fit model).

Table 5.2: Probabilities of point source detection.

A1413		FI+BI counts (0.5–10.0 keV) ‖						
ID		OBS	BGD	f_{leak}	A^*_{sr}	A^*_{bg}	$C_{sr} \pm \delta_{sr}$	C_{sr}/δ_{sr}
11	.....	!!361 ± 19	838 ± 29	1.24	4.33	16.35	207 ± 30.5	6.79
12	.....	481 ± 22	$2,003 \pm 45$	1.40	6.06	30.92	122 ± 32.6	3.74
13	.....	467 ± 22	$1,888 \pm 43$	1.40	6.06	30.92	134 ± 32.0	4.17
14	.....	367 ± 19	990 ± 31	1.32	5.13	19.38	161 ± 32.1	5.02
15	.....	504 ± 22	$1,539 \pm 39$	1.45	6.06	30.92	283 ± 33.2	8.53
AWM7 East		FI+BI counts (0.5–10.0 keV) ‖						
ID		OBS	BGD	f_{leak}	A^*_{sr}	A^*_{bg}	$C_{sr} \pm \delta_{sr}$	C_{sr}/δ_{sr}
01	.....	150 ± 12	473 ± 22	147.0	1.52	7.97	83 ± 17.9	4.64
02	.....	277 ± 17	1086 ± 33	149.0	1.52	7.97	98 ± 24.8	3.96
03	.....	305 ± 17	1077 ± 33	157.0	1.52	6.72	96 ± 29.4	3.26
04	.....	308 ± 18	473 ± 22	147.0	1.52	7.08	302 ± 26.5	11.38
AWM7 South		FI+BI counts (0.5–10.0 keV) ‖						
ID		OBS	BGD	f_{leak}	A^*_{sr}	A^*_{bg}	$C_{sr} \pm \delta_{sr}$	C_{sr}/δ_{sr}
01	.....	341 ± 18	1329 ± 36	161.0	1.52	7.97	127 ± 28.4	4.47
02	.....	468 ± 22	1649 ± 41	149.0	1.52	7.97	215 ± 32.1	6.71
03	.....	430 ± 21	1658 ± 41	154.0	1.14	7.97	248 ± 27.6	8.98
04	.....	573 ± 24	1511 ± 39	155.0	1.50	6.95	371 ± 38.1	9.73
05	.....	218 ± 15	1052 ± 32	156.0	0.64	4.38	84 ± 20.0	4.20
06	.....	337 ± 18	1052 ± 32	136.0	1.52	7.55	173 ± 26.8	6.45

* The unit is arcmin^2.

Table 5.3: Best-fit parameters of detected point sources of AWM7.

OFFSET East					
ID	(R.A., Dec.) in J2000	Γ	$F_{\rm x}^{\ddagger}$	χ^2/dof	$f_{\rm leak}$
01	($3^{\rm h}0^{\rm m}41\overset{\rm s}{.}6$,$41^{\rm d}34^{\rm m}46\overset{\rm s}{.}1$)	$4.75^{+-1.20}_{-1.92}$	$0.37^{+4.10}_{-2.63}$	7.5 / 2	1.47
02	($3^{\rm h}0^{\rm m}8\overset{\rm s}{.}1$,$41^{\rm d}33^{\rm m}48\overset{\rm s}{.}2$)	$1.12^{+0.68}_{-0.70}$	$2.16^{+1.00}_{-0.81}$	5.5 / 8	1.49
03	($2^{\rm h}59^{\rm m}49\overset{\rm s}{.}6$,$41^{\rm d}33^{\rm m}22\overset{\rm s}{.}3$)	$1.64^{+1.76}_{-1.28}$	$1.09^{+0.88}_{-0.73}$	7.6 / 10	1.57
04	($2^{\rm h}59^{\rm m}47\overset{\rm s}{.}8$,$41^{\rm d}35^{\rm m}51\overset{\rm s}{.}6$)	$2.39^{+0.53}_{-0.42}$	$1.27^{+0.47}_{-0.37}$	10.9 / 10	1.47
Total		$1.75^{+0.31}_{-0.28}$	$1.48^{+0.33}_{-0.30}$	49.2 / 47	1.49
OFFSET South					
ID	(R.A., Dec.) in J2000	Γ	$F_{\rm x}^{*}$	χ^2/dof	$f_{\rm leak}$
01	($2^{\rm h}53^{\rm m}5\overset{\rm s}{.}3$,$40^{\rm d}45^{\rm m}38\overset{\rm s}{.}8$)	$2.78^{+3.03}_{-1.23}$	$0.70^{+1.12}_{-0.49}$	12.9 / 11	1.61
02	($2^{\rm h}52^{\rm m}39\overset{\rm s}{.}1$,$40^{\rm d}34^{\rm m}58\overset{\rm s}{.}7$)	$2.44^{+0.83}_{-0.64}$	$0.41^{+0.55}_{-0.30}$	30.3 / 19	1.49
03	($2^{\rm h}52^{\rm m}42\overset{\rm s}{.}5$,$40^{\rm d}33^{\rm m}23\overset{\rm s}{.}7$)	$2.20^{+0.59}_{-0.47}$	$2.24^{+0.95}_{-0.79}$	23.9 / 16	1.54
04	($2^{\rm h}52^{\rm m}26\overset{\rm s}{.}4$,$40^{\rm d}32^{\rm m}32\overset{\rm s}{.}8$)	$1.67^{+0.41}_{-0.36}$	$5.16^{+1.69}_{-1.40}$	38.7 / 23	1.55
05	($2^{\rm h}52^{\rm m}30\overset{\rm s}{.}8$,$40^{\rm d}30^{\rm m}26\overset{\rm s}{.}1$)	$1.71^{+0.55}_{-0.47}$	$8.55^{+3.27}_{-0.02}$	10.4 / 7	1.56
06	($2^{\rm h}52^{\rm m}11\overset{\rm s}{.}9$,$40^{\rm d}35^{\rm m}4\overset{\rm s}{.}7$)	$1.64^{+0.76}_{-0.61}$	$2.54^{+1.48}_{-1.10}$	12.1 / 11	1.36
Total		$1.84^{+0.17}_{-0.16}$	$3.02^{+0.44}_{-0.41}$	132.3 / 112	1.52

* Unit of flux is 10^{-14} erg cm^{-2} s^{-1} (2–10 keV).

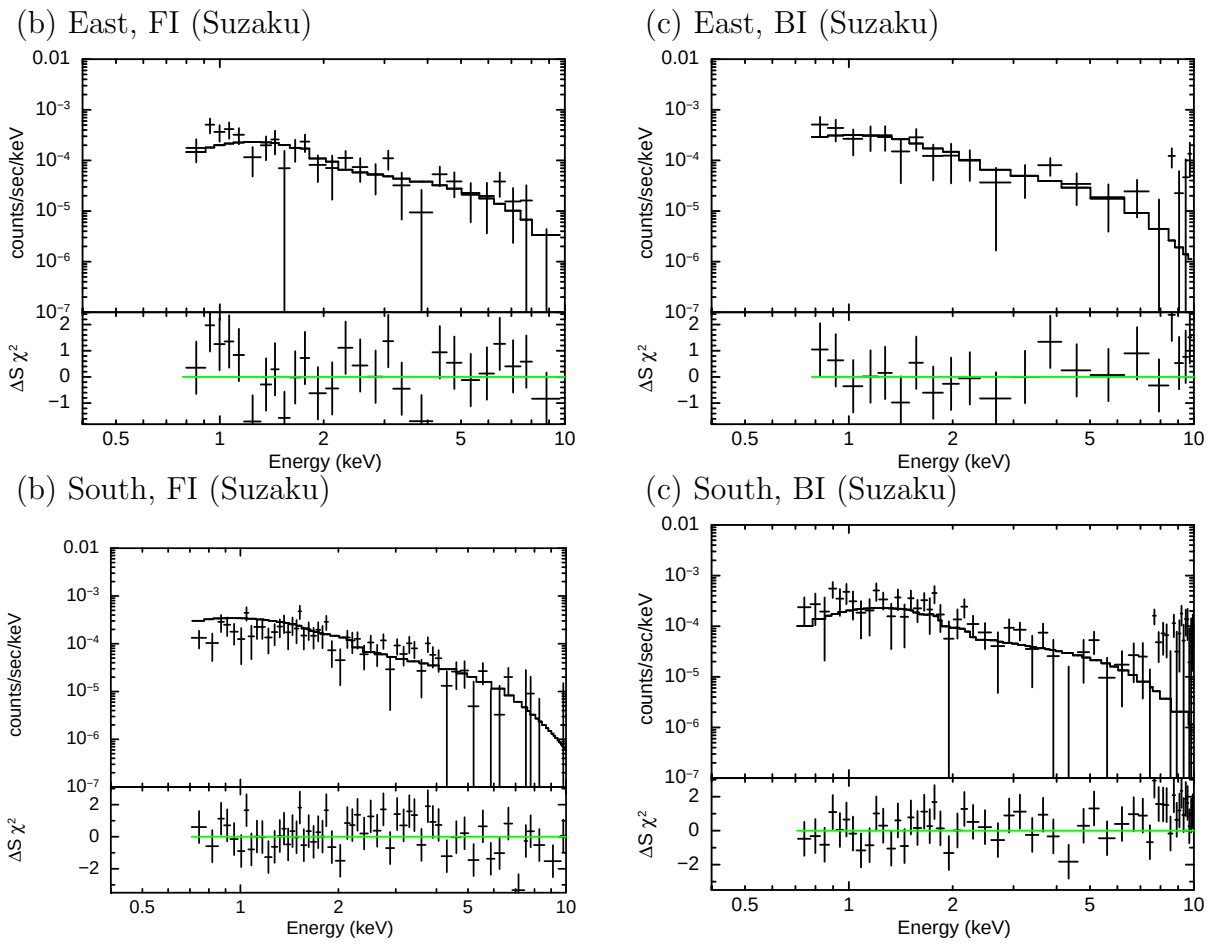

Fig. 5.2: Power-law model fit to the sum of all point source spectra of AWM7 Offset east and south. (a) East, FI, (b) East, BI, (c) South, FI, and (d) South, BI (cross: source spectra, line: best-fit model).

PSF. We show in table 5.5 the results for the FI+BI detectors in the 0.5–5 keV band which is simulated with *xissim*. These numbers agree well within 1% for individual sensors and other reasonable energy bands. About 70% in A1413 and about 60-90% of the photons detected in each region actually come from the corresponding sky region. Serlemitsos et al. (2007) gives an upper limit on the error in the simulation at $20'$. He reported that the actual stray intensity levels were less than twice those predicted by *xissim* due to the XRT reflector alignment errors and reflections from the pre-collimator blades. To estimate these stray light photon distributions, we produced simulated ICM image modeled by KBB model for A1413, 2β model for A2204, and 2 β egg model that is explained in the individual result of AWM7.

Especially, we concerned the actual stray photon spectra because XIS - FOVs is about $0.7r_{200}$. We found out the corrected spectra by subtracting stray photon spectra from raw data. We show stray photon spectra in figureC.11 and figure C.12. We fitted *apec* model for each spectrum to parametrize these components. We show the best-fit parameters in table 5.4. Because stray light photon spectra are affected by large angular refrection or other non thermal instrumental effects, these spectra do not express thermal prasma models. Then the χ^2/dof is not agreeable. To correct raw spectra for stray light, we subtracted the stray light spectra of figure C.12(e) and figure C.11 (e) from raw spectra. In the simulation, the actual temperatures in $50' - 70'$ of east and south are apeared with softer about 1 keV in the merged ICM photon.

5.3 Solar Wind Charge Exchange

The solar component includes the fluorescence lines of nitrogen and oxygen from the earth's atmosphere and scattered solar X-rays. It is noted that the XIS sometimes detects the emission lines created by the charge exchange between neutral atoms in the earth's magnetosheath and heavy ions in the solar wind (Fujimonto et al. 2007). It is difficult to eliminate these lines by filtering with ehe elevation angles. However, by referring to the solar wind data, i.e., solar proton and X-ray flux, the evaluation of this components is possible.

I referred proton density and flow speed by ACE satellite [1] for each target of A1413 and A2204 in figure5.3.

Flow velocity is in the range from 240-360 km/s and 350-650 km/s for A1413 and A2204. If we think the typical solar wind velocity is about 500 km/s, these velocity is not seemed to be so extra-ordinal activities. Then we considered light curves of proton density.

Typically, over 10 cm^{-3} of the proton density, we know the affection of solar wind charge exchange in their spectra. In A2204 case, we cannot ignore the proton density level. Actually, its intensities of $O_{\rm VII}$ and O_{VIII} lines under 1 keV is 10 times stronger

[1] CDAWeb/GSFC (http://cdaweb.gsfc.nasa.gov/istp_public/)

Table 5.4: The best fitting parameters of the spectral fits with 90% confidence errors for one parameter. Energy band is in FI:0.5-10.0 keV and BI:0.4-10.0 keV.

Nominal (a) *		kT (keV)	Abundance ($Z_\odot$)	$Norm$ §	$F_{\rm X}$ ‖	χ^2/dof
Offset East						
$0' - 10'$	....	1.29 ± 0.06	0.33 ± 0.13	3.73 ± 0.66	2.60 ± 0.46	181.4 / 62
$10' - 50'$	....	1.43 ± 0.17	0.44 ± 0.26	1.38 ± 0.37	1.07 ± 0.29	151.3 / 62
$50' - 70'$	....	3.64 ± 0.20	0.78 ± 0.21	15.04 ± 0.94	15.31 ± 0.96	679.6 / 62
$70' - 169'$	....	$1.81^{+0.65}_{-0.0}$	0.14 ± 0.0	0.62 ± 0.0	0.36 ± 0.0	45.7 / 62
All	....	2.95 ± 0.10	0.87 ± 0.15	20.51 ± 1.09	20.72 ± 1.10	696.0 / 62
$0 - 50' + 70 - 169'$	....	1.36 ± 0.04	0.30 ± 0.08	6.43 ± 0.73	4.28 ± 0.49	285.6 / 62
Offset South						
$0' - 10'$	....	1.26 ± 0.04	0.24 ± 0.05	3.85 ± 0.32	2.34 ± 0.20	315.2 / 62
$10' - 50'$	....	1.22 ± 0.05	0.51 ± 0.14	1.28 ± 0.23	1.11 ± 0.20	191.1 / 62
$50' - 70'$	....	4.05 ± 0.12	0.54 ± 0.09	11.40 ± 0.33	14.28 ± 0.41	528.3 / 62
$70' - 100'$	....	$1.41^{+0.30}_{-0.15}$	$0.31^{+0.66}_{-0.21}$	$0.42^{+0.02}_{-0.02}$	$0.29^{+0.01}_{-0.01}$	49.9 / 62
All	....	2.76 ± 0.06	0.85 ± 0.08	16.14 ± 0.50	18.85 ± 0.58	624.1 / 62
$0 - 50' + 70 - 169'$	....	1.29 ± 0.03	0.29 ± 0.04	6.19 ± 0.39	4.06 ± 0.26	406.5 / 62

§ Normalization of the apec component scaled with a factor of $SOURCE\_RATIO\_REG/\Omega_{\rm e}$
$Norm = SOURCE\_RATIO\_REG/\Omega_{\rm e} \int n_{\rm e} n_{\rm H} dV \,/\, (4\pi\,(1+z)^2 D_{\rm A}^2) \times 10^{-20}$ cm^{-5} arcmin^{-2}, where $D_{\rm A}$ is the angular diameter distance to the source.

‖ Surface brightness in unit of 10^{-15} erg cm^{-2} s^{-1} arcmin^{-2} (0.5–10 keV).

Table 5.5: Emission weighted radius and estimated fractions of the ICM photons accumulated in detector regions coming from each sky region for FI+BI in the 0.5–5 keV band.

A1413								
Detector region	Emission weighted radius *		Sky region 0–2.7′	2.7–7′	7–10′	10–15′	15–20′	20–26′
$2'.7 - 7'$	.....	$4.7^{+2.3}_{-2.0}$	21.5%	73.2%	5.1%	0.2%	0.0%	0.0%
$7' - 10'$	.....	$8.0^{+2.0}_{-1.0}$	16.0%	21.8%	54.9%	7.3%	0.1%	0.0%
$10' - 15'$	.....	$11.0^{+4.0}_{-1.0}$	6.7%	7.3%	14.0%	67.3%	4.7%	0.0%
$15' - 20'$	.....	$18.6^{+1.5}_{-3.6}$	4.1%	2.7%	2.7%	16.8%	67.1%	5.4%
$20' - 26'$	.....	——	6.7%	6.7%	0.0%	0.0%	20.0%	66.7%

A2204							
Detector region	Emission weighted radius *		Sky region 0–2.7′	2.7–7′	7–10′	10–15′	15–19′.5
$0' - 3'.5$	.....	$0.78^{+2.72}_{-0.78}$	89.6%	9.2%	1.1%	0.0 %	0.0 %
$3'.5 - 7'$	.....	$4.60^{+2.4}_{-1.10}$	17.9%	73.9%	7.7%	0.5%	0.0%
$7' - 11'.5$	.....	$9.16^{+2.34}_{-2.16}$	0.8%	14.4%	79.2%	5.6%	0.1%
$11'.5 - 15'.5$	.....	$13.5^{+2.00}_{-2.00}$	0.2%	0.7%	17.9%	79.8%	1.4%
$15'.5 - 19'.5$	.....	——	0.8%	1.5%	5.2%	35.1%	57.3%

AWM7				
Detector region		Sky region 0–10′	10–50′	50–70′	70–1000′
East	.....	16.0%	7.5%	74.3%	2.2%
South	.....	19.9%	10.2%	67.5%	2.4%

* Emission weighted radius from the surface brightness peak of the XMM-Newton.

than that of A1413 in the figure 5.5 and table5.6. Then we decided to ignore under 0.7 keV in the A2204 spectra for each region.

5.4 Cosmic X-ray Background

An ICM temperature measurement in the outer regions of a cluster is very sensitive to the CXB level. We took the 100% CXB surface brightness to be $I_0 = 6.38 \times 10^{-8}$ erg cm^{-2} s^{-1} sr^{-1} based on the ASCA-GIS measurements (Kushino et al. 2002). Moretti et al. (2008) summarized measurements (Gruber et al. 1999; McCammon et al. 1983;

(a): A1413

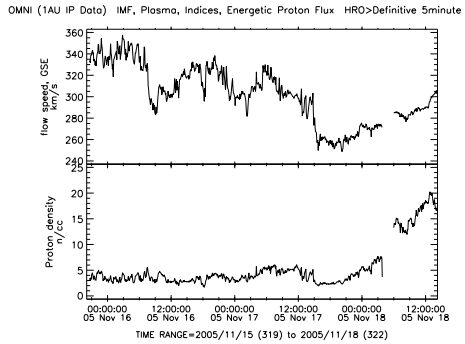

(b): A2204

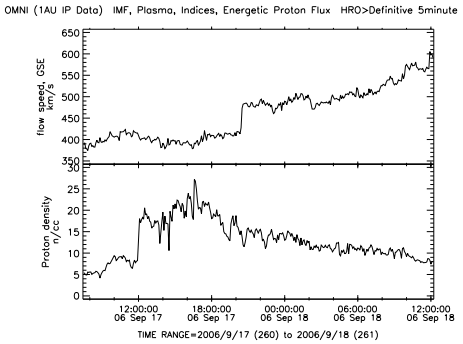

Fig. 5.3: Light curve of Flow speed (upper) and proton density (lower) by ACE satellite. (a) A1413 and (b) A2204

(a): AWM7 OFFSET South1

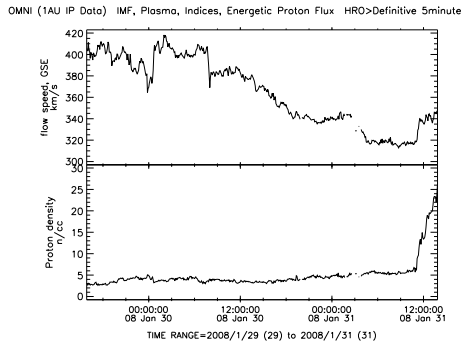

(b): AWM7 OFFSET South2

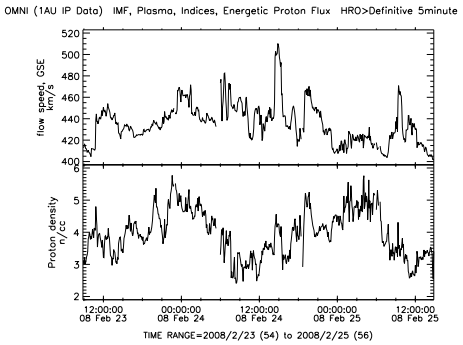

(c): AWM7 OFFSET East

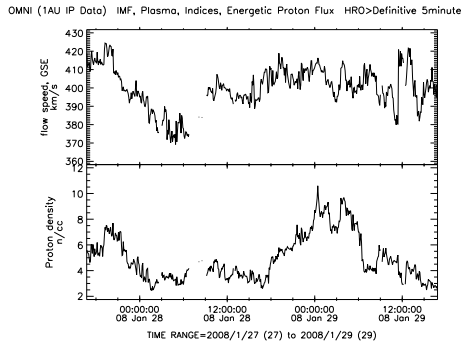

Fig. 5.4: Light curve of Flow speed (upper) and proton density (lower) by ACE satellite. (a) AWM7 OFFSET South1, (b) AWM7 OFFSET South2, and (c) AWM7 OFFSET East

Table 5.6: Intensity of redshifted O_{VII} (0.503 keV) and O_{VIII} (0.564 keV) lines

Region		$S^{\dagger}_{OVIII}$	$S^{\dagger}_{OVII}$
$0' - 3'.5$	.....	< 0.079	< 0.224
$3'.5 - 7'$	.....	< 0.227	< 0.585
$7' - 11'.5$	.....	$0.297^{+0.090}_{-0.087}$	$0.477^{+0.202}_{-0.174}$
$11'.5 - 15'.5$	.....	$0.368^{+0.109}_{-0.106}$	$0.439^{+0.249}_{-0.215}$

† in unit of 10^{-6} photons cm^{-2} s^{-1} arcmin^{-2} with 2σ upper limits or 90% confidence errors for a single parameter.

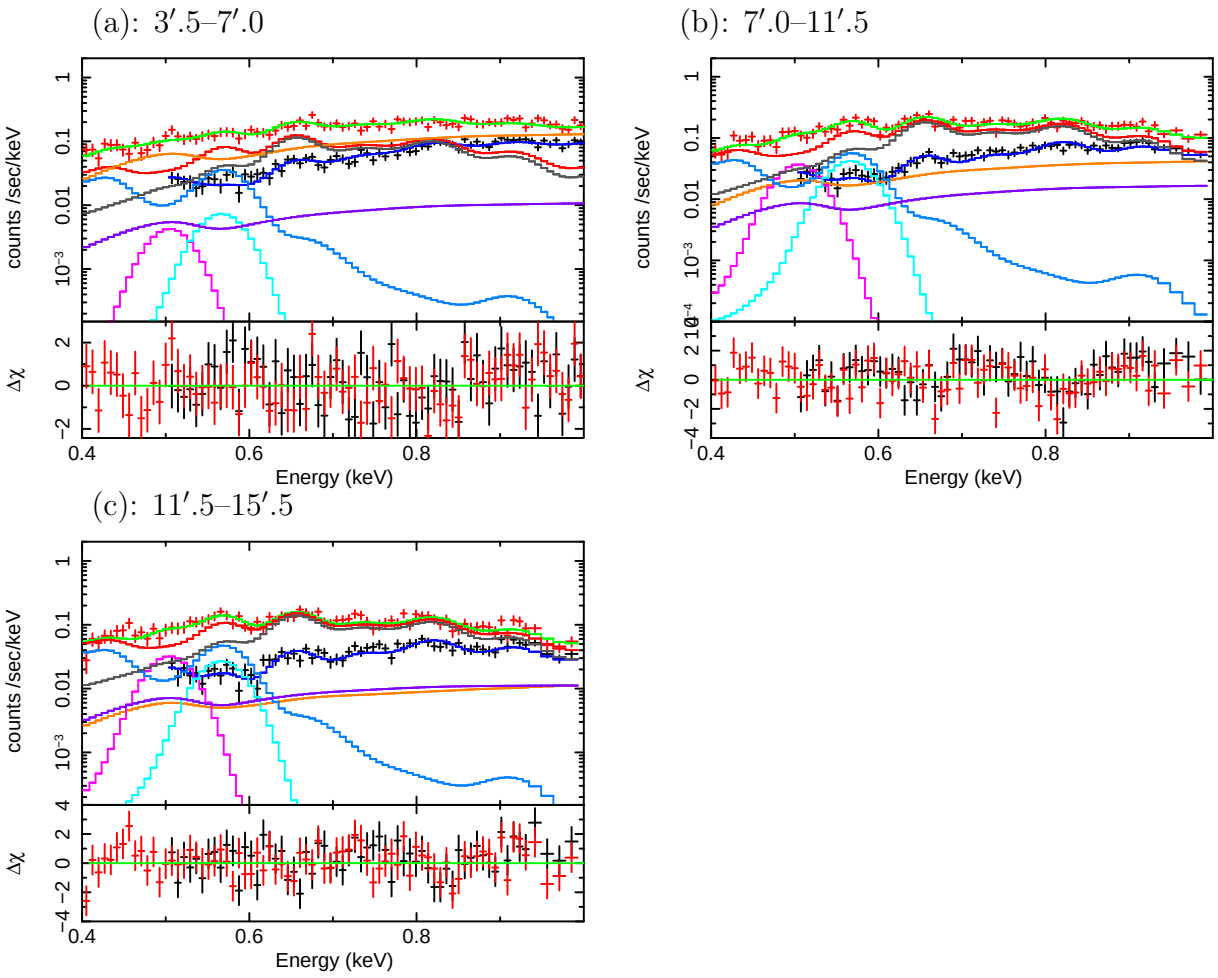

Fig. 5.5: The upper panels show the observed spectra fitted with ICM model "constant×(apec)" and galactic-2T-III background model "constant×(apec+gauss+gauss+wabs×(apec+powerlaw))" in FI:0.5 – 1.0 keV, BI:0.4–1.0 keV, after subtracting the NXB for the annular regions : (a) 3′.5-7′, (b) 7′-11′.5, and (d)11′.5-15′.5. Each components are BI (red cross), FI (black crosses), CXB of BI (purple), GAL1 of BI(grey), GAL2 of BI (sky blue), ICM of BI (orange), total model spectra of BI (green) and FI (blue) respectively. The lower panels show the residuals in units of σ.

Gendreau et al. 1995; Vecchi et al. 1999; Kushino et al. 2002; Revnivtsev et al. 2003; DeLuca et al. 2004; Revnivtsev et al. 2005; Hickox et al. 2006) of the CXB level, including their new result with *XMM-Newton*. The measured CXB surface brightnesses show a significant range from the HEAO1 value of $(5.41 \pm 0.56) \times 10^{-8}$ erg cm^{-2} s^{-1} sr^{-1} (Gruber et al. 1999) to $(7.71 \pm 0.33) \times 10^{-8}$ erg cm^{-2} s^{-1} sr^{-1} with SAX-MECS (Vecchi et al. 1999) in the 2–10 keV band. Recent measurements show the flux to be within about 10% of the level reported by Kushino et al. (2002).

We estimated the remaining CXB surface brightness after the above point-source subtraction by the following three methods: (1) subtracting the summed point source fluxes measured with Suzaku from the 100% CXB, (2) subtracting the summed point source fluxes estimated using the $\log N$–$\log S$ relation, and (3) fitting a power-law model to the diffuse emission in the $20' - 26'$ region after the point sources are excised.

In case (1), we subtracted contribution of the excised sources of $1.80^{+0.22}_{-0.21} \times 10^{-8}$ erg cm^{-2} s^{-1} sr^{-1} from the 100% CXB, dividing $F_{\rm X} = 4.83^{+0.60}_{-0.56} \times 10^{-13}$ erg cm^{-2} s^{-1} of the Suzaku total by $17'.8 \times 17'.8$ area of the XIS FOV. In case (2), we calculated the integrated point source flux per steradian from

$$I(S > S_0) \;=\; \frac{k_0}{\gamma - 2}\, S_0^{-\gamma+2}, \tag{5.2}$$

where k and γ are the differential $\log N$–$\log S$ normalization and slope, respectively. We take nominal values, $k_0 = 1.58 \times 10^{-15}$ sr^{-1} (erg cm^{-2} s^{-1})$^{\gamma-1}$ and $\gamma = 2.5$, from Kushino et al. (2002). S_0 is taken as 2×10^{-14} erg cm^{-2} s^{-1}, which is slightly higher than our flux limit, because the assumed $\log N$–$\log S$ in equation (5.2) does not take into account the flattening of the relation in the fainter flux end. In case (3), we fit the spectra from the solid angle in the $20' - 26'$ annulus that remain after the source excision by a power-law model using a uniform flux ancillary response file (ARF; see section 4.2.1). The ARF assumes that X-ray photons comes into the detectors uniformly from the sky direction within $20'$ radius from the optical axes of the respective XRTs. The model fit is *apec* + *wabs* × (*apec* + *powerlaw*) where the two *apec* components represent the galactic emission. This is the 2T-III model described in section 5.6. In this case, value of the $I_0 - I_{\rm X}$ column is determined by the spectral fit, and then $I_{\rm X}$ is calculated assuming $I_0 = 6.38 \times 10^{-8}$ erg cm^{-2} s^{-1} sr^{-1} in table 5.7.

We summarize our estimations of the remaining CXB surface brightness, $I_0 - I_{\rm X}$, in table 5.7. All three methods give consistent results. Hereafter we will use a nominal diffuse cosmic X-ray background spectrum (after subtraction of point sources brighter than $\sim 1 \times 10^{-14}$ erg cm^{-2} s^{-1} in 2–10 keV band) described by a power-law with a photon index $\Gamma = 1.37$, and surface brightness 4.73×10^{-8} erg cm^{-2} s^{-1} sr^{-1} in the 2–10 keV band, which comes from the 2T-III (a) row of the method (3). We adopt this method because it directly measures the quantity of interest in our observations.

To estimate the amplitude of the CXB fluctuations, we scaled the measured fluctuations from Ginga (Hayashida 1989) to our flux limit and FOV area. The fluctuation

width is given by the following relation,

$$\frac{\sigma_{\rm Suzaku}}{I_{\rm CXB}} = \frac{\sigma_{\rm Ginga}}{I_{\rm CXB}} \left(\frac{\Omega_{\rm e,Suzaku}}{\Omega_{\rm e,Ginga}} \right)^{-0.5} \left(\frac{S_{\rm c,Suzaku}}{S_{\rm c,Ginga}} \right)^{0.25}, \tag{5.3}$$

where $(\sigma_{\rm Suzaku}/I_{\rm CXB})$ means the fractional CXB fluctuation width due to the statistical fluctuation of discrete source number in the FOV. Here, we adopt $\sigma_{\rm Ginga}/I_{\rm CXB} = 5\%$, with $S_{\rm c}$ (Ginga: 6×10^{-12} erg cm^{-2} s^{-1}) representing the upper cut-off of the source flux, and $\Omega_{\rm e}$ (Ginga: 1.2 deg^2) representing the effective beam size (or effective solid angle) of the detector. We show the result, $\sigma/I_{\rm CXB}$, for each spatial region in table 5.10.

In the case of A2204, we also looked into CXB level.

We estimated the remaining CXB surface brightness by the following three methods: 100% CXB by Kushino et al. (2002) with abandunce model Feldman (1992) (2) fitting a power-law model to the diffuse emission in the $15'.5 - 19'.5$ region with abundance model of Anders & Grevesse (1989) and (3) fitting a power-law model to the diffuse emission in the $15'.5 - 19'.5$ region with abundance model of Feldman (1992).

In the case of A2204, The CXB flux within $20'$ circle is stronger than the value of Kushino et al. (2002) in table 5.7. It is possible that CXB value is also affected with SWCX mentioned before. CXB intensities measured for A2204 are stronger than that of A1413. We suspect it because of small background region with 15'.5-19'.5. To give background enough effective area, we utilized 11'.5-19.5 region which is out of virial radius as background in the test (d) of A2204. However, the background intensity is not considered different result from other cases.

In AWM7, we fixed CXB flux subtracted value from 100% CXB by Kushino et al. (2002) to point source flux like as table5.7, because we did not observed background region with them.

5.5 Non X-ray Background

The non X-ray background (NXB) spectra were estimated from the Suzaku database of dark earth observations using the procedure of Tawa et al. (2008). We accumulated data for the same detector area, for the same distribution of COR2 as the A1413 observation using the *xisnxbgen* FTOOLS covering 30 days before to 90 days after the observation period of A1413. To increase the A1413 signal-to-noise ratio by reducing the NXB count rate, we required COR2 to be > 8 GV and PINUD to be between 100 and 300 cts s^{-1}. After this screening the exposure time dropped from 108 ks to 72 ks, nevertheless the fit residuals were reduced. We also tested other screening criteria, such as COR2 > 8 GV and COR2 > 5 GV, both with no PINUD screening. The former criterion did not affect the final spectral results significantly, but the latter gave different ICM temperatures. To test a possible NXB uncertainity systematic error, we varied its intensity by $\pm 3\%$ as investigated by Tawa et al. (2008).

5.6 Galactic Components

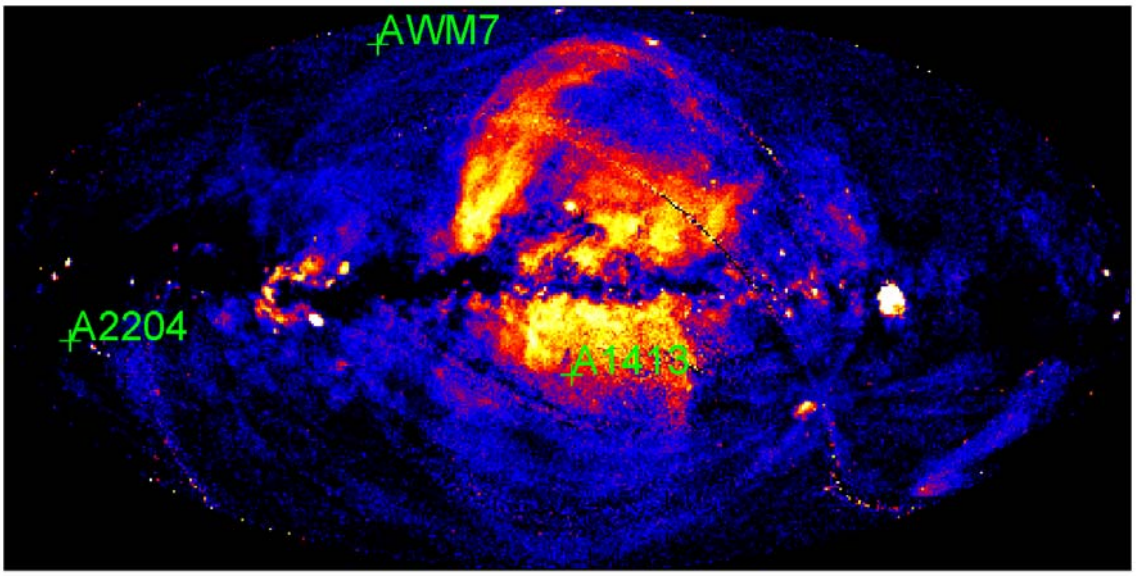

Fig. 5.6: Rosat ALL Sky Survay map (R45 band:R4=52-69, R5=70-90)

We fit the data in the $20' - 26'$ region to constrain the foreground Galactic emission, using the same uniform-sky ARF as the CXB component. We investigated the best model to use and the best-fit model parameters. In all cases, we also included a power-law model to represent the CXB. We tried a single temperature thermal plasma model, 1T: $apec + wabs \times powerlaw$, a two temperature model, 2T: $wabs \times (apec_1 + apec_2 + powerlaw)$, and a two temperature model following Tawa et al. (2009), 2T-III: $apec_1 + wabs \times (apec_2 + powerlaw)$. In all models, redshift and abundance of the *apec* components were fixed at 0.0 and 1.0, respectively. The two temperature variants try to model the Local Hot Babble (LHB) and the Milky Way Halo (MWH). We tried three types of the 2T model: both temperatures fixed to 0.204 keV and 0.074 keV given by Lumb et al. (2002), one temperature fixed to 0.074 keV and the second temperature free, both temperatures free. We call the first model as 2T-I, and the second model as 2T-II. The third model did not converge in the fitting, so that we do not discuss it further.

We found that the 1T and 2T-I models gave worse χ^2 values compared with the 2T-II and 2T-III fits. We show the best-fit parameters in table 5.8 for the 2T-III model, which we adopt. We find that the LHB and MWH temperatures are $0.112^{+0.009}_{-0.005}$ keV and $0.278^{+0.029}_{-0.019}$ keV, respectively. These values are consistent with those obtained by Tawa et al. (2009). We also show in table 5.8 how the best-fit parameters change as a result of systematic changes in the CXB and NXB levels and of the abundance model used (labeled (a) or (b)). The variations are small: less than $\pm 10\%$ for the temperatures and $\pm 15\%$ for the normalizations. Finally, our baseline CXB+GAL model is denoted 2T-III (a), $apec_1 + wabs * (apec_2 + powerlaw)$ with abundances from Anders & Grevesse (1989). We link all parameters of this model, except an overall normalization, when performing

the fits for the different spatial regions.

In the case of A2204, the intensity of galactic components are stronger in order than A2204 case. That is due to the SWCX or the affection of our galactic components in real. However as shown in figure 5.6, diffuse distribution suggests that A2204 is locate not so specific address. We also thought that this property of galactic and CXB intensities is due to the possibility with the inconsistency of β model and ICM surface brightness profile. However, we could not recognized difference of considerable results between β profile and 2β profile which modeled with *Suzaku* 1.0-10.0 keV image. Then we conclude that A2204 is much affected with SWCX contamination below 1 keV.

In the case of AWM7, we fixed LHB component with 0.074 keV which is the averaged LHB temperature by Lumb et al. (2002). because its normalization is diverged. we listed the value of galactic components in table 5.9. The nominal best-fit value of its flux is $0.231^{+0.050}_{-0.087}$erg cm^{-2} s^{-1} sr^{-1}in east and $0.143^{+0.104}_{-0.097}$erg cm^{-2} s^{-1} sr^{-1}in south. Because MWH components of There are no different result between Anders & Grevesse (1989) and Feldman (1992). The nominal best-fit value of MWH flux are $0.728^{+0.213}_{-0.152}$erg cm^{-2} s^{-1} sr^{-1}in east and $0.503^{+0.490}_{-0.245}$ erg cm^{-2} s^{-1} sr^{-1}in south.

When we subtraced simulated stray light spectra from raw spectra – 2T-III(c), in the south region, LHB and MWH fluxes are about twice stronger than other cases, instead of zero normalization of ICM component. Then we fixed all of galactic components to the nominal value – 2T-III(a) in the south region.

5.7 Background Fraction in Each Region

Table 5.10, table 5.11, and table 5.12 present many properties of the spatial regions of A1413, A2204, and AWM7 we analyzed. The columns are the annular boundaries; the actual solid angle of each region observed, Ω_e; the coverage fraction of each annulus which is the ratio of Ω_e to the total solid angle of the annulus, *Coverage*; the fraction of the simulated cluster photons which fall in the region compared with the total photons from the entire simulated cluster, *SOURCE_RATIO_REG*; the CXB fluctuations due to unresolved point sources, $\sigma/I_{\rm CXB}$; the observed counts, OBS; the estimated counts for each background component, NXB, CXB, and GAL; and the fraction of background photons given by $f_{\rm BGD} \equiv$ (NXB+CXB+GAL)/OBS.

The NXB count rates are calculated from the dark earth data. We simulated the CXB and GAL components spectra using *xissim* with the flux and spectral parameters given in row 2T-III (a) of table 5.7, table 5.8, and table 5.9, assuming a uniform surface brightness that fills the 20 arcmin radius of the assumed field. We plot the NXB and CXB spectra in figures C.2 and figure C.3 for A1413, figure C.5 and figure C.6 for A2204, and figure C.10 for AWM7. These spectra gave the count rates in table 5.10, table 5.11, and table 5.12. In the outermost region of $f_{\rm BGD}$ is consistent with 100% in A1413 and A2204. This confirms the accuracy of our background estimation.

Table 5.7: Estimation of the CXB surface brightness after the point source excision of A1413, A2204, and AWM7.

A1413			
	$I_0 - I_X$ *	I_X †	Γ ‡
(1)	$4.58^{+0.22}_{-0.21}$	$1.80^{+0.22}_{-0.21}$	1.41 (fixed)
(2) §	4.15	2.23	1.41 (fixed)
(3) 2T-III (a) ‖	$4.73^{+0.13}_{-0.22}$	$1.65^{+0.13}_{-0.22}$	$1.37^{+0.04}_{-0.05}$
(3) 2T-III (b) ♯	$4.69^{+0.18}_{-0.18}$	$1.69^{+0.18}_{-0.18}$	$1.40^{+0.05}_{-0.07}$
(3) 2T-III (c) ‖	$5.16^{+0.12}_{-0.58}$	$1.22^{+0.12}_{-0.58}$	$1.44^{+0.03}_{-0.05}$
(3) contami+20% ‖	$5.04^{+0.16}_{-0.35}$	$1.34^{+0.16}_{-0.35}$	$1.45^{+0.05}_{-0.05}$
(3) contami−20% ‖	$4.95^{+0.13}_{-0.33}$	$1.33^{+0.13}_{-0.33}$	$1.44^{+0.06}_{-0.04}$

A2204		
	$I_0 - I_X$ *	Γ ‡
(3) 2T-III (a) ‖	$7.23^{+0.82}_{-0.87}$	1.41 (fixed)
(3) 2T-III (b) ♯	$6.67^{+0.85}_{-0.91}$	1.41 (fixed)
(3) contami+20% ‖	$7.10^{+0.79}_{-1.00}$	1.41 (fixed)
(3) contami−20% ‖	$7.29^{+0.91}_{-0.89}$	1.41 (fixed)
(3) NXB+5% ‖	$6.75^{+1.00}_{-0.84}$	1.41 (fixed)
(3) NXB−5% ‖	$7.67^{+0.80}_{-0.92}$	1.41 (fixed)

AWM7			
	$I_0 - I_X$ *	I_X †	Γ ‡
East	6.20 (fixed)	0.18	1.41 (fixed)
South	5.65 (fixed)	0.73	1.41 (fixed)

* Estimated surface brightness of the CXB after the point source excision in unit of 10^{-8} erg cm^{-2} s^{-1} sr^{-1} (2–10 keV).

† Contribution of the resolved point sources in unit of 10^{-8} erg cm^{-2} s^{-1} sr^{-1} (2–10 keV).

‡ Assumed or estimated photon index of the CXB.

§ Surface brightness of 100% of CXB is assumed as $I_0 = 6.38 \times 10^{-8}$ erg cm^{-2} s^{-1} sr^{-1} (2–10 keV). Integrated point source contribution, I_X, is calculated with equation (5.2). See section 5.4 for details.

‖ See section 5.6 for definition. Abundance model is by Anders & Grevesse (1989).

♯ See section 5.6 for definition. Abundance model is by Feldman (1992).

♯♯ Four-regions simoltanious fitting with $11'.5 - 19'.5$ as background region. Abundance model is by Anders & Grevesse (1989).

Table 5.8: Galactic components best fit parameters and 90% confidence errors.

A1413				
	kT_1 (keV)	$F_{\rm x1}$ ‖	kT_2 (keV)	$F_{\rm x2}$ ‖
2T-III (a) * ...	$0.112^{+0.009}_{-0.005}$	$0.685^{+0.051}_{-0.056}$	$0.278^{+0.029}_{-0.019}$	$0.349^{+0.092}_{-0.067}$
2T-III (b) † ...	$0.110^{+0.003}_{-0.006}$	$0.702^{+0.047}_{-0.049}$	$0.314^{+0.029}_{-0.025}$	$0.424^{+0.087}_{-0.083}$
2T-III (c) ‡ ...	$0.113^{+0.003}_{-0.003}$	$0.623^{+0.065}_{-0.036}$	$0.260^{+0.964}_{-0.033}$	$0.352^{+0.114}_{-0.049}$
contami+20%	$0.111^{+0.002}_{-0.010}$	$0.733^{+0.041}_{-0.072}$	$0.269^{+0.818}_{-0.013}$	$0.396^{+0.093}_{-0.077}$
contami−20%	$0.113^{+0.005}_{-0.006}$	$0.633^{+0.057}_{-0.054}$	$0.286^{+0.920}_{-0.070}$	$0.316^{+0.100}_{-0.072}$
A2204				
	kT_1 (keV)	$F_{\rm x1}$ ‖	kT_2 (keV)	$F_{\rm x2}$ ‖
2T-III (a) *....	0.074 (fixed)	$4.835^{+5.446}_{-4.835}$	$0.249^{+0.020}_{-0.013}$	$12.337^{+2.446}_{-2.563}$
2T-III (b) † ...	0.074 (fixed)	$11.965^{+4.720}_{-4.805}$	$0.285^{+0.009}_{-0.008}$	$10.838^{+0.893}_{-0.903}$
2T-III (d) ♯ ...	0.074 (fixed)	$4.541^{+5.833}_{-4.541}$	$0.250^{+0.021}_{-0.014}$	$12.278^{+2.503}_{-2.487}$
contami+20%*	0.074 (fixed)	$9.111^{+5.585}_{-6.565}$	$0.254^{+0.021}_{-0.014}$	$12.758^{+2.515}_{-2.518}$
contami−20%*	0.074 (fixed)	$1.170^{+5.164}_{-1.169}$	$0.244^{+0.019}_{-0.011}$	$11.869^{+1.947}_{-2.361}$
$\rm CXB_{max}$ *	0.074 (fixed)	$5.657^{+6.018}_{-5.663}$	$0.248^{+0.019}_{-0.014}$	$12.061^{+2.674}_{-2.084}$
$\rm CXB_{min}$ *	0.074 (fixed)	$4.675^{+5.941}_{-4.651}$	$0.249^{+0.021}_{-0.014}$	$12.381^{+2.548}_{-2.437}$
NXB+5% * ...	0.074 (fixed)	$4.819^{+5.815}_{-4.819}$	$0.249^{+0.021}_{-0.014}$	$12.314^{+2.527}_{-2.433}$
NXB−5% * ...	0.074 (fixed)	$4.867^{+5.453}_{-4.874}$	$0.249^{+0.021}_{-0.013}$	$12.341^{+2.432}_{-2.494}$

* Abundance model is by Anders & Grevesse (1989).

† Abundance model is by Feldman (1992).

‡ Including two gaussian models of $\rm O_{VII}$ and $\rm O_{VIII}$. Abundance model is by Anders & Grevesse (1989).

‖ Surface brightness in unit of 10^{-8} erg cm^{-2} s^{-1} str^{-1} (0.5–10 keV).

♯ Abundance model is by Anders & Grevesse (1989). And CXB model is fixed to Kushino et al. (2002)

Table 5.9: Galactic components best fit parameters and 90% confidence errors of AWM7.

AWM7 OFFSET East				
	kT_1 (keV)	$F_{\rm x1}$ ‖	kT_2 (keV)	$F_{\rm x2}$ ‖
2T-III (a) *	0.074 (fixed)	$0.231^{+0.060}_{-0.087}$	$0.279^{+0.034}_{-0.045}$	$0.728^{+0.213}_{-0.152}$
2T-III (b) †	0.074 (fixed)	$0.229^{+0.056}_{-0.052}$	0.296 (fixed)	$0.816^{+0.183}_{-0.160}$
2T-III (c) ‡	0.074 (fixed)	$0.251^{+0.067}_{-0.089}$	$0.287^{+0.036}_{-0.050}$	$0.763^{+0.229}_{-0.145}$
contami−20%	0.074 (fixed)	$0.164^{+0.048}_{-0.061}$	$0.291^{+0.035}_{-0.046}$	$0.604^{+0.150}_{-0.142}$
contami+20%	0.074 (fixed)	$0.322^{+0.074}_{-0.101}$	$0.280^{+0.031}_{-0.040}$	$0.886^{+0.231}_{-0.175}$
$\rm CXB_{min}$	0.074 (fixed)	$0.232^{+0.053}_{-0.052}$	0.279 (fixed)	$0.804^{+0.127}_{-0.122}$
$\rm CXB_{max}$	0.074 (fixed)	$0.200^{+0.063}_{-0.086}$	$0.258^{+0.038}_{-0.052}$	$0.722^{+0.234}_{-0.181}$
NXB−5%	0.074 (fixed)	$0.251^{+0.059}_{-0.066}$	$0.293^{+0.030}_{-0.040}$	$0.800^{+0.136}_{-0.166}$
NXB+5%	0.074 (fixed)	$0.189^{+0.079}_{-0.076}$	$0.255^{+0.052}_{-0.034}$	$0.708^{+0.192}_{-0.204}$
$\rm CXB_{min}$,NXB−5%	0.074 (fixed)	$0.255^{+0.058}_{-0.057}$	$0.295^{+0.030}_{-0.032}$	$0.818^{+0.145}_{-0.139}$
$\rm CXB_{max}$,NXB+5%	0.074 (fixed)	$0.222^{+0.062}_{-0.113}$	$0.284^{+0.034}_{-0.043}$	$0.717^{+0.218}_{-0.145}$
AWM7 OFFSET South				
	kT_1 (keV)	$F_{\rm x1}$ ‖	kT_2 (keV)	$F_{\rm x2}$ ‖
2T-III (a) *	0.074 (fixed)	$0.143^{+0.104}_{-0.097}$	$0.196^{+0.067}_{-0.046}$	$0.503^{+0.490}_{-0.245}$
2T-III (b) †	0.074 (fixed)	$0.150^{+0.096}_{-0.071}$	$0.196^{+0.074}_{-0.053}$	$0.473^{+0.340}_{-0.245}$
contami−20%	0.074 (fixed)	$0.092^{+0.085}_{-0.079}$	$0.189^{+0.089}_{-0.045}$	$0.446^{+0.448}_{-0.226}$
contami+20%	0.074 (fixed)	$0.225^{+0.116}_{-0.144}$	$0.208^{+0.072}_{-0.059}$	$0.586^{+0.613}_{-0.180}$
$\rm CXB_{min}$	0.074 (fixed)	$0.217^{+0.076}_{-0.110}$	$0.253^{+0.034}_{-0.064}$	$0.644^{+0.213}_{-0.182}$
$\rm CXB_{max}$	0.074 (fixed)	$0.117^{+0.104}_{-0.109}$	$0.181^{+0.043}_{-0.057}$	$0.462^{+0.848}_{-0.267}$
NXB−5%	0.074 (fixed)	$0.161^{+0.114}_{-0.049}$	$0.207^{+0.078}_{-0.025}$	$0.508^{+0.424}_{-0.202}$
NXB+5%	0.074 (fixed)	$0.123^{+0.101}_{-0.107}$	$0.187^{+0.085}_{-0.044}$	$0.497^{+0.553}_{-0.270}$
$\rm CXB_{min}$,NXB−5%	0.074 (fixed)	$0.284^{+0.049}_{-0.097}$	$0.275^{+0.025}_{-0.045}$	$0.810^{+0.191}_{-0.210}$
$\rm CXB_{max}$,NXB+5%	0.074 (fixed)	$0.103^{+0.107}_{-0.104}$	$0.174^{+0.036}_{-0.063}$	$0.466^{+1.322}_{-0.256}$

* Abundance model is by Anders & Grevesse (1989).

† Abundance model is by Feldman (1992).

‡ Subtracting simulated stray light photon from raw spectra.

‖ Surface brightness in unit of 10^{-8} erg cm^{-2} s^{-1} str^{-1} (0.5–10 keV).

♯ Four-regions simoltanious fitting with $11'.5 - 19'.5$ as background region. Abundance model is by Anders & Grevesse (1989).

Table 5.10: Properties of the spatial regions used in A1413

Region *		Ω_e † (arcmin^2)	*Coverage* †	*SOURCE_RATIO_REG* ‡	σ/I_{CXB} § (%)	FI counts (0.5–10 keV) ‖ OBS	NXB	CXB	GAL	f_{BGD}
$2'.7 - 7'$	...	18.6	14.2%	2.60%	15.4	$3,828 \pm 62$	855 ± 86	560 ± 86	81 ± 9	$39.1 \pm 3.5\%$
$7' - 10'$	...	25.6	16.0%	1.49%	13.1	$3,568 \pm 60$	$1,241 \pm 124$	966 ± 127	131 ± 11	$65.5 \pm 5.3\%$
$10' - 15'$	...	55.0	14.0%	1.40%	9.0	$6,340 \pm 80$	$2,428 \pm 242$	$2,460 \pm 220$	296 ± 17	$81.8 \pm 5.3\%$
$15' - 20'$	...	86.5	15.7%	1.27%	7.1	$9,156 \pm 96$	$4,162 \pm 416$	$4,035 \pm 288$	499 ± 22	$95.0 \pm 5.6\%$
$20' - 26'$	...	38.6	4.5%	0.47%	10.7	$4,547 \pm 67$	$2,523 \pm 252$	$1,907 \pm 204$	272 ± 16	$103.4 \pm 7.3\%$
Region *		Ω_e † (arcmin^2)	*Coverage* †	*SOURCE_RATIO_REG* ‡	σ/I_{CXB} § (%)	BI counts (0.4–10.0 keV) ‖ OBS	NXB	CXB	GAL	f_{BGD}
$2'.7 - 7'$	...	18.4	14.0%	2.60%	15.5	$2,042 \pm 45$	748 ± 75	208 ± 32	85 ± 9	$50.9 \pm 4.6\%$
$7' - 10'$	...	25.5	15.9%	1.56%	13.1	$2,546 \pm 50$	$1,088 \pm 109$	392 ± 51	144 ± 12	$63.8 \pm 5.1\%$
$10' - 15'$	...	54.9	14.0%	1.41%	9.0	$4,447 \pm 67$	$2,277 \pm 228$	$1,012 \pm 91$	331 ± 18	$81.4 \pm 5.7\%$
$15' - 20'$	...	87.4	15.9%	1.32%	7.1	$7,425 \pm 86$	$4,418 \pm 441$	$1,857 \pm 132$	631 ± 25	$93.0 \pm 6.3\%$
$20' - 26'$	...	24.6	2.8%	0.37%	13.3	$2,984 \pm 55$	$1,954 \pm 195$	706 ± 94	264 ± 16	$98.0 \pm 7.5\%$

* Radii are from the XMM-Newton surface brightness peak in figure 8.4(a).

† The average value of the four detectors.

‡ $SOURCE\_RATIO\_REG \equiv Coverage \times \int_{r_{in}}^{r_{out}} S(r)\, r\, dr / \int_0^\infty S(r)\, r\, dr$,where $S(r)$ represents the assumed radial profile of A1413. We confined $S(r)$ to a $60' \times 60'$ region on the sky.

§ $S_c = 1 \times 10^{-14}$ erg cm^{-2} s^{-1} is assumed for all regions.

‖ OBS denotes the total observed counts. NXB, CXB and GAL are the estimated counts. $f_{BGD} \equiv (\mathrm{NXB} + \mathrm{CXB} + \mathrm{GAL})/\mathrm{OBS}$.

Table 5.11: Properties of the spatial regions used in A2204

Region *		Ω_e † (arcmin^2)	*Coverage* †	*SOURCE_RATIO_REG* ‡	σ/I_{CXB} § (%)	FI counts (0.5–10 keV) ‖ OBS	NXB	CXB	GAL	f_{BGD}
$0' - 3'.5$	...	41.2	14.2%	54.46%	50.2	$179,520 \pm 424$	$1,162 \pm 34$	$1,638 \pm 24$	1633 ± 43	$2.0^{+0.2}_{-0.1}$%
$3'.5 - 7'$	...	64.4	16.0%	8.04%	41.0	$28,977 \pm 170$	$2,161 \pm 46$	$3,138 \pm 33$	2857 ± 58	$23.0^{+0.2}_{-0.1}$%
$7' - 11'.5$	...	99.7	14.0%	3.74%	32.9	$16,614 \pm 129$	$3,141 \pm 56$	$3,704 \pm 41$	3310 ± 72	$59.9^{+0.5}_{-0.4}$%
$11'.5 - 19'.5$	...	3.4	4.5%	0.06%	178.2	$9,231 \pm 40$	$2,774 \pm 12$	$2,492 \pm 8$	2563 ± 15	$119.7^{+7.7}_{-0.9}$%
Region *		Ω_e † (arcmin^2)	*Coverage* †	*SOURCE_RATIO_REG* ‡	σ/I_{CXB} § (%)	BI counts (0.4–10.0 keV) ‖ OBS	NXB	CXB	GAL	f_{BGD}
$0' - 3'.5$	...	29.2	14.0%	40.90%	60.8	$76,337 \pm 276$	895 ± 30	574 ± 14	1140 ± 34	$2.9^{+1.1}_{-1.2}$
$3'.5 - 7'$	...	61.4	15.9%	6.77%	41.9	$16,557 \pm 129$	$1,810 \pm 43$	1295 ± 21	2391 ± 49	$28.4^{+0.9}_{-0.9}$%
$7' - 11'.5$	...	105.3	14.0%	3.89%	32.0	$11,835 \pm 109$	$3,021 \pm 55$	1646 ± 27	3121 ± 62	$64.0^{+1.9}_{-1.8}$%
$15'.5 - 19'.5$	...	16.1	2.8%	0.24%	81.9	$7,990 \pm 35$	$2,826 \pm 23$	$1,243 \pm 9$	2782 ± 23	$91.3^{+7.2}_{-6.9}$%

* Each position of area is from surface brightness peak in figure 8.4(b).

† The average values among four sensors are presented.

‡ SOURCE_RATIO_REG $\equiv$ COVERAGE $\times \int_{r_{in}}^{r_{out}} S(r)\, r\, dr / \int_0^{\infty} S(r)\, r\, dr$,where $S(r)$ represents the assumed radial profile of A 1413, and we defined $S(r)$ in $20' \times 20'$ region on the sky.

$\diamond$ S_c is assumed $2{\times}10^{-14}$ [erg cm^{-2} s^{-1}] for all.

§ OBS denotes the observed counts including NXB, CXB and GAL. NXB, CXB and GAL are the estimated counts.

Table 5.12: Properties of the spatial regions used in AWM7

Region *		Ω_e † (arcmin^2)	*Coverage* †	*SOURCE_RATIO_REG* ‡	σ/I_{CXB} § (%)	FI counts (0.5–10 keV) ‖ OBS	NXB	CXB	GAL	f_{BGD}
Offset East	...	268.2	%	4.29%	4.6	$16,292 \pm 128$	$7,423 \pm 86$	5837 ± 76	1281 ± 36	$89.2 \pm 1.1\%$
Offset South	...	264.6	%	4.30%	5.5	$10,444 \pm 170$	$5,512 \pm 46$	3541 ± 33	939 ± 58	$95.7 \pm 1.8\%$
Region *		Ω_e † (arcmin^2)	*Coverage* †	*SOURCE_RATIO_REG* ‡	σ/I_{CXB} § (%)	BI counts (0.4–10.0 keV) ‖ OBS	NXB	CXB	GAL	f_{BGD}
Offset East	...	276.5	3.37%	4.86%	4.6	$16,992 \pm 130$	$10,276 \pm 101$	3640 ± 60	2376 ± 49	95.9 ± 1.1
Offset South	...	270.0	3.29%	4.87%	5.5	$23,378 \pm 152$	$15,164 \pm 123$	4383 ± 66	3609 ± 60	$99.1 \pm 0.9\%$

* Each position of area is from surface brightness peak in figure 8.4(b).

† The average values among four sensors are presented.

‡ SOURCE_RATIO_REG $\equiv$ COVERAGE $\times \int_{r_{in}}^{r_{out}} S(r)\ r\,dr / \int_0^\infty S(r)\ r\,dr$,where $S(r)$ represents the assumed radial profile of A 1413, and we defined $S(r)$ in $20' \times 20'$ region on the sky.

◇ S_c is assumed $2{\times}10^{-14}$ [erg cm^{-2} s^{-1}] for all.

§ OBS denotes the observed counts including NXB, CXB and GAL. NXB, CXB and GAL are the estimated counts.

Chapter 6

Individual Analysis and Results

6.1 A1413

We observed the northern region of A1413 with the Suzaku XIS detectors. In table 4.3, we give the details of our observation, and in figure 8.4(a), we show the XIS field of view (FOV) superimposed on the *XMM-Newton* image of A1413. The XIS instrument consists of 4 CCD chips; one back-illuminated (BI: XIS1) and three front-illuminated (FI: XIS0, XIS2, XIS3), with each is combined with an X-ray telescope (XRT). The IR/UV blocking filters had accumulated a significant contamination by the time of the observation since its launch (July 2005); we include its effects on the effective area in our analysis. The XIS was operated with normal clocking mode, in 5×5 or 3×3 editing modes. The spaced-row charge injection (SCI) was not applied, and all the four CCDs were working at the time of the observation.

6.1.1 Surface brightness

To create Ancillary Response File (ARF) by feeding an image for analysis of *Suzaku* observations, we constructed surface brightness profiles from KBB model by Pratt & Arnaud (2002).

6.1.2 Spectral fitting

We used XSPEC version 12.4.0y for all spectral fitting. The FI and BI spectra were fitted simultaneously. We employed a *wabs* $\times$ *apec* model for the ICM emission of the cluster as absorbed thermal plasma. The *wabs* component models the photoelectric absorption by the Milky Way, parameterized by the hydrogen column density that was fixed at the 21 cm value (Dickey & Lockman 1990). The *apec* is a thermal plasma model. Its fitting parameters are normalization, kT and the ICM abundance. The redshift was fixed at the optical spectroscopic value ($z = 0.1427$). Additional fitting parameters are the two normalizations and temperatures of the GAL components, and the normalization and photon index of the power-law model for the CXB component, as described previously. We did not fit the ICM component in the outermost $20' - 26'$ region because we can explain

the observed spectrum without it, as we show in figure C.4(e). This situation was planned as we wanted to have an in-field measurement of the background. In figures C.2 and C.3, we compared the intensities of the observed spectra minus the NXB to the spectra of the NXB and CXB components. Figure C.2(a) shows very strong Mn-K$_\alpha$ line at 5.9 keV from the ^{55}Fe calibration source, therefore we ignored the 5–7 keV energy band when we fit the FI spectrum of this annulus.

6.1.3 Results

In figure C.4, we show the best-fit spectra in each spatial region. These figures show the observed spectra after subtraction of the NXB, as well as the best-fit. These figures show that individual spectra are well fitted by the model in each region. The normalization for the ICM component was fixed to zero in the $20' - 26'$ annulus to estimate the background. The ICM spectra did not show strong emission lines. Because of the low S/N ratio, it was difficult to constrain the model parameters in the $15' - 20'$ annulus. Therefore, we linked the ICM temperature and abundance in this region to that of the region next interior to it, the $10' - 15'$ annulus. The best-fit parameters were consistent within the systematic errors for the two regions. The emission weighted average radius for the combined region is $12'.42^{+1'.04}_{-1'.07}$.

Table 6.1 shows the best-fit parameters for the ICM model in each region. We fitted with two different solar abundances, namely Anders & Grevesse (1989) and Feldman (1992). The derived abundance values are higher when we adopt the Feldman (1992) abundance, than the Anders & Grevesse (1989) case, because the Fe abundance relative to H in the former model is lower than the latter.

In figure 6.1(a), we show temperature profiles observed with Chandra (Vikhlinin et al. 2005), *XMM-Newton* (Snowden et al. 2008), and Suzaku (this work). These profiles are consistent with each other in the range $7' - 15'$. The Chandra temperatures are about 20% higher than the *XMM-Newton* values at $2'.7 - 7'$. The tendency that Chandra gives higher temperature than *XMM-Newton* typically becoming significant above $kT \sim 5$–6 keV is pointed out in figure 12 of Snowden et al. (2008). This discrepancy is due mainly to a Chandra calibration problem, namely the ground calibration of the HRMA effective area had some errors especially at the Ir edge (0.62 keV), and there also was uncertainity about the IR/UV blocking filter contamination. These uncertainties caused a large discrepancy between the Chandra and *XMM-Newton* measurements for high-temperature clusters. Recent updates of the Chandra CALDB, HRMA AXEFFA version N0008,[1] corrected most of this discrepancy. However, there still remains some differences in cluster temperature by about 10% especially in hot objects. For temperatures below ~ 5 keV, Chandra and *XMM-Newton* results are mostly consistent with each other.

We therefore used the *XMM-Newton* temperatures measured by Snowden et al. (2008). In fact, their values are higher than those of Pratt & Arnaud (2002) who used the same

[1] http://cxc.harvard.edu/ciao4.1/why/caldb4.1.1_hrma.html

Table 6.1: Best fitting parameters of the spectral fits with 90% confidence errors for one parameter.

2T-III (a) *		kT (keV)	Abundance ($Z_\odot$)	$Norm$ §	S ‖	χ^2/dof
$2'.7 - 7'$	.....	$7.03^{+1.57}_{-1.11}$	$0.44^{+0.62}_{-0.39}$	$16.35^{+1.16}_{-1.26}$	$5.77^{+0.41}_{-0.45}$	77.4/107
$7' - 10'$	.....	$4.13^{+0.97}_{-0.65}$	$0.54^{+0.21}_{-0.26}$	$4.53^{+0.30}_{-0.46}$	$2.12^{+0.14}_{-0.22}$	98.7/116
$10' - 15'$	.....	$3.60^{+0.77}_{-0.62}$	$0.39^{+0.17}_{-0.24}$	$2.29^{+0.19}_{-0.25}$	$0.90^{+0.08}_{-0.10}$	130.1/118
$15' - 20'$	.....	↑	↑	$0.82^{+0.11}_{-0.26}$	$0.31^{+0.04}_{-0.10}$	109.5/116
$20' - 26'$	.....	—	—	—	—	152.7/113
Total	.....	—	—	—	—	568.4/570
2T-III (b) †		kT (keV)	Abundance ($Z_\odot$)	$Norm$ §	S ‖	χ^2/dof
$2'.7 - 7'$	.....	$7.14^{+1.62}_{-1.17}$	$0.58^{+0.42}_{-0.40}$	$16.04^{+2.54}_{-0.97}$	$5.75^{+0.91}_{-0.35}$	77.1/107
$7' - 10'$	.....	$4.41^{+0.95}_{-0.79}$	$0.66^{+0.23}_{-0.36}$	$4.43^{+0.24}_{-0.46}$	$2.11^{+0.11}_{-0.22}$	100.6/116
$10' - 15'$	.....	$4.03^{+0.91}_{-0.66}$	$0.77^{+0.20}_{-0.51}$	$2.07^{+0.12}_{-0.17}$	$0.90^{+0.05}_{-0.07}$	129.6/118
$15' - 20'$	.....	↑	↑	$0.72^{+0.09}_{-0.23}$	$0.31^{+0.04}_{-0.10}$	114.7/116
$20' - 26'$	.....	—	—	—	—	149.2/113
Total	.....	—	—	—	—	571.3/570
2T-III (c) ‡		kT (keV)	Abundance ($Z_\odot$)	$Norm$ §	S ‖	χ^2/dof
$2.7' - 7'$	.....	$7.20^{+1.58}_{-1.20}$	$0.43^{+0.22}_{-0.21}$	$26.54^{+0.92}_{-0.90}$	$9.41^{+0.33}_{-0.32}$	76.7/105
$7' - 10'$	.....	$4.33^{+0.92}_{-0.70}$	$0.68^{+0.21}_{-0.22}$	$11.02^{+0.66}_{-0.60}$	$5.44^{+0.33}_{-0.30}$	99.8/114
$10' - 15'$	.....	$3.97^{+0.82}_{-0.66}$	$0.53^{+0.22}_{-0.21}$	$2.07^{+0.14}_{-0.13}$	$0.89^{+0.06}_{-0.06}$	125.2/116
$15' - 20'$	.....	↑	↑	$0.66^{+0.11}_{-0.13}$	$0.34^{+0.06}_{-0.07}$	104.3/114
$20' - 26'$	.....	—	—	—	—	154.5/113
Total	.....	—	—	—	—	560.5/562

* Abundance model is Anders & Grevesse (1989).

† Abundance model is Feldman (1992).

‡ Including two gaussian models of O_{VII} and O_{VIII} WHIM emission. Abundance model is Anders & Grevesse (1989)

§ Normalization of the apec component scaled with a factor of $SOURCE\_RATIO\_REG/\Omega_e$ in table 5.10,
$Norm = SOURCE\_RATIO\_REG/\Omega_e \int n_e n_H dV \,/\, (4\pi\,(1+z)^2 D_A^2) \times 10^{-20}$ cm^{-5} arcmin^{-2}, where D_A is the angular diameter distance to the source.

‖ Surface brightness in unit of 10^{-6} photons cm^{-2} s^{-1} arcmin^{-2} (0.4–10 keV).

Table 6.2: Same as table 6.1 except NXB±3%, CXB_{MAX} and CXB_{MIN} and contami±20%. Abundance model is Anders & Grevesse (1989).

NXB−3%, CXB_{MIN}		kT (keV)	Abundance ($Z_\odot$)	$Norm$ *	S †	χ^2/dof
$2'.7-7'$	.....	$7.57^{+1.78}_{-1.28}$	$0.47^{+0.76}_{-0.31}$	$16.94^{+0.70}_{-1.00}$	$5.99^{+0.25}_{-0.35}$	78.7/107
$7'-10'$	.....	$4.84^{+1.11}_{-0.81}$	$0.60^{+0.32}_{-0.29}$	$4.91^{+0.23}_{-0.50}$	$2.34^{+0.11}_{-0.24}$	98.6/116
$10'-15'$	.....	$4.64^{+0.88}_{-0.71}$	$0.51^{+0.22}_{-0.30}$	$1.07^{+0.10}_{-0.18}$	$0.43^{+0.04}_{-0.07}$	130.6/116
$15'-20'$	.....	↑	↑	$0.98^{+0.10}_{-0.18}$	$0.41^{+0.04}_{-0.08}$	114.2/116
$20'-26'$	.....	—	—	—	—	157.1/115
Total	.....	—	—	—	—	579.1/572
NXB+3%, CXB_{MAX}		kT (keV)	Abundance ($Z_\odot$)	$Norm$ *	S †	χ^2/dof
$2'.7-7'$	.....	$6.60^{+1.57}_{-1.08}$	$0.40^{+0.86}_{-0.40}$	$15.96^{+0.86}_{-1.69}$	$5.51^{+0.30}_{-0.59}$	76.6/107
$7'-10'$	.....	$3.59^{+0.80}_{-0.64}$	$0.53^{+0.27}_{-0.25}$	$4.16^{+0.28}_{-0.72}$	$1.87^{+0.13}_{-0.32}$	104.3/116
$10'-15'$	.....	$2.52^{+0.53}_{-0.39}$	$0.35^{+0.14}_{-0.19}$	$2.14^{+0.18}_{-0.31}$	$0.76^{+0.06}_{-0.11}$	130.3/116
$15'-20'$	.....	↑	↑	$0.53^{+0.10}_{-0.19}$	$0.18^{+0.04}_{-0.06}$	118.6/116
$20'-26'$	.....	—	—	—	—	150.1/115
Total	.....	—	—	—	—	579.9/572
contami+20%		kT (keV)	Abundance ($Z_\odot$)	$Norm$ *	S †	χ^2/dof
$2'.7-7'$	.....	$6.89^{+1.63}_{-1.05}$	$0.45^{+0.60}_{-0.40}$	$16.31^{+1.19}_{-1.20}$	$5.74^{+0.42}_{-0.42}$	77.7/107
$7'-10'$	.....	$4.01^{+0.93}_{-0.63}$	$0.54^{+0.25}_{-0.25}$	$4.54^{+0.32}_{-0.45}$	$2.10^{+0.15}_{-0.21}$	99.0/116
$10'-15'$	.....	$3.17^{+0.81}_{-0.51}$	$0.29^{+0.17}_{-0.17}$	$2.41^{+0.22}_{-0.26}$	$0.90^{+0.08}_{-0.10}$	131.3/118
$15'-20'$	.....	↑	↑	$0.84^{+0.13}_{-0.24}$	$0.30^{+0.05}_{-0.09}$	109.6/116
$20'-26'$	.....	—	—	—	—	153.4/113
Total	.....	—	—	—	—	571.0/570
contami−20%		kT (keV)	Abundance ($Z_\odot$)	$Norm$ *	S †	χ^2/dof
$2'.7-7'$	.....	$7.08^{+1.56}_{-1.13}$	$0.42^{+0.59}_{-0.30}$	$16.36^{+0.86}_{-1.08}$	$5.78^{+0.30}_{-0.38}$	77.4/107
$7'-10'$	.....	$4.19^{+0.97}_{-0.65}$	$0.54^{+0.26}_{-0.25}$	$4.49^{+0.31}_{-0.45}$	$2.11^{+0.15}_{-0.21}$	99.0/116
$10'-15'$	.....	$3.82^{+0.77}_{-0.67}$	$0.44^{+0.16}_{-0.26}$	$2.21^{+0.17}_{-0.21}$	$0.89^{+0.07}_{-0.08}$	128.4/118
$15'-20'$	.....	↑	↑	$0.79^{+0.10}_{-0.23}$	$0.31^{+0.04}_{-0.09}$	109.1/116
$20'-26'$	.....	—	—	—	—	153.2/113
Total	.....	—	—	—	—	567.1/570

* Normalization of the apec component scaled with a factor of $SOURCE\_RATIO\_REG/\Omega_e$ in table 5.10,
$Norm = SOURCE\_RATIO\_REG/\Omega_e \int n_e n_H dV \,/\, (4\pi\,(1+z)^2 D_A^2) \times 10^{-20}$ cm^{-5} arcmin^{-2}, where D_A is the angular diameter distance to the source.

† Surface brightness in unit of 10^{-6} photons cm^{-2} s^{-1} arcmin^{-2} (0.4–10 keV).

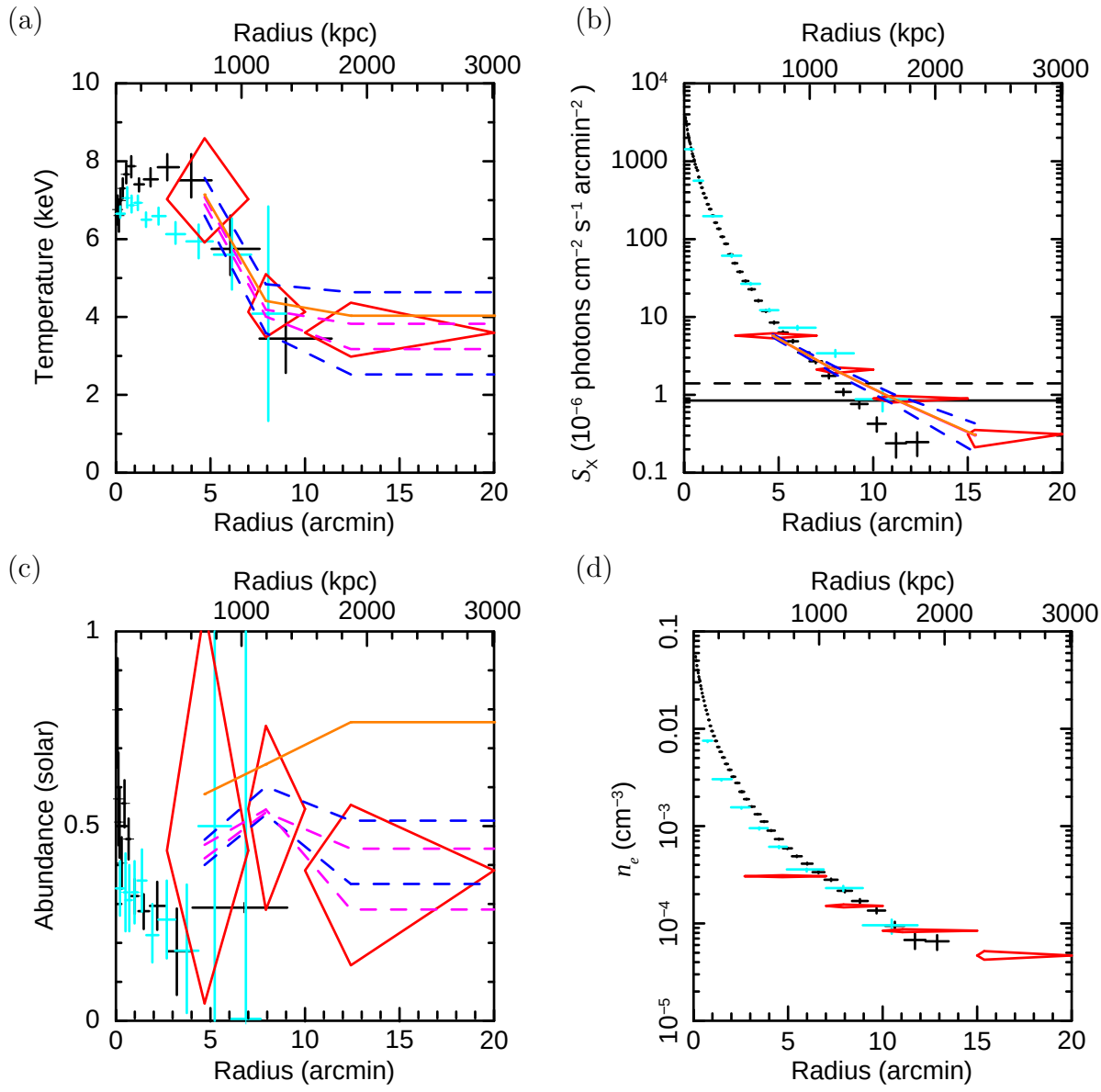

Fig. 6.1: Radial profiles for (a) temperature, (b) surface brightness (0.4–10 keV), (c) abundance, and (d) electron density. Red diamonds show our Suzaku results assuming the metal abundances of Anders & Grevesse (1989). Orange line indicates the best-fit profile using the Feldman (1992) abundances. Chandra results by Vikhlinin et al. (2005) are the black crosses, and the cyan crosses are the *XMM-Newton* results by Snowden et al. (2008). The uncertainty range due to the combined ±3% variation of the NXB level and the maximum/minimum fluctuation of CXB is shown by two blue dashed lines. We show by magenta dashed lines the uncertainties induced by a ±20% uncertainty in the amount of contamination in the IR/UV blocking filters. We also show in panel (b) the CXB level (horizontal dashed line) and the Galactic emission (horizontal solid line).

data set. This difference may partly be due to the different backgrounds used. Therefore, we assigned rather large errors of 10% even in the inner region of $r < 2'.7$ for these data. We will quantify the systematic error of the Suzaku ICM temperature in the following section.

We plot the related quantities, surface brightness, $S_{\rm X}$, and electron density, $n_{\rm e}$, in figures 6.1(b) and (d). We derived the Chandra surface brightness from the emission measures provided by A. Vikhlinin (private communication). The *XMM-Newton* surface brightness is from Snowden et al. (2008). The Suzaku surface brightness comes from the normalization of the *apec* model fit. The surface brightness results are consistent with each other within $10'$. In the outer region, the Suzaku surface brightness is significantly higher than the Chandra values. The cause of this discrepancy could be the different region of the cluster observed. In particular, Suzaku observed mainly along the major axis, while Chandra observed the minor axis, as we show in figure 8.4(a). We obtained the electron density by deprojecting the emission measure with method described Kriss et al. (1983).

We show the abundance profile in figure 6.1(c). Our nominal values are higher than the results of Chandra and *XMM-Newton*. However, our errors are large and it is difficult to draw firm conclusions.

6.1.4 Systematic Errors

To estimate the systematic errors on our electron density, temperature and abundance profiles, we examined the effects of varying the background spectra from their nominal levels. We adopted a systematic error for the NXB intensity of $\pm 3\%$ and the level of the CXB fluctuation was scaled from the Ginga result (Hayashida 1989) as shown in table 5.10. We considered a $\pm 20\%$ error for the contamination thickness on the IR/UV blocking filters in front of the XIS sensors. As mentioned earlier, we also looked into the effect of the difference between the Anders & Grevesse (1989) and Feldman (1992) abundance models.

We give the outcome of these variations in figure 6.1 and table 6.1 for the abundance model comparison, and in figure 6.1 and table 6.2 for the other comparisons. Systematic variations of the surface brightness are comparable to its statistical error for all the systematics we examined. The same is true of the temperature except for uncertainties on the UV/IR filter contamination, where the maximum possible range allowed is about 40% larger than the nominal statistical errors. Systematics on the abundance profile were less than the statistical uncertainties except for the outer two spatial bins with the Feldman (1992) abundance models. We conclude from this investigation that our statistical errors also encompass most possible systematic effects.

(a) FI+BI, $10' - 15'$ (b) FI+BI, $15' - 20'$

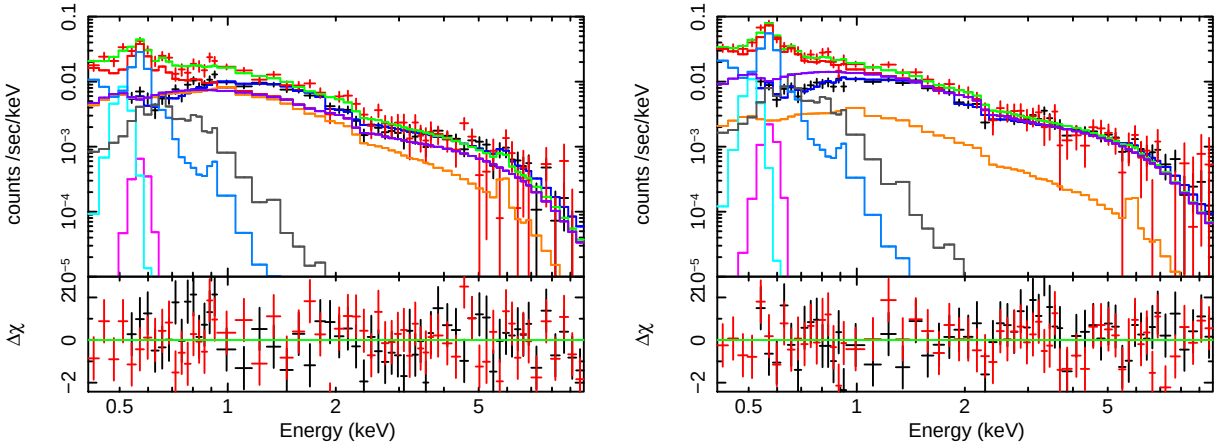

Fig. 6.2: O_{VII} (cyan) and O_{VIII} (pink) line spectra in $10' - 15'$ and $15' - 20'$ annuli.

Table 6.3: Intensity of redshifted O_{VII} (0.508 keV) and O_{VIII} (0.569 keV) lines in unit of 10^{-6} photons cm^{-2} s^{-1} arcmin^{-2} with 2σ upper limits or 90% confidence errors for a single parameter.

Region		S_{OVIII}	S_{OVII}
$2'.7 - 7'$	.....	< 0.119	< 0.135
$7' - 10'$	.....	< 0.075	< 0.091
$10' - 15'$	.....	< 0.085	$0.094^{+0.059}_{-0.061}$
$15' - 20'$	.....	< 0.095	$0.081^{+0.048}_{-0.051}$

6.1.5 Search for WHIM lines

We searched for the warm-hot intracluster medium (WHIM) which could exist in the filaments of large-scale structures of the universe. The outer regions of clusters may be connected to these filaments and are considered to be promising regions to search for possible WHIM emission.

We analyzed the regions $2.'7 - 7'$, $7' - 10'$, $10' - 15'$, and $15' - 20'$. We fitted the FI+BI spectra simultaneously. We added two gaussian lines to model the oxygen emission lines. They had fixed redshifted energies of 0.508 keV (O_{VII}) and 0.569 keV (O_{VIII}), with a fixed width of $\sigma = 0.0$. The ICM spectra fitted with the additional two gaussian lines are shown in figure 6.2, and table 6.1(c) gives the fit results. The best temperatures are consistent with the results of the previous fit without the lines. Because redshifted line energies overlapped with those of the Galactic lines, we were unable to distinguish these emission lines directly. Table 6.3 gives our result for the line intensities which are either 2σ upper limits or marginal detections.

Table 6.4: Best-fit parameter of double $s\beta$ model

$\beta 1$	0.70±0.03
r_{c1} (arcmin)	1.22±0.006
S_1(counts s^{-1} Ms^{-1} $pixel^{-1}$)	66.81±0.28
$\beta 2$	0.71±0.002
r_{c2} (arcmin)	777±83
S_2(counts s^{-1} Ms^{-1} $pixel^{-1}$)	0.22±0.002
β	837.5±169

6.2 A2204

We extracted pulse-height spectra in five annular regions from the XIS event files. The inner and outer radii of the regions were $0' - 3'.5$, $3'.5 - 7'$, $7' - 11'.5$, $11'.5 - 15'.5$, and $15'.5 - 19'.5$ respectively, measured from the *XMM-Newton* surface brightness peak of A2204 at (R.A., Dec.) = ($16^h32^m45\overset{s}{.}7$, $05°34'43''$) in J2000. We analyzed the spectra in FI:0.5–10 keV and BI:0.4-10.0 keV except for FI:0.5-5.0,7.0-10.0 keV in $15'.5 - 19.5$ range. However Below 0.7 keV range we think it is contaminated by SWCX. In the the $15'.5 - 19'.5$ annulus, we utilized as a background region. Because positions of the calibration sources themselves were masked out using masked calibration source area for each detector using the *calmask* calibration database (CALDB) file, we included Mn-K_α (5.9 keV) energy band from the ^{55}Fe calibration source. Because this region is not large area, we also found out the difference of background area with $11'.5 - 19'.5$.

6.2.1 Surface brightness

There are no references for a surface brightness profile of A2204, We constructed β model fit to *Newton* image in 0.35-1.25 keV, first. However, the β model is not consistent with the observed data over $10'$ which the background was subtracted like in figure 6.3 (a). Then we modeled 2β model profile from *Suzaku* in 0.5-10.0 keV. With spectral fitting of $15'.5 - 19'.5$ of background region by fixing 100% CXB intencity by Kushino et al. (2002) we strained intensity of galactic component. After that, we subtracted 100% CXB, GAL, and NXB from observed image. We show the last result of surface brightness profile compared with background intensity in figure6.3 (b) in 0.5-5.0 keV. We show the best-fit parameters in table6.4. Because of Suzaku angular resolution, the peak of the simulated ICM is smoothed in the figure 6.3 (b). The best-fit 2β model is traced the observed profile.

(a): XMM-*Newton* (b): *Suzaku*

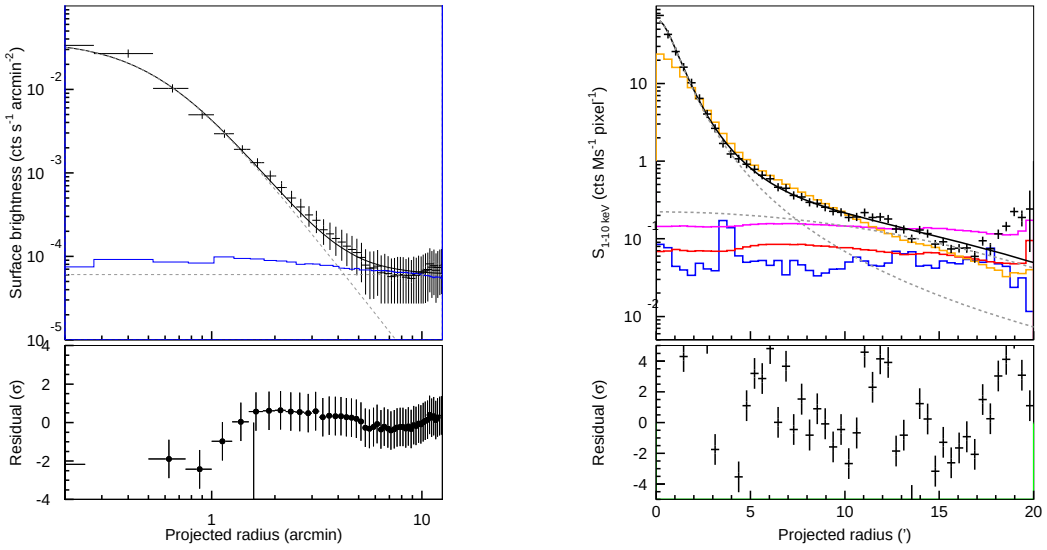

Fig. 6.3: Surface brightness profile of A2204 in 0.5-5.0 keV energy band in Suzaku (a) and *XMM-Newton* in 0.35-1.25 keV (b).

6.2.2 Spectral fitting

We assumed thermal plasma model for ICM as "*phabs* × *apec*" and energy range is in 0.7–10.0 keV that we excluded the contaminated energy by SWCX below 0.7 keV. First, we fitted the model with observed data using background region in $15'.5 - 19'.5$ in which we strain CXB and galactic components with fitting. We also found out CXB intensity as fixing the value subtracted point source flux from 100% CXB by Kushino et al. (2002). Galactic components are LHB and MWH we assumed. Because MWH temperature exists below the lower limits of spectral energy range, 0.7 keV, we fixed it to 0.074 keV (Lumb et al. 2002). When we did not freeze the power law index of CXB, $\Gamma = 1.220^{+0.063}_{-0.055}$ with χ^2/dof = 3921.27 / 3517. But we could not strain temperature error enough. Then we fixed $\Gamma = 1.41$ (Kushino et al. 2002). which value is from the averaged CXB. When we looked into the case excluding substructure which exist in south west of $11'.5 - 15'.5$, we could not detect the significant ICM temperature in $11'.5 - 15'.5$. Reiprich et al. (2009) ordered in this manner.

6.2.3 Results

We show the best-fit parameters and profiles of temperature, abundance, surface brightness, and electron density in table 6.5 and figure 6.4. The temperature in $0' - 3'.5$ region is slight decreasing because of cooling flow mentioned by Sanders et al. (1999). Temperature profile is isothermal-like within r_{200}. Our *Suzaku* observation result is smoothly connected with *XMM-Newton* result by Snowden et al. (2008) in figure 6.4 (a). In the $11'.5 - 15'.5$ region, Reiprich et al. (2009) mentioned here is the "cluster free" region because of outside of r_{200}. We also looked into if there is some cluster component in $11'.5 - 15'.5$. We detected ICM component in $11'.5 - 15'.5$ in figureC.7 though the normalization is lower

than that of CXB in all energy band.

We looked into spectral fitting with abundance model as Anders & Grevesse (1989) and Feldman (1992). We measured about 2 keV higher by Feldman (1992) than that by Anders & Grevesse (1989). Because Feldman (1992) define less Fe amount than Anders & Grevesse (1989), Feldman (1992) leads higher profile than Anders & Grevesse (1989).

6.2.4 Systematic Errors

To strain systematic errors, we found out NXB±5%, CXB fluctuations mentioned before chapter, and contamination of IR/UV blocking filters contamination ± 20%. The best-fit parameters of these results are shown in table 6.6. By NXB fluctuations of -5%, temperature is varied for 6 keV in $11'.5 - 15'.5$. And abundance is varied for 0.2 Z$\odot$ in $11'.5 - 15'.5$. We also found out fluctuation of contamination with 20%. It also affected with measurement of temperature and abundance.

6.3 AWM7

6.3.1 Position Angle

We looked into AWM7 spatial distribution with *XMM-Newton* observation. We are interested in the spatial distribution of surface brightness profile because morphological studies suggest evolutions of clusters of galaxies. AWM7 has the ellipse shape in the center region. Though x-ray image is elliptically elongated east and west in parallel to the filament structure of Pisces-Perseus super cluster with the ratio to minor to major axis of ∼0.8 (Neumann & Boehringer 1995), Past analysis is worked on the isotropic double beta distribution of X-ray photon. We considered elongation from East to West. First we looked into Position angle depending on the radius from emission peak.

With elliptical image in each region, we fitted sine curve surface bright ness model such as

$$S_X(r,\theta) = S_1(r)\cos\left(2\left(\theta+\alpha\right)\right) + S_2(r)\cos\left(\theta+\alpha\right) + \bar{S}(r) \tag{6.1}$$

, in which θ means azimuthal angle. $S_1(r)$ and $S_2(r)$ means normalization. $\bar{S(r)}$ is equal to the mean intensity of surface brightness at r.α is the angle from horizontal axis. Then the position angle is equal to (90 - α) deg because of its definition: the angle from north pole. Because the descrepancy of image, the surface brightness profiles distribute like sine curve. The highest intensity angle means the long axis of elliptical distribution shown as figure 6.5 (a).

We show the best fit paramters of sine curve model in $5' - 10'$ region in table6.7. P.A. $= 85.7 \pm 2.36$ deg. We also looked into the difference of the position angle in each region because if there is merging activity in the past, the outer structure would be in the complex distribution not in elliptical distribution. We fitted the sine curve model of the

Table 6.5: The best fitting parameters of the spectral fits of A2204 with 90% confidence errors for one parameter in 0.7–10.0 keV.

Nominal (a) *	kT (keV)	Abundance ($Z_\odot$)	$Norm$ §	S ‖	χ^2/dof
$0' - 3'.5$	$7.26^{+0.15}_{-0.07}$	$0.41^{+0.02}_{-0.02}$	$911.37^{+5.02}_{-5.50}$	$321.40^{+1.77}_{-1.94}$	1835.6 / 1444
$3'.5 - 7'$	$7.55^{+0.36}_{-0.35}$	$0.35^{+0.06}_{-0.06}$	$36.28^{+0.77}_{-0.75}$	$12.38^{+0.26}_{-0.26}$	1100.9 / 1124
$7' - 11'.5$	$5.94^{+0.74}_{-0.74}$	$0.25^{+0.13}_{-0.13}$	$8.57^{+0.53}_{-0.52}$	$2.74^{+0.17}_{-0.17}$	455.8 / 480
$11'.5 - 15'.5$	$4.32^{+1.54}_{-1.01}$	$0.52^{+0.55}_{-0.46}$	$3.35^{+0.79}_{-0.66}$	$1.11^{+0.26}_{-0.22}$	318.8 / 318
$15'.5 - 19'.5$	—	—	—	—	210.8 /152
Total	—	—	—	—	3921.9 /3518
Nominal (b) †	kT (keV)	Abundance ($Z_\odot$)	$Norm$ §	S ‖	χ^2/dof
$0' - 3'.5$	$7.27^{+0.15}_{-0.07}$	$0.41^{+0.02}_{-0.02}$	$912.03^{+5.00}_{-5.49}$	$321.65^{+1.76}_{-1.93}$	1736.0 / 1444
$3'.5 - 7'$	$7.63^{+0.35}_{-0.34}$	$0.35^{+0.06}_{-0.06}$	$36.68^{+0.65}_{-0.65}$	$12.52^{+0.22}_{-0.22}$	1101.6 / 1124
$7' - 11'.5$	$6.26^{+0.68}_{-0.61}$	$0.24^{+0.13}_{-0.12}$	$9.02^{+0.38}_{-0.38}$	$2.90^{+0.12}_{-0.12}$	456.5 / 480
$11'.5 - 15'.5$	$4.96^{+1.48}_{-0.97}$	$0.52^{+0.51}_{-0.41}$	$3.85^{+0.58}_{-0.53}$	$1.30^{+0.20}_{-0.18}$	318.6 / 318
$15'.5 - 19'.5$	—	—	—	—	211.6 / 153
Total	—	—	—	—	3924.3 / 3519
Nominal (c) ‡	kT (keV)	Abundance ($Z_\odot$)	$Norm$ §	S ‖	χ^2/dof
$0' - 3'.5$	$7.30^{+0.12}_{-0.08}$	$0.61^{+0.03}_{-0.03}$	$885.76^{+5.33}_{-8.09}$	$321.62^{+1.93}_{-2.94}$	1818.4 / 1444
$3'.5 - 7'$	$7.80^{+0.35}_{-0.35}$	$0.52^{+0.09}_{-0.09}$	$35.38^{+0.58}_{-0.71}$	$12.41^{+0.20}_{-0.25}$	1088.2 / 1124
$7' - 11'.5$	$6.90^{+1.01}_{-0.75}$	$0.31^{+0.19}_{-0.18}$	$8.36^{+0.32}_{-0.58}$	$2.77^{+0.11}_{-0.19}$	441.0 / 480
$11'.5 - 15'.5$	$6.49^{+3.02}_{-1.89}$	$0.64^{+0.89}_{-0.61}$	$3.18^{+0.29}_{-0.58}$	$1.13^{+0.10}_{-0.21}$	324.2 / 318
$15'.5 - 19'.5$	—	—	—	—	213.3 /152
Total	—	—	—	—	3885.0 / 3518

* Abundance model is Anders & Grevesse (1989).

† Abundance model is Anders & Grevesse (1989). CXB parameters is fixed with Kushino et al. (2002).

‡ Abundance model is Feldman (1992).

§ Normalization of the apec component scaled with a factor of $SOURCE\_RATIO\_REG/\Omega_e$ in table 5.10,
$Norm = SOURCE\_RATIO\_REG/\Omega_e \int n_e n_H dV \,/\, (4\pi\,(1+z)^2 D_A^2) \times 10^{-20}$ cm^{-5} arcmin^{-2}, where D_A is the angular diameter distance to the source.

‖ Surface brightness in unit of 10^{-6} photons cm^{-2} s^{-1} arcmin^{-2} (0.7–10 keV).

Table 6.6: Same as table 6.5. Abundance model is Anders & Grevesse (1989). Energy band is in 0.7–10.0 keV.

NXB+5%, CXB_{MAX}		kT (keV)	Abundance ($Z_\odot$)	$Norm$ §	S ‖	χ^2/dof
$0' - 3'.5$	.....	$7.22^{+0.15}_{-0.07}$	$0.41^{+0.02}_{-0.02}$	$909.15^{+4.64}_{-4.90}$	$320.14^{+1.63}_{-1.73}$	1832.9 / 1444
$3'.5 - 7'$	.....	$7.17^{+0.38}_{-0.37}$	$0.35^{+0.06}_{-0.06}$	$35.21^{+0.67}_{-0.39}$	$11.93^{+0.23}_{-0.13}$	1100.8 / 1124
$7' - 11'.5$	.....	$4.78^{+0.66}_{-0.58}$	$0.26^{+0.14}_{-0.13}$	$7.77^{+0.43}_{-0.57}$	$2.38^{+0.13}_{-0.18}$	457.1 / 480
$11'.5 - 15'.5$	.....	$1.59^{+0.84}_{-0.47}$	$0.05^{+0.24}_{-0.05}$	$3.56^{+2.84}_{-1.25}$	$0.63^{+0.51}_{-0.22}$	322.8 / 318
$15'.5 - 19'.5$	.....	—	—	—	—	209.0 / 151
Total	.....	—	—	—	—	3922.4 / 3517
NXB−5%, CXB_{MIN}		kT (keV)	Abundance ($Z_\odot$)	$Norm$ §	S ‖	χ^2/dof
$0' - 3'.5$	.....	$7.30^{+0.14}_{-0.07}$	$0.41^{+0.02}_{-0.02}$	$914.34^{+4.69}_{-5.76}$	$322.97^{+1.66}_{-2.04}$	1835.7 / 1444
$3'.5 - 7'$	.....	$7.92^{+0.31}_{-0.33}$	$0.35^{+0.06}_{-0.06}$	$37.67^{+0.60}_{-0.65}$	$12.93^{+0.21}_{-0.22}$	1101.7 / 1124
$7' - 11'.5$	.....	$7.19^{+0.62}_{-0.71}$	$0.25^{+0.12}_{-0.12}$	$9.73^{+0.20}_{-0.36}$	$3.20^{+0.07}_{-0.12}$	456.3 / 480
$11'.5 - 15'.5$	.....	$7.12^{+2.22}_{-1.64}$	$0.58^{+0.43}_{-0.37}$	$4.89^{+0.47}_{-0.54}$	$1.77^{+0.17}_{-0.19}$	321.6 / 318
$15'.5 - 19'.5$	.....	—	—	—	—	222.2 / 151
Total	.....	—	—	—	—	3937.5 / 3517
contami+20%		kT (keV)	Abundance ($Z_\odot$)	$Norm$ §	S ‖	χ^2/dof
$0' - 3'.5$	.....	$7.04^{+0.11}_{-0.09}$	$0.40^{+0.02}_{-0.02}$	$926.20^{+4.39}_{-3.50}$	$325.77^{+1.54}_{-1.23}$	1842.9 / 1444
$3'.5 - 7'$	.....	$7.30^{+0.33}_{-0.33}$	$0.34^{+0.04}_{-0.05}$	$36.89^{+0.60}_{-0.61}$	$12.56^{+0.20}_{-0.21}$	1099.0 / 1124
$7' - 11'.5$	.....	$5.93^{+0.57}_{-0.61}$	$0.24^{+0.09}_{-0.10}$	$8.75^{+0.45}_{-0.48}$	$2.78^{+0.14}_{-0.15}$	453.5 / 480
$11'.5 - 15'.5$	.....	$4.82^{+1.52}_{-0.99}$	$0.52^{+0.36}_{-0.34}$	$3.36^{+0.29}_{-0.53}$	$1.11^{+0.10}_{-0.17}$	322.7 / 318
$15'.5 - 19'.5$	.....	—	—	—	—	212.3 / 151
Total	.....	—	—	—	—	3930.5 / 3517
contami−20%		kT (keV)	Abundance ($Z_\odot$)	$Norm$ §	S ‖	χ^2/dof
$0' - 3'.5$	.....	$7.55^{+0.12}_{-0.09}$	$0.42^{+0.02}_{-0.02}$	$896.19^{+4.75}_{-5.24}$	$317.08^{+1.68}_{-1.85}$	1887.34 / 1444
$3'.5 - 7'$	.....	$7.81^{+0.37}_{-0.36}$	$0.36^{+0.06}_{-0.06}$	$35.67^{+0.77}_{-0.72}$	$12.20^{+0.26}_{-0.25}$	1100.58 / 1124
$7' - 11'.5$	.....	$5.97^{+0.76}_{-0.77}$	$0.26^{+0.13}_{-0.13}$	$8.42^{+0.60}_{-0.62}$	$2.70^{+0.19}_{-0.20}$	453.02 / 480
$11'.5 - 15'.5$	.....	$3.97^{+1.29}_{-1.29}$	$0.52^{+0.59}_{-0.43}$	$3.38^{+0.75}_{-0.76}$	$1.12^{+0.25}_{-0.25}$	324.42 / 318
$15'.5 - 19'.5$	.....	—	—	—	—	221.12 / 151
Total	.....	—	—	—	—	3986.48 / 3517

* Normalization of the apec component scaled with a factor of $SOURCE\_RATIO\_REG/\Omega_e$ in table 5.10,
$Norm = SOURCE\_RATIO\_REG/\Omega_e \int n_e n_H dV \,/\, (4\pi\,(1+z)^2 D_A^2) \times 10^{-20}$ cm^{-5} arcmin^{-2}, where D_A is the angular diameter distance to the source.

† Surface brightness in unit of 10^{-6} photons cm^{-2} s^{-1} arcmin^{-2} (0.7–10 keV).

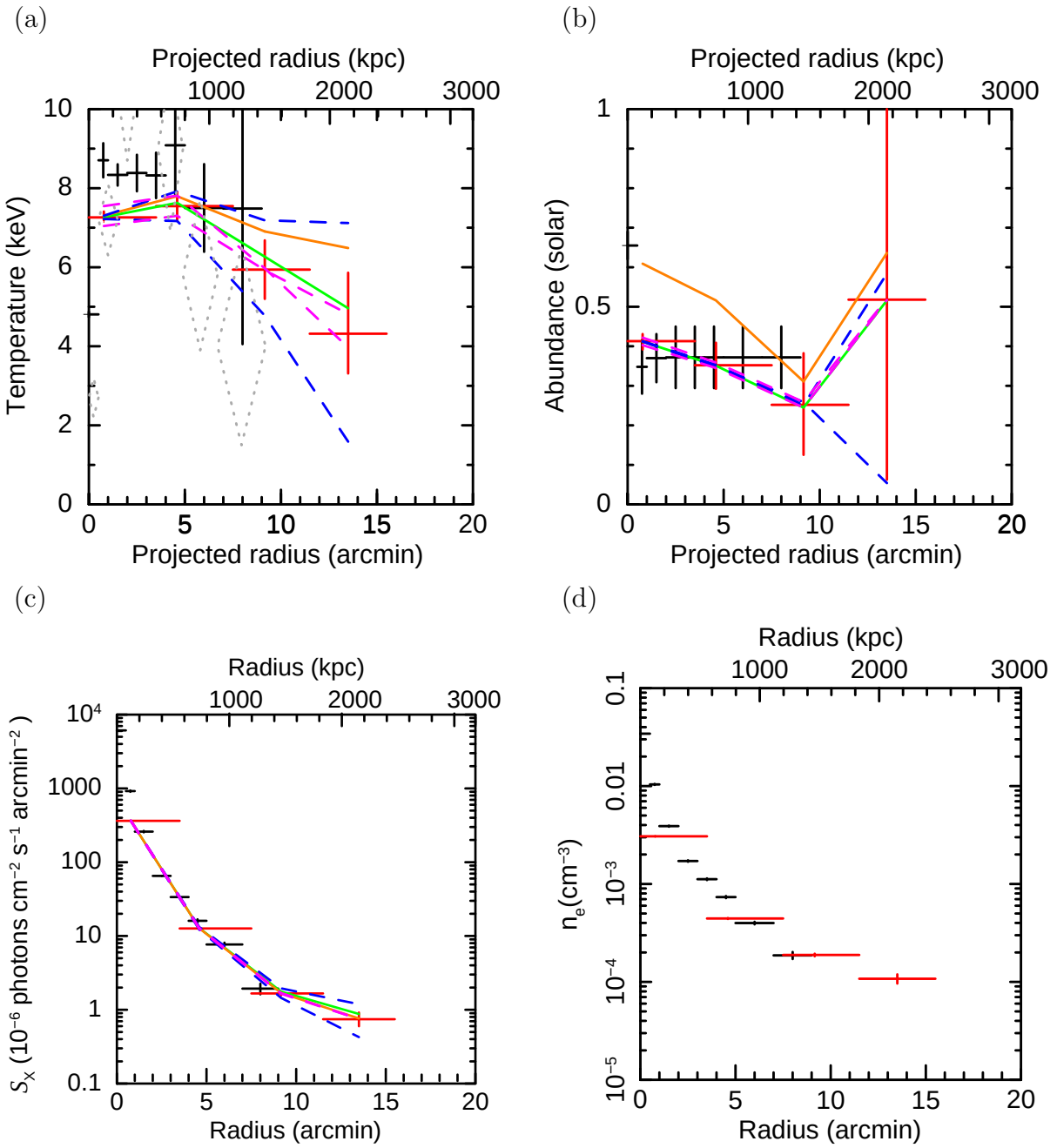

Fig. 6.4: Radial profiles in FI:0.5-10.0 keV and BI:0.5-10.0 keV for (a) temperature, (b) surface brightness, (c) abundance, and (d) electron density. Red diamonds show our Suzaku results assuming the metal abundances of Anders & Grevesse (1989). Orange line indicates the best-fit profile using the Feldman (1992) abundances. Chandra results by Vikhlinin et al. (2005) are the black crosses, and the cyan crosses are the *XMM-Newton* results by Snowden et al. (2008). The uncertainty range due to the combined ±5% variation of the NXB level and the maximum/minimum fluctuation of CXB is shown by two blue dashed lines. We show by magenta dashed lines the uncertainties induced by a ±20% uncertainty in the amount of contamination in the IR/UV blocking filters. We also show in panel (b) the CXB level (horizontal dashed line) and the Galactic emission (horizontal solid line).

equation 6.1 in each $1'$ width region from $1'$ to $14'$, total 16 regions in the table 6.8. We show the position angle profile in figure D.1 in the Appendix D. Averaged position angle is 91.1± 2.0 deg. The profiles of $S1(r)$ and $S2(r)$ changes at 6' 6.5(c).

Table 6.7: The best fit parameters of double cosin function in $5' - 10'$.

α [deg]	4.34 ± 2.36
S_1^*	31.49 ± 2.78
S_2^*	-22.13 ± 2.94
B^*	116.06 ± 1.97
χ^2 / dof	12.88 / 27.00

* Surface brightness in unit of counts Msec^{-1} pix^{-1}.(0.5–10 keV). In the unit size of image pixel is equal to 0.066 deg.

Table 6.8: The best fit parameters of double cosine function in each region.

Region	α [deg]	S_1^*	S_2^*	$\bar{S}^*$	χ^2 / dof	P.A. [deg]
$1'.46^{+0.54}_{-0.46}$	7.67 ± 4.22	32.24 ± 5.26	14.64 ± 5.97	295.05 ± 30.34	16.0/21	82.33 ± 4.22
$2'.47^{+0.53}_{-0.47}$	4.31 ± 3.01	35.03 ± 3.64	-5.67 ± 3.87	197.50 ± 27.65	21.1/27	85.67 ± 3.01
$3'.47^{+0.53}_{-0.47}$	1.84 ± 3.51	24.12 ± 3.10	-17.89 ± 3.23	140.94 ± 22.08	15.0/27	88.16 ± 3.51
$4'.48^{+0.52}_{-0.48}$	-0.37 ± 3.32	21.69 ± 2.67	-18.58 ± 2.82	106.64 ± 20.15	11.5/27	90.37 ± 3.32
$5'.47^{+0.53}_{-0.47}$	-2.05 ± 5.18	14.3 ± 2.48	-7.93 ± 2.89	71.73 ± 12.92	20.5/21	92.05 ± 5.17
$6'.48^{+0.52}_{-0.48}$	2.57 ± 8.43	7.99 ± 2.29	-4.67 ± 2.70	57.44 ± 8.53	17.3/21	87.43 ± 8.43
$7'.48^{+0.52}_{-0.48}$	-3.03 ± 7.42	8.43 ± 2.07	-1.00 ± 2.44	49.52 ± 8.85	17.3/21	93.03 ± 7.42
$8'.48^{+0.52}_{-0.48}$	4.59 ± 4.01	11.70 ± 1.70	-6.79 ± 1.82	42.95 ± 9.73	9.4/21	85.41 ± 4.01
$9'.49^{+0.51}_{-0.49}$	-2.11 ± 7.02	7.13 ± 1.69	-2.39 ± 1.94	33.30 ± 6.18	9.4/21	92.11 ± 7.02
$10'.48^{+0.52}_{-0.48}$	-2.14 ± 8.39	5.57 ± 1.59	-1.59 ± 1.82	29.26 ± 5.67	10.1/21	92.14 ± 8.39
$11'.48^{+0.52}_{-0.48}$	-6.50 ± 7.11	6.06 ± 1.41	-1.50 ± 1.65	23.92 ± 5.37	10.1/21	96.50 ± 7.11
$12'.47^{+0.53}_{-0.47}$	-6.51 ± 6.84	5.32 ± 1.22	-0.11 ± 1.44	18.38 ± 4.79	10.7/21	96.51 ± 6.84
$13'.46^{+0.54}_{-0.46}$	75.71 ± 30.62	0.50 ± 1.07	2.00 ± 0.91	9.23 ± 5.33	68.4/21	14.28 ± 30.62

* Surface brightness in unit of counts Msec^{-1} pix^{-1}.(0.5–10 keV). In the unit size of image pixel is equal to 0.066 deg.

6.3.2 Surface Brightness

To look into the difference of profiles in the long and short axis, we compared the surface brightness profile along to each axis with position angle of 85.7 deg. We extracted "fan-shaped" region of each 10 deg along to long and short axis from center of surface brightness

(b): The best fit position angle profile in $5' - 10'$.

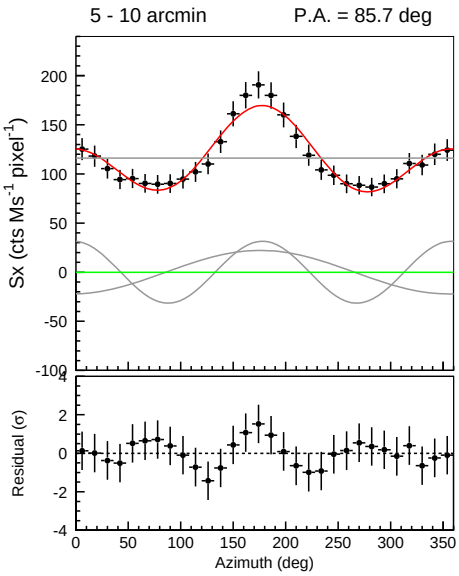

(a): Position angle for each region

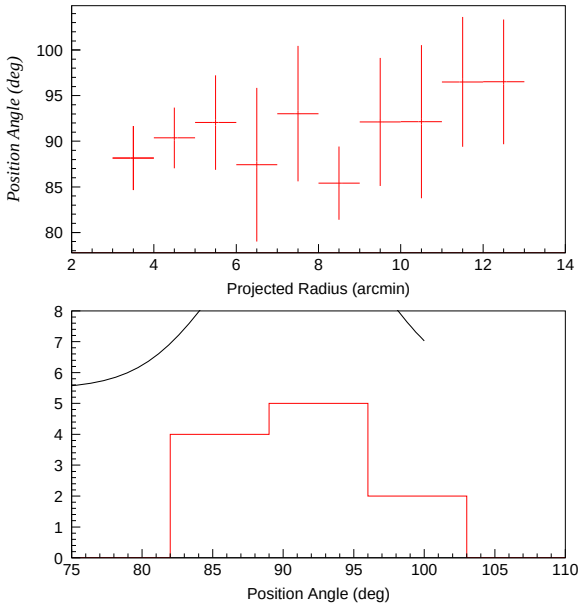

(c): $S1(r)$ and $S2(r)$ profiles

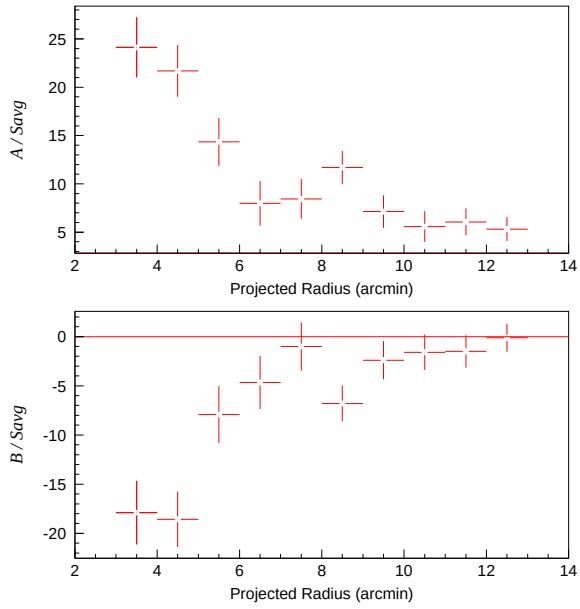

Fig. 6.5:

peak to 15' for each direction within 0.35-1.25 keV energy band shown as figure4.3 (c). Then for each axis, there are two extracted regions. We compared surface brightness profiles with 2β model,

$$S_X(r) = S_1 \left(1 + \left(\frac{r}{r_{c1}}\right)^2\right)^{-3\beta_1+0.5} + S_2 \left(1 + \left(\frac{r}{r_{c2}})^2\right)\right)^{-3\beta_2+0.5} + B \tag{6.2}$$

, in which S_1 and S_2 is the normalization of each β model. r is radius from the surface brightness peak. r_{c1} and r_{c2} is the core radius. $\beta 1$ and $\beta 2$ strains gradient of this profile. B is assumed background level. We looked into the difference of profile between north and south. In fugure6.6 (b), we show the surface brightness profile along to the short axis, the direction from north to south. The profile is consistent with each other in this axis. However the long axis profile of figure 6.6 (a) profiles which is the direction from east to west, have turburance in the outer region in 5'-15'. It makes affect with the best fit parameters, r_{c1} of 2β model profile in table 6.9. Finally we found out vertical, horizontal, and global profile in figure 6.6 (c). Because horizontal profile is elongate to outer region, the difference of profiles are clear over $10'$ region.

(a): East, West, and horizontal directions

(b): North, South, and vertical directions

(d): Horizontal, vertical and global directions

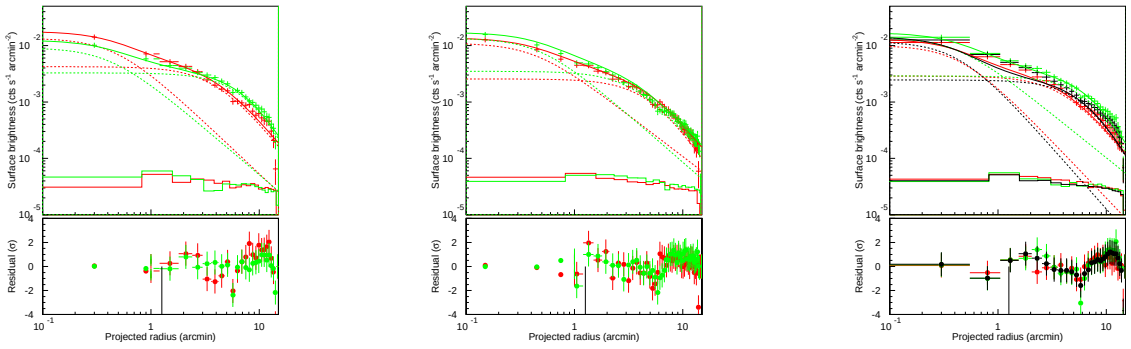

Fig. 6.6: Surface brightness profiles of AWM7. (a) East (red) and west (green) directions, (b) North (red) and south (green) directions, and (c) horizontal (red), vertical (green), and global (black) directions.

2 dimensional β egg model profile

Looking into the surface brightness profile of AWM7, we modeled the new type profile modifying 2β model. As shown in the former section, we considered anti-symmetric and elliptical profiles for each annulus with double cosine function. This double cosine function means the averaged surface brihtness value at r and it fluctuation because of elliptical shape of clusters. We applied this double cosine function to the 2β profile as the following equation,

$$S_(r) \quad = \quad S(r)R\,(1 + Acos(2(\theta + \alpha)) + Bcos(\theta + \alpha)) \tag{6.3}$$

Table 6.9: The best fit parameters of 2β model

Axis	S_0^*	β_1	r_{c1}	S_2^*	β_1	r_{c2}	χ^2 / dof
	10^{-2}couts/s/arcmin^{-2}		arcmin	10^{-2}couts/s/arcmin^{-2}		arcmin	
West	$0.42^{+0.17}_{-0.13}$	$0.57^{+0.15}_{-0.06}$	$4.11^{+1.95}_{-1.00}$	$1.14^{+0.39}_{-0.24}$	$0.47^{0.33}_{-0.19}$	$0.47^{-0.33}_{-0.20}$	52.7 / 20
East	$0.32^{+0.09}_{-0.08}$	$0.82^{+1.08}_{-0.33}$	$8.73^{+7.65}_{-2.47}$	$0.92^{+0.30}_{-0.18}$	$0.44^{0.42}_{-0.20}$	$0.42^{-0.36}_{-0.07}$	14.9 / 20
North	$0.26^{+0.07}_{-0.06}$	$0.66^{+0.25}_{-0.09}$	$5.28^{+2.24}_{-1.19}$	$1.11^{+0.08}_{-0.09}$	$0.41^{+0.09}_{-0.06}$	$0.43^{+0.09}_{-0.04}$	36.6 / 45
South	$0.35^{+0.01}_{-0.08}$	$0.55^{+0.08}_{-0.04}$	$3.69^{+0.92}_{-0.76}$	$1.36^{+0.11}_{-0.16}$	$0.45^{+0.21}_{-0.08}$	$0.49^{+0.30}_{-0.07}$	61.6 / 45
Horizontal	$0.28^{+0.13}_{-0.10}$	$0.58^{+0.22}_{-0.07}$	$4.28^{+2.29}_{-1.13}$	$1.02^{+0.12}_{-0.16}$	$0.50^{0.23}_{-0.14}$	$0.45^{-0.26}_{-0.06}$	17.0 / 25
Vertical	$0.29^{+0.08}_{-0.07}$	$0.99^{+1.98}_{-0.28}$	$9.47^{+11.51}_{-2.93}$	$1.40^{+0.14}_{-0.12}$	$0.43^{+0.10}_{-8.99}$	$0.42^{+0.07}_{-0.04}$	50.1 / 25
Global	$0.25^{+0.09}_{-0.07}$	$0.81^{+1.17}_{-0.19}$	$7.45^{+8.34}_{-2.38}$	$1.18^{+0.10}_{-0.11}$	$0.53^{+0.12}_{-0.11}$	$0.44^{+0.09}_{-0.04}$	29.0 / 25

* Surface brightness in unit of counts Msec^{-1} pix^{-1}.(0.5–10 keV). In the unit size of image pixel is equal to 0.066 deg.

Table 6.10: The best fit parameters of 2β model

Axis	S_0^* 10^{-2}couts/s/arcmin^{-2}	β_1	r_{c1} arcmin	S_2^* 10^{-2}couts/s/arcmin^{-2}	β_1	r_{c2} arcmin	χ^2 / dof
Horizontal	$1.74 \pm 0.02 \times 10^{-3}$	0.55 ± 0.01	4.05 ± 0.41	$2.77 \pm 0.35 \times 10^{-3}$	1.10 ± 0.59	0.88 ± 0.64	0.49 / 195
Vertical	$1.17 \pm 0.36 \times 10^{-3}$	0.55 ± 0.02	4.08 ± 0.79	$1.98 \pm 0.49 \times 10^{-3}$	0.98 ± 0.97	0.79 ± 1.07	0.35 / 195
Global	$1.38 \pm 0.40 \times 10^{-3}$	0.55 ± 0.01	4.17 ± 0.66	$3.13 \pm 0.59 \times 10^{-3}$	0.79 ± 0.54	0.67 ± 0.54	0.38 / 195

* Surface brightness in unit of counts Msec^{-1} pix^{-1}.(0.5–10 keV). In the unit size of image pixel is equal to 0.066 deg.

, in which we utilized the best-fit patameters by Sato et al. (2008) for $S(r)$ of 2β profile. We show the rest of the best-fit parameters of the equation 6.3 in table6.11. To the 2β egg model image, we fitted the 2β model. We show the best fit parameters in table 6.10. However, it is difficult to recognize the difference between vertical and horizontal direction.

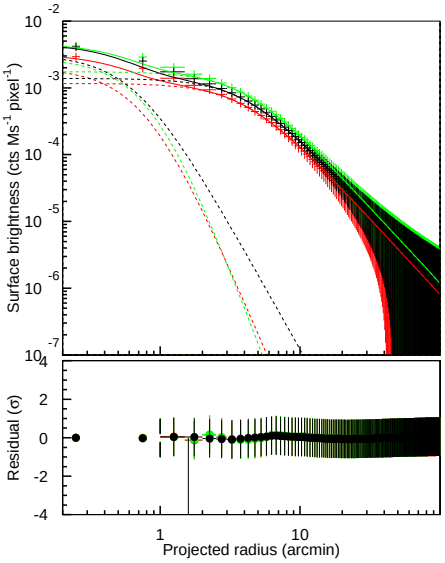

Fig. 6.7: The best-fit surface brightness profiles of 2β egg model (red:vertical, green:horizontal, and black:global)

Table 6.11: The best fit parameters of 2dimensional β egg model.

R	84.961 ± 0.51
α [deg]	3.296 ± 0.513
A [counts s^{-1} arcmin^{-2}]	0.183 ± 0.082
B [counts s^{-1} arcmin^{-2}]	-0.078 ± 0.008
χ^2 / dof	306.2 / 308

* Surface brightness in unit of counts Msec^{-1} pix^{-1}.(0.5–10 keV). In the unit size of image pixel is equal to 0.066 deg.

6.3.3 Spectral analysis

To comparing direction effect of AWM7, we observed two pointing of east and south offset of AWM7 with *Suzaku*. These FOVs are range from 50.0 arcmin to 71.5 arcmin if we assume spherical shape for this cluster morphology. As we mensioned in the former section, AWM7 has a elliptical shape. Then we assumed 2dimensional egg model profile

as a cluster image for the cluster response simulations with"*xissimarfgen*". We excluded detected point sources described in the former chaper with 60" radius circle. Then we excluded four in east and six in south. CXB background is fixed with the value in the table5.7 for each region which each value is subtracted from 100% CXB Kushino et al. (2002) by total point source flux in each region. NXB background is estimated by night earth spectra with *xisnxbgen*. We assumed gaalactic components as LHB and MWH components by *apec+wabs*×*apec* thermal plasma model.

We assumed absorbed thermal plasma model of "*wabs*× *apec*" for the ICM component. We fixed N_H value at the values in table 4.1. The energy range used in the fit was FI:0.5-10.0 keV and BI:0.4-10.0 keV respectively. There was no energy interval excluded from the fit.

6.3.4 Results

We show the best-fit paramters of spectral fitting in table 6.12. The errors indicate 90% confidence limits for single parameters. In this table, we found out systematic errors to the nominal value of 2T-III (a) which means the fit results with nominal background intensities. When NXB is varied to the limit of systematic error, ±5%, temperature varidities is the range of about ±0.8 keV from the nominal value. When CXB is varied to the limit of systematic erros, temperature varied about 0.5 keV.

We show the best fit spectra and model in east and south region in figure 6.9. Red and black plots are FI and BI spectra subtracted NXB. The oranges line indicate ICM component. purple lines are CXB. Grey and light blue lines are MWH and LHB components. We also show comparison of subtracted NXB spectra with NXB and CXB in figure C.10. ICM components are weaker than CXB in all energy range. The surface brightness of the ICM emission is $F_x = 9.40 \times 10^{-9}$erg cm^{-2} s^{-1} sr^{-1}in 2.0-10.0 keV, which is 14% of the CXB level in this energy band in east offset. Interestingly, the nominal temperature in offset east is higher than that in offset south, though these FOV is located in the same distance from the brightness peak of AWM7.

When we correct effects of stray light from near sky region to FOV by simulated spectra with *xissim*, south components are explained to background only because galactic flux is about twice higher than nominal value. When we fixed galactic value to 2T-III(a) to the nominal, the ICM temperature in the south is $0.27^{+0.03}_{-0.03}$ keV. East components has 2.5 keV which is higher than uncorrected temperature with lower normalization.

We show temperature profiles of AWM7 with our results and Sato et al. (2008) in figure6.10. Temperatures are significantly different value in east and south.

Table 6.12: The best fitting parameters of the spectral fits with 90% confidence errors for one parameter. Energy band is in FI:0.5-10.0 keV and BI:0.4-10.0 keV.

Nominal (a) *		kT (keV)	Abundance ($Z_\odot$)	$Norm$ §	S ‖	χ^2/dof
Offset east						
2T-III (a) *	.....	$1.62^{+0.62}_{-0.37}$	$0.07^{+0.17}_{-0.06}$	$23.73^{+5.63}_{-5.93}$	$6.01^{+1.43}_{-1.50}$	319.2 / 302
2T-III (b) †	.....	$1.69^{+0.74}_{-0.35}$	$0.10^{+0.28}_{-0.09}$	$22.49^{+6.13}_{-5.85}$	$6.15^{+1.68}_{-1.60}$	318.7 / 303
2T-III (c) ‡	.....	$2.53^{+3.88}_{-1.50}$	$0.14^{+1.00}_{-0.14}$	$8.30^{+7.31}_{-3.41}$	$2.55^{+2.24}_{-1.05}$	329.1 / 302
contami−20%	.....	$3.31^{+1.05}_{-0.78}$	$0.20^{+0.39}_{-0.20}$	$22.10^{+3.43}_{-3.78}$	$7.89^{+1.22}_{-1.35}$	324.5 / 302
contami+20%	.....	$1.62^{+0.58}_{-0.34}$	$0.07^{+0.16}_{-0.06}$	$25.21^{+8.08}_{-6.21}$	$6.66^{+2.13}_{-1.64}$	316.5 / 302
CXB_{min}	.....	$2.08^{+0.93}_{-0.43}$	$0.11^{+0.27}_{-0.09}$	$24.20^{+4.92}_{-5.33}$	$6.90^{+1.40}_{-1.52}$	320.5 / 303
CXB_{max}	.....	$1.31^{+0.50}_{-0.32}$	$0.04^{+0.13}_{-0.04}$	$25.18^{+10.02}_{-8.13}$	$5.85^{+2.33}_{-1.89}$	318.7 / 302
NXB−5%	.....	$2.89^{+1.08}_{-1.07}$	$0.27^{+0.47}_{-0.24}$	$18.43^{+6.23}_{-3.77}$	$6.58^{+2.22}_{-1.35}$	336.0 / 302
NXB+5%	.....	$1.30^{+0.40}_{-0.31}$	$0.04^{+0.10}_{-0.04}$	$27.55^{+8.29}_{-6.69}$	$6.25^{+1.88}_{-1.52}$	343.2 / 302
CXB_{min},NXB−5%	.....	$3.68^{+1.16}_{-1.03}$	$0.36^{+0.53}_{-0.31}$	$19.32^{+4.12}_{-3.34}$	$7.46^{+1.59}_{-1.29}$	336.7 / 302
CXB_{max},NXB+5%	.....	$1.06^{+0.43}_{-0.39}$	$0.03^{+0.09}_{-0.02}$	$30.20^{+30.40}_{-11.63}$	$5.86^{+5.90}_{-2.26}$	349.3 / 302
Offset south						
2T-III (a) *	.....	$0.45^{+0.13}_{-0.06}$	$0.01^{+0.01}_{-0.01}$	$119.64^{+65.03}_{-49.42}$	$9.07^{+4.93}_{-3.75}$	391.1 / 302
2T-III (b) †	.....	$0.45^{+0.09}_{-0.06}$	$0.01^{+0.01}_{-0.01}$	$119.26^{+65.65}_{-32.27}$	$9.20^{+5.06}_{-2.49}$	391.0 / 302
2T-III (c) ‡	.....	$0.27^{+0.03}_{-0.03}$	$0.01^{+0.02}_{-0.01}$	$167.43^{+88.16}_{-70.08}$	$5.86^{+3.09}_{-2.45}$	418.9 / 305
contami−20%	.....	$0.47^{+0.13}_{-0.07}$	$0.01^{+0.01}_{-0.01}$	$100.58^{+46.43}_{-39.63}$	$8.01^{+3.70}_{-3.16}$	388.5 / 302
contami+20%	.....	$0.44^{+0.11}_{-0.06}$	$0.01^{+0.01}_{-0.01}$	$143.22^{+92.99}_{-33.06}$	$10.17^{+6.60}_{-2.35}$	395.6 / 302
CXB_{min}	.....	$0.64^{+0.27}_{-0.15}$	$0.00^{+0.01}_{0.00}$	$70.34^{+50.23}_{-27.33}$	$7.80^{+5.57}_{-3.03}$	382.0 / 302
CXB_{max}	.....	$0.38^{+0.07}_{-0.04}$	$0.01^{+0.01}_{-0.01}$	$154.77^{+55.74}_{-58.04}$	$9.13^{+3.29}_{-3.42}$	414.1 / 302
NXB−5%	.....	$0.48^{+0.23}_{-0.07}$	$0.01^{+0.01}_{-0.01}$	$107.32^{+48.16}_{-59.19}$	$9.03^{+4.05}_{-4.98}$	365.4 / 302
NXB+5%	.....	$0.42^{+0.06}_{-0.06}$	$0.01^{+0.01}_{-0.01}$	$135.19^{+69.26}_{-44.42}$	$9.10^{+4.66}_{-2.99}$	497.6 / 302
CXB_{min},NXB−5%	.....	$1.13^{+0.41}_{-0.51}$	$0.01^{+0.05}_{-0.01}$	$31.39^{+44.35}_{-9.47}$	$6.45^{+9.12}_{-1.95}$	369.2 / 302
CXB_{max},NXB+5%	.....	$0.37^{+0.07}_{-0.04}$	$0.01^{+0.01}_{-0.01}$	$169.54^{+87.75}_{-66.68}$	$9.05^{+4.68}_{-3.56}$	540.0 / 302

* Abundance model is Anders & Grevesse (1989).

‡ Abundance model is Feldman (1992).

‡ Subtracting simulated stray light photon from raw spectra.

§ Normalization of the apec component scaled with a factor of $SOURCE\_RATIO\_REG/\Omega_e$ in table 5.10,
$Norm = SOURCE\_RATIO\_REG/\Omega_e \int n_e n_H dV \,/\, (4\pi\,(1+z)^2 D_A^2) \times 10^{-20}$ cm^{-5} arcmin^{-2}, where D_A is the angular diameter distance to the source.

‖ Surface brightness in unit of 10^{-6} photons cm^{-2} s^{-1} arcmin^{-2} (0.5–10 keV).

(a) FI+BI, East (b) FI+BI, South

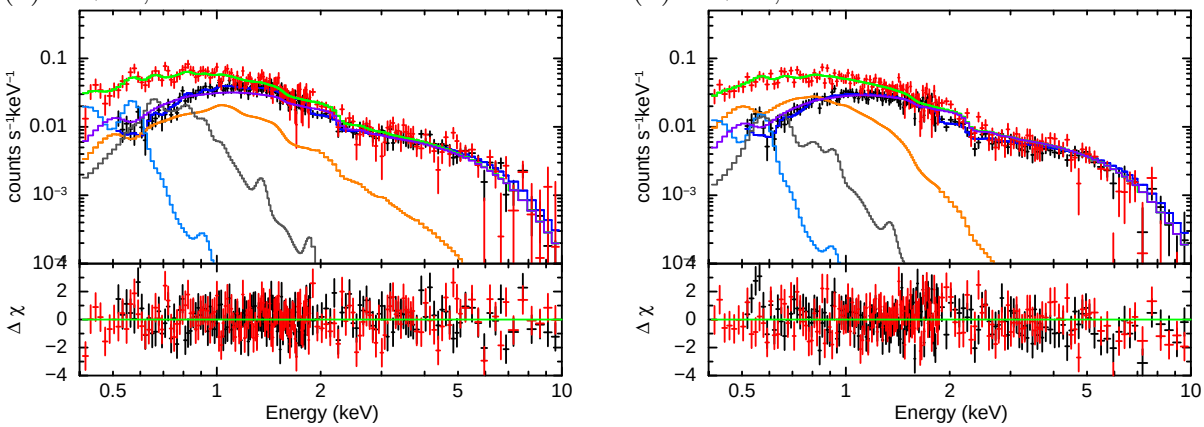

Fig. 6.8: The best-fit model and FTI+BI spectra of AWM7. The definition of colors are same as C.2.

(a) FI+BI, East (b) FI+BI, South

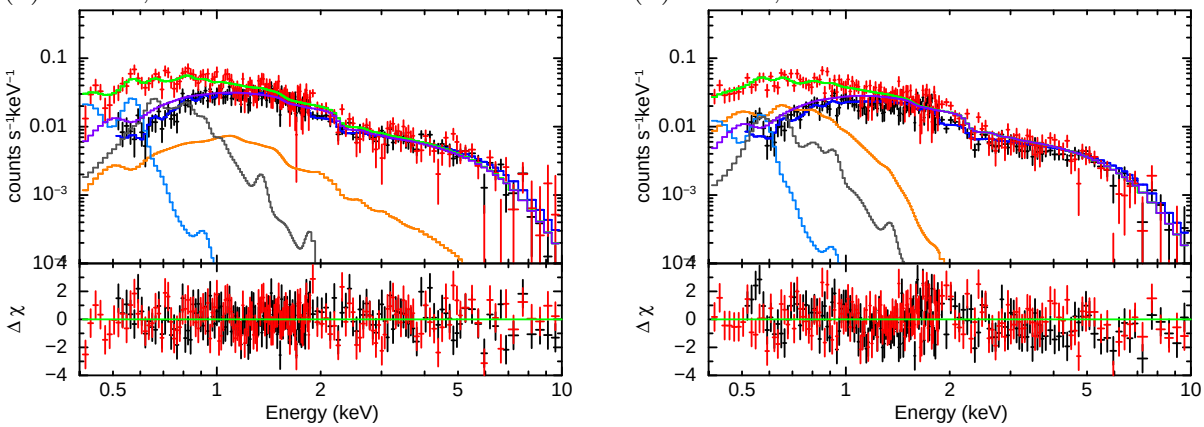

Fig. 6.9: The best-fit model and FTI+BI spectra corrected stray light of AWM7 . The definition of colors are same as C.2.

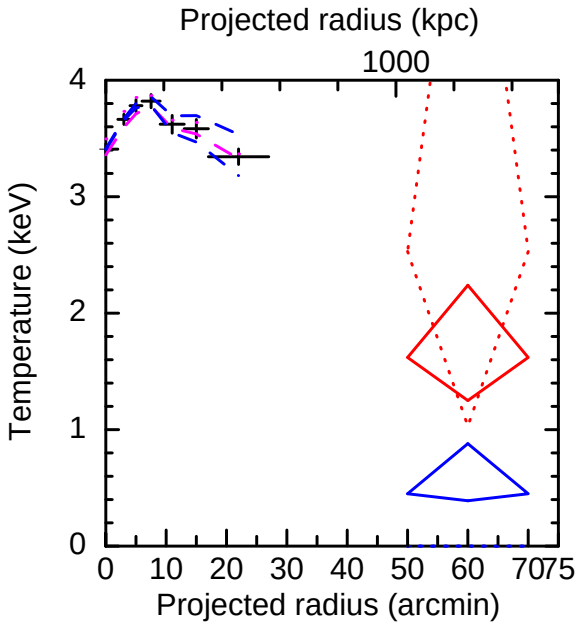

Fig. 6.10: Radial profiles in FI:0.5-10.0 keV and BI:0.4-10.0 keV of temperature. Red diamonds show nominal 2T-III (a) and corrected 2T-III (c) results *Suzaku* offset east and blue diamond shows *Suzaku* offset south results assuming the metal abundances of Anders & Grevesse (1989). Other results are Sato et al. (2008) with *Suzaku*.

Chapter 7

Discussion

Based on the observaed results shown in the previous chapter, we will look into the physical properties of ICM in the outermost region of clusters, including possible deviation from thermal equilibrium.

7.1 Temperature and brightness profiles

Numerical simulations indicate that the intracluster gas is almost in hydrostatic equilibrium within the virial radius. For example, Roncarelli et al. (2006) showed that the radial density profiles are smooth out to $\sim 2r_{200}$, while the electron temperature profile has a discontinuity around 1.3–1.5 r_{200}. Eke et al. (1998) performed hydrodynamic simulations in a ΛCDM universe, and discussed the possibility of nonequilibrium around r_{100} because the ratio of kinetic to thermal energy gradually increased from the center to this radius.

Recent X-ray studies of the outer regions of clusters of galaxies with Chandra and XMM-Newton showed significant negative temperature gradients out to a typical radius of r_{500} which is about half of r_{200} (Vikhlinin et al. 2006; Pratt & Arnaud 2002; Snowden et al. 2008). Even though the errors are large, it is significant that our temperatures continue this steady decline, going from about 7.5 keV near the center of A1413 to ~ 3.5 keV at r_{200}. Recent Suzaku results for the A2204 (Reiprich et al. 2009), PKS0745−191 (George et al. 2008), and A1795 (Bautz et al. 2009) clusters also show a temperature drop to 2–3 keV at r_{200}. The similar temperatures at r_{200} are at least partly due to the fact that all these clusters have similar average temperatures of 5–7 keV. What is likely more significant is the factor of ~ 2 decrease in all cases. We show the temperature profiles normalized by mean temperatures in figure 7.1. Temperature profiles of A1413 and A2204 are measured up to r_{200}.

We attempted to compare our measured temperature and surface brightness profiles with theoretical predictions for relaxed clusters. Suto et al. (1998) gave ICM properties for clusters whose potentials follow NFW (Navarro et al. 1996) and modified NFW models, assuming that the ICM can be described by a polytrope. These models have 6 parameters and give a wide range of temperature and density distributions with radius.

We found that, although we could fit either one of the temperature or surface bright-

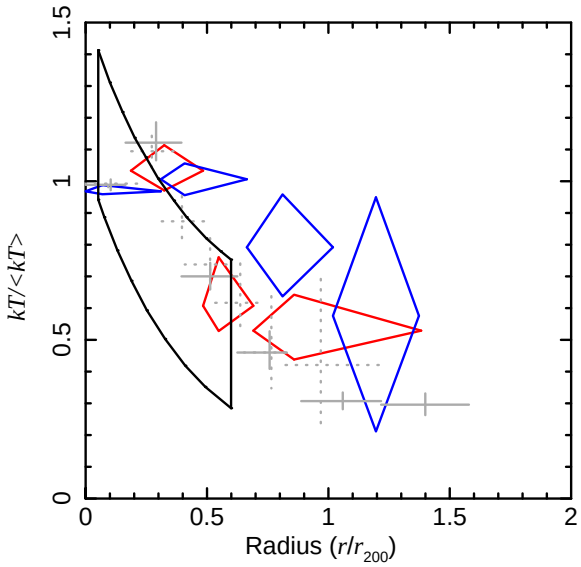

Fig. 7.1: Averaged temperature profiles observed with *Suzaku*. A1413(red), A2204(blue), A1795(grey dotted cross), and PKS0745-191 (grey solid cross).

ness profile with the model, it was not possible to fit both profiles simultaneously despite an exhaustive search of the 6-parameter space. When we fixed the scale radius to be $r_s = 350$ kpc and jointly fit the temperature and brightness profiles of A1413, we obtained reduced χ^2 values of 2.0 using only the Chandra data and 3.7 for combined Chandra and Suzaku data, respectively. The likely reason for this result is that the ICM is out of equilibrium in the outer regions of the cluster. We examine this hypothesis in the next section using the entropy profile. We described this topic in the chapter 8.

7.2 Entropy profile

Entropy carries information about the thermal history of the ICM, which is thought to be heated by accretion shocks outside the virial radius. The central regions of clusters often exhibit complicated physical phenomena, such as AGN heating and cooling flows, therefore it is difficult to trace the long-term evolution of clusters there. In contrast, the outer regions of clusters are where signatures of the structure formation history can be more clearly seen with the entropy profiles. We use the customary X-ray astronomy definition of entropy as

$$S = kTn_e^{-2/3}. \tag{7.1}$$

We show the entropy profiles for A1413 and A2204 derived from our data in figure 7.2(a) and figure 7.3(a). The compared entropy profiles with other objects are also shown in figure7.7(a) and (b). To compare the observed profile with simulation results, we fit the *XMM-Newton* data from $0'.5$ to $7'$ and the *Suzaku* data from $7'$ to $20'$ with a power-law model, given by $S \propto r^{\gamma}$. For A1413, the *XMM-Newton* data outside of $7'$ have poorer

quality than the *Suzaku* data, and one *Suzaku* point inside of $7'$ was also excluded because it is near the field edge with rather low data quality.

We found the best-fit power-law indexes to be 0.90 ± 0.10 in $2'$ to $7'$ and 0.97 ± 0.45 in $7'$ to $20'$ for A1413. The dividing radius of $7'$ corresponds to $0.47\ r_{200}$. If we fit all the 7 data points from $2'$ to $20'$, then the slope becomes 0.90 ± 0.12. These results indicate that there is no difference in the entropy slopes between the inner and outer regions.

In the case of A2204, we fit the *XMM-Newton* data from $1'.0 - 9'.0$ and the *Suzaku* data from $3'.5 - 15'.5$ with the same model as A1413. we found the best-fit power-law indices to be 1.03 ± 0.06 in $1'.0 - 9'.0$. and 0.45 ± 0.27 in $3'.5 - 15'.5$. We found the tendency of a flattening profile clearly in A2204 in figure 7.3 (a). We also show the result of Basu et al. (2009) which is measured with APEX-SZ. Their result is also flattening profile in the outer region.

Voit (2005) reported $S \propto r^{1.1}$ based on numerical simulations of adiabatic cool gas accretion, and our observational result shows a significantly flatter slope, at least for $r < 7'$. This feature is similar but less pronounced for those reported for A1795 (Bautz et al. 2009) in which the power-law index flattened ($\gamma \approx 0.74$) for $r > 4' \sim 0.15\ r_{200}$. For PKS0745−191, George et al. (2008) also found a flatter entropy profile in the outer regions. Our result for A1413 and A2204 suggest that the entropy profile starts to flatten from $\sim 0.5\ r_{200}$. We show entropy profiles of A1795, PKS0795-191, and A1689 in figure 7.5 (a), figure 7.4 (a), and figure 7.6. These entropy profiles change slope around 1Mpc or $0.5\ r_{200}$. We show the power-law index of each object in table 7.1.

To compare the entropy profiles with the simulated slope of 1.1, we divided the entropy by $S \propto r^{1.1}$ as shown in figure 7.7(b). There appears to be a deviation from the numerical simulation in the range of $r > 0.2\ r_{200}$, indicating the flattening of the entropy profiles. We note that the flattening is common to three clusters.

We then compared our result with a hydrodynamical simulation by Takizawa (1998) that allowed for different electron and ion temperatures. We fit a β-model density profile (parameters n_0, r_c, β) and a polytrope electron temperature profile (parameter polytrope index $\gamma_{\rm p}$) using the simulated data in his tables 1 and 2. The resulting entropy profile shows a slope of $\gamma_{\rm p} = 0.42$ in the outer regions for the case of flat universe with $(\Omega_0, \Lambda_0) = (0.2, 0.8)$. Even though this result might be an extreme case, it shows that a difference in the electron and ion temperatures can cause a flattening of the entropy profile. A2204 is almost consistent with Takizawa (1998). Then we considered that it is suggestive result for our discussion.

7.3 Equilibration timescale

Ions carry most of the kinetic energy in the cluster outskirts, and they will be thermalized fairly quickly after accretion shocks or mergers. However, heating of the electrons takes a long time because of the inefficient energy transfer between ions and electrons; the equilibration time for electron-ion collisions ($t_{\rm ei}$) is about 2000 times longer than electron-

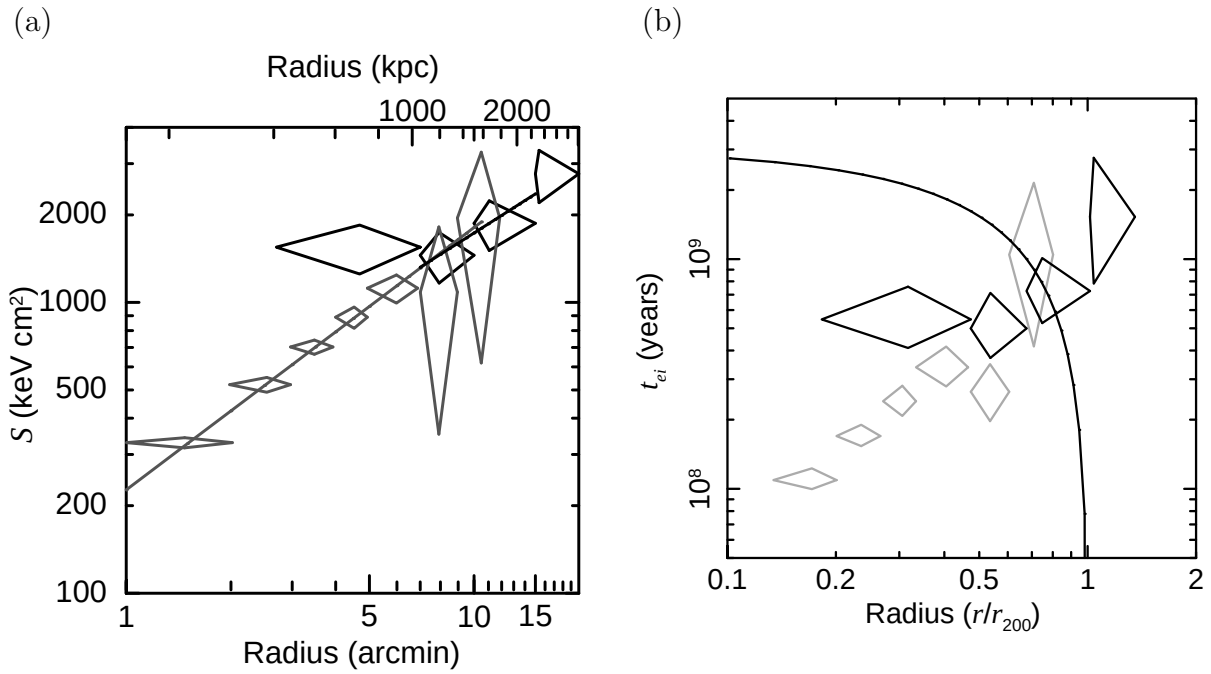

Fig. 7.2: (a) Entropy profile (black diamond: *Suzaku*, grey diamond: *XMM-Newton*, black solid line: fitted model to Suzaku in $7' - 20'$, grey solid line: fitted model to *XMM-Newton* in $0'.5 - 7'$). (b): $t_{\rm ei}$ profile (black diamonds: *Suzaku* and grey diamonds: *XMM-Newton*) compared with $t_{\rm elapsed}$ (black solid line).

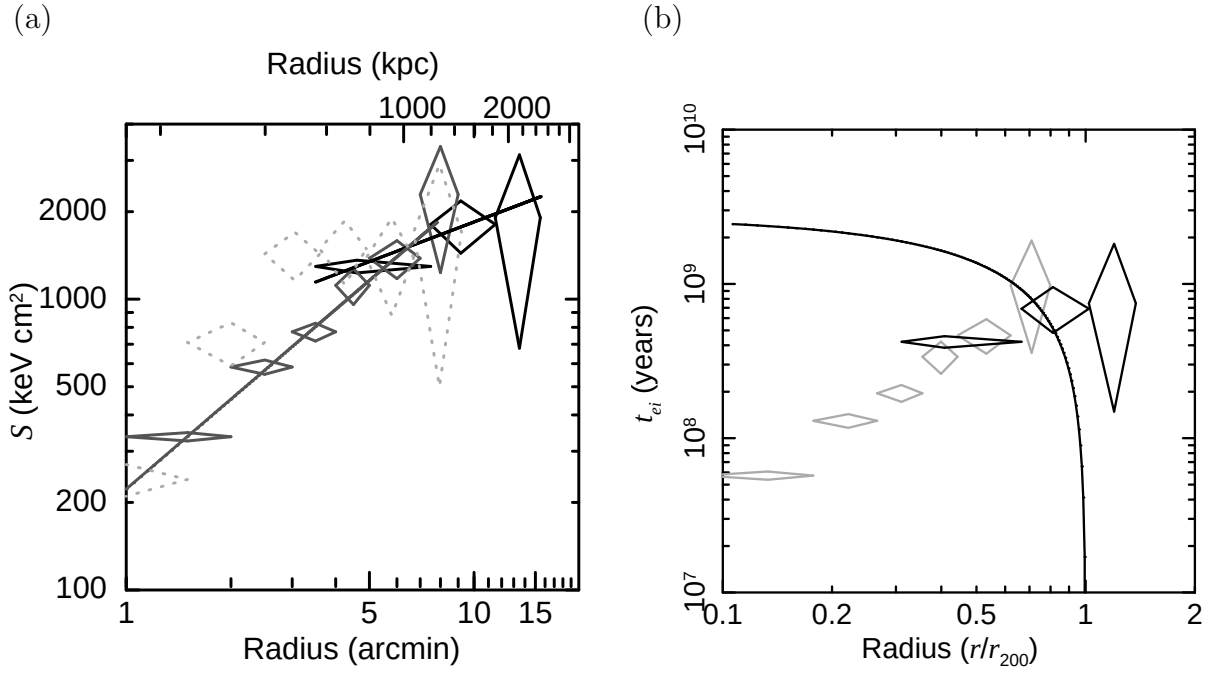

Fig. 7.3: (a): Entropy profile (black diamond: *Suzaku*, grey diamond: *XMM-Newton*, black solid line: fitted model to *Suzaku* in $3.5' - 15'.5$, dotted diamond: Basu et al. (2009), grey solid line: fitted model to *XMM-Newton* in $1'.0 - 9'.0$ for A2204). (b) : $t_{\rm ei}$ profile (black diamonds: Suzaku, and grey diamond: XMM-Newton) compared with $t_{\rm elapsed}$ (black solid line)

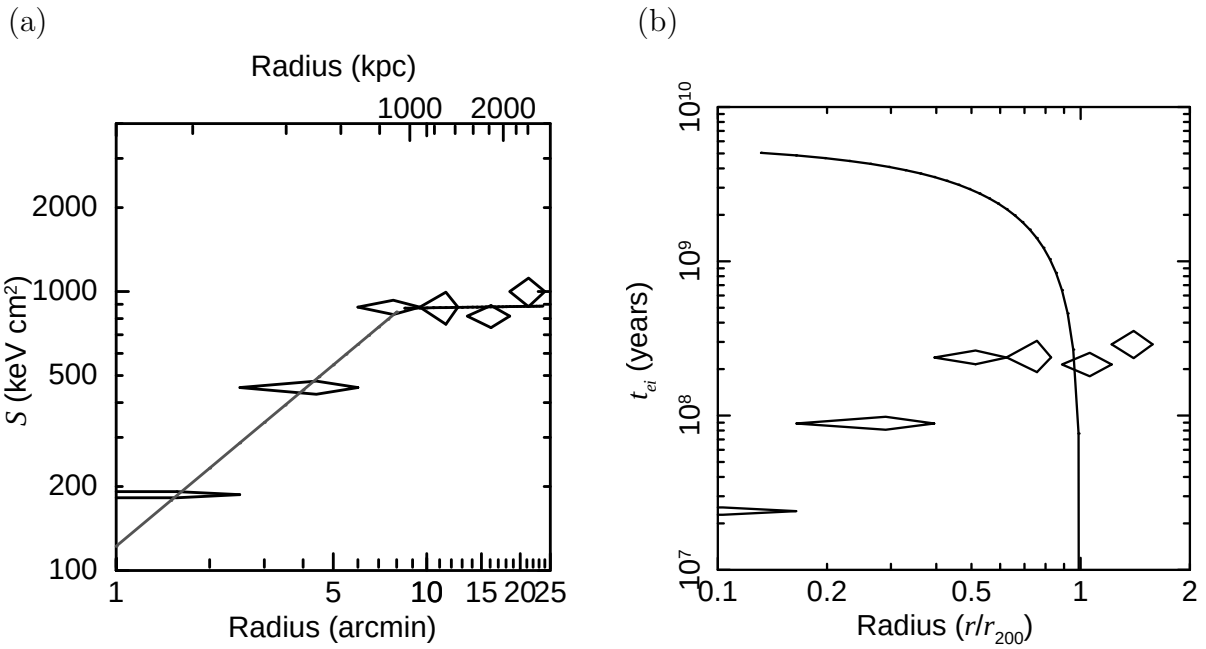

Fig. 7.4: Entropy (a) and equilibration time scale (b) of PKS-0745191(George et al. 2008). (a): entropy profile (black diamond: Suzaku, black solid line: fitted model). (b): $t_{\rm ei}$ profile (diamonds) compared with $t_{\rm elapsed}$ (black solid line).

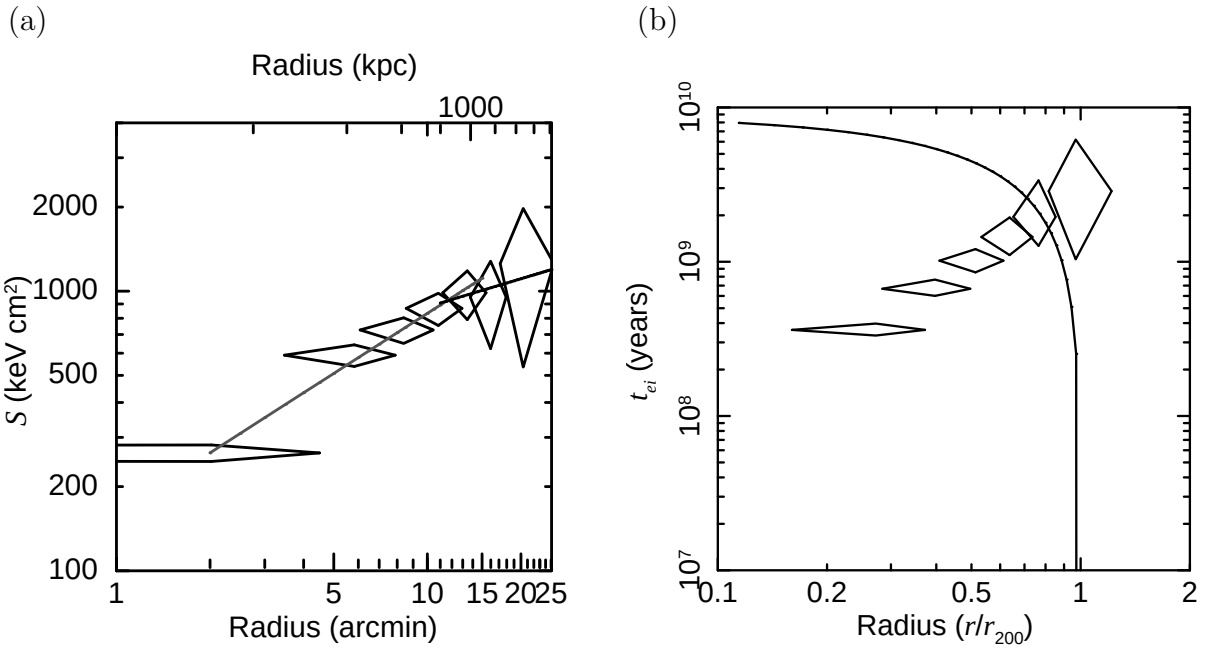

Fig. 7.5: Entropy (a) and equilibration time scale (b) of A1795(Bautz et al. 2009). (a): entropy profile (black diamond: Suzaku, black solid line: fitted model). (b): $t_{\rm ei}$ profile (diamonds) compared with $t_{\rm elapsed}$ (black solid line).

(e) A1689 (f) A1689

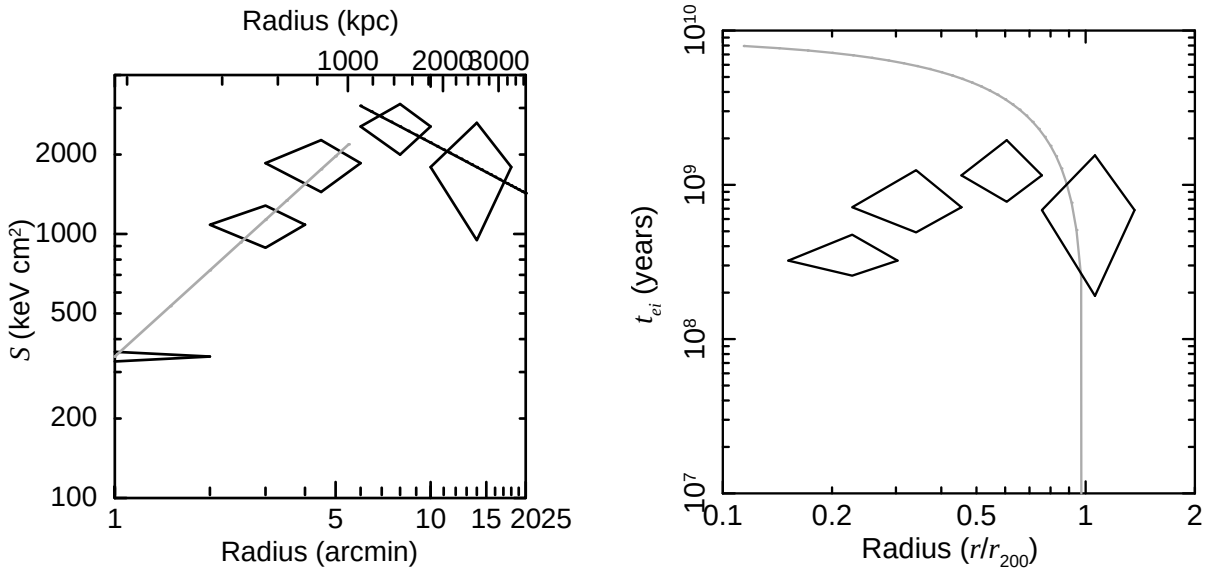

Fig. 7.6: Entropy (a) and equilibration time scale (b) of A1689(Kawaharada, et al. 2010). (a): entropy profile (black diamond: Suzaku, black solid line: fitted model). (b): $t_{\rm ei}$ profile (diamonds) compared with $t_{\rm elapsed}$ (black solid line).

Table 7.1: The best fit parameters of entropy profile model.

	$r < 0.5\ r_{200}$	$r > 0.5\ r_{200}$
A1413	0.90 ± 0.10	0.97 ± 0.45
A2204	1.03 ± 0.06	0.45 ± 0.27
A1795*	0.71 ± 0.06	0.33 ± 1.7
PKS0745-191†	0.93 ± 0.04	0.02 ± 0.12
A1689‡	1.08 ± 0.12	-0.43 ± 1.30

* The observed data is from Bautz et al. (2009).

† The observed data is from George et al. (2008).

‡ The observed data is from Kawaharada, et al. (2010). Only this case, we fit $S = S_0 + Sr^{\gamma}$ in $r > 0.5\ r_{200}$ because its slope is clearly negative.

electron process ($t_{\rm ee}$) and about 45 times longer than ion-ion relaxation time ($t_{\rm ii}$).

According to Fox & Loeb (1997), Takizawa (1998), and Rudd & Nagai (2009), the electron–ion timescale including contributions from both protons and He^{2+} is estimated as (Spitzer 1956)

$$t_{\rm ei} \approx 2.0 \times 10^8 \ {\rm yr} \ \frac{(T_{\rm e}/10^8 \ {\rm K})^{3/2}}{(n_{\rm i}/10^{-3} \ {\rm cm}^{-3}) \ (\ln\Lambda/40)}, \tag{7.2}$$

where $\ln\Lambda$ is the Coulomb logarithm. We simply assume that ions are initially heated through accretion shocks at r_{200}. In the post-shock region, ions achieve thermal equilibrium with a timescale of $t_{\rm ii}$ after this heating. The ion temperature $T_{\rm i}$ will then be significantly higher than the electron temperature $T_{\rm e}$. Eventually, thermal energy is transferred from ions to electrons through Coulomb collisions, and $T_{\rm e}$ will be equal to $T_{\rm i}$ after the relaxation time $t_{\rm ei}$.

We can compare the position-dependent time since the shock heating, $t_{\rm elapsed}$, with the equilibration timescale $t_{\rm ei}$. If $t_{\rm ei}$ is longer than $t_{\rm elapsed}$, then $T_{\rm e}$ would be expected to be significantly lower than $T_{\rm i}$ at that position. Denoting the velocity of inward propagation of the shock front as $v_{\rm shock}$, we obtain

$$r_{200} - r \simeq t_{\rm elapsed} \ v_{\rm shock}. \tag{7.3}$$

The free-fall velocity of the gas at r_{200} is $v_{\rm ff,200} = \sqrt{2GM_{200}/r_{200}}$. Using the strong shock approximation and neglecting the post-shock gas velocity compared with $v_{\rm shock}$, Takizawa (1998) found

$$v_{\rm shock} \simeq \frac{1}{3} \ v_{\rm ff,200}. \tag{7.4}$$

Then, we can derive

$$t_{\rm elapsed} \simeq 3 \ \frac{r_{200} - r}{v_{\rm ff,200}}, \tag{7.5}$$

which is independent of M_{200}. In figure 7.2(b), figure 7.3(b), figure 7.4(b), figure 7.5 (b), and figure 7.6 (b), we show $t_{\rm elapsed}$ compared with $t_{\rm ei}$, estimated from the data for A1413, A2204, PKS0745-191, A1795, and A1689 respectively. In the region outside of $r \sim 0.9 \ r_{200}$, $t_{\rm ei}$ is significantly longer than $t_{\rm elapsed}$. Based on these calculation, it is likely that $T_{\rm e}$ and $T_{\rm i}$ are significantly different in the outer regions of all cluster samples; A1413, A2204, PKS0745-191, A1795, and A1689.

7.4 Difference between Electron and Ion Temperatures

Fox & Loeb (1997) were the first to investigate the two-temperature nature of the ICM. Takizawa (1998) showed that in a one-dimensional numerical simulation there existed a

(a) Entropy

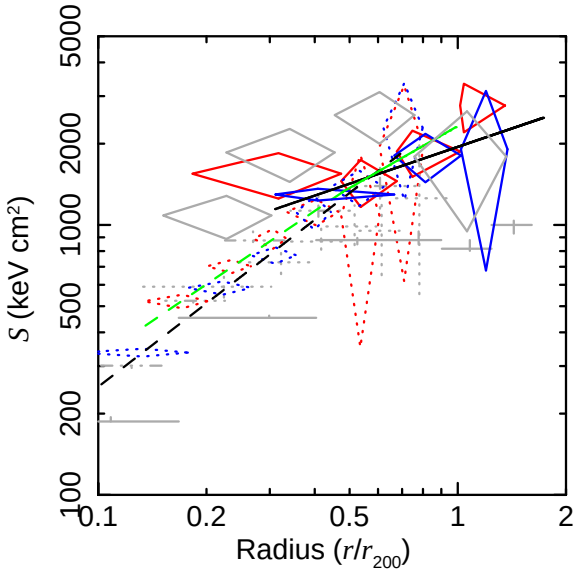

(b) Entropy / $r^{1.1}$

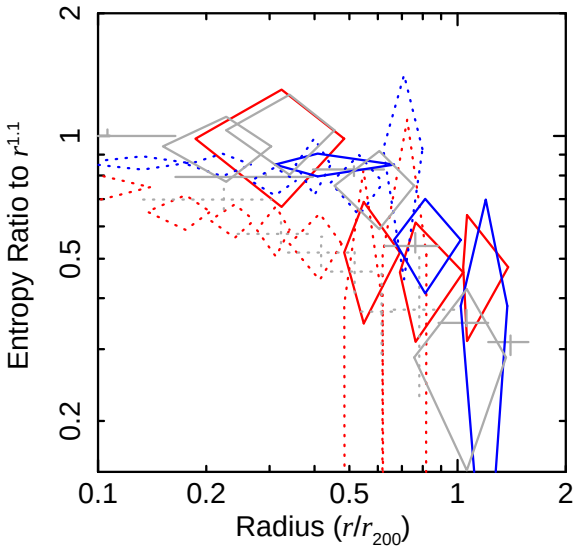

(c) $kT_{\rm e}/kT_{\rm gas}$

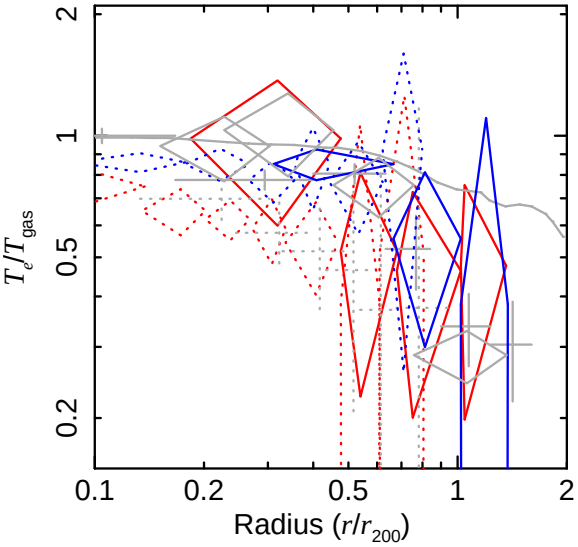

Fig. 7.7: (a) Entropy profiles (black diamond: Suzaku, grey diamond: XMM-Newton, black solid line: fitted model to Suzaku in $7' - 20'$, black dashed line: fitted model to XMM-Newton in $0'.5 - 7'$, grey solid cross: PKS0745−191, grey dotted cross: A1795, grey diamond: A1689). (b) Entropy normalized to $\propto r^{1.1}$ profile. (c) $T_{\rm e}/T_{\rm gas}$ profiles compared with the simulated result by Rudd & Nagai (2009).

significant difference between the electron and ion temperatures, which will affect the entropy profile and the inferred gravitational mass. Recently, Rudd & Nagai (2009) reported the results of simulations which indicated that the temperature difference had a maximum of about 30% at r_{200}. We will examine here a possible deviation between electron and ion temperatures. These studies can help us understand how the cluster gas obtains hydrostatic equilibrium over large volumes.

We define the average gas temperature as,

$$T_{\rm gas} = \frac{n_{\rm e}T_{\rm e} + n_{\rm i}T_{\rm i}}{n_{\rm e} + n_{\rm i}}, \tag{7.6}$$

which will change over a typical electron-ion equilibration timescale, $t_{\rm ei}$. We estimate the average gas temperature, $kT_{\rm gas} = S\,n_{\rm e}^{2/3}$, by assuming a single power-law with $\gamma = 1.1$ for the radial entropy profile, normalized in the cluster inner regions where $T_{\rm i} = T_{\rm e}$ because the relaxation times are much shorter there. Figure 7.7(c) shows the ratio of the observed electron temperature to the estimated average gas temperature, where we have adopted $n_{\rm i} = 0.92\ n_{\rm e}$ (including He^{2+}) for a fully ionized gas with $X = 0.7$ and $Y = 0.28$. Temperature difference between $T_{\rm e}$ and $T_{\rm gas}$ is even larger than the simulation sample result (Rudd & Nagai 2009).

The rapid $T_{\rm e}$ decrease in the cluster outer regions can be explained by either the ICM not being in hydrostatic equilibrium or by differences between $T_{\rm e}$ and $T_{\rm i}$. We can determine which interpretation is correct if we could directly estimate $T_{\rm i}$ from the line width. This measurement should be made possible in the near future using the microcalorimeters on the ASTRO-H mission (Takahashi et al. 2008).

7.5 Mass Estimation to r_{200}

We calculated the gravitational mass of A1413 and A2204 to r_{200} assuming spherical symmetry and hydrostatic equilibrium. From numerical simulations, these assumptions are valid within $\sim 2\ r_{200}$ except for the core region at $r < 0.3\ r_{200}$, where cooling and heating of AGN give significant effects on the physical state of the gas (Roncarelli et al. 2006; Borgani et al. 2006). Previous X-ray studies mainly showed gravitational mass within r_{500} because of instrumental limitations. In this section, we determine the mass profile in the outer region of A1413.

Assuming hydrostatic equilibrium, the total integrated gravitational mass, $M_{<R}$, within the 3-dimensional radius R is given by (Fabricant et al. 1980)

$$M_{<R} = -\frac{R^2}{\rho_g G}\frac{dP_g}{dR} \tag{7.7}$$

$$= -\frac{kTR}{\mu m_p G}\left(\frac{d\ln\rho_g}{d\ln R} + \frac{d\ln T}{d\ln R}\right). \tag{7.8}$$

where G is the gravitational constant, μ is the mean molecular weight of the gas and m_p is the proton mass. We derive the above temperature and gas density profiles using the observed projected temperature and surface brightness profiles. We use the

projected temperature directly, but discuss the validity of this assumption below. We calculate the gas density from the normalization of the ICM spectral fit by taking into account the projection effect. The *apec* normalization parameter is defined as $Norm = 10^{-14} \int n_{\rm e} n_{\rm H} dV/(4\pi(1+z)^2 D_{\rm A}^2)$ cm^{-5}, with $D_{\rm A}$ the angular diameter distance to the source. We estimated the de-projected $n_{\rm e} n_{\rm H}$ values assuming spherical symmetry and a constant temperature in each annular region as described in Kriss et al. (1983), and then assumed $n_{\rm e} = 1.2\ n_{\rm H}$ (excluding He^{2+}) as described above.

Allowing for the possibility of $T_{\rm e} \neq T_{\rm i}$, we consider two cases for T: the electron temperature and the average gas temperature. We show the integrated mass profiles in figure 7.8 (b) and figure 7.9 (b) based on $kT_{\rm e}$ and $kT_{\rm gas}$. These profiles are obtained without using any particular model since we calculate the derivatives by differencing the temperatures and densities of adjacent radial bins. The integrated mass within $13'.2^{+4'.3}_{-0'.7}$, which encompasses r_{200} ($14'.8$) is $(8.8 \pm 2.3) \times 10^{14} M_\odot$ using $kT_{\rm gas}$ for A1413. This mass is about 30% larger than that obtained using $kT_{\rm e}$ of $(6.6 \pm 2.3) \times 10^{14} M_\odot$ for A1413, although the difference is not statistically significant. The 30% difference in the temperatures propagates almost directly to the mass difference. Our mass determination for A1413 agrees with that of Vikhlinin et al. (2006), but not with Pointecouteau et al. (2005). These masses imply an overdensity within r_{200} with respect to the critical density of 177±47 and 132±47, where the errors are only from the mass errors.

In the above mass estimation, we assumed that the observed projected temperature is the 3-dimensional value at the observed radius. We need to examine the systematic error caused by this assumption. In the following we denote the true 3-dimensional temperature of the ICM by $T_{\rm 3d}$, which varies with radius. We derive the temperature from the spectral fit as a weighted mean of different temperatures projected along the line of sight. Often the projected temperature is defined as the emission-weighted temperature $T_{\rm ew}$,

$$T_{\rm ew} \equiv \frac{\int n^2 \Lambda(T) T dV}{\int n^2 \Lambda(T) dV} \ . \tag{7.9}$$

However, Mazzotta et al. (2004) discussed how the spectral response of an actual instrument could affect that $T_{\rm ew}$ was quite different from what would be measured with that instrument for a non-isothermal temperature distribution. For a better approximation, they introduced a spectroscopic-like temperature $T_{\rm sl}$ defined as,

$$T_{\rm sl} \equiv \frac{\int n^2 T^{a-1/2} dV}{\int n^2 T^{a-3/2} dV} \quad , \tag{7.10}$$

with $a = 0.75$, which empirically gave a good estimate of T measured with *XMM-Newton* or *Chandra*. Rasia et al. (2005) reported that the difference between $T_{\rm ew}$ and $T_{\rm sl}$ can be as large as 30%. We carried out comparison of observed temperature with $kT_{\rm ew}$ and $kT_{\rm sl}$ in figure 7.8(a) and (c). The difference between $kT_{\rm ew}$ and $kT_{\rm sl}$ takes the largest value of about 8.2% in the radius $2'.6 - 7'.0$ in A1413. These temperatures are consistent with the observed data with XMM-Newton. Taking a conservative value for the temperature difference, our mass estimate would be more than 30% different from the true value

(a) Temperature (b) Integrated Mass

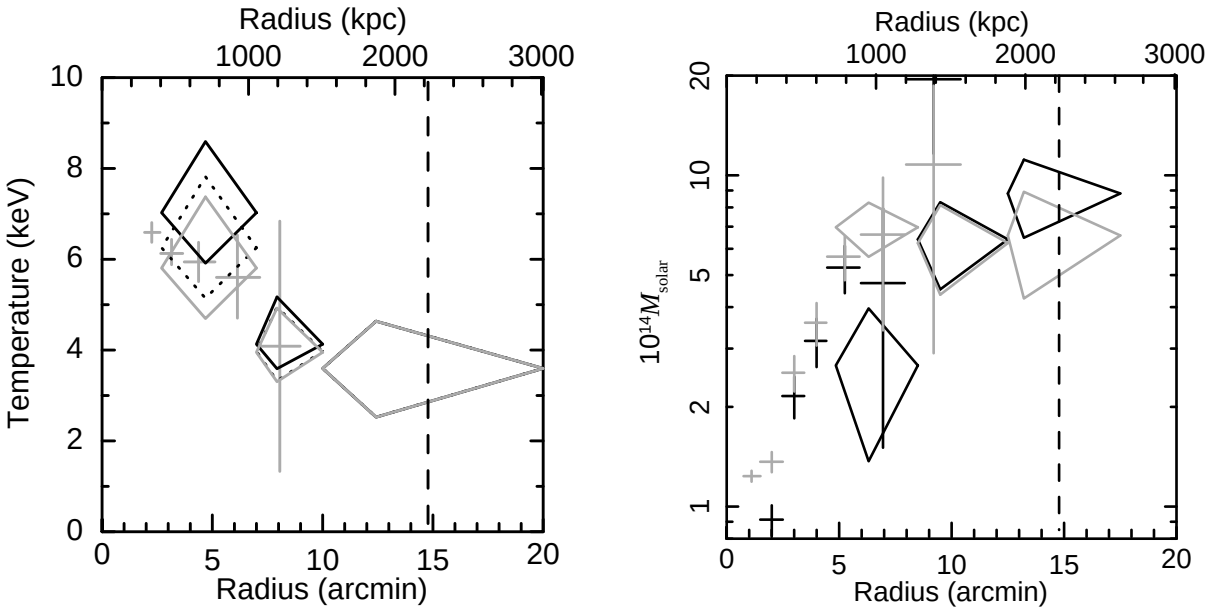

Fig. 7.8: (a)Comparing observed temperature of A1413 (black diamonds) with kT_{ew}(dot diamonds), and kT_{sl} (grey diamonds). Grey cross is $kT_{\rm 3d}$ observed with $XMM-Newton$ by Snowden et al. (2008). (b)Integrated mass profile of A1413 (black diamonds: Suzaku with $T_{\rm gas}$, grey diamonds: Suzaku with $T_{\rm e}$, black crosses: XMM-Newton with $T_{\rm gas}$, and grey crosses: XMM-Newton with $T_{\rm e}$). Vertical dashed line shows $r_{200} = 14'.8$.

because of our employment of the observed projected temperature as the 3-dimensional one.

(a) Temperature (b) Integrated Mass

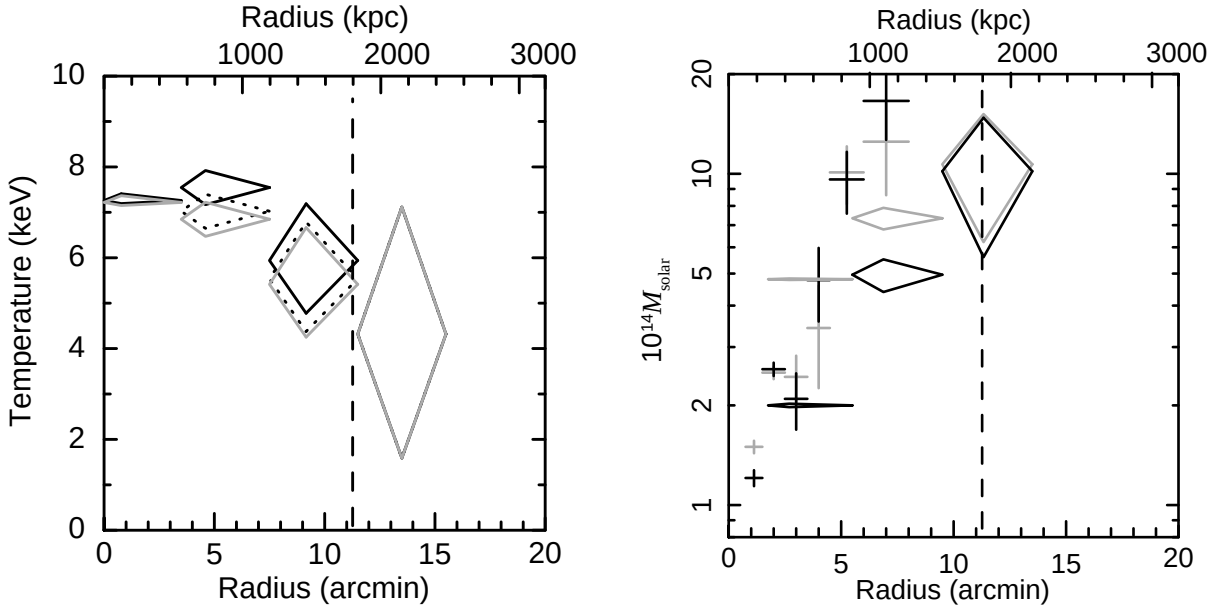

Fig. 7.9: (a)Comparing observed temperature of A2204 (black diamonds) with kT_{ew}(dot diamonds), and kT_{sl} (grey diamonds). Grey cross is $kT_{\rm 3d}$ observed with $XMM-Newton$ by Snowden et al. (2008). (b)Integrated mass profile of A2204 (black diamonds: Suzaku with $T_{\rm gas}$, grey diamonds: Suzaku with $T_{\rm e}$, black crosses: XMM-Newton with $T_{\rm gas}$, and grey crosses: XMM-Newton with $T_{\rm e}$). Vertical dashed line shows $r_{200} = 14'.8$.

Chapter 8

Non-isothermal SSM-NFW model

In this section, we explain the analysis of mass profile comparing observed data with non-isothermal SSM-NFW model.

We attempted to compare our measured temperature and surface brightness profiles with theoretical predictions for relaxed clusters. Suto et al. (1998) gave ICM properties for clusters whose potentials follow NFW (Navarro et al. 1996) and modified NFW models, assuming that the ICM can be described by a polytrope. These models have 6 parameters and give a wide range of temperature and density distributions with radius.

We found that, although we could fit either the temperature or surface brightness profile, it was not possible to simultaneously fit both despite an exhaustive search of parameter space. The likely reason for this result is that the ICM is out of equilibrium in the outer regions of the cluster. We examined this hypothesis in the next section using the entropy profile.

Non-isothermal SSM-NFW model has five independent parameters, n,kT_0,r_s, ρ_{g0}, and r_{200}. n defines the polytropic index $\Gamma = 1 + 1/n$. kT_0 defines the highest temperature in the cluster. ρ_{g0} defines the highest density of the cluster. r_{200} is the 200 times radius against the critical density. Because these parameters are related to each other in the parameter B_p of the equation (2.62), sometimes it is difficult to strain all of them for the actual clusters of galaxies.

In our study, we looked into straining theses parameters in the following method. First, we strain the range of r_{200} and r_s with integral mass profile. Second, we strain parameters with temperature profile to strain kT_0 and n. Last, we strain the parameter ρ_{g0}.

We looked into the combined data set of "*Suzaku+Chandra*" for A1413 and "*Suzaku+XMM-Newton*" for A2204. In A2204 we utilized data including point sources.

8.1 Method for model fitting

In this section, we explain the SSM-NFW model fitting for integral mass, temperature and surface brightness profiles. Assuming spherical symmetry and hydrostatic equilibrium, we can derive mass equation depending on temperature and gas density profiles.

Table 8.1: best-fit parameters of integral mass model with XMM+Suzaku

data	r_{200} (kpc)	r_s (kpc)	χ^2 / dof
A1413	1995.7 ±157.5	335.5 ± 95.8	13.3 / 25
A2204	1837.0 ± 62.5	111.1 ± 19.2	15.3 / 5

It means that temperature and gas density profiles represent mass profiles. In the SSM-NFW model, Integral mass is the same as the isothermal model because of its definition. However it is useful to strain r_{200} and r_s. We fitted this model with integral mass data by Suzaku, and Chandra for A1413 and Suzaku and XMM-Newton for A2204. We could well fitted this model.

Then, we strain n and kT_0 by fixing r_s and r_{200} to the best-fit value which is strained by the integral mass fitting. We also looked into χ^2 distribution around the best fit parameters for error ranges.

Finally, we fitted surface brightness data with NFW-SSM density model by projection. We can strain the last parameter ρ_{g0} by this fitting with fixing other parameters.

8.2 Result

We show the best-fit parameters of integrated mass fitting in the table8.5. By the fitting, we could strain r_s and r_{200}. In A2204, our *XMM-Newton+Suzaku* data set did not lead consistent result with previous works which report $r_{200} \sim 11.8\ Mpc$(Reiprich et al. 2009). If we fit the *Suzaku* data to the integral mass model, $r_{200} = 1920.1 \pm 75.6$ kpc and $r_{200} = 42.3 \pm 20.5$ kpc with $\chi^2/dof = 0.19$ / 2 . These parameters are connected with each other by $c = r_{200}/r_s$ which is called as concentration parameter. Especially the relation of r_{200} to r_s is c_{200}. c_{200} is known as one of the typical self consistent parameters which has a relation of $c_{200} \propto M_{200}$. Our result is also consistent with previous results.

Then, we looked into temperature profile fitting with these results of integral mass fitting. In table8.3, we show the best-fit parameters for temperature profile fitting fixing r_{200} and r_s. We could reproduce observed profile by SSM-NFW model well in this case. We scanned χ^2 distribution around the best fit parameters to estimate 1σ error ranges. Because parameter n has complicated relation to other parameters through B_p, the shape of χ^2 distribution is not expressed in "parabolic" shown as figure 8.3.

Finally, we estimate the parameter ρ_{g0} by fitting for surface brightness profile independently with fixing other parameters which is estimated former fitting for integral mass and temperature profiles.

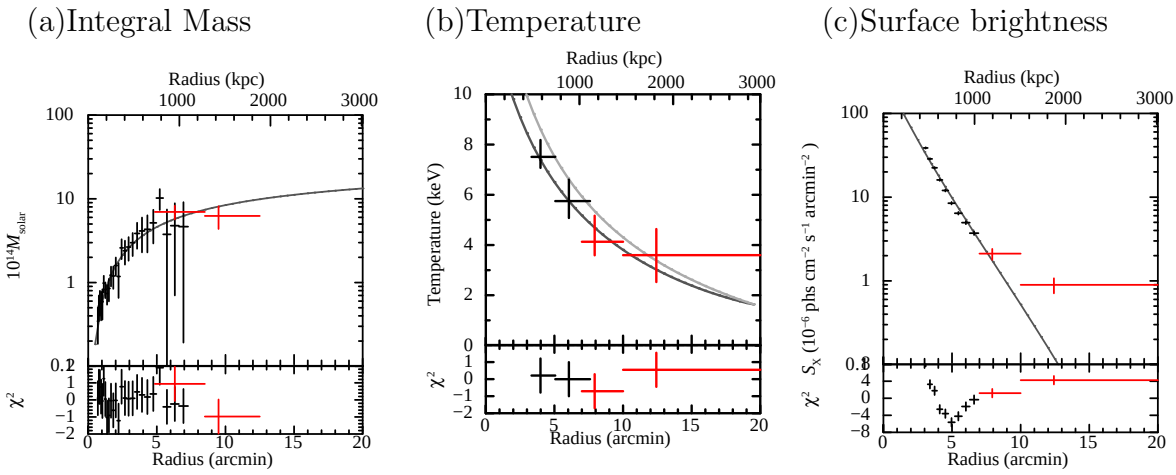

Fig. 8.1: The best-fit profiles with *Chandra* and *Suzaku* data of A1413. (a) integral mass, (b) temperature and (c) surface brightness.

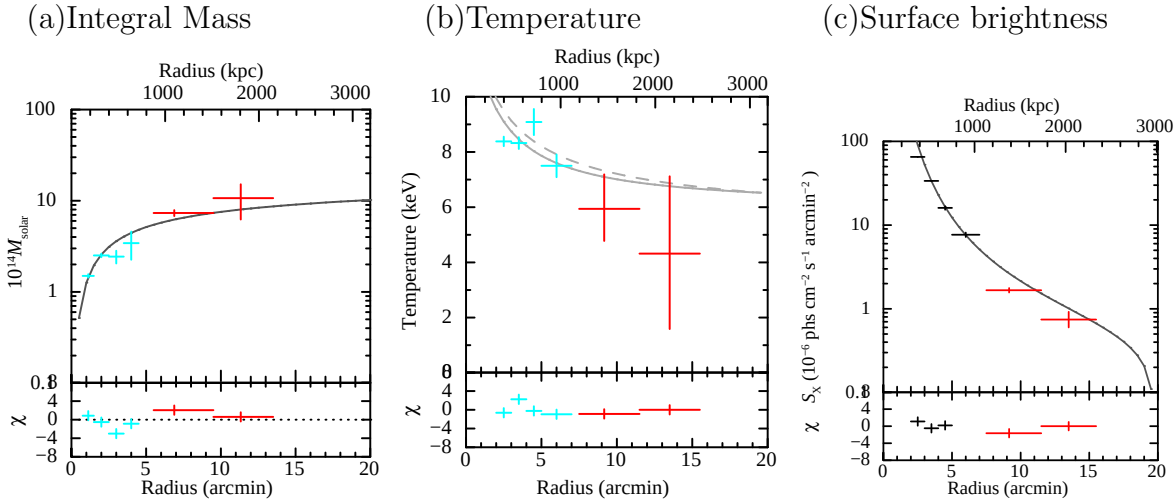

Fig. 8.2: The best-fit profiles with *XMM-Newton* and *Suzaku* data of A2204. (a) integral mass, (b) temperature and (c) surface brightness.

Table 8.2: M_{200},δ_c and c_{200}

data	M_{200} (10^{15} $M_\odot$)	δ_c	c_{200}
A1413	$1.02^{+0.26}_{-0.98}$	$1.30^{+2.15}_{-0.69} \times 10^4$	$5.95^{+3.04}_{-1.69}$
A2204	$2.91^{+0.26}_{-0.22}$	$5.72^{+2.25}_{-1.47} \times 10^3$	$4.15^{+0.66}_{-0.53}$

Table 8.3: The best-fit parameters of temperature fitting

Target	$r_{200}(kpc)$	n	R_s (kpc)	kT_0 (keV)	χ^2 / dof
A1413	1995 (fix)	$2.51^{+4.57}_{-1.30}$	350 (fix)	$16.23^{+5.27}_{-5.27}$	0.20 / 2
A2204	1837.0 (fix)	9.28± 0.01	111.1 (fix)	15.09± 0.01	7.2 / 3

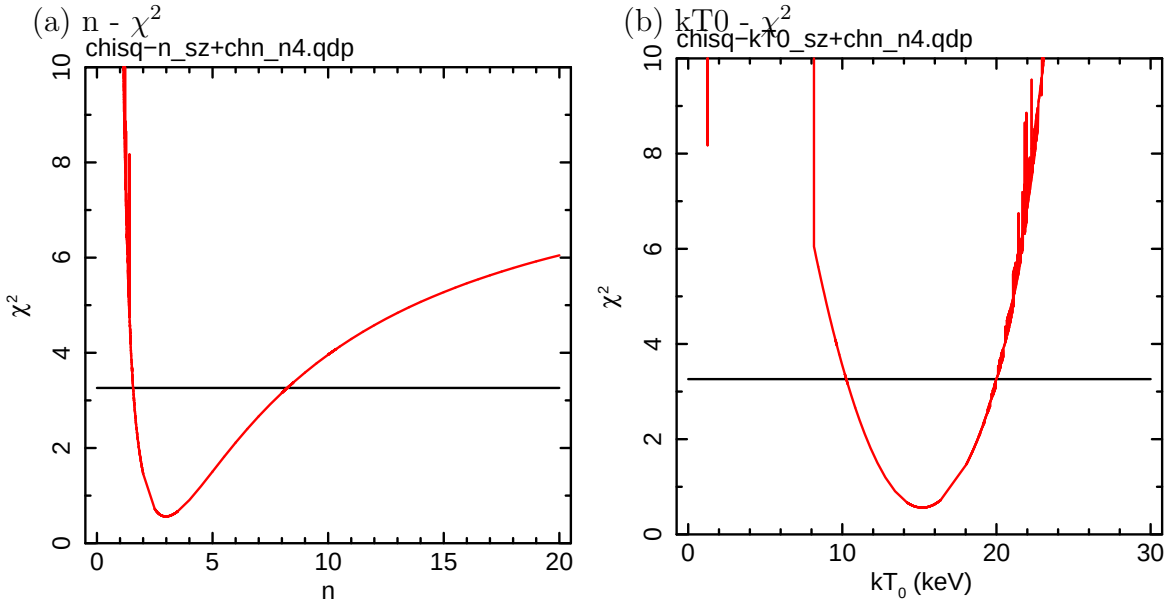

Fig. 8.3: χ^2 distribution for temperature model with *Suzaku*+*Chandra* data set freezed $r_{200} = 1995$ kpc, $r_s = 350$ kpc.

Table 8.4: The best-fit parameters of surface brightness fitting

Target	$r_{200}(kpc)$	n	R_s (kpc)	ρ_{g0} ($10^{14} M_\odot$/Mpc^3)	kT_0 (keV)	χ^2 / dof
A1413	1995 (fix)	2.51 (fixed)	350 (fix)	2.17	16.23 (fixed)	76.17 / 4
A2204	1837 (fix)	9.28 (fixed)	111.1 (fix)	1590.2 ± 0.2	15.09 (fixed)	95.6 / 4

Table 8.5: The best-fit parameters of simultaneously fitting

data	r_{200}	n	R_s	ρ_0 $(10^{-26} g/cm^3)$	kT_0	χ^2 / dof
sz	$1663.9^{+100.0}_{-100.0}$	$1.77^{+0.23}_{-0.37}$	350 (fix)	$0.415^{+0.033}_{-0.075}$	$14.54^{+1.79}_{-2.00}$	3.77 / 2.0
sz+chn	$1731.9^{+100.0}_{-75.0}$	$9.51^{+8.49}_{-2.76}$	350 (fix)	$6.354^{+2.816}_{-1.496}$	$7.29^{+1.73}_{-1.25}$	40.92 / 11.0
chn	$1894.1^{+128.5}_{-21.5}$	$9.00^{+4.62}_{-1.61}$	350 (fix)	$5.034^{+3.090}_{-0.162}$	$9.27^{+1.03}_{-0.75}$	29.9 / 15.0

8.3 Comparing with simultaneous fitting

Assuming spherical symmetry and hydrostatic equilibrium, we can derive mass equation depending on temperature and gas density profiles. It means that temperature and gas density profiles represent mass profiles.

We fitted $T(x)$ and $\rho_g(x)$ to temperature and surface brightness profiles simultaneously to find best fit parameters. Temperature profile of non-isothermal SSM model can represents the gradient in the outer region of the cluster.

(a) Temperature

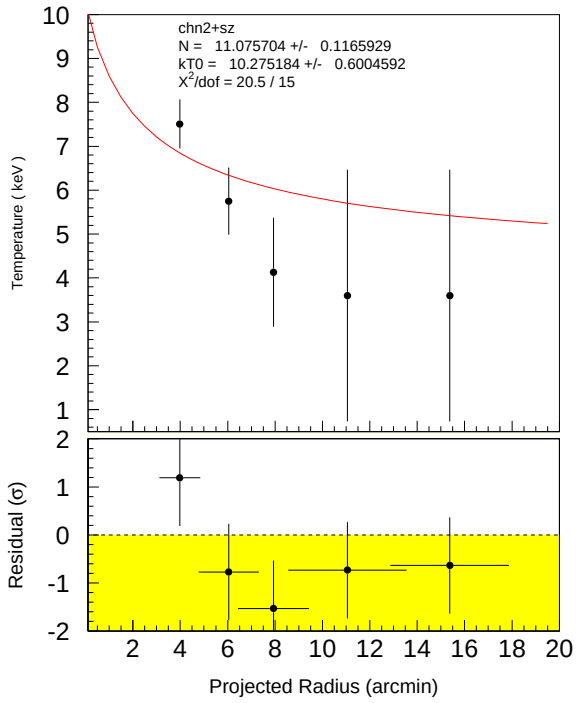

(b) Surface brightness

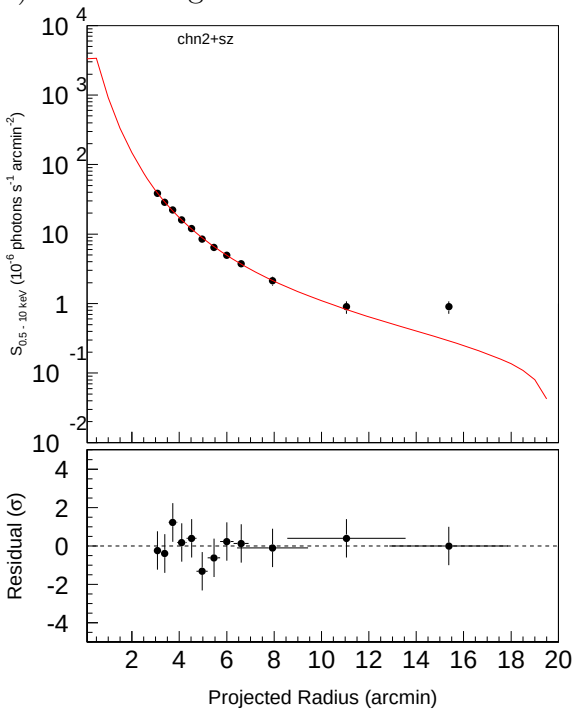

Fig. 8.4: (a)Temperature and (b) surface brightness profile by simultaneous fitting.

8.4 Performance of non-isothermal SSM-NFW model

In this section, we show performance of SSM-NFW model against the parameter, n. n which is the parameter of polytropic index, $\Gamma = 1/n + 1$, indicates the tendency of temperature slope. When $n \to \infty$, temperature shows isothermal profiles. We show temperature, surface brightness, integral mass, and density model profiles in the range from $n = 1$ to 40 in figure8.5.

These figures suggest that small n values make temperature profiles steep, and the large make them flattening. Surface brightness profiles changes their shapes over 1 Mpc. In the case of A1413, "Chandra+Suzaku" combined data is different sample numbers between temperature and surface brightness. Moreover, because of small errors of surface brightness, the simultaneous fitting of SSM-NFW model has strong indication to suit its model with surface brightness data. Then we could not reproduce temperature profiles.

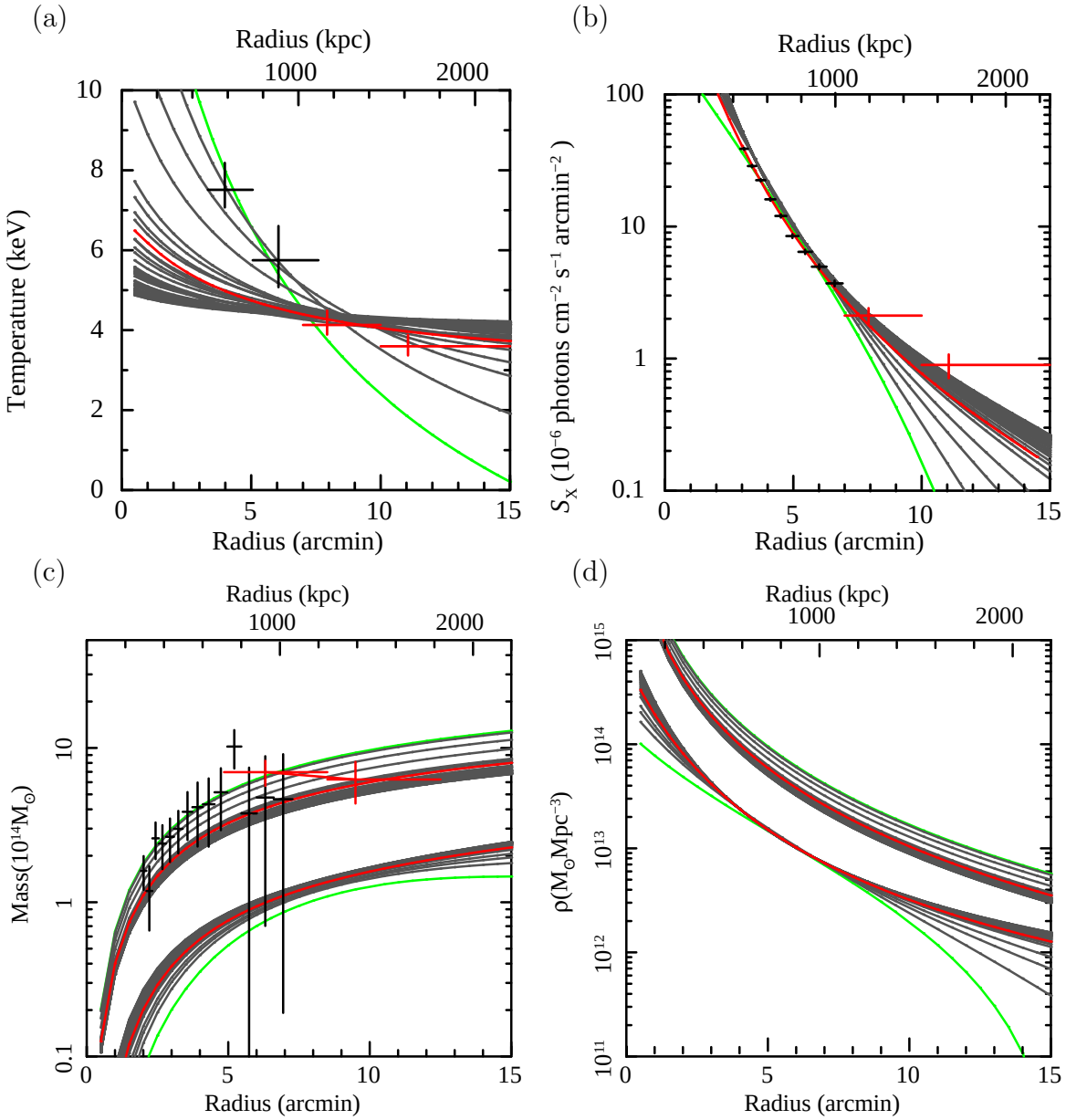

Fig. 8.5: Radial profile of (a) temperature, (b) surface brightness, (c) integral mass, and (d) density from $n = 1$ to $n = 40$. Green line means $n = 1$. Red line: the best-fit profile.

Chapter 9

Summary and Conclusion

- Northern outskirts of the relaxed cluster of galaxies A1413 was observed with Suzaku in the radial range of $2.'7 - 26'$ covering the virial radius of $r_{200} = 14'.8$. We excised 15 point sources above a flux of $\sim 1 \times 10^{-14}$ erg cm^{-2} s^{-1} (2–10 keV), and the CXB level after the point source excision was evaluated. We quantify all known systematic errors, and show statistical errors are dominant. Suzaku detected X-ray emission of the ICM up to the $15' - 20'$ annulus beyond the virial radius.Significant temperature decrease to ~ 3 keV (factor of ~ 2) at r_{200} is confirmed. Such profile is also reported in a few other clusters, PKS0745−191 (George et al. 2008), A1795 (Bautz et al. 2009).

- We also analyzed the outer regions of A2204 with *Suzaku* and *XMM-Newton*, which was published by Reiprich et al. (2009). A2204 is $z = 0.1523$ and $r_{200} = 11'.5$. We extracted four cluster region ($0' - 3'.5$, $3'.5 - 7'.5$, $7'.5 - 11'.5$, and $11'.5 - 15'.5$) and background region in $15'.5 - 19'.5$. We fixed CXB normalization as 100% CXB of Kushino et al. (2002). Because in the observation period of *Suzaku*, proton density origined by solar activities is relatively high, the energy spectra is contaminated by SWCX below 1 keV. For example, oxygen line emissions are 10 times higher than in the case of A1413. In the spectral analysis, we ignored below 0.7 keV. We could measured temperature profile of A2204 within r_{200}. We could measured temperature over r_{200}.

- We analyzed two pointing observation of the outer region of AWM7 to find out difference of direction to filament. AWM7 has anti-symmetric elliptical shape with about 0.8 of ellipticity. We fit 2 dimensional 2β egg model to *XMM-Newton* image. We generated ARF with this simulated image. We detected 4 and 6 point sources in east and south region. We measured electron temperature in east and south FOVs with $1.62^{+0.62}_{-0.37}$ keV and $0.45^{+0.13}_{-0.06}$ keV. When we correct stray light with *xissim* simulation, the south ICM component is negligible and the east temperature is turn to $2.53^{+3.88}_{-1.50}$ keV.

- We tried to explain our measured temperature and surface brightness of A1413

and A2204 with SSM model which is cluster model with 6 parameters assuming spherical symmetry and hydrostatistic equilibrium. We found that, although we could fit either the temperature or surface brightness profile, it was not possible to simultaneously fit both despite an exhaustive search of parameter space. The likely reason for this result is that the ICM is out of equilibrium in the outer regions of the cluster.

- Our entropy profile in the outer region ($> 0.5\ r_{200}$) joins smoothly onto that of XMM-Newton at 0.15–0.5 r_{200}, and shows a flatter slope of $\gamma = 0.90 \pm 0.12$ for A1413 and $\gamma = 0.45 \pm 0.27$ for A2204 in $3'.5 - 15'.5$ than $\gamma = 1.1$ (Voit 2005) obtained with numerical simulations of adiabatic gas accretion. The flattening of entropy profile also can be measured by PKS0745-191 and A1795. These common point is that entropy profiles wind and start flattening from about 1 Mpc except for A1413. Because A1413 shows different trend, it is possible not to be the universal profile. These indication suggests that electron and ion temperatures are different in clusters of galaxies depending on their evolution. Especially, over the 1 Mpc which is about $0.6r_{200}$, their thermal conditions have the border of their phase observationally because of the out of their equilibration timescale.

- Deviation of the entropy profile would show electron temperature is not equal to gas temperature in outer region, where equilibration timescale for electron-ion collision, $t_{\rm ei}$, is longer than the elapsed time after the shock heating, $t_{\rm elapsed}$.

- The integrated mass of the cluster at the virial radius is approximately $7.5 \times 10^{14}\ M_{\odot}$ for A1413 and varies by $\sim 30\%$ depending on temperatures ($T_{\rm e}$, $T_{\rm gas}$) and < 8.2 % depending on definition of temperatuers ($T_{\rm ew}$, and $T_{\rm sl}$) which we use.

Appendix A

Projection

In order to estimate the 3-dimensional effects of the emission from the objects, we need to calculate the effects from the flux of the outer shell to that of the inner shell of the object. We estimate the effects the following method. In figure A.1, the volume, V_N, is calculated as,

$$V_N = \frac{4}{3}\pi \left(r_N^2 - r_{N-1}^2\right)^{\frac{3}{2}}, \tag{A.1}$$

and the volume, V_N^m, for $m < N$ is

$$V_N^m = \frac{4}{3}\pi \left\{(r_N^2 - r_{m-1}^2)^{\frac{3}{2}} - (r_N^2 - r_m^2)^{\frac{3}{2}} - (r_{N-1}^2 - r_{m-1}^2)^{\frac{3}{2}} + (r_{N-1}^2 - r_m^2)^{\frac{3}{2}}\right\}. \tag{A.2}$$

The observed flux $F_m^{\rm obs}$ in the projected $r_{m-1} < r < r_m$ annulus is the sum of flux from the volumes, V_m, V_{m+1}^m, ..., V_N^m. If we define the flux from the volume V_i as f_i,

$$F_m^{\rm obs} = f_m + \frac{V_{m+1}^m}{V_{m+1}} f_{m+1} + ... + \frac{V_N^m}{V_N} f_N = \sum_{i=m}^{N} \frac{V_i^m}{V_i} f_i, \tag{A.3}$$

assuming the spherical symmetry and $V_i^i \equiv V_i$. Because the volume of the $r_{m-1} < r < r_m$ crust is $W_m = \frac{4}{3}\pi \left(r_m^3 - r_{m-1}^3\right)$, the flux contribution in the 3-dimensional range of $r_{m-1} < r < r_m$ is

$$F_m^{\rm 3D} = \frac{W_m}{V_m} f_m = \frac{r_m^3 - r_{m-1}^3}{(r_m^2 - r_{m-1}^2)^{3/2}}\, f_m. \tag{A.4}$$

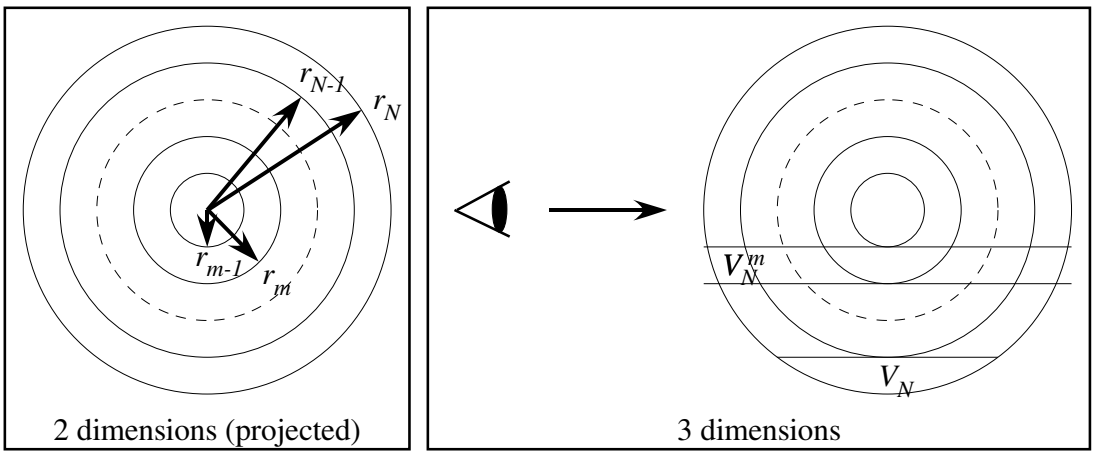

Fig. A.1: deprojection image

Appendix B

Deviation of SSM-NFW Model

B.1 Assumption

We assume the DM halo model

$$\rho_{DM}(x) = \frac{\delta_c \rho_{c0}}{(r/r_s)(1+(r/r_s))^2}, \tag{B.1}$$

where $x = r/r_s$ and r_s is a scaling radius. Makino et al. 1998 shows r_s is about $0.22 r_{200}$. we assume gas is in hydrostatic equiliblium and spherical symmetric on DM potential. We ignore self gravity of gas itself.

B.2 Calculation

We calculate mass within radius r

$$\begin{aligned} M(r) &= \int_0^r 4\pi r'^2 \rho_{DM}(r') dr' && \text{(B.2)} \\ &= 4\pi\delta_c\rho_{c0} r_s^3 \int_0^x \frac{u}{(1+u)^2} du && \text{(B.3)} \\ &= 4\pi\delta_c\rho_{c0} r_s^3 \left[\log(x+1) - \frac{x}{1+x}\right]_0^x && \text{(B.4)} \\ &= 4\pi\delta_c\rho_{c0} r_s^3 \left[\log(x+1) - \frac{x}{1+x}\right] && \text{(B.5)} \end{aligned}$$

The equation of hydrostatic equiliblium,

$$\begin{aligned} \frac{1}{\rho_g}\frac{dP_g}{dr} &= -\frac{GM}{r^2} && \text{(B.6)} \\ & && \text{(B.7)} \end{aligned}$$

gas is polytrope and ideal gas.

$$\begin{aligned} P_g &= P_0 \left(\frac{\rho_g}{\rho_{g0}}\right)^{1+1/n} && \text{(B.8)} \\ T_g &= T_{g0} \left(\frac{\rho_g}{\rho_{g0}}\right)^{1/n} && \text{(B.9)} \end{aligned}$$

The left hand side (LHS) of the equation is

$$\begin{aligned} \mathrm{LHS} &= \frac{1}{\rho_g}\frac{d}{dr}\left[P_0\left(\frac{\rho_g}{\rho_{g0}}\right)^{1+1/n}\right] && \text{(B.10)} \\ &= (n+1)\left(\frac{P_0}{\rho_{g0}}\right)\frac{d}{dr}\left(\frac{T_g}{T_{g0}}\right) && \text{(B.11)} \\ & && \text{(B.12)} \end{aligned}$$

Because we assumed gas is the ideal,

$$P_0 = \frac{\rho_g}{\mu_g m_p} k_B T_g \tag{B.13}$$

$$(n+1)\frac{k_B T_{g0}}{\mu_g m_p}\frac{d}{dr}\left(\frac{T_g}{T_{g0}}\right) = -\frac{GM}{r^2} \tag{B.14}$$

$$\begin{aligned} x &\equiv \frac{r}{r_c} && \text{(B.15)} \\ \epsilon &= \frac{T_g(r_c x)}{T_{g0}} && \text{(B.16)} \\ & && \text{(B.17)} \end{aligned}$$

We insert $M(r)$ to the equatioin (B.14)

$$\begin{aligned} \frac{d\epsilon}{dx} &= \frac{1}{n+1}\frac{\mu_g m_p}{k_B T_{g0}} r_c(-1)\frac{G}{r_c^2 x^2} 4\pi\delta_c\rho_{c0} r_c^3\left[\log(x+1) - \frac{x}{1+x}\right] && \text{(B.18)} \\ &= -\frac{4\pi G}{n+1}\frac{\mu_g m_p \delta_c \rho_{c0} r_c^2}{k_b T_{g0}}\left[\frac{\log(x+1)}{x^2} - \frac{1}{x(1+x)}\right] && \text{(B.19)} \\ &= -B_p\left[\frac{\log(x+1)}{x^2} - \frac{1}{x(1+x)}\right] && \text{(B.20)} \end{aligned}$$

Then, we should solve the below differential equation,

$$\frac{d\epsilon(x)}{dx} = -B_p\left[\frac{\log(x+1)}{x^2} - \frac{1}{x(1+x)}\right]. \tag{B.21}$$

When we calculate the integral member,

$$\begin{aligned} \int \frac{\log(x+1)}{x^2}dx &= -\frac{\log(x+1)}{x} + \log(x) - \log(x+1) && \text{(B.22)} \\ \int \frac{1}{x(1+x)}dx &= \int \frac{1}{x}dx - \int \frac{1}{x+1}dx && \text{(B.23)} \\ &= \log(x) - \log(x+1) && \text{(B.24)} \end{aligned}$$

Then,

$$\epsilon(x) = B_p\frac{\log(1+x)}{x} + C \tag{B.25}$$

the requirement of the border is $\epsilon(0) = 1$ for $x = 0$.

$$\epsilon(0) = B_p + C = 1 \tag{B.26}$$

$$C = 1 + \frac{3}{9}\pi B_p \tag{B.27}$$

We utilized the limiting value as below,

$$\lim_{x\to 0} \frac{\log(1+x)}{x} = \lim_{x\to 0} \frac{1}{x}\left(\frac{x}{1+x} + \ldots\right) \to 1. \tag{B.28}$$

Then the equation ϵ is,

$$\epsilon(x) = 1 - B_p\left[1 - \frac{\log(x+1)}{x}\right]. \tag{B.29}$$

f(x),m(x), and δ_c of politropic gas on isothermal DM model are

$$f(x) = 1 - \frac{\log(x+1)}{x} \tag{B.30}$$

$$m(x) = \log(1+x) - \frac{x}{x+1} \tag{B.31}$$

$$\delta_c = \frac{200}{3}\frac{c^3}{\log(1+c) - c/(c+1)}. \tag{B.32}$$

Appendix C

Individual spectra of clusters

In this appendix, we show the comparison of raw data, NXB, CXB and galactic components, point source spectra, spectrum and the best-fit model for each annular region and each sample cluster, i.e. A1413, A2204, and AWM7.

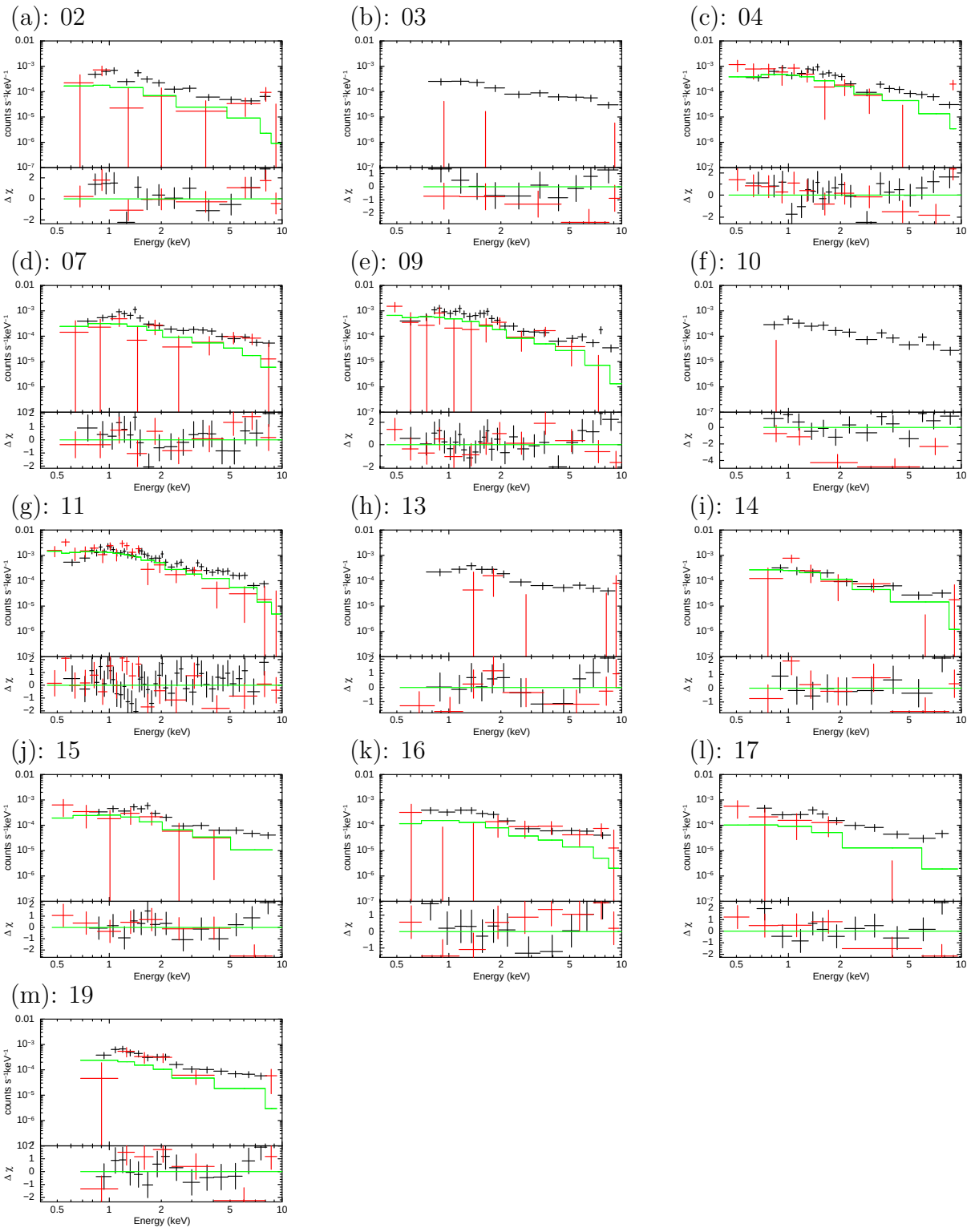

Fig. C.1: A1413:The point source spectra of FI (black), BI (red), and the best-fit FI model (green).

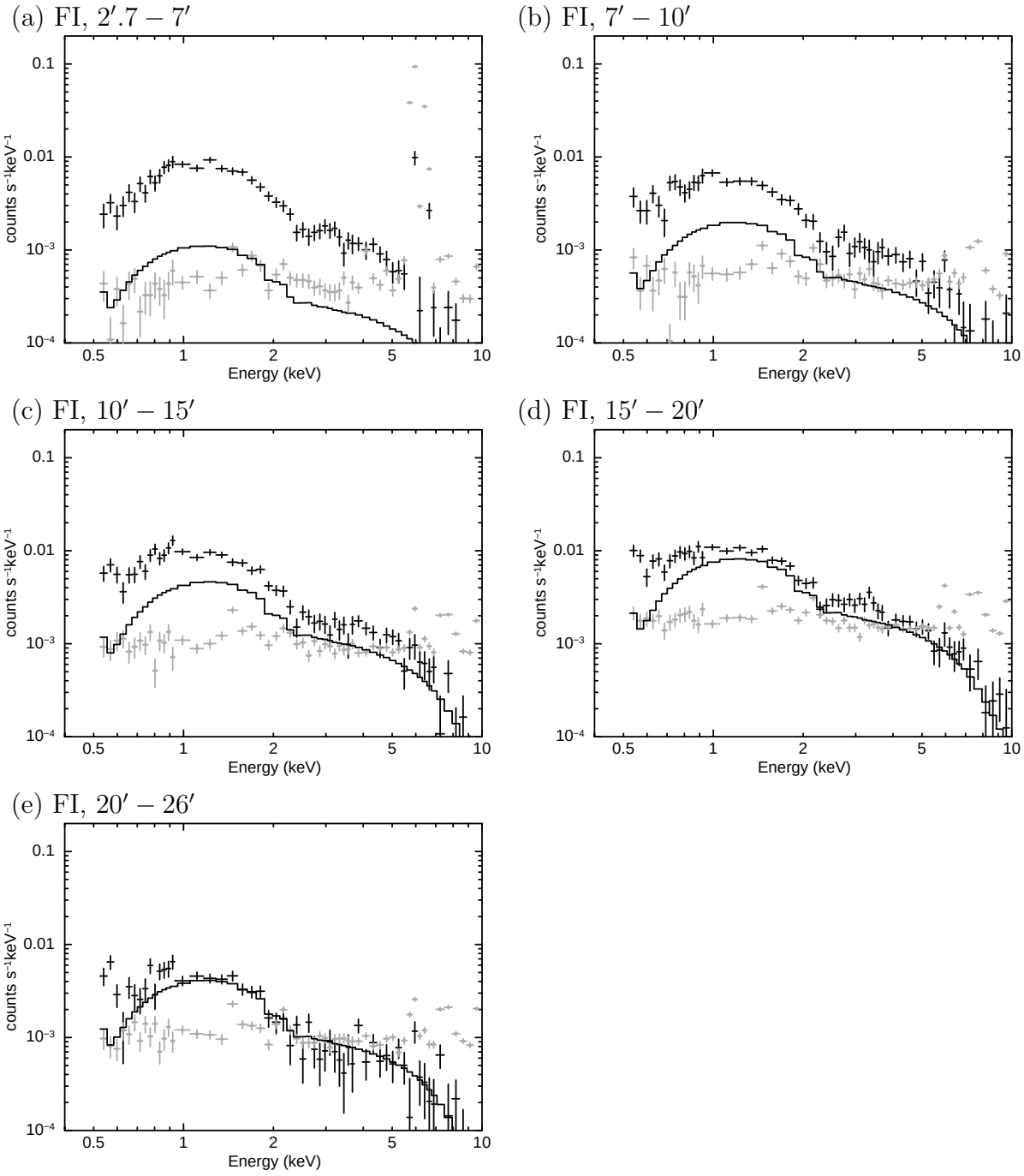

Fig. C.2: A1413 spectra for the individual annular regions observed with the FI sensors. The total observed spectrum minus the estimated NXB is the black crosses, the estimated NXB is the grey crosses, and the fitted CXB component is the solid line. The screening used are COR2 > 8 GV and $100 <$ PINUD < 300 cts s^{-1}. ^{55}Fe calibration source regions, namely *calmask*, are excluded except for (a).

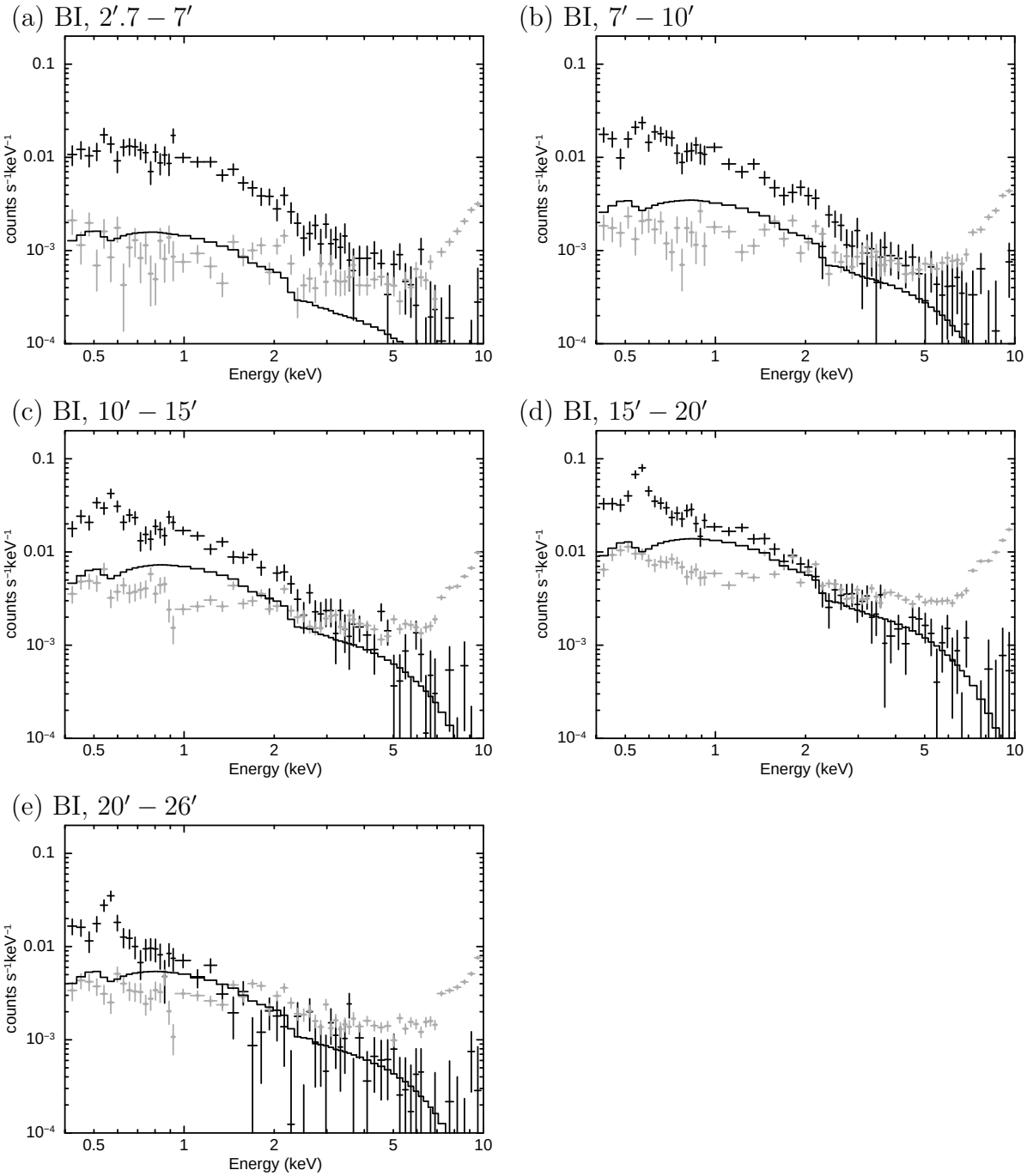

Fig. C.3: Same as figure C.2, but for the BI detector. All the ^{55}Fe calibration source regions are excluded.

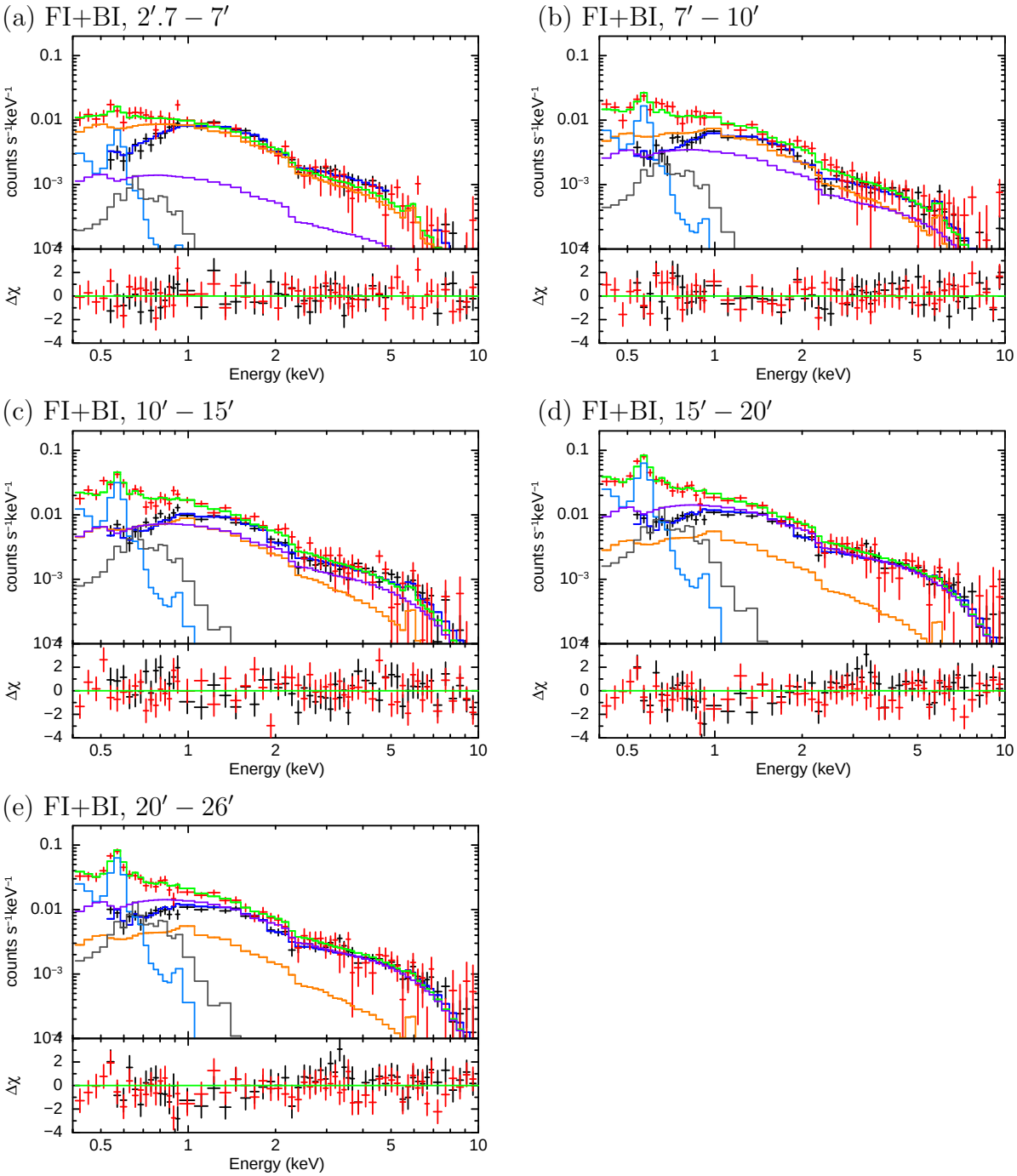

Fig. C.4: The upper panels show the observed spectra of A1413 after subtracting the NXB, that is fitted with the ICM: *wabs* × *apec* model plus the GAL+CXB: $apec_1$ + *wabs* × ($apec_2$ + *powerlaw*) model in the energy range 0.5–10 keV for FI and 0.4–10 keV for BI. The annular regions are: (a) 2′.7 – 7′, (b) 5′ – 10′, (c) 10′ – 15′, (d) 15′ – 20′, and (e) 20′ – 26′. The symbols denote BI data (red crosses), FI data (black crosses), CXB of BI (purple), $apec_1$ of BI (grey), *wabs* × $apec_2$ of BI (light blue), ICM of BI (orange), the total model spectra of BI (green), and that of FI (blue). The lower panels show the residuals in units of σ.

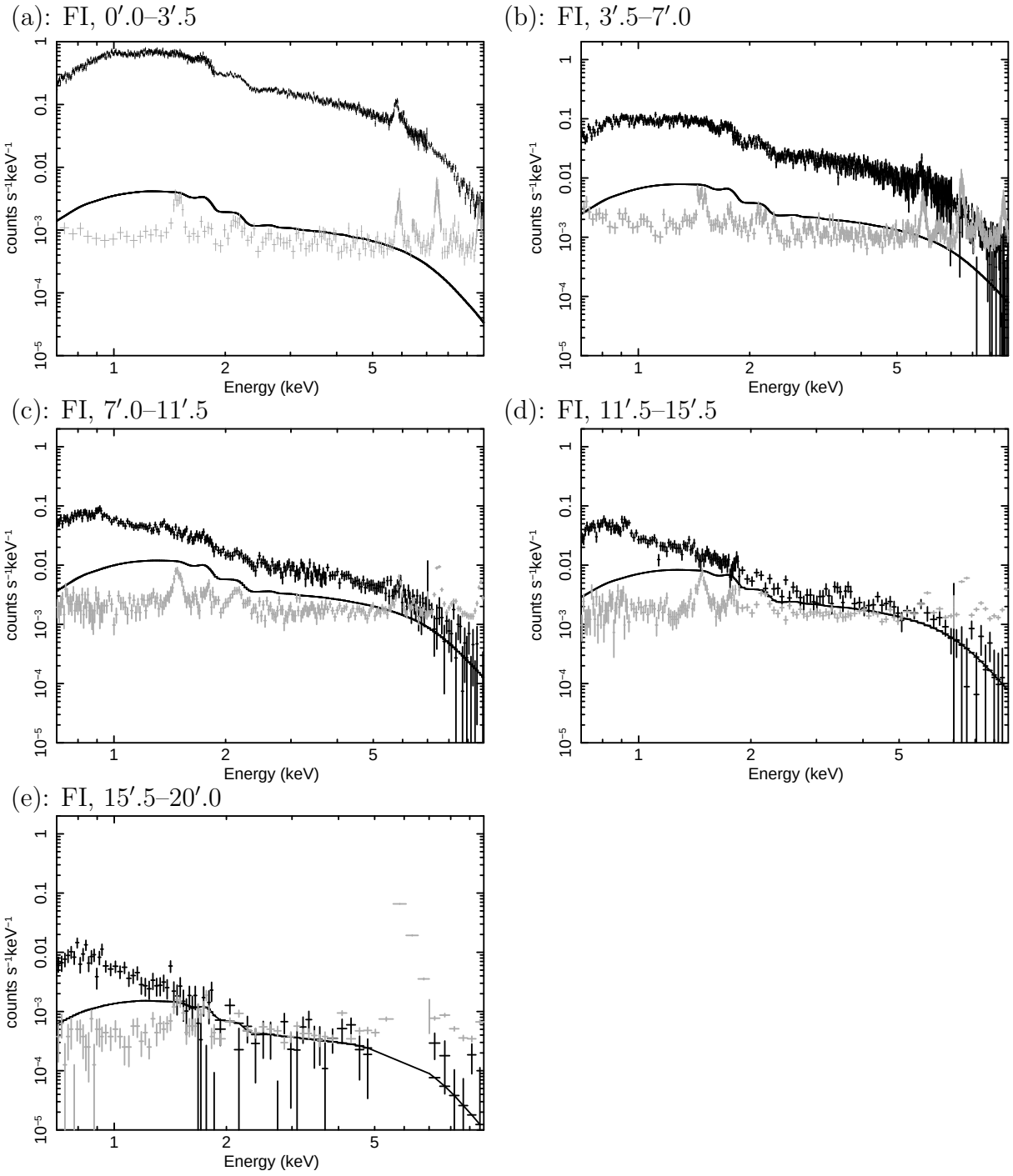

Fig. C.5: ICM and background spectra of A2204 at the annular regions for (a)–(e) FI sensors 2T-III model: The colors indicate ICM (black cross), NXB (grey cross), CXB (solid line) respectively. Estimated components of the NXB is subtracted in actual model fitting. The COR > 8GV and PINUD 100 - 300 cts/s screening are applied. The ^{55}Fe calibration source areas are excluded except (e).

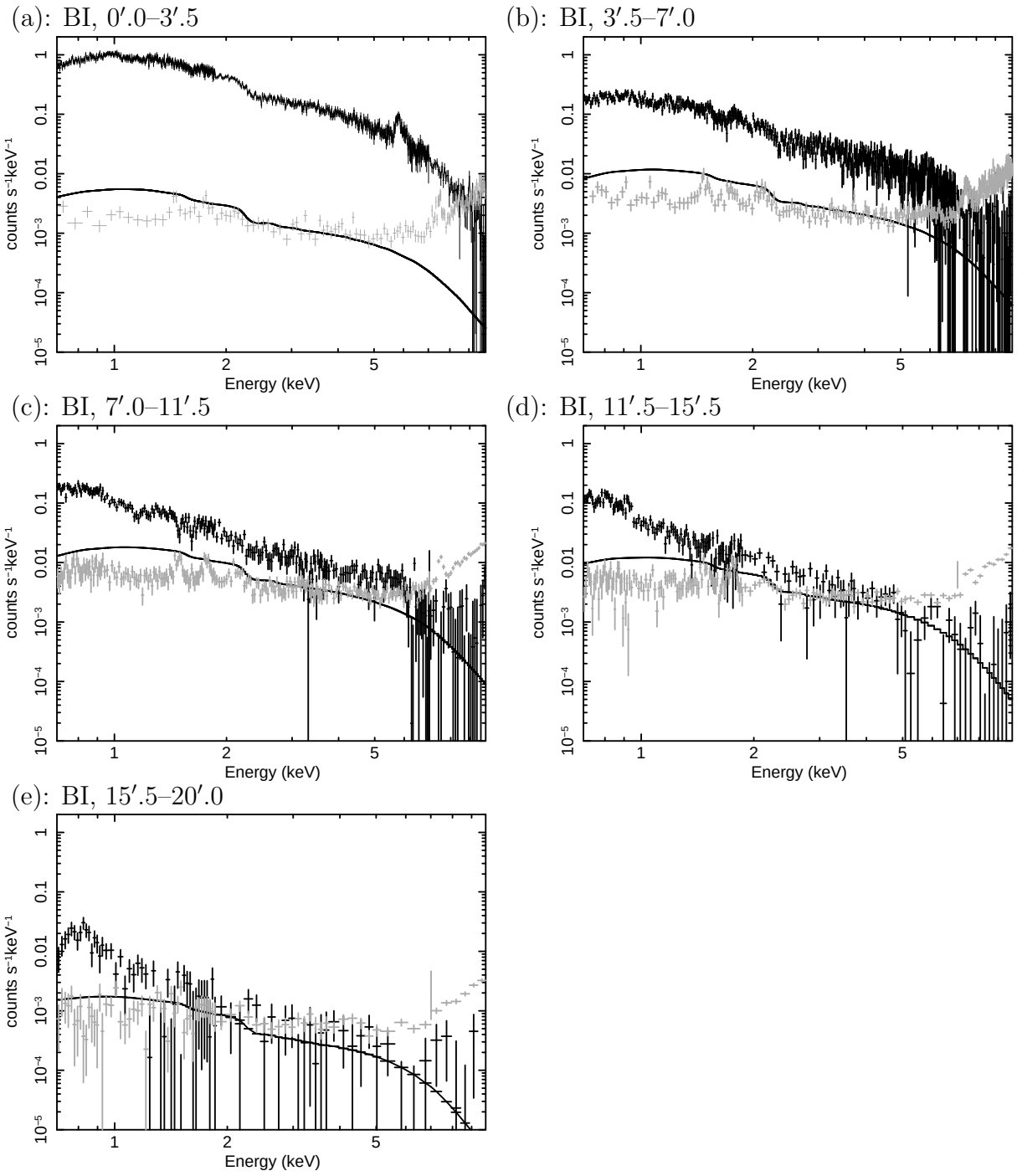

Fig. C.6: Same as figure.C.2 except for BI sensors. All ^{55}Fe calibration source areas are excluded.

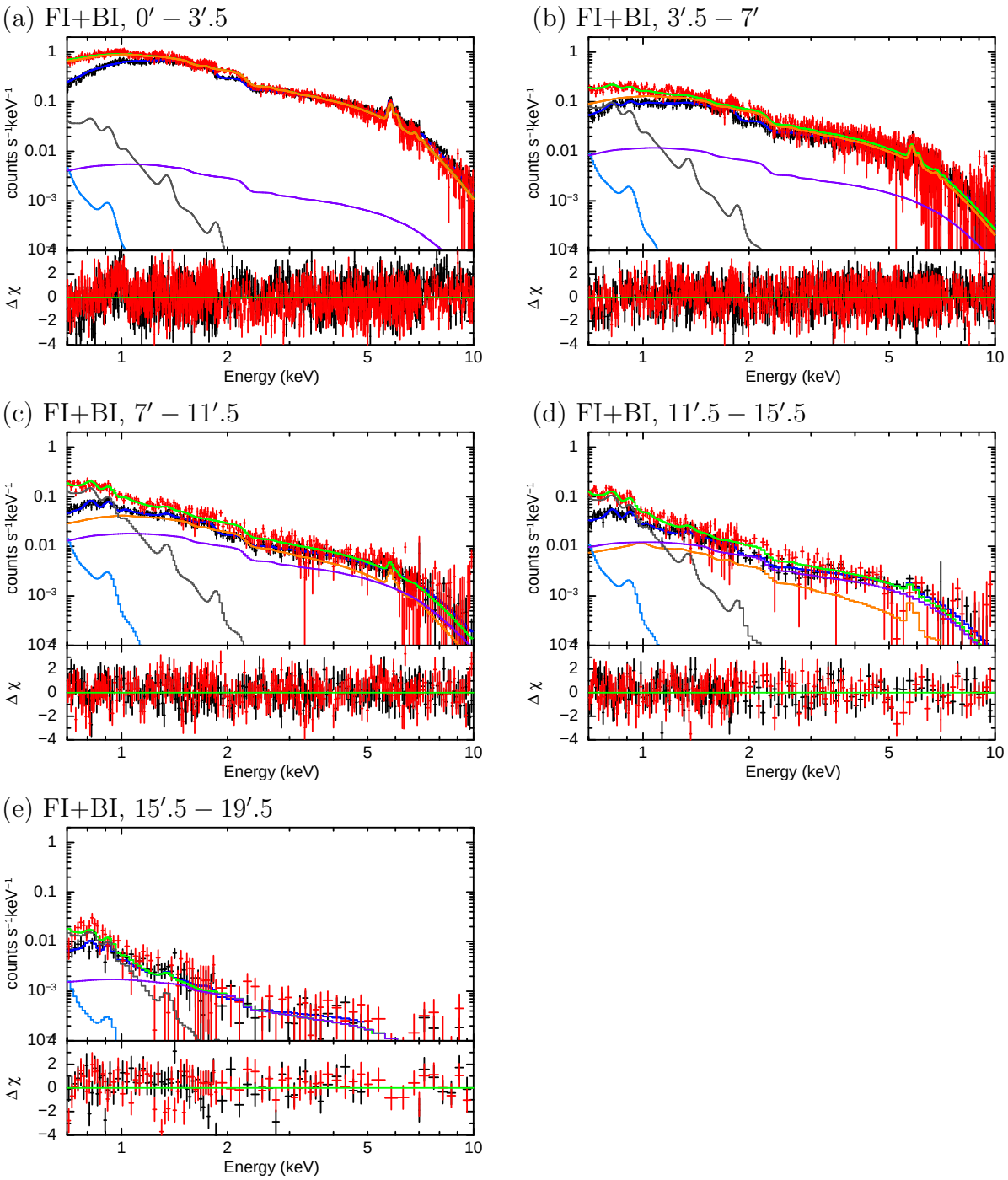

Fig. C.7: The upper panels show the observed spectra of A2204 after subtracting the NXB, that is fitted with the ICM: *phabs* × *apec* model plus the GAL+CXB: $apec_1$ + *wabs* × ($apec_2$ + *powerlaw*) model in the energy range 0.7–10 keV for FI and BI. The annular regions are: (a) 0′ – 3′.5, (b) 3′.5 – 7′, (c) 7′ – 11′.5, (d) 11′.5 – 15′.5, and (e) 15′.5 – 19′.5. The symbols denote BI data (red crosses), FI data (black crosses), CXB of BI (purple), $apec_1$ of BI (grey), *phabs* × $apec_2$ of BI (light blue), ICM of BI (orange), the total model spectra of BI (green), and that of FI (blue). The lower panels show the residuals in units of σ.

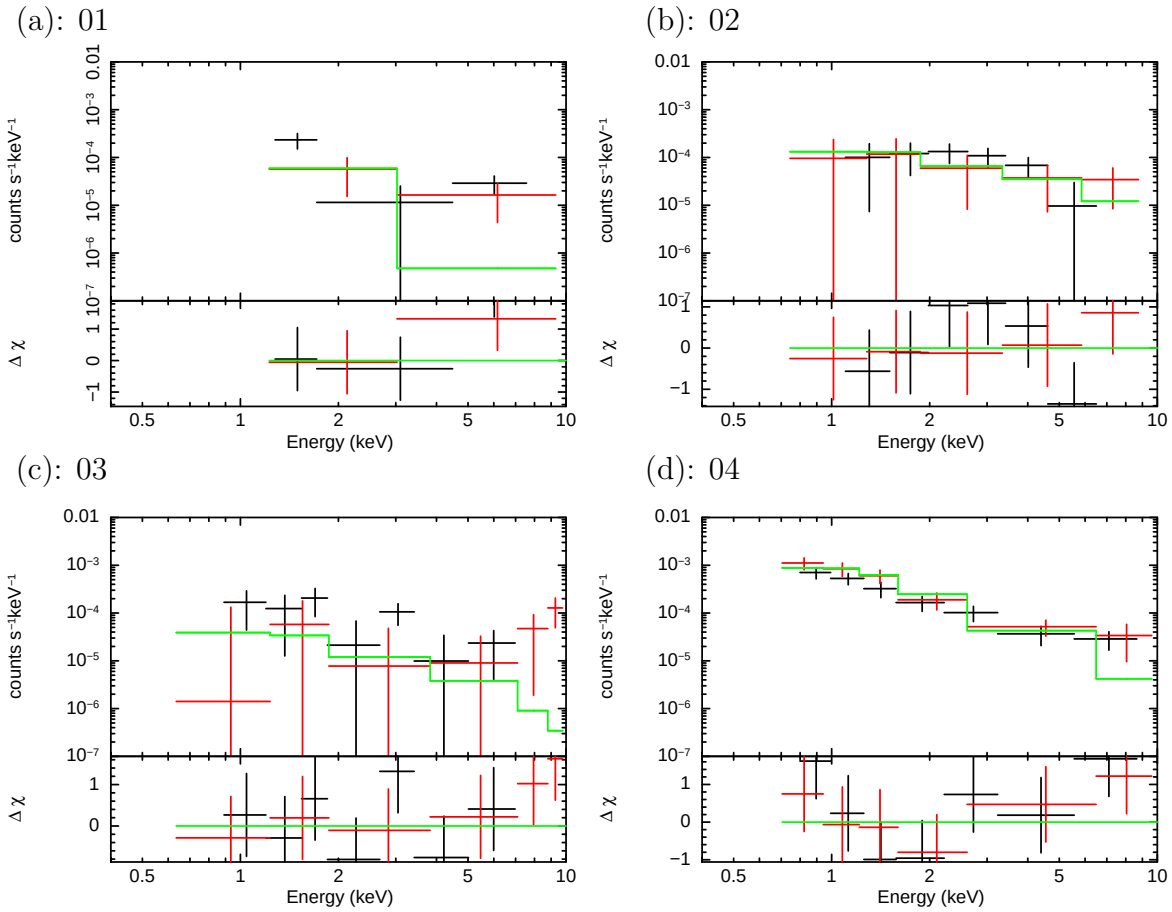

Fig. C.8: The best-fit model profiles (green) and FI (black), and BI (red) data of point source spectra detected in XIS FOV in AWM7 OFFSET East.

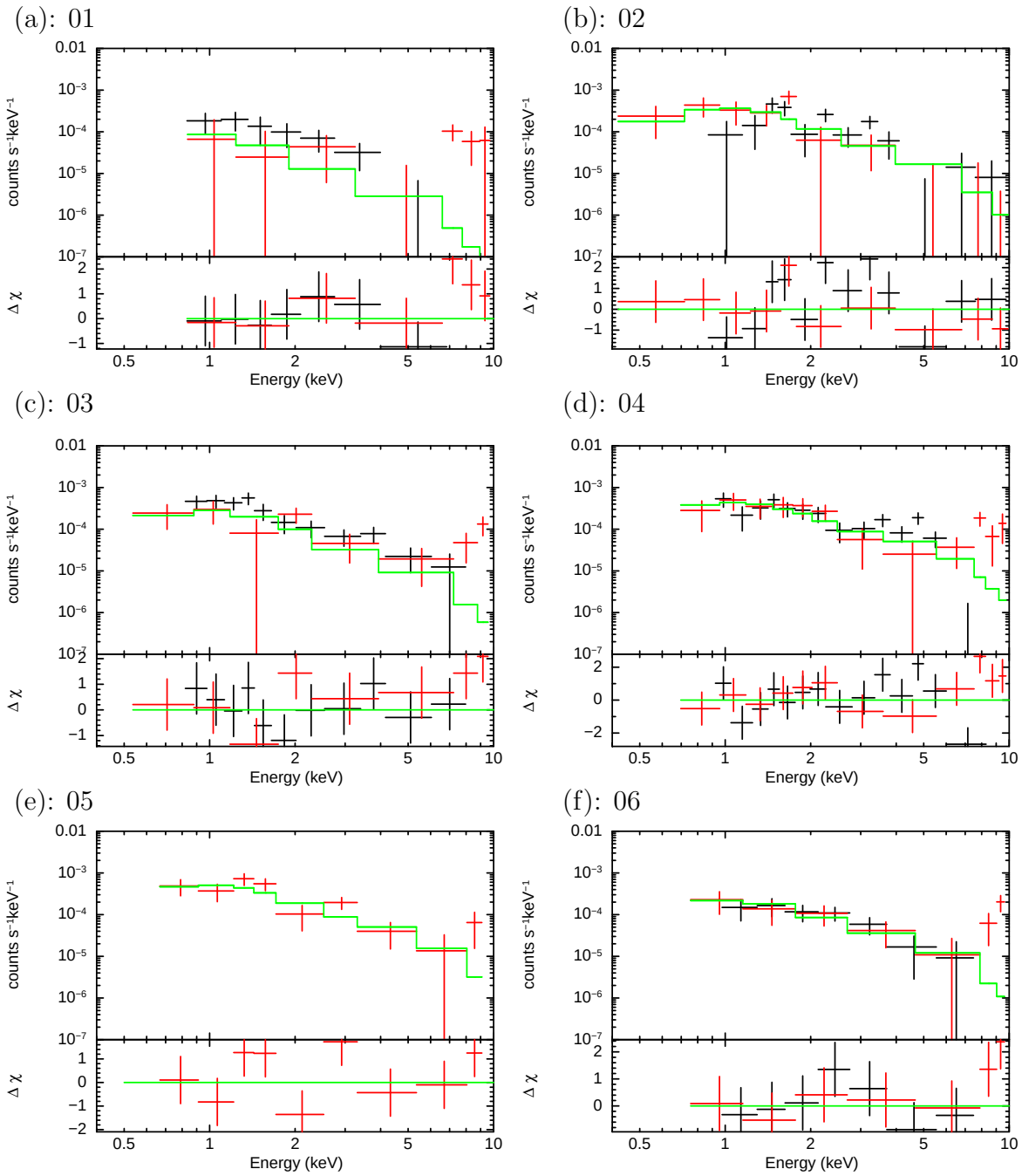

Fig. C.9: The best-fit model profiles (green) and FI (black), and BI (red) data of point source spectra detected in XIS FOV in AWM7 OFFSET South.

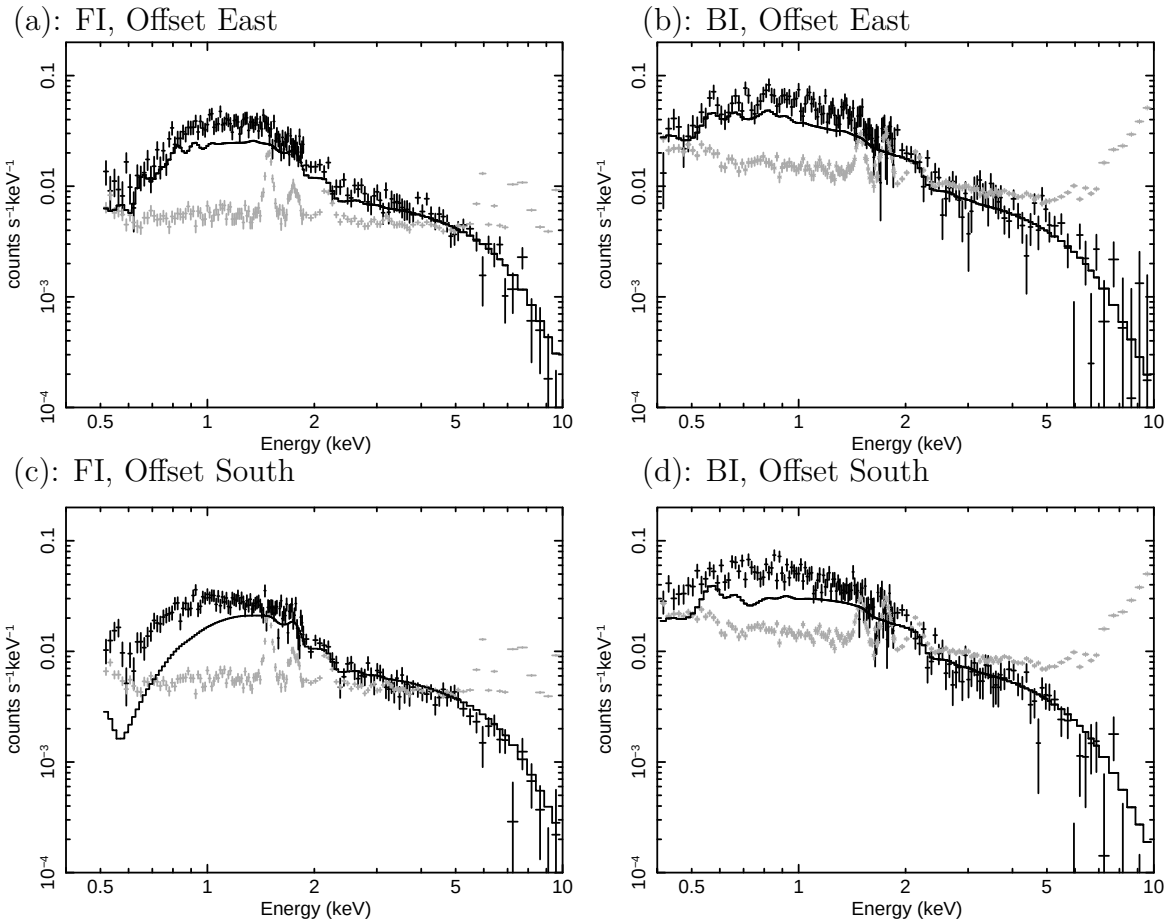

Fig. C.10: Comparison of NXB subtracted spectra (black cross) with NXB (grey cross) and CXB (black line).

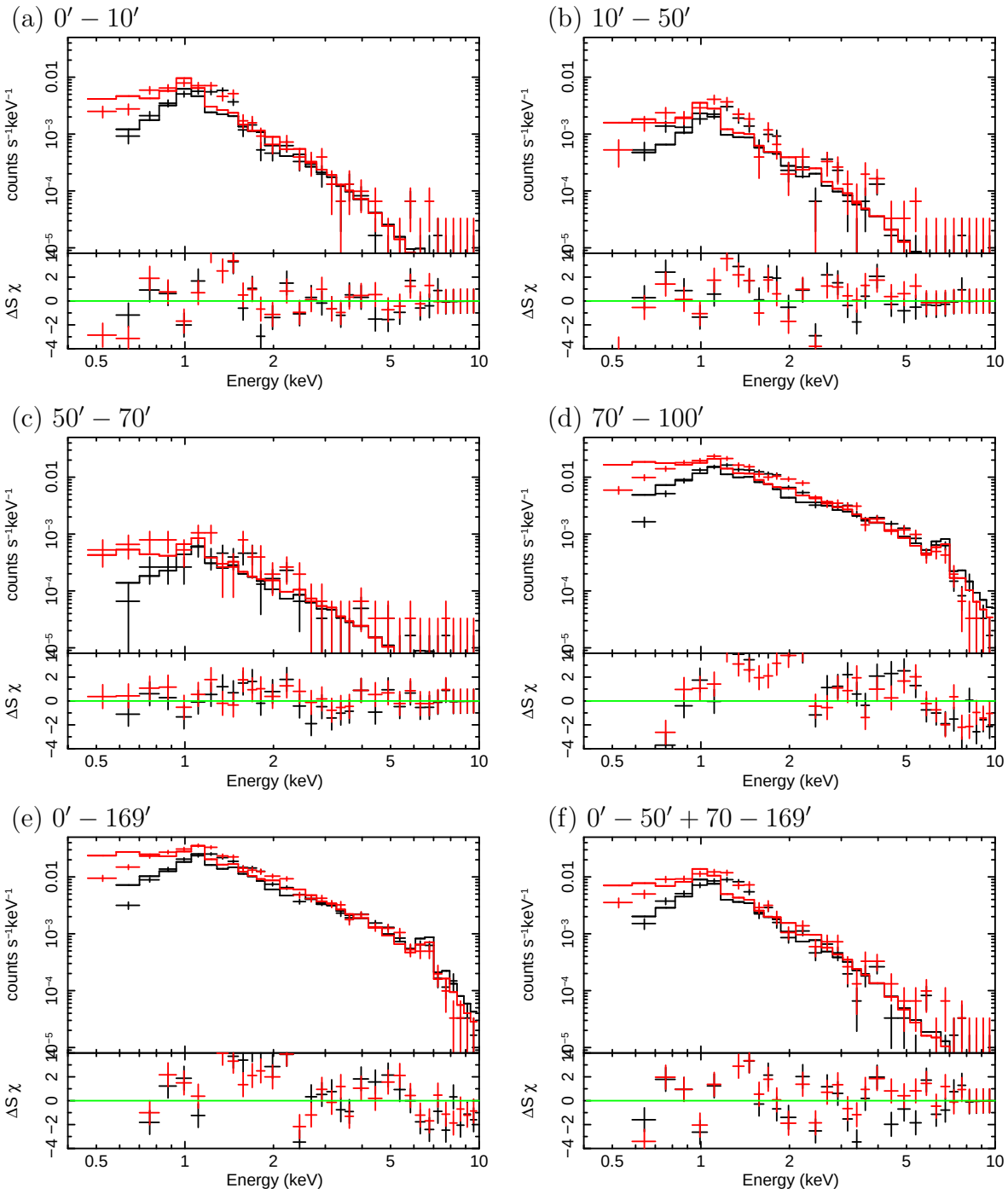

Fig. C.11: Stray photon spectra of AWM7 offset south. Red cross: BI data, black cross: FI data, red line: the best-fit model of BI, and black line: the best-fit model of FI.

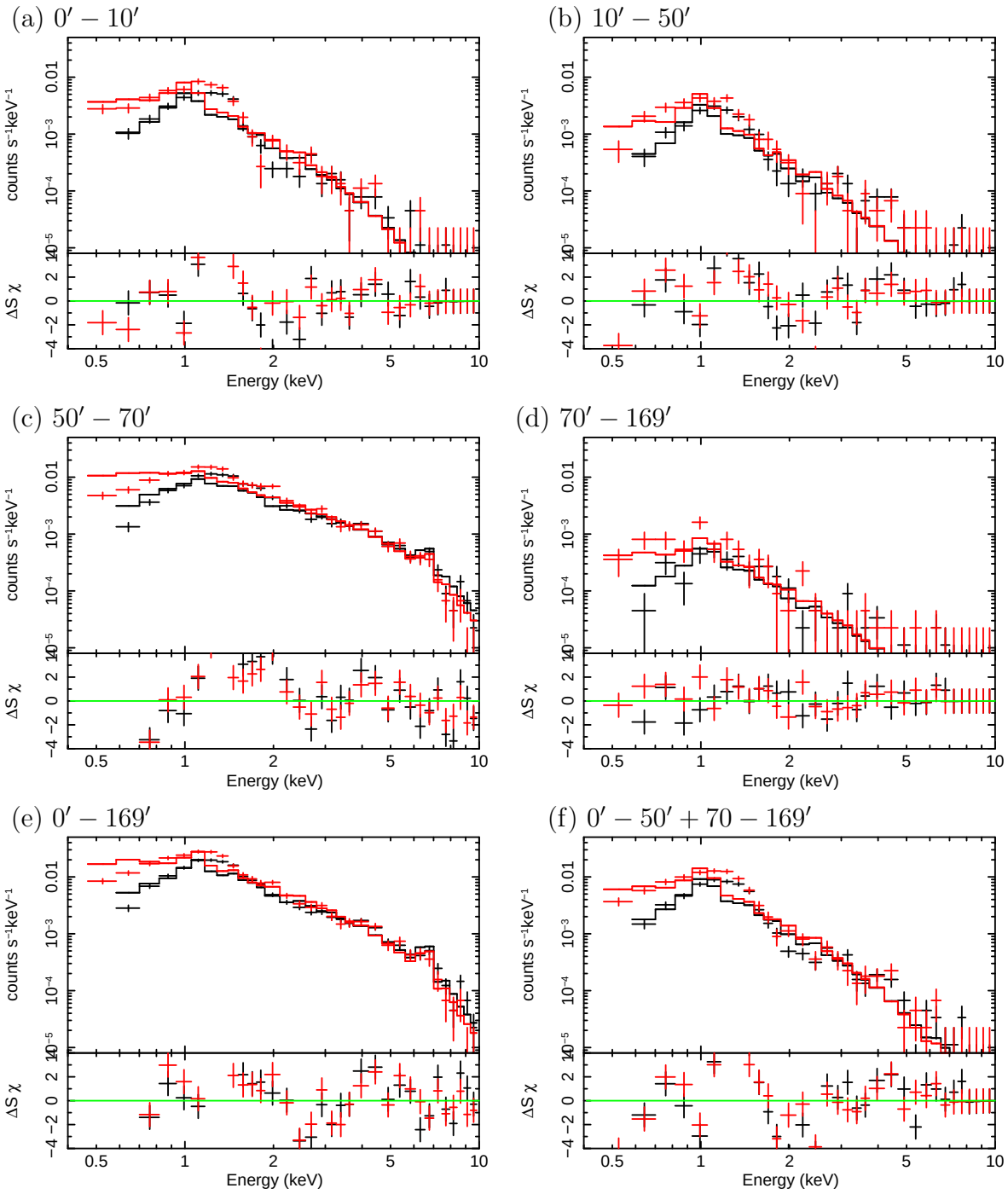

Fig. C.12: Stray photon spectra of AWM7 offset south. Red cross: BI data, black cross: FI data, red line: the best-fit model of BI, and black line: the best-fit model of FI.

Appendix D

Azimuthal surface brightness profiles

In this appendix, we show the azimuthal surface brightness profiles of AWM7 and the best-fit model.

(a): 1'-2'

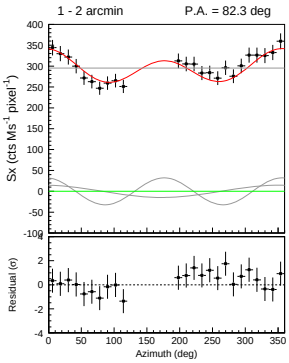

(b): 2'-3'

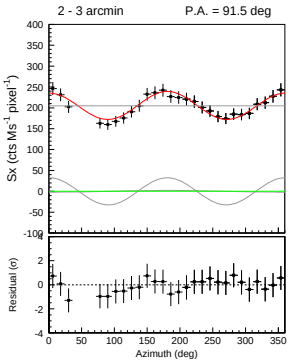

(c): 3'-4'

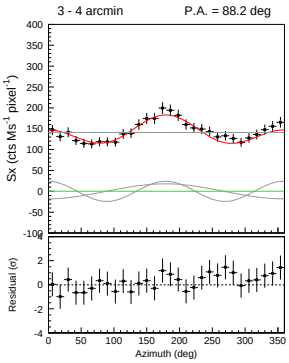

(d): 4'-5'

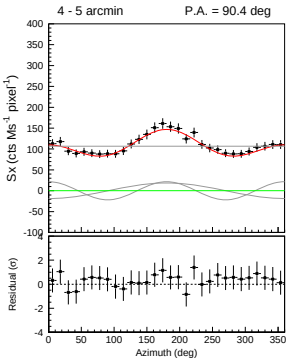

(e): 5'-6'

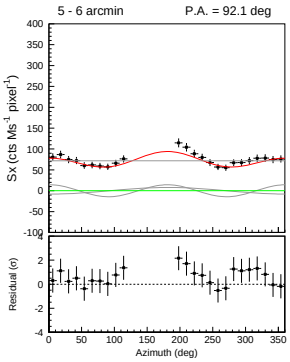

(f): 6'-7'

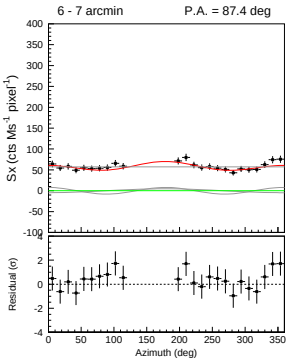

(g): 7'-8'

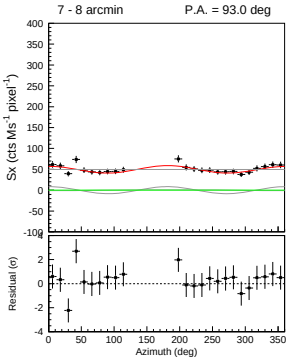

(h): 8'-9'

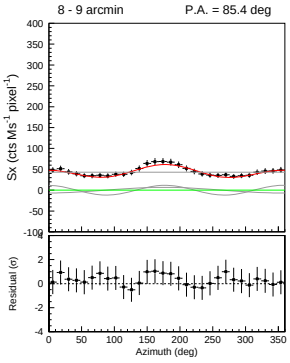

(i): 10'-11'

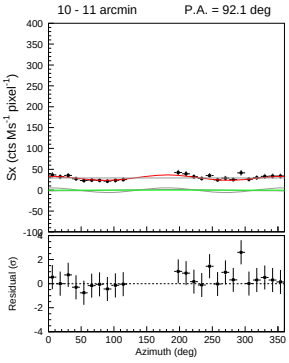

(o): 11'-12'

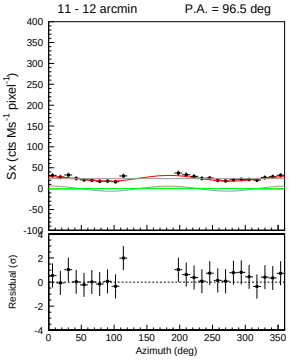

(p): 12'-13'

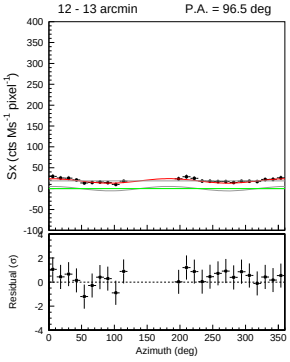

Fig. D.1: Azimuthal surface brightness profiles and the best-fit sine curve model of AWM7

Bibliography

Akahori,T., 2008, "Thermal and Dynamical Evolution of Galaxy Clusters", (Dissertation for a degree of doctor of science; Tokyo Metropolian University), 2008

Anders, E., & Grevesse, N. 1989, Geochim. Cosmochim. Acta, 53, 197

Andreon,S., Maughan,B., Trinchieri,G., Kurk,J., 2008, arXiv, 0812.1699v1

Arnaud, M., Rothenflug, R., Boulade, O., Vigroux, L., & Vangioni-Flam, E. 1992, A&A, 254, 49

Baldi, A., Ettori, S., Mazzotta, P., Tozzi, P., & Borgani, S. 2007, ApJ, 666, 835

Balucinska-Church, M., & McCammon, D., 1998, ApJ, 496, 1044

Basu,K., ZhangY.-Y., Sommer,M.W., Bender, A.N., Bertoldi, F., Dobbs, M., Eckmiller,H., Halverson, N.W., Holzapfel, W.L., Horellou, C., Jaritz, V., Johansson, D., Johnson, B., Kennedy, J., Kneissl, R., Lanting,T., Lee, A.T., Menten, K.M., Navarrete, F.P., Pacaud, F., Reichardt, C.L., Reiprich, T.H., Richards,P.L., Schwan,D., & Westbroock, B., 2009, arXiv:0911.3905v1

Bautz,M.W., Miller, E.D., Sanders,J.S., Hayashida, K., Henry, J.P., Hughes, J.P., & Tamura,T, 2009, arXiv:0906.3515v1

Böhringer, H., et al. 2000, ApJS, 129, 435

Böhringer, H., Matsushita, K., Churazov, E., Finoguenov, A., & Ikebe, Y. 2004, A&A, 416, L21

Borgani,S., Diaferio,A.,Dolag,K.,& Schindler,S., 2007, EAS Publications Series, 24, 145

Borgani,S., & Guzzo,L., 2001, Nature, 409, 39-45

Borgani, S., et al. 2004, MNRAS, 348, 1078

Borgani, S., et al. 2006, MNRAS, 367, 1641

Bryan,G,L. and Norman, M.L., 1998, ApJ, 495, 80

Bullock, J. S., Kolatt, T. S., Sigad, Y., Somerville, R. S., Kravtsov, A. V., Klypin, A. A., Primack, J. R. and Dekel, A., 2001, MNRAS, 321, 559

Condon,J.J. 1974, AJ, 188, 279

De Grandi, S., & Molendi, S. 2002, ApJ, 567, 163

De Grandi, S., Ettori, S., Longhetti, M., & Molendi, S. 2004, A&A, 419, 7

De Luca,A., & Molendi, S., 2004, A&A, 419, 837

Dickey, J. M., & Lockman, F. J. 1990, ARA&A, 28, 215

Dubinski, J., and Carlberg, R.G., 1991, ApJ, 378, 496

Eke,V.,R., Navarro,J.,F., & Frenk,C.,S., 1998, ApJ, 503, 569

Eke, V. R. and Navarro, J. F. and Steinmetz, M., 2001, ApJ, 554, 114

Evrard, A. E., Metzler, C. A., & Navarro, J. F., 1996, ApJ, 469, 494

Ezawa, H., Fukazawa, Y., Makishima, K., Ohashi, T., Takahara, F., Xu, H., & Yamasaki, N. Y. 1997, ApJL, 490, L33+

Fabricant, D., Lecar, M., & Gorenstein, P. 1980, ApJ, 241, 552

Feldman, U. 1992, Phys. Scr., 46, 202

Finoguenov, A. and Ponman, T. J., 1999, MNRAS, 395, 325

Finoguenov, A., David, L. P., & Ponman, T. J. 2000, ApJ, 544, 188

Finoguenov, A., Arnaud, M., & David, L. P. 2001, ApJ, 555, 191

Finoguenov, A., Matsushita, K., Böhringer, H., Ikebe, Y., & Arnaud, M. 2002, A&A, 381, 21

Fox,D.,C., & Loeb,A., 1997, ApJ, 491, 459

Fukazawa, Y., Makishima, K., Tamura, T., Ezawa, H., Xu, H., Ikebe, Y., Kikuchi, K., & Ohashi, T. 1998, PASJ, 50, 187

Fukazawa, Y., Makishima, K., Tamura, T., Nakazawa, K., Ezawa, H., Ikebe, Y., Kikuchi, K., & Ohashi, T. 2000, MNRAS, 313, 21

Fukazawa, Y., Kawano, N., & Kawashima, K. 2004, ApJL, 606, L109

Fukugita, M, Hogan, C.J., & Peebles,P.J.E., 1998, ApJ,503, 518

Fujita, Y, Tawa, N., Hayashida, K., Takizawa, M., Matsumoto,H., Okabe, N., &, Reiprich,T., 2008, PASJ, 60, S343

Gehrels,N. and Williams, E.D., 1993, ApJL, 418, 25

Gendreau,K.C., Mushotzky,R., Fabian,A.C., et al., 1995, PASJ, 47, L5

George,M.R., Fabian, A. C., Sanders,J. S., Young., A. J., and Russell, H. R., 2008, MNRAS, 395, 657

Gruber,D. E., Matteson,J.L., Peterson,L.E., & Jung, G.V., 1999, ApJ, 520, 124

Gunn, J.E. and Gott, III,J.R., 1972, ApJ, 176, 1

Hayakawa, A., Hoshino, A., Ishida, M., Furusho, T., Yamasaki, N. Y., & Ohashi, T. 2006, PASJ, 58, 695

Hayakawa, A. 2006, PhD thesis, Tyokyo Metropolitan Univ., (2006)

Hashimoto,Y., Barcons,X., Böhringer,H., Fabian,A.C., Hasinger,G.,Mainieri,V., Brunner,H., 2004, A&A, 417, 819

Hayashida,K. 1989, *PhD. dissertation of Univ. of Tokyo*, ISAS RN 466

Hayashida, K., Inoue, H., Koyama, K., 1989, PASJ, 41, 1373

Henry, J. P. 2000, ApJ, 534, 565

Henry, J. P., Evrard, A. E., Hoekstra, H., Babul, A., & Mahdavi, A. 2009, ApJ, 691, 1307

Hickox,R.C.,& Markevitch, M., 2006, ApJ, 645, 95

Ishisaki,Y. 1997, *PhD. dissertation of Univ. of Tokyo*, ISAS RN 613

Ishisaki, Y., et al. 2007, PASJ, 59, 113

Jansen, F., Lumb, D., Altieri, B., Clavel, J., Ehle, M., Erd, C., Gabriel, C., Guainazzi, M., Gondoin, P., Much, R., Munoz, R., Santos, M., Schartel, N., Texier, D., & Vacanti, G. 2001, A&A, 365, L1

Kriss, G. A. and Cioffi, D. F. and Canizares, C. R., 1983, ApJ, 272, 439

Kawaharada, M., Okabe, N., Umetsu,K., Takizawa,M., Matsushita, K., Fukazawa, Y., Hamana, T., Miyazaki,S., Nakazawa, K., & Ohashi, T., 2010 in print

Kokubun, M., Makishima, K., Takahashi, T., Murakami, T., Tashiro, M., Fukazawa, Y., Kamae, T., Madejski, G. M., Nakazawa, K., Yamaoka, K., Terada, Y., Yonetoku, D., Watanabe, S., Tamagawa, T., Mizuno, T., Kubota, A., Isobe, N., Takahashi, I., Sato, G., Takahashi, H., Hong, S., Kawaharada, M., Kawano, N., Mitani, T., Murashima, M., Suzuki, M., Abe, K., Miyawaki, R., Ohno, M., Tanaka, T., Yanagida, T., Itoh, T., Ohnuki, K., Tamura, K., Endo, Y., Hirakuri, S., Hiruta, T., Kitaguchi, T., Kishishita, T., Sugita, S., Takahashi, T., Takeda, S., Enoto, T., Hirasawa, A., Katsuta, J., Matsumura, S., Onda, K., Sato, M., Ushio, M., Ishikawa, S., Murase, K., Odaka, H., Suzuki, M., Yaji, Y., Yamada, S., Yamasaki, T., & Yuasa, T. 2006, ArXiv Astrophysics e-prints

Komatsu, E., & Seljak, U. 2002, MNRAS, 336, 1256

Komatsu,E., Dunkley,J., Nolta,M.R., Bennett,C.L., Gold,B., Hinshaw,G., Jarosik,N., Larson,D., Lomon,M., Page,L., Spergel,N.D., Halpern,.M, Hill,.M., Hill,R.S., Kogut,A., Meyer,S.S., Tucker,G.S., Weiland,J.L., Wollanck,E., Wright,E.L., 2008, ArXiv, 0803.0547K

Koyama, K., et al. 2007, PASJ, 59, 23

Kushino, A., Ishisaki, Y., Morita, U., Yamasaki, N. Y., Ishida, M., Ohashi, T., & Ueda, Y. 2002, PASJ, 54, 327

Loken, C., Norman, M. L., Nelson, E., Burns, J., Bryan, G. L., & Motl, P. 2002, ApJ, 579, 571

Lumb, D. H., Warwick, R. S., Page, M., & De Luca, A. 2002, A&A, 389, 93

Makishima, K., Ezawa, H., Fukuzawa, Y., Honda, H., Ikebe, Y., Kamae, T., Kikuchi, K., Matsushita, K., Nakazawa, K., Ohashi, T., Takahashi, T., Tamura, T., & Xu, H. 2001, PASJ, 53, 401

Makino, N., Suto,Y., Sasaki, S., 1998, ApJ, 497, 555

Markevitch, M., Forman, W. R., Sarazin, C. L., & Vikhlinin, A. 1998, ApJ, 503, 77

Matsushita, K. 1997, PhD thesis, Ph. D. thesis, Univ. Tokyo, (1997)

Matsushita, K., Finoguenov, A., & Böhringer, H. 2003, A&A, 401, 443

Matsushita, K., Böhringer, H., Takahashi, I., & Ikebe, Y. 2007, A&A, 462, 953

Mazzotta,P., Rasiz,E., Moscardini,L., & Tormen,G., 2004, MNRAS, 354, 10

McCammon,D., Burrows,D.N., Sanders,W.T., & Kraushaar, W.L., 1983, ApJ, 269, 107

Misaki, K., Kunieda, H., Maeda, Y., Haba, Y., Itoh, K., Mori, H., Iizuka, R., Itoh, A., Inoue, H., Okada, S., Yokoyama, Y., Ogasaka, Y., Tamura, K., Furuzawa, A., Shibata, R., Tanaka, T., Naitou, M., Ishida, M., Hayakawa, A., Inoue, C., Hayashi, A., Shimizu, T., Serlemitsos, P. J., Soong, Y., Chan, K.-W., Okajima, T., & Lehan, J. P. 2004, in Optics for EUV, X-Ray, and Gamma-Ray Astronomy. Edited by Citterio, Oberto; O'Dell, Stephen L. Proceedings of the SPIE, Volume 5168, pp. 294-305 (2004)., ed. O. Citterio & S. L. O'Dell, 294–305

Mitsuda, K., et al. 2007, PASJ, 59, 1

Moretti,A.,Pagani, C., Cusumano,G. et. al., 2008, ArXiv e-prints,0811.1444M

Mori, H., Iizuka, R., Shibata, R., Haba, Y., Hayakawa, A., Hayashi, A., Inoue, C., Inoue, H., Ishida, M., Itoh, A., Itoh, K., Kunieda, H., Maeda, Y., Misaki, K., Naitou, M., Okada, S., Shimizu, T., & Yokoyama, Y. 2005, PASJ, 57, 245

Navarro, J. F., Frenk, C. S., & White, S. D. M. 1996, ApJ, 462, 563

Navarro, J. F. and Frenk, C. S. and White, S. D. M., 1997, ApJ, 490, 493

Neumann, D. M. and Boehringer, H., 1995, A&A, 308, 865

Peterson, J. R., et al. 2001, A&A, 365, L104

Piffaretti, R., Jetzer, P., Kaastra, J. S., & Tamura, T. 2005, A&A, 433, 101

Pointecouteau, E., Arnaud, M., & Pratt, G. W. 2005, A&A, 435, 1

Ponman, T. J., Sanderson, A. J. R., & Finoguenov, A. 2003, MNRAS, 343, 331

Pratt, G. W., & Arnaud, M. 2002, A&A, 394, 375

Pratt, G. W., & Arnaud, M. 2005, A&A, 429, 791

Pratt, G. W., Böhringer, H., Croston, J. H., Arnaud, M., Borgani, S., Finoguenov, A., & Temple, R. F. 2007, A&A, 461, 71

Pratt, G. W., Arnaud, M., Piffaretti, R., Böhringer,H., Ponman, T.J., Croston, J.H., Voit,G.M., & Borgani, S., 2009, astroph, arXiv:0909.3776

Rasia, E., Mazzotta,P., Bologani,S., Moscardini,L., Dolag,K., Tormen,G., Diaferio,A., Murante,G., 2005, ApJ, 618,L1

Reiprich,T. H., Hudson, D.S., Zhang,Y.-Y., Sato,K, Ishisaki,Y., Hoshino,A, Ohashi,T, Ota,N, & Fujita, Y, 2009, A&A, 501, 899

Rees,M.J., 1992, in NATO ASIC Proc., 366: "Clusters and Superclusters of Galaxies", 1-10

Renzini, A., Ciotti, L., D'Ercole,A., & Pellegrini, S. 1993, ApJ, 419, 52

Revnivtsev,M., Gilfanov,M.,Sunyaev,R., Jahoda,K.,& Markwardt, C., 2003, A&A, 411, 329

Revnivtsev, M., Gilfanov,M., Jahoda,K.,& Sunyaev, R., 2005, A&A, 444, 381

Roncarelli, M., Ettori, S., Dolag, K., Moscardini, L., Borgani, S., & Murante, G. 2006, MNRAS, 373, 1339

Rudd,D.H., & Nagai,D., 2009, ApJ, 701, L16

Sanders,J.S., Fabian,A,C, & Taylor, G.B., 2009 MNRAS, 393, 71

Sarazin,C.L., 1986, Rev. Mod. Phys., 58, 1

Sarazin,C.L., 1988, "X-ray emission from clusters of galaxies", (Cambridge: Cambridge University Press), ch2, 4, 5

Sato, K. 2007, PhD thesis, Ph. D. thesis,Tokyo Metropolitan Univeristy, (2007)

Sato, K., Matsushita, K., Ishisaki, Y., Yamasaki, N. Y., Ishida, M., Sasaki, S., Ohashi, T., 2008, PASJ, 60, 333

Serlemitsos, P. J., et al. 2007, PASJ, 59, 9

Snowden,S.L., Mushotzky, R,F., Kuntz,K.D., & Davis,D.S, 2008, A&A, 478 , 615

Spitzer,L.Jr., 1956, Physics of Fully Ionized Gases, New York: Interscience

Struble, M. F. and Rood, H. J., 1987, ApJ, 323, 468

Suto,Y., Sasaki, S., Makino, N. 1998, ApJ, 509, 544

Takahashi, T. e. a. 2007, PASJ, 57, 743

Takahashi, T., et al. 2008, Proc. SPIE, 7011,

Takizawa,M., 1998, ApJ, 509, 579

Takizawa,M., & Mineshige,S., 1998, ApJ, 499, 82

Tamura, T., Kaastra, J. S., Makishima, K., & Takahashi, I. 2003, A&A, 399, 497

Tamura, T., Kaastra, J. S., den Herder, J. W. A., Bleeker, J. A. M., & Peterson, J. R. 2004, A&A, 420, 135

Tawa, N., et al. 2008, PASJ, 60, 11

Tawa, N., 2008, ISAS Research Note 839

Tsuru, T., Ikebe, Y., Ohashi, T., Makishima, K., Hatsukade, I., Yamashita, K., Forman, W. and Arnaud, M., 1992, Frontiers Science Series, 485

Turner, M. J. L., Reeves, J. N., Ponman, T. J., Arnaud, M., Barbera, M., Bennie, P. J., Boer, M., Briel, U., Butler, I., Clavel, J., Dhez, P., Cordova, F., Dos Santos, S., Ferrando, P., Ghizzardi, S., Goodall, C. V., Griffiths, R. G., Hochedez, J. F., Holland, A. D., Jansen, F., Kendziorra, E., Lagostina, A., Laine, R., La Palombara, N., Lortholary, M., Mason, K. O., Molendi, S., Pigot, C., Priedhorsky, W., Reppin, C., Rothenflug, R., Salvetat, P., Sauvageot, J., Schmitt, D., Sembay, S., Short, A., Strüder, L., Trifoglio, M., Trümper, J., Vercellone, S., Vigroux, L., Villa, G., & Ward, M. 2001, A&A, 365, L110

Vecchi,A., Molendi,S.,Guainazzi,M., Fiore,F.,& Parmar, A.N., 1999, A&A, 349, L73

Vikhlinin, A., Markevitch, M., Murray, S. S., Jones, C., Forman, W., & Van Speybroeck, L. 2005, ApJ, 628, 655

Vikhlinin, A., Kravtsov, A., Forman, W., Jones, C., Markevitch, M., Murray, S. S., & Van Speybroeck, L. 2006, ApJ, 640, 691

Voit,G,M.,2005,RvMP,77,207

Wechsler, R. H. Bullock, J. S., Primack, J. R., Kravtsov, A. V. & Dekel, A., 2002, ApJ, 568, 52

Wong, K.-W., & Sarazin, C.L., 2009, ApJ, 707, 1141

Xu, H., Ezawa, H., Fukazawa, Y., Kikuchi, K., Makishima, K., Ohashi, T., & Tamura, T. 1997, PASJ, 49, 9

Zhang, Y.-Y., Böhringer, H., & Finoguenov,A., 2005,Adv.Sp.Res, 36, 667

Zhang, Y.-Y., Finoguenov,A., Böhringer, H., Kneib, J.-P., Smith, C.P., Czoske,O.,& Soucail,G., 2007,A&A, 467, 437